

*EIT Reconstruction Algorithms for Respiratory
Intensive Care*

Crabb, Michael

2014

MIMS EPrint: **2014.75**

Manchester Institute for Mathematical Sciences
School of Mathematics

The University of Manchester

Reports available from: <http://eprints.maths.manchester.ac.uk/>

And by contacting: The MIMS Secretary
School of Mathematics
The University of Manchester
Manchester, M13 9PL, UK

ISSN 1749-9097

EIT RECONSTRUCTION ALGORITHMS FOR RESPIRATORY INTENSIVE CARE

A THESIS SUBMITTED TO THE UNIVERSITY OF MANCHESTER
FOR THE DEGREE OF DOCTOR OF PHILOSOPHY
IN THE FACULTY OF ENGINEERING AND PHYSICAL SCIENCES

2014

Michael Crabb
School of Mathematics

Contents

| | |
|---|-----------|
| Abstract | 12 |
| Declaration | 13 |
| Copyright Statement | 14 |
| Acknowledgements | 15 |
| Abbreviations | 17 |
| 1 Introduction to lung EIT | 18 |
| 1.1 Respiratory monitoring | 19 |
| 1.2 Current state | 20 |
| 1.3 Future challenges | 22 |
| 1.3.1 Boundary shape and dimension | 22 |
| 1.3.2 Forward modelling | 23 |
| 1.3.3 Spatial resolution testing | 24 |
| 1.3.4 Clinically meaningful parameters | 24 |
| 1.3.5 Anisotropic media | 25 |
| 1.4 Thesis Outline | 26 |
| 2 Forward modelling in EIT | 27 |
| 2.1 Conductivity equation | 27 |
| 2.1.1 Electrode modelling | 28 |
| 2.1.2 Weak formulation | 30 |
| 2.2 High order finite elements | 33 |
| 2.2.1 Reference elements and boundaries | 37 |

| | | |
|----------|--|-----------|
| 2.2.2 | Polynomial approximation | 41 |
| 2.2.3 | Convergence study | 43 |
| 2.3 | Conclusions | 50 |
| 2.3.1 | Modelling errors and lung EIT | 52 |
| 3 | Inverse problem in EIT | 53 |
| 3.1 | Ill-posed inverse problems | 54 |
| 3.1.1 | Mild and severe ill-posedness | 55 |
| 3.1.2 | Singular value decomposition | 57 |
| 3.1.3 | Reconstruction algorithms for ill-posed problems | 58 |
| 3.2 | The Dirichlet-to-Neumann map | 60 |
| 3.2.1 | Fréchet differentiability | 61 |
| 3.2.2 | Numerical approximation | 62 |
| 3.2.3 | Calderón fields | 64 |
| 3.3 | Non-linear inverse conductivity problem | 65 |
| 3.3.1 | Boundary identifiability | 65 |
| 3.3.2 | Interior determination | 67 |
| 3.3.3 | Exact reconstruction methods and lung EIT | 69 |
| 3.4 | Anisotropic media | 71 |
| 3.4.1 | Geometric problem | 72 |
| 3.4.2 | Non-uniqueness result | 75 |
| 3.4.3 | Elasticity | 77 |
| 3.4.4 | Anisotropy with eigenspace constraints | 82 |
| 4 | Shape and electrode position corrections | 89 |
| 4.1 | Inaccurately known external shape | 89 |
| 4.2 | Global uniqueness | 91 |
| 4.2.1 | Configuration manifolds | 91 |
| 4.2.2 | Conformal flatness | 93 |
| 4.3 | Reconstruction algorithms | 97 |
| 4.3.1 | Fréchet differentiability: Continuum model | 98 |
| 4.3.2 | Fréchet differentiability: CEM | 105 |
| 4.3.3 | Shape derivative calculation | 109 |

| | | |
|----------|--|------------|
| 4.3.4 | Simultaneous retrieval procedure | 111 |
| 4.4 | Numerical results | 117 |
| 4.4.1 | Sensitivity study | 117 |
| 4.4.2 | Simultaneous reconstruction | 122 |
| 4.5 | Conclusions | 126 |
| 5 | MRI-informed dynamic lung EIT | 168 |
| 5.1 | Data collection and model generation | 168 |
| 5.1.1 | MRI and EIT data collection | 168 |
| 5.1.2 | Finite element model generation | 169 |
| 5.2 | Dynamic reconstruction algorithms | 170 |
| 5.2.1 | Electrode movement Jacobian | 170 |
| 5.2.2 | Shape correction algorithm | 171 |
| 5.3 | Standard and shape correction algorithms | 173 |
| 5.3.1 | Gravitational effects in the supine position | 174 |
| 5.4 | EIT and MR image co-registration | 175 |
| 5.5 | EIT and MR mutual information | 179 |
| 5.6 | Conclusions and extensions | 180 |
| 6 | Coupling EIT and mechanical ventilation | 183 |
| 6.1 | Mechanical ventilation and EIT | 183 |
| 6.1.1 | Inverse homogenization | 184 |
| 6.2 | CFD and mechanical modelling | 185 |
| 6.2.1 | Electric and hydrodynamic analogies | 186 |
| 6.2.2 | Single and double compartment model | 187 |
| 6.3 | Multi-compartment coupled ODE model | 190 |
| 6.3.1 | Inverse problem | 192 |
| 6.3.2 | Numerical differentiation | 194 |
| 6.4 | Multi-compartment lung results | 197 |
| 6.5 | Conclusions and extensions | 201 |
| 7 | Conclusions and future research | 205 |
| 7.1 | Thesis Summary | 205 |

| | | |
|-------|---|------------|
| 7.2 | Future Research | 207 |
| 7.2.1 | Optimal measurement strategies | 207 |
| 7.2.2 | Absolute lung EIT | 209 |
| | Bibliography | 210 |
| | A Mathematical notation | 228 |
| A.1 | PDE theory | 228 |
| A.1.1 | Sobolev spaces | 230 |
| A.1.2 | Symmetric hyperbolic PDEs | 232 |
| A.2 | Manifolds and Riemannian geometry | 234 |
| A.2.1 | Differentiable manifolds | 234 |
| A.2.2 | Riemannian geometry | 237 |
| A.2.3 | Frobenius' theorem | 242 |
| | B High order FEM code in EIDORS | 244 |
| B.1 | Forward problem | 244 |
| B.2 | Inverse problem | 245 |
| B.3 | Shape functions | 247 |
| B.4 | Quadrature rules | 249 |
| | C Shape derivative code | 252 |
| C.1 | Driver code | 252 |
| C.2 | Geometry and Jacobian calculation | 257 |
| C.3 | Electrode position inverse solver | 263 |
| C.4 | Electrode and conductivity inverse solver | 268 |
| | D Mechanical ODE modelling code | 276 |

List of Tables

| | | |
|-----|--|-----|
| 4.1 | 2-norm errors of SVD image for central perturbation with $A = 1$ and $A = 23$ measurement strategy. | 121 |
| 4.2 | 2-norm errors of SVD image for boundary perturbation with $A = 1$ and $A = 23$ measurement strategy. | 121 |
| 6.1 | Analogous variables in mechanical, hydrodynamical and electrical systems. | 187 |
| 6.2 | 2-norm errors of estimated elastances and compliances. | 201 |
| B.1 | Nodes and weights for quadrature over the interval $[-1, 1]$ in 1D | 250 |
| B.2 | Nodes and weights for quadrature over the unit triangle in 2D | 250 |
| B.3 | Nodes and weights for quadrature over the unit tetrahedron in 3D | 251 |

List of Figures

| | | |
|-----|---|-----|
| 1.1 | Current streamlines and equipotentials in thoracic EIT | 18 |
| 1.2 | Swisstom BB ² developed by SwissTom. | 21 |
| 2.1 | Local mapping from an element to unit tetrahedron. | 38 |
| 2.2 | Local mapping from a unit triangle to boundary simplex. | 41 |
| 2.3 | Uniform triangulations of square domain | 45 |
| 2.4 | Convergence of continuum model | 46 |
| 2.5 | Point and complete electrode model with neighbourhood removed. . . . | 47 |
| 2.6 | Convergence of point electrode model. | 48 |
| 2.7 | Convergence of point electrode model away from driven electrodes. . . . | 49 |
| 2.8 | Convergence of the CEM with $z = 1000$ | 50 |
| 2.9 | Convergence of the CEM with $z = 1000$ away from driven electrodes . . | 51 |
| 3.1 | Plot of CGO solutions at the boundary of the unit disc. | 65 |
| 4.1 | Voltage error on unit disc as a function of electrode perturbation | 91 |
| 4.2 | Conformal and non-conformal maps on a unit disc | 94 |
| 4.3 | Singular value decay for boundary shape Jacobian on cylindrical domain with $A = 1$ measurement strategy. | 129 |
| 4.4 | Singular value decay for boundary shape Jacobian on cylindrical domain with different measurement strategies. | 129 |
| 4.5 | Singular value decay for conductivity Jacobian on cylindrical domain with different measurement strategies. | 130 |
| 4.6 | Singular vectors for boundary shape Jacobian on cylindrical domain with $A = 1$ measurement strategy and measurements recorded driven electrodes. | 131 |

| | | |
|------|--|-----|
| 4.7 | Singular vectors for boundary shape Jacobian on cylindrical domain with $A = 1$ measurement strategy with no measurements on drive electrodes. | 132 |
| 4.8 | Singular vectors for boundary shape Jacobian on cylindrical domain with $A = 23$ measurement strategy with measurements recorded on driven electrodes. | 133 |
| 4.9 | Singular vectors for movement Jacobian on cylindrical domain with $A = 23$ measurement strategy and no measurements on drive electrodes. . . | 134 |
| 4.10 | SVD projections on xy slice of spherical interior inclusion. | 135 |
| 4.11 | SVD projections on xz slice of spherical interior inclusion. | 136 |
| 4.12 | SVD projections on xy slice of spherical boundary inclusion. | 137 |
| 4.13 | SVD projections on xz slice of spherical boundary inclusion. | 138 |
| 4.14 | Sphere: Initial fine discretisation and coarse discretisation. | 139 |
| 4.15 | Sphere: Unknown conductivity and electrode positions with $p = 0.1$. . . | 139 |
| 4.16 | Sphere: Reconstructed conductivity with electrode positions known. . . | 140 |
| 4.17 | Sphere: Reconstructed conductivity without shape correction $p = 0.1$. | 141 |
| 4.18 | Sphere: Reconstructed conductivity using shape correction algorithm $p = 0.1$ | 142 |
| 4.19 | Sphere: Reconstructed conductivity lineplots with $p = 0.1$ | 143 |
| 4.20 | Sphere: Electrode position and voltage convergence with $p = 0.1$ and $A = 23$ | 143 |
| 4.21 | Sphere: Electrode position convergence with $p = 0.1$ | 144 |
| 4.22 | Cylinder: Initial fine discretisation and coarse discretisation. | 145 |
| 4.23 | Cylinder with cylindrical inclusion: Unknown conductivity and electrode positions with $p = 0.1$ | 145 |
| 4.24 | Cylinder with cylindrical inclusion: Reconstructed conductivity with electrode positions known and $A = 1$ | 146 |
| 4.25 | Cylinder with cylindrical inclusion: Reconstructed conductivity without shape correction $p = 0.1$ and $A = 1$ | 147 |
| 4.26 | Cylinder with cylindrical inclusion: Reconstructed conductivity using shape correction algorithm $p = 0.1$ and $A = 1$ | 148 |

| | | |
|------|---|-----|
| 4.27 | Cylinder with cylindrical inclusion: Reconstructed conductivity lineplots with $p = 0.1$ and $A = 1$ | 149 |
| 4.28 | Cylinder with cylindrical inclusion: Electrode position and voltage convergence with $p = 0.1$ and $A = 1$ | 149 |
| 4.29 | Cylinder with cylindrical inclusion: Electrode position convergence with $p = 0.1$ and $A = 1$ | 150 |
| 4.30 | Cylinder with two cylindrical inclusions: Unknown conductivity and electrode positions with $p = 0.1$ | 151 |
| 4.31 | Cylinder with two cylindrical inclusions: Reconstructed conductivity with electrode positions known and $A = 1$ | 152 |
| 4.32 | Cylinder with two cylindrical inclusions: Reconstructed conductivity without shape correction $p = 0.1$ and $A = 1$ | 153 |
| 4.33 | Cylinder with two cylindrical inclusions: Reconstructed conductivity using shape correction algorithm $p = 0.1$ and $A = 1$ | 154 |
| 4.34 | Cylinder with two cylindrical inclusions: Reconstructed conductivity lineplots with $p = 0.1$ and $A = 1$ | 155 |
| 4.35 | Cylinder with two cylindrical inclusions: Initial electrode position and voltage convergence with $p = 0.1$ and $A = 1$ | 155 |
| 4.36 | Cylinder with two cylindrical inclusions: Electrode position convergence with $p = 0.1$ and $A = 1$ | 156 |
| 4.37 | Cylinder with spherical inclusion: Unknown conductivity and electrode positions with $p = 0.075$ and $A = 1$ | 157 |
| 4.38 | Cylinder with spherical inclusion: Reconstructed conductivity with electrode positions known and $A = 1$ | 158 |
| 4.39 | Cylinder with spherical inclusion: Reconstructed conductivity without shape correction $p = 0.075$ and $A = 1$ | 159 |
| 4.40 | Cylinder with spherical inclusion: Reconstructed conductivity using shape correction algorithm $p = 0.075$ and $A = 1$ | 160 |
| 4.41 | Cylinder with spherical inclusion: Reconstructed conductivity lineplots with $p = 0.075$ and $A = 1$ | 161 |
| 4.42 | Cylinder with spherical inclusion: Initial electrode position and voltage convergence with $p = 0.075$ and $A = 1$ | 161 |

| | | |
|------|--|-----|
| 4.43 | Cylinder with spherical inclusion: Electrode position convergence with $p = 0.075$ and $A = 1$ | 162 |
| 4.44 | Cylinder with spherical inclusion: Reconstructed conductivity with electrode positions known and $A = 23$ | 163 |
| 4.45 | Cylinder with spherical inclusion: Reconstructed conductivity without shape correction $p = 0.075$ and $A = 23$ | 164 |
| 4.46 | Cylinder with spherical inclusion: Reconstructed conductivity using shape correction algorithm $p = 0.075$ and $A = 23$ | 165 |
| 4.47 | Cylinder with spherical inclusion: Reconstructed conductivity lineplots with $p = 0.075$ and $A = 23$ | 166 |
| 4.48 | Cylinder with spherical inclusion: Initial electrode position and voltage convergence with $p = 0.075$ and $A = 23$ | 166 |
| 4.49 | Cylinder with spherical inclusion: Electrode position convergence with $p = 0.075$ and $A = 23$ | 167 |
| 5.1 | Electrode configuration on subject and MRI fiducial markers | 170 |
| 5.2 | Segmented MR slice and extruded ‘2.5D’ finite element model | 171 |
| 5.3 | Comparison of standard and shape corrected reconstruction in 3D. | 173 |
| 5.4 | Comparison of standard and shape corrected reconstruction in 2D. | 174 |
| 5.5 | Normalized conductivity reconstruction lineplots at max inhalation. | 175 |
| 5.6 | Conductivity time series in sitting and supine position. | 176 |
| 5.7 | MRI and EIT image co-registration process. | 177 |
| 5.8 | MRI and EIT image co-registration for sitting and supine subject and using standard and shape corrected reconstruction algorithms. | 178 |
| 5.9 | Mutual information as a function of regularisation parameter. | 181 |
| 6.1 | Single mechanical chamber and electric circuit analogue. | 188 |
| 6.2 | Electric circuit diagram of multi-compartment lung model. | 191 |
| 6.3 | Sinusoidal pressure forcing time series at mouth with $\text{SNR} = 100$ | 197 |
| 6.4 | Raw volume time series for two compartments with low elastance and high resistance with $\text{SNR} = 100$ | 198 |
| 6.5 | Reconstructed flow time series in two compartments with low elastance and high resistance with $\text{SNR} = 100$ | 199 |

| | | |
|------|--|-----|
| 6.6 | Reconstructed volume time series in two compartments with low elasticity and high resistance with SNR = 100. | 199 |
| 6.7 | Reconstructed flow time series with SNR = 50 and 25. | 200 |
| 6.8 | Reconstructed volume time series with SNR = 50 and 25. | 200 |
| 6.9 | Actual parameter matrix and error in parameter matrix with SNR = ∞ | 201 |
| 6.10 | Error in parameter matrices with SNR = 100 and 25. | 202 |
| 6.11 | Parameters estimated as a function of noise level through time integration of equations. | 203 |
| 6.12 | Parameters estimated as a function of noise level through inverse integration. | 204 |
| B.1 | Local positions of nodes on quadratic reference tetrahedron. | 248 |
| B.2 | Local positions of nodes on quadratic reference boundary triangle. | 249 |

The University of Manchester

Michael Crabb

Doctor of Philosophy

EIT Reconstruction Algorithms for Respiratory Intensive Care

December 15, 2014

Electrical impedance tomography (EIT) is an emerging medical imaging technique that aims to reconstruct the internal conductivity distribution of a subject from electrical measurements obtained on the skin. In this thesis we explore the promising application of EIT to the respiratory monitoring of humans.

We pay particular focus to the forward problem, highlighting the need to have an accurately known external boundary shape and electrode positions on a reconstruction model. A theoretical study of uniqueness results of EIT with an unknown external boundary shape is presented. A novel sensitivity study of the external boundary shape is presented as well as results from a reconstruction algorithm to account for errors in electrode position with simulated data in 3D. We also demonstrate results of a shape correction algorithm from a pilot study of lung EIT with data collected using the fEITER system, and MR images used to inform the external boundary shape of healthy subjects. After image co-registration of the resulting dynamic 3D EIT reconstruction images with the lung-segmented MR image, we outline a novel mutual information performance criterion to measure the quality of reconstructed images. We also outline the computation of the forward problem of the complete electrode model in 3D using high order polynomial finite elements and present convergence results in 2D for the continuum, point and complete electrode model. Our numerical study demonstrates that the convergence rate of the forward problem is independent of the polynomial approximation order for the complete electrode model and there is no global convergence for the point electrode model in the energy norm.

Reconstructed conductivity images can be difficult to interpret at the bedside. Moreover clinicians would like clinically meaningful indices, such as regional lung compliance, to determine the pathologies of patients in real time. By modelling the respiratory system as a coupled time dependent system of simple mechanical functional units, we propose a novel methodology to couple mechanical ventilation and EIT. The mechanical properties of the lungs are estimated through an inverse coefficient problem on coupled ODEs, with the measurable data being the time series of pressure at airway opening and interior air volume data. We present results with simulated data as well as a discussion on extensions and limitations to the mechanical models.

Finally we present a theoretical discussion of anisotropic EIT. It is well known that any diffeomorphism fixing points on the boundary gives rise to a conductivity with the same electrical measurements on the skin, generating a large class of conductivities that are electrically equivalent. We define novel classes of anisotropic media with constraints on their eigenspace: *prescribed eigenvalues*, *prescribed orthogonal coordinates*, *prescribed eigenvectors*, *fibrous* and *layered* conductivities. By drawing analogies with elasticity theory, we discuss how these constraints on the eigenspace restrict the set of diffeomorphisms fixing points on the boundary, and present two uniqueness results for anisotropic conductivities with prescribed eigenvalues and prescribed eigenvectors.

Declaration

No portion of the work referred to in the thesis has been submitted in support of an application for another degree or qualification of this or any other university or other institute of learning.

Copyright Statement

- i.** The author of this thesis (including any appendices and/or schedules to this thesis) owns certain copyright or related rights in it (the “Copyright”) and s/he has given The University of Manchester certain rights to use such Copyright, including for administrative purposes. All registered trademarks are recognised.
- ii.** Copies of this thesis, either in full or in extracts and whether in hard or electronic copy, may be made **only** in accordance with the Copyright, Designs and Patents Act 1988 (as amended) and regulations issued under it or, where appropriate, in accordance with licensing agreements which the University has from time to time. This page must form part of any such copies made.
- iii.** The ownership of certain Copyright, patents, designs, trade marks and other intellectual property (the “Intellectual Property”) and any reproductions of copyright works in the thesis, for example graphs and tables (“Reproductions”), which may be described in this thesis, may not be owned by the author and may be owned by third parties. Such Intellectual Property and Reproductions cannot and must not be made available for use without the prior written permission of the owner(s) of the relevant Intellectual Property and/or Reproductions.
- iv.** Further information on the conditions under which disclosure, publication and commercialisation of this thesis, the Copyright and any Intellectual Property and/or Reproductions described in it may take place is available in the University IP Policy (see <http://documents.manchester.ac.uk/DocuInfo.aspx?DocID=487>), in any relevant Thesis restriction declarations deposited in the University Library, The University Library’s regulations (see <http://www.manchester.ac.uk/library/aboutus/regulations>) and in The University’s Policy on Presentation of Theses.

Acknowledgements

I would like to thank a number of people who have helped during this project. In particular my supervisor, Bill Lionheart, for his guidance, support and patience throughout the process, and for always providing me with a source of new ideas. Thanks also to Philips Research for the Philips Industrial CASE Studentship (EPSRC Ref: EP/H50141X/1), as well as Cees van Berkel for his hospitality during my time at Philips in Cambridge in 2012. Thank you to Andy Adler and Andrea Borsic for their useful comments during the write up, and to my examiners Andrew Hazel and Ville Kolehmainen. I would also like to thank the other members of the Inverse Problems group: Russell, Sophia, Henry, Naeem, Francis, Kyriakos, Taufiq, Will and Nicola. Finally a special thanks to my family for their constant source of support throughout.

Abbreviations

The following abbreviations are commonly used in this thesis, with the number in brackets indicating the page number of the first occurrence:

- BEM - Boundary element method (33).
- CEM - Complete electrode model (29).
- CFD - Computational fluid dynamics (186).
- CGO - Complex geometric optics (60).
- CT - Computerised tomography (19).
- DtN - Dirichlet-to-Neumann (60).
- EIT - Electrical impedance tomography (18).
- FE(M) - Finite element (method) (24).
- FPS - Frames per second (169).
- FDM - Finite difference method (33).
- HFOV - High frequency oscillatory ventilator (19).
- ICU - Intensive care unit (19).
- LPV - Lung protective ventilation (19).
- MRI - Magnetic resonance imaging (19).
- NtD - Neumann-to-Dirichlet (61).
- ODE - Ordinary differential equation (184).

- PDE - Partial differential equation (23).
- PEEP - Positive end expiratory pressure (19).
- PSDO - Pseudo-differential operator (66).
- RK4 - Runge-Kutta 4 (192).
- SNR - Signal to noise ratio (90).
- SVD - Singular value decomposition (57).
- VILI - Ventilator induced lung injury (19).

Chapter 1

Introduction to lung EIT

Electrical impedance tomography (EIT) is an imaging modality that aims to reconstruct the internal conductivity distribution of a given object from electrical measurements obtained on the periphery. Low-frequency alternating currents are applied on a set of electrodes on the boundary of a body and the interior conductivity distribution distorts the equipotential field lines. The objective of EIT is to infer the interior conductivity distribution from measurements of the potential on the same electrodes (see figure 1.1).

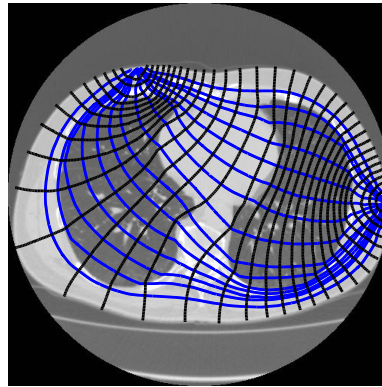


Figure 1.1: Simulation of current streamlines and equipotentials in thoracic EIT when current is applied between two electrodes. Conductivity of the lungs and ‘background’ is 0.3 and 1 respectively in arbitrary units. Current streamlines are in blue and equipotentials, which are distorted at the lung boundary, are in black.

EIT is inherently a severely ill-posed problem and high resolution imaging is not presently a realistic possibility using the technique. However high resolution imaging is not always of fundamental importance in applications. For example, clinicians in

respiratory monitoring are often interested in low resolution questions such as is the left or right lung dominating ventilation or is there excessive liquid in the lungs. EIT is excellent at detecting high conductivity contrasts and thus shows promise in answering these questions raised by the clinicians.

1.1 Respiratory monitoring

A current exciting application area for EIT is for patients in intensive care units (ICU) with acute lung injuries such as acute respiratory distress syndrome (ARDS). These patients are typically mechanically ventilated using high frequency oscillatory ventilation (HFOV), designed to recruit collapsed regions of the lung. These ventilators work by an operator choosing a baseline pressure, and superimposing a square wave at high frequency, to force air in and out of patients lungs. Mechanical ventilation of patients is often a life saving intervention for patients suffering from ARDS [1], but the technique can create ventilator induced lung injury (VILI) due to excessive mechanical forces in the lung. Choosing too small a positive end expiratory pressure (PEEP) or frequency leads to ineffective ventilation and alveolar collapse, and too high a pressure or frequency can over distend lung tissue causing irreversible damage. Consequently lung protective ventilation (LPV) techniques have been developed to optimise pressure and frequency settings to trade off alveolar collapse and over-distension. Despite the use of LPV it is estimated that 33 – 55% of patients with ARDS still develop VILI [2].

In the ICU there is little or no means of observing the distribution of air and liquid inside a patient's lungs in real time. Many clinical decisions are made on the intuition and experience of trained clinicians, which has made choosing appropriate ventilator settings an art rather than a science with potentially severe consequences. Magnetic resonance imaging (MRI) and computerised tomography (CT) are readily available in hospitals and are high resolution techniques. However MRI and CT are not portable making them almost impossible to use for bedside monitoring. Less importantly these techniques are also very expensive to maintain. On the other hand a typical EIT system is portable and quick, making it ideal for an ICU, and the running cost is orders of magnitude smaller than MRI and CT. There is also negligible safety risk with EIT for sufficiently small amplitude and high frequency injected currents (see [3])

for a discussion of safety.)

Different tissues and organs in the human body have significantly different conductivities, for example blood, bone, heart, liver and lung have resistivity values of $\approx 151, 1.2 \times 10^8, 175, 342$ and $157 \Omega\text{cm}$ respectively [4]. Generating a conductivity image of the thorax potentially allows one to infer the internal distribution of tissues and organs. EIT as a biomedical imaging technique was originally developed at Sheffield University by Barber and Brown in the early 1980s [5]. The authors also presented an early review of possible applications of EIT [6], including respiratory monitoring, and published the first EIT images of a cross-section of a human thorax. Since the 1980s there has been widespread interest in the clinical application of thoracic EIT. Several review articles [7, 8, 9, 10, 11, 12] provide the reader with the current status of clinical activity and also detail the broad spectrum of specific thoracic EIT application areas. Applications include the assessment of pulmonary ventilation [11, 13], lung perfusion [14], pulmonary oedema [15], changes in tissue impedance due to gravity [16, 17], emphysema [18] and lung injury [19]. These studies demonstrate that thoracic EIT promises to become a routine bedside monitoring tool for critically ill patients who undergo mechanical ventilation, and is already beginning to play an important role in optimizing ventilator settings for such patients.

1.2 Current state

Experimental data over the last 25 years from clinical researchers has mostly been collected from variants of Sheffield data collection systems in which adjacent-adjacent current and measurements are deployed [5, 20]. However recent research argues that adjacent stimulation and measurement are the worst patterns for detecting interior conductivity changes in 2D [21]. Early reconstruction algorithms were also based on crude algorithms such as Sheffield backprojection, and since the early 1980s much research has been undertaken to establish efficient, accurate and repeatable reconstruction algorithms [22]. This important issue was addressed at the 2007 ICEBI conference in Graz, Austria, where a common consensus was made for lung EIT, namely GREIT (Graz consensus Reconstruction algorithm for EIT) [23]. The aim of the consensus was to develop an agreement between mathematicians, engineers and clinicians on

measures of quality for a reconstruction algorithm for 2D linearised EIT, such as amplitude response, position error, resolution and shape deformation. The objective of the GREIT algorithm is then to optimise against these performance criteria to ensure robust and repeatable imaging.

Almost all reconstructions from real lung data are based on *difference* or *dynamic* imaging. Difference imaging is where two sets of data are obtained at different times when a change of interior conductivity is known to have occurred. The forward operator mapping the conductivity to the measurements is assumed to be linear and a linearised regularised inversion is performed to estimate the conductivity change. Differential imaging is unsatisfactory from a mathematical perspective because the assumption of linearity between the conductivity and measurements is not true. Moreover this technique results in a differential conductivity image for which one can not resolve the forward problem, and thus it is unclear how well the new parameters for the conductivity fit the measured voltage data. More desirable in the ICU is *absolute* EIT, where a conductivity image is reconstructed from electrical data recorded at a single time instant. A theme of this thesis will be understanding how we can make absolute EIT a realistic possibility in the ICU and why it is so important.

Although EIT is not currently in common use in the ICU, commercial systems have been designed and are used largely in clinical trials. The PulmoVista 500, developed by Dräger [24] is a chest height touchscreen system with 16 electrodes, with image reconstruction based on a linearised difference imaging technique. SwissTom have also developed an instrument, Swisstom BB², using difference imaging based on the GREIT algorithm.



Figure 1.2: Swisstom BB² developed by SwissTom. (Image used with permission from SwissTom www.swisstom.com.)

1.3 Future challenges

The major downfall with EIT is the poor spatial resolution of reconstructed images when compared to MRI and CT, stemming from the severely ill-posed nature of the problem as well as the partial, limited and noisy electrical boundary data available in practice. It is desirable to perform absolute EIT but this has proven to be extremely difficult in practice in a clinical setting. Absolute EIT requires the measurement error and modelling error from inaccurately known contact impedance, electrode positions and boundary shape to be sufficiently small, as well as using better *a-priori* estimates of the conductivity in non-linear reconstruction algorithms. In this thesis we identify how some of these aspects of forward modelling in EIT can be improved. We note that in geophysical applications of EIT absolute imaging is standard with the reconstruction software RES3DINV, developed by Loke [25], being commonly used in geophysical surveys [26, 27]. However geophysical surveys are usually sufficiently large that electrodes can be modelled as point sources, and capturing the boundary shape is trivial, under the assumption that the surface is flat. Moreover corrections due to breathing can generally be ignored in geophysical applications too (although landslides could potentially create analogous effects). The RPI group are the exceptions to this trend who obtained the first absolute EIT images for tank and chest data in [28] and [29] respectively, although in the case of chest data it is still difficult to physically interpret the resulting absolute reconstructions.

Clinicians are often unsure how to interpret reconstructed conductivity images, and we explore how reconstructed images can be converted to physiologically meaningful quantities such as lung compliance and airway resistance, and also importantly how this relies on performing absolute EIT.

1.3.1 Boundary shape and dimension

Perhaps the most important challenge for a step change in lung EIT is to have sufficiently accurate thorax cross sections, as well as using reconstruction models with the correct number of (three) spatial dimensions. Mathematically, assuming full knowledge of the current-to-voltage map on the body and the conductivity is isotropic, the data measured on the body will only be consistent with an isotropic conductivity in the

model domain if the body and model domain are related by a conformal map [30, 31]. It is unlikely that the true and model domain will be related by a conformal map and this effect creates large artefacts in reconstructed images [32, 33]. Most current EIT systems assume that the thorax is not only 2D but the cross section is circular, elliptical or at best some generic thorax cross section. The problem is exacerbated because of the patient's breathing. As the patient breathes the boundary shape and the internal organs move relative to a fixed geometrical model of the torso, and these breathing effects create image artefacts on static reconstruction models. We explore the use of a shape correction algorithm to account for breathing and display results from real and simulated data in 3D.

To determine the boundary shape of the patient's thorax one can use other high resolution modalities such as MRI or CT, because this information is often available in the ICU. This requires generation of finite element models of a patient's thorax as well as electrodes embedded into the surface of these models. The embedding of electrodes makes model generation somewhat unique to standard segmentation and meshing software, although accurate model generation has been presented in breast EIT by Forsyth *et al.* [34] and brain EIT by Tizzard *et al.* [35].

1.3.2 Forward modelling

Iterative reconstruction algorithms simulate voltages at the current best estimate of the conductivity by computing the solution of a boundary value problem of an elliptic partial differential equation (PDE) for every measurement per iteration. Clearly the voltages must be computed sufficiently accurately so as not to be the dominant source of error during reconstruction. However, quantification of the dominant source of modelling error is difficult and depends on a number of factors. This includes inaccurately known contact impedances, electrode positions and boundary shape, poor prior information of the conductivity, and also not accounting for anisotropic conductivities. It is the opinion of the author that the combination of these sources of modelling error is the leading reason why the vast majority of groups working in lung EIT still only perform differential imaging, in the sense that the modelling error largely cancels when constructing voltage difference data. Nissinen *et al.* have recently developed a Bayesian approximation error approach to explicitly account for modelling

and approximation errors in reconstruction algorithms [36, 37].

The forward modelling can be improved in a number of ways which we explore in this thesis. Firstly, and most importantly, the dimension, boundary shape and electrode positions should be as accurate as possible as discussed in the previous section. Secondly, more prior information on the anatomy such as the lungs, liver, heart and rib cage can be incorporated into the forward model, using patient specific MRI or CT. Thirdly, more advanced mathematical techniques, such as high order finite element methods (FEM) can be adopted to solve the forward problem more accurately than standard piecewise linear finite elements.

1.3.3 Spatial resolution testing

Difference imaging techniques result in conductivity images that are the linearised difference of conductivity between two time frames. The forward problem can not be resolved on a difference image, and so it is difficult to assess how reliable the resulting EIT reconstructions are. The spatial resolution of EIT has been assessed in several experimental and clinical studies involving spontaneous and artificial ventilation against well established imaging techniques e.g. X-ray CT, positron emission tomography and single photon emission CT [38, 39, 40, 41, 42, 43]. However, such studies have not made direct comparisons of the spatial accuracy of EIT with a second high resolution modality using image co-registration. In this thesis an empirical approach is proposed to assess the quality of EIT reconstructions through co-registration and a novel mutual information calculation with another high resolution technique such as MRI or CT.

1.3.4 Clinically meaningful parameters

Clinicians in the ICU often have difficulty interpreting conductivity images at the bedside. Moreover clinicians are often interested in questions about the distribution of liquid in the lungs and regional compliance, and not necessarily electrical conductivity. Thus in order for EIT to be used as a useful diagnostic for respiratory monitoring in the ICU, it would be desirable if conductivity images can be converted to clinically meaningful parameters.

A novel method is proposed to couple EIT with mechanical ventilation by first

assuming that absolute regional time series of conductivity can be converted to time series of regional air volume. We model the respiratory system as a coupled time dependent system of mechanical functional units [44], with time series of air volume and the pressure at airway opening as states of the model, and the regional compliance and resistance as parameters. Mechanical ventilators additionally provide time series of pressure, volume and flow at the mouth, as well as heart rate data. We set up an inverse coefficient problem with the regional air volume time series obtained from EIT and the pressure time series at airway opening as data. We outline what information can be determined from this data, and why generating absolute conductivity images is a fundamental step to compute such parameters.

1.3.5 Anisotropic media

Almost all reconstruction algorithms in EIT assume that the underlying conductivity distribution is isotropic, or locally invariant under the rotation group $SO(n)$, where n is the number of spatial dimensions. Anisotropic conductivities are definitely present in medical applications, for example muscle fibres have a preferred electrical direction. The isotropic assumption simplifies EIT reconstructions because the inverse problem in EIT is known to be non-unique under diffeomorphisms fixing the boundary [45, 46].

For some classes of anisotropy, however, the equivalence class of diffeomorphisms reduces to just the identity, for example for isotropic and conformally flat conductivities [31]. There is very little known about which constraints are required for more general anisotropic conductivities for unique determination from the electrical boundary data. We define anisotropic media that have constraints on their eigenspace, such as *prescribed eigenvalues*, *prescribed orthogonal coordinates*, *prescribed eigenvectors*, *layered* and *fibrous* media. By drawing analogies with elasticity theory, we discuss how such constraints restrict the set of diffeomorphisms fixing points on the boundary. We demonstrate a local uniqueness result for anisotropic conductivities with prescribed eigenvalues, and a uniqueness results for anisotropic conductivities with prescribed eigenvectors assuming a globally defined coordinate system.

1.4 Thesis Outline

In chapter 2 there is a discussion of the forward problem in EIT along with boundary conditions. The implementation of high order polynomial tetrahedral finite elements for the complete electrode model in 3D will be outlined, and a novel convergence study under different electrode models in 2D will be performed. In chapter 3 a literature review of uniqueness of the inverse conductivity problem is discussed, including a discussion of exact methods and their potential application in lung EIT. The geometric and anisotropic inverse conductivity problem is posed, and the possibility of unique recovery of certain novel subclasses of anisotropic conductivities where the permitted eigenspace has been constrained, will be discussed. Two novel uniqueness results for conductivities with prescribed eigenvalues and prescribed eigenvectors are made. In chapter 4 a literature review of theoretical uniqueness results for the simultaneous recovery of the external shape and electrode positions and an isotropic conductivity is presented. A novel calculation of the Fréchet derivative with respect to the external shape is outlined for the continuum model and an original sensitivity study for boundary shape perturbations is performed in 3D. Results from a novel absolute reconstruction algorithm to simultaneously recover the electrode positions and conductivity in 3D are displayed. In chapter 5 we discuss results from a pilot study at the University of Manchester on MRI-informed lung EIT. An MR image is used to inform a 3D finite element model of the thorax, and a robust electrode position error correction algorithm is deployed to account for the effects of breathing. The resulting EIT reconstructions are co-registered with the original MR images, and an assessment of quality is measured using a novel mutual information performance criteria. Finally in chapter 6 we discuss a novel method to obtain clinically meaningful parameters from EIT reconstructions using lumped parameter mechanical ODE models. We exhibit results using simulated data for a simple mechanical model, and discuss possible limitations and extensions to such models.

Chapter 2

Forward modelling in EIT

In this chapter we review the forward problem and different electrode models in EIT. We outline the computation of high order FEM in 3D for the complete electrode model, and a novel convergence study for high order FEM in 2D is performed for the continuum, point and complete electrode models, which also includes a novel analytic solution to the CEM on a square domain.

2.1 Conductivity equation

An equation governing the relationship between the interior voltage and conductivity distribution can be derived from Maxwell's equations assuming time harmonic electric and magnetic fields [47, 48]. In Cartesian coordinates, using Einstein summation convention, we arrive at a second order linear elliptic PDE

$$\nabla \cdot ((\sigma + i\omega\epsilon)\nabla u) := \frac{\partial}{\partial x^i} ((\sigma^{ij} + i\omega\epsilon^{ij}) \frac{\partial u}{\partial x^j}) = 0 \quad x \in \Omega, \quad (2.1)$$

where $\Omega \subset \mathbb{R}^n$ is the domain of the body, n is the number of spatial dimensions, $u : \Omega \rightarrow \mathbb{R}$ is the electric potential, ω is the frequency and $\sigma : \Omega \rightarrow \mathbb{R}^{n \times n}$ and $\epsilon : \Omega \rightarrow \mathbb{R}^{n \times n}$ are the conductivity and permittivity tensors respectively. In this thesis the frequency is assumed sufficiently small that the permittivity can be neglected (see section 2.1.1). The conductivity is a symmetric positive definite matrix almost everywhere with $\sigma^{ij} \in L^\infty(\Omega)$. In the isotropic case, $\sigma^{ij}(x) = \alpha(x)\delta^{ij}$, this condition reduces to $0 < c \leq \alpha(x) \leq C$ almost everywhere for constants $c, C \in \mathbb{R}$.

2.1.1 Electrode modelling

The simplest boundary conditions in EIT are Neumann boundary conditions on the conductivity equation (2.1), by supplying the current flux density, f , on $\partial\Omega$. Let ν denote the outward pointing unit normal at $x \in \partial\Omega$. The Ohmic current density is given by $f = (\sigma \nabla u) \cdot \nu|_{\partial\Omega}$, and the current passing into a region $B \subset \partial\Omega$ is the integral of f over B , $I_B = \int_B f$. As a consequence of the divergence theorem, integrating (2.1) over Ω implies

$$0 = \int_{\Omega} \nabla \cdot (\sigma \nabla u) = \int_{\partial\Omega} f. \quad (2.2)$$

This gives us a consistency condition that the integral of current density over the whole boundary must be 0. Secondly the electrical potential is only defined up to a constant. This can be written mathematically by choosing a ground point x_g , so that $u(x_g) = 0$, or by setting the average potential over the boundary to 0, $\int_{\partial\Omega} u = 0$.

An important consideration in EIT is the modelling of the electrodes, which has been studied extensively in [49, 50]. Let the subset of the boundary in contact with the l^{th} electrode be $E_l \subset \partial\Omega$, and the portions of the boundary in contact and not in contact with any electrode be $E_T := \bigcup_l E_l$ and $E'_T = \partial\Omega \setminus E_T$ respectively. The most important electrode models in EIT are the *continuum*, *point electrode*, *shunt* and *complete electrode* models. It is assumed that $(\sigma \nabla u) \cdot \nu|_{E'_T} = 0$ away from the electrodes because the surrounding air is an insulator to a good level of approximation. In medical applications of EIT an alternating current is applied on the subject typically with a frequency of 10 – 100 kHz with maximum permissible current in this range of $100F \mu\text{A}$, where F is the frequency in kHz [3]. In this thesis the frequency is assumed sufficiently small that capacitive coupling is ignored, so that $\frac{\omega\epsilon}{\sigma} \approx 0$, which justifies our assumption that ϵ can be assumed to be zero [51].

Continuum model

In the continuum model, the current injection boundary conditions are

$$\sigma \frac{\partial u}{\partial \nu} \Big|_{\partial\Omega} := (\sigma \nabla u) \cdot \nu|_{\partial\Omega} = f, \quad (2.3)$$

where $f : \partial\Omega \rightarrow \mathbb{R}$ is a current injection function, with $\int_{\partial\Omega} f = 0$ to satisfy the consistency condition (2.2). This model assumes every point of the boundary is accessible

to input current, and so there are effectively an infinite number of electrodes. This is clearly not realistic but is the nicest model to work with from a theoretical perspective.

Point electrode model

In the point electrode model, the current injection function f , defined in (2.3), is

$$f = \sum_{l=1}^L I_l \delta(x - x_l). \quad (2.4)$$

This is a model of an L electrode system, all of negligible size, where x_l is the spatial coordinate of the l^{th} electrode and $\sum_{i=1}^L I_i = 0$ to satisfy the consistency condition (2.2). The vast majority of EIT systems use pair drive excitation i.e. between two electrodes, which must have equal and opposite injected currents. This model is non-physical because the electrodes are of finite size in practice.

Shunt model

This model assumes that the potential on each electrode is constant, $u|_{E_l} = U_l$, with the resulting currents given by $I_l = \int_{E_l} \sigma \frac{\partial u}{\partial \nu}$, leading to the following boundary conditions

$$\int_{E_l} \sigma \frac{\partial u}{\partial \nu} = I_l \quad l = 1, \dots, L, \quad u = U_l \quad l = 1, \dots, L, \quad \sigma \frac{\partial u}{\partial \nu} = 0 \quad x \in E'_T.$$

This model takes into account the finite size of the electrodes but is still non-physical because it ignores the formation of contact impedances under the electrodes.

Complete electrode model

When electrodes are placed in contact with an object, a contact impedance layer exists between the electrode and the object and the voltage under the electrode is no longer constant [49]. If electrode l is a perfect conductor, the upper voltage on the electrode, U_l , is still constant and there is a voltage drop across the contact impedance layer, $(u + z_l \sigma \frac{\partial u}{\partial \nu})|_{E_l} = U_l$. The contact impedance, z_l , is assumed to be constant for each electrode and positive, $z_l > 0$. The full complete electrode model (CEM) consists of the conductivity equation (2.1) along with the boundary conditions

$$(u + z_l \sigma \frac{\partial u}{\partial \nu})|_{E_l} = U_l \quad l = 1, \dots, L, \quad \int_{E_l} \sigma \frac{\partial u}{\partial \nu} = I_l, \quad \sigma \frac{\partial u}{\partial \nu} = 0 \quad x \in E'_T, \quad (2.5)$$

along with the consistency condition that $\sum_{l=1}^L I_L = 0$. This model is currently the most widely used in practical EIT systems (see [49] for experimental validation.)

A classical solution u to (2.1) lies in $C^2(\bar{\Omega})$. If we have non-smooth domains, or discontinuous boundary conditions, then there may not exist a solution u with such regularity. We introduce the standard weak formulation of the PDE [52] (see appendix A.1 for relevant notation on PDE theory.)

2.1.2 Weak formulation

Assume $u \in C^2(\bar{\Omega})$, $\sigma \in C^1(\bar{\Omega})$ and an interior current source $q \in C^0(\bar{\Omega})$. We multiply the governing equation (2.1) by a test function, v , and integrate over Ω

$$\int_{\Omega} v \nabla \cdot (\sigma \nabla u) = \int_{\Omega} qv \quad x \in \Omega. \quad (2.6)$$

Using the vector identity for scalar fields u and v and a matrix field σ

$$\nabla \cdot (v(\sigma \nabla u)) = (\sigma \nabla u) \cdot \nabla v + v \nabla \cdot (\sigma \nabla u), \quad (2.7)$$

and invoking the divergence theorem, (2.6) can be written as

$$\int_{\Omega} (\sigma \nabla u) \cdot \nabla v - \int_{\partial\Omega} v(\sigma \nabla u) \cdot \nu = - \int_{\Omega} qv. \quad (2.8)$$

Assuming $q = 0$

$$\int_{\Omega} (\sigma \nabla u) \cdot \nabla v = \int_{\partial\Omega} v(\sigma \nabla u) \cdot \nu. \quad (2.9)$$

This is the weak form of the conductivity equation and we have shown a strong solution $u \in C^2(\bar{\Omega})$ satisfies it. The smoothness assumptions can be reduced to $u \in H^1(\Omega)$, $\sigma \in L^\infty(\Omega)$ and $q \in H^{-1}(\Omega)$ as we demonstrate for the continuum model.

Continuum model

The weak formulation for the continuum boundary conditions (2.3) is: Given $f \in H^{-\frac{1}{2}}(\partial\Omega)$, such that $\int_{\partial\Omega} f = 0$, find $u \in H^1(\Omega)$ such that

$$a(u, v) = f(v) \quad \forall v \in H^1(\Omega), \quad (2.10)$$

where

$$a(u, v) = \int_{\Omega} (\sigma \nabla u) \cdot \nabla v, \quad f(v) = \int_{\partial\Omega} fv. \quad (2.11)$$

The forward problem for the continuum model is well-posed as we demonstrate for completeness. We show the problem is compatible with the Lax-Milgram conditions in theorem A.1.1. Firstly the bilinear form $a(., .)$ is bounded

$$|a(u, v)| = \left| \int_{\Omega} (\sigma \nabla u) \cdot \nabla v \right| \leq b \|\nabla u\|_{L^2(\Omega)} \|\nabla v\|_{L^2(\Omega)} \leq b \|u\|_{H^1(\Omega)} \|v\|_{H^1(\Omega)},$$

and $a(., .)$ is elliptic

$$a(u, u) = \int_{\Omega} (\sigma \nabla u) \cdot \nabla u \geq a \|\nabla u\|_{L^2(\Omega)}^2 \geq \frac{a}{1 + C(\Omega)^2} \|u\|_{H^1(\Omega)}^2, \quad (2.12)$$

where a, b are lower and upper bounds for the eigenvalues of σ respectively (which are positive because σ is positive definite almost everywhere), and $C(\Omega)$ is the constant from the Poincaré-Freidrich's inequality, $\|u\|_{L^2} \leq C(\Omega) \|\nabla u\|_{L^2}$ [53]. Since $v \in H^1(\Omega)$, by the trace theorem A.1.2 there is a unique $v|_{\partial\Omega} \in H^{\frac{1}{2}}(\partial\Omega)$, and so we identify the right hand side as the dual pairing of $f \in H^{-\frac{1}{2}}(\partial\Omega)$ and $v|_{\partial\Omega} \in H^{\frac{1}{2}}(\partial\Omega)$. In particular $\partial\Omega$ can be considered as an $n - 1$ -dimensional manifold and is covered by a collection of coordinate charts (U_i, ψ_i) that are homeomorphic to an open set in $V \subset \mathbb{R}^{n-1}$, through $\psi_i : U_i \rightarrow V$. Hence instead of $\partial\Omega$ we can work on \mathbb{R}^{n-1} using the composition functions $f \circ \psi^{-1} : \mathbb{R}^{n-1} \rightarrow \mathbb{R}$ (with an abuse of notation we denote f as $f \circ \psi^{-1}$ and neglect the sum over coordinate charts)

$$\begin{aligned} |f(v)| &= \left| \int_{\mathbb{R}^{n-1}} f(x)v(x) \right| = \left| \int_{\mathbb{R}^{n-1}} \tilde{f}(k)\tilde{v}(k) \right| = \left| \int_{\mathbb{R}^{n-1}} \tilde{f}(k)(1 + |k|^2)^{-\frac{1}{2}}\tilde{v}(k)(1 + |k|^2)^{\frac{1}{2}} \right| \\ &\leq \left(\int_{\mathbb{R}^{n-1}} |\tilde{f}(k)|^2(1 + |k|^2)^{-1} \right)^{\frac{1}{2}} \left(\int_{\mathbb{R}^{n-1}} |\tilde{v}(k)|^2(1 + |k|^2) \right)^{\frac{1}{2}} = \|f\|_{H^{-\frac{1}{2}}} \|v\|_{H^{\frac{1}{2}}}, \end{aligned}$$

where the second equality and fourth inequality follow from Plancherel's theorem (A.4) and the Cauchy-Schwarz theorem respectively. Hence $f(v)$ is a bounded linear functional (because the current density $f \in H^{-\frac{1}{2}}(\partial\Omega)$), and the conditions of the Lax-Milgram theorem are satisfied.

So given any compatible σ and f , there is a unique $u \in H^1(\Omega)$, which can be written as $u = T(\sigma)f$, where $T : H^{-\frac{1}{2}}(\partial\Omega) \rightarrow H^1(\Omega)$. The boundary conditions for the point electrode model are a special case of the continuum model with $f = \sum_{l=1}^L I_l \delta(x - x_l)$. Of course, the Dirac delta is a *distribution* or generalised function, and care is required to interpret the regularity of u . In particular the solution for this boundary value problem is not necessarily bounded in the H^1 -norm. We demonstrate this regularity result explicitly because we will use this when performing a convergence study in section 2.2.3.

The first Sobolev embedding theorem (A.8) asserts that $H^s(M) \subset C^0(M)$ for all $s > n/2$ for a compact manifold M of dimension n . In particular $\partial\Omega$ can be considered as an $(n-1)$ -dimensional manifold, and thus $H^s(\partial\Omega) \subset C^0(\partial\Omega)$ for all $s > (n-1)/2$. Thus if $f \in H^{(n-1)/2+\epsilon}(\partial\Omega)$, for all $\epsilon > 0$, then f is continuous. To apply a delta distribution to a function $f : \partial\Omega \rightarrow \mathbb{R}$, i.e. $\delta(f) = \langle \delta, f \rangle$, then f must be continuous and thus the Dirac delta distribution belongs to the dual space of $H^{(n-1)/2+\epsilon}(\partial\Omega)$, $\delta \in H^{-(n-1)/2-\epsilon}(\partial\Omega)$ for all $\epsilon > 0$. For $n \geq 2$ it can be deduced that $u \in H^{\min\{(4-n)/2-\epsilon, 1\}}(\Omega)$ for all $\epsilon > 0$ (see [54] for a rigorous justification). In particular there is no guarantee u is $H^1(\Omega)$ regular. This strengthens the non-physicality of delta distribution current sources in the sense that the resulting solutions are unbounded in the energy norm.

Complete electrode model

As for the continuum case we again pose a weak formulation of the problem. Multiplying (2.1) by $v \in H^1(\Omega)$, integrating over Ω , using the divergence theorem and the first boundary condition in (2.5) we have

$$\int_{\Omega} (\sigma \nabla u) \cdot \nabla v = \int_{\partial\Omega} v \nu \cdot (\sigma \nabla u) = \sum_{l=1}^L \int_{E_l} \frac{U_l - u}{z_l} v.$$

From the second condition in (2.5) we can write, for any $V \in \mathbb{R}^L$

$$\sum_{l=1}^L V_l \int_{E_l} \frac{U_l - u}{z_l} = \sum_{l=1}^L I_l V_l$$

Combining these equations we have

$$B_{\sigma,z}((u, U), (v, V)) := \int_{\Omega} (\sigma \nabla u) \cdot \nabla v + \sum_{l=1}^L \int_{E_l} \frac{(u - U_l)(v - V_l)}{z_l} = \sum_{l=1}^L V_l I_l. \quad (2.13)$$

We introduce the quotient space $\dot{H}(\Omega) = (H^1(\Omega) \oplus \mathbb{R}^L) \setminus \mathbb{R}$ i.e. $(u, U), (v, V) \in H^1(\Omega) \oplus \mathbb{R}^L$ are equivalent if

$$u - v = U_1 - V_1 = \dots = U_L - V_L = C$$

for some constant $C \in \mathbb{R}$. This quotient space exactly reflects the fact that the potential is only defined up to a constant. The forward problem is then: given $\sigma \in$

$L_+^\infty(\Omega)$, $z \in \mathbb{R}^L$ and $I \in \mathbb{R}^L$, find $(u, U) \in \dot{H}(\Omega)$ such that

$$B_{\sigma,z}((u, U), (v, V)) = \sum_{l=1}^L I_l V_l \quad \text{for all } (v, V) \in \dot{H}(\Omega), \quad (2.14)$$

where the set of currents I_l additionally satisfy the consistency condition $\sum_{l=1}^L I_l = 0$.

In [55] it is shown that this problem is well-posed

Theorem 2.1.1 (Existence and uniqueness of CEM). *Given that $\sum_{l=1}^L I_l = 0$, (2.14) has a unique solution $(u, U) \in \dot{H}(\Omega)$.*

An analysis of the CEM for $\sigma \in C^\infty(\Omega)$ show that the potential has improved regularity $u \in H^{2-\epsilon}(\Omega)$ for all $\epsilon > 0$ [54, 56]. We will use this result when performing a convergence study in section 2.2.3. The CEM is also the discretisation of a Robin boundary value problem

$$(z\nu \cdot (\sigma \nabla u) + \eta u)|_{\partial\Omega} = h, \quad (2.15)$$

where $z \in C^\infty(\partial\Omega)$ is now a *function* describing the contact impedance on the boundary, with $z|_{E_j} = z_j$ and $\eta = \sum_{j=1}^L \chi_{E_j}$, where χ_{E_j} is the characteristic function of the j^{th} electrode and h is a function of the input voltage data [57]. The CEM is thus a discretisation of the above continuous model in the limit that h is non-zero and constant only on subsets of the boundary corresponding to the electrodes, and in the limit that z is zero off electrodes and constant on electrodes. The Robin boundary value problem will be used when discussing external shape corrections in section 4.2.

2.2 High order finite elements

To perform image reconstruction in EIT some simulated voltage data is normally required for a conductivity sufficiently close to the true conductivity, known as the *forward problem*. The forward problem can only be solved analytically for simple domain geometries, conductivities and boundary conditions, and a numerical method is almost always required to compute a solution. A number of different methods are available including the finite difference method (FDM), boundary element method (BEM) or the FEM. The FDM can be used to solve such problems, but is inefficient especially when attempting to represent curved boundaries. In the BEM only surfaces of regions are discretised, and within each region the conductivity is assumed to be

constant and analytic expressions for Green's functions are used. The BEM results in a dense matrix and its computational advantages diminish as the number of regions in the model increases. The FEM has the advantage that it can be applied to domains with curved boundaries, complex boundary conditions and non-homogeneous coefficients making it the most appealing to lung EIT.

In this section the implementation of the FE method with high order polynomial basis functions for the potential and anisotropic piecewise constant conductivities is discussed. Texts on computational aspects of the method include [53, 58, 59, 60, 61]. In the FE method Ω is decomposed into a set of N_E elements. In this thesis the elements are chosen to be triangles in 2D and tetrahedra in 3D. Within each element each corner point is called a *vertex* and there are N_V vertices in total over Ω . On each element a number of *nodes* are defined, of which the vertices are subset, and a total of N_n distinct nodes over Ω . One looks for an approximate solution to the potential of the form

$$u_h = \sum_{i=1}^{N_n} u_i \psi_i(x) \quad (2.16)$$

where ψ_i are known as the *shape* functions, which are associated with each node in the domain. The shape functions are chosen to satisfy the interpolation property

$$\psi_j(x_i) = \delta_{ij} \quad i, j = 1, \dots, N_n, \quad (2.17)$$

where x_i is the spatial coordinate of node i and δ_{ij} is the Kronecker delta. From (2.16) the vector $u = (u_1, \dots, u_{N_n}) \in \mathbb{R}^{N_n}$ represents the discretised approximation to the potential, u . If the k^{th} element has n_k local degrees of freedom, corresponding to the number of nodes used in the element to interpolate the potential, then there are n_k basis functions not identically 0 on the element. The element shape functions are the restriction of the n_k global shape functions ψ_i in (2.17). The restriction of the global shape functions form a basis set $\Pi^k = \{\psi_1^{(k)}, \psi_2^{(k)}, \dots, \psi_{n_k}^{(k)}\}$, and the solution to the potential within element k is given by

$$u_h|_k = \sum_{i=1}^{n_k} u_i^k \psi_i^{(k)}.$$

A piecewise constant conductivity approximation over elements is used,

$$\sigma = \sum_{i=1}^{N_E} \sigma_i \chi_i, \quad (2.18)$$

where χ_i is the characteristic function of the i^{th} finite element and $\sigma_i \in \mathbb{R}^{n \times n}$ is the conductivity matrix of the i^{th} element.

Continuum FE approximation

In the Galerkin finite element method, a finite dimensional subspace, $S_h^1(\Omega) \subset H^1(\Omega)$, is chosen to represent the approximate potential u_h , and the test function v_h chosen to lie in the same space $S_h^1(\Omega)$, that is $v_h = \sum_{i=1}^{N_n} c_i \psi_i$ for some coefficients c_i [53]. The finite dimensional weak formulation of the problem is: Given $f \in H^{-\frac{1}{2}}(\partial\Omega)$, such that $\int_{\partial\Omega} f = 0$, find $u_h \in S_h^1(\Omega)$ such that

$$\int_{\Omega} (\sigma \nabla u_h) \cdot \nabla v_h = \int_{\partial\Omega} f v_h \quad \forall v_h \in S_h^1(\Omega). \quad (2.19)$$

Substituting the expression for the approximate potential (2.16) yields

$$\int_{\Omega} ((\sigma \nabla \psi_i) \cdot \nabla \psi_j) u_i = \int_{\partial\Omega} f \psi_j \quad j = 1 \dots N_n, \quad (2.20)$$

and substituting the point electrode boundary conditions yields

$$\int_{\Omega} ((\sigma \nabla \psi_i) \cdot \nabla \psi_j) u_i = \int_{\partial\Omega} \sum_{l=1}^L I_l \psi_j(x_l) \quad j = 1 \dots N_n.$$

The vector of nodal potential value, $u \in \mathbb{R}^{N_n}$, is the solution of the linear system

$$Au = f, \quad (2.21)$$

where f has I_l at the index corresponding to the node of the l^{th} electrode and the matrix A has entries

$$A_{ij} = \int_{\Omega} (\sigma \nabla \psi_i) \cdot \nabla \psi_j. \quad (2.22)$$

The potential u is only defined up to a constant resulting in a one-dimensional null space of A . This difficulty can be resolved by choosing, say, the g^{th} interior node, with coordinate x_g , to be at zero potential i.e. $u(x_g) = 0$. The g^{th} row and column of A and the g^{th} row of f and u are removed to generate \tilde{A} , \tilde{f} and \tilde{u} respectively. The $N_n - 1$ dimensional system $\tilde{A}\tilde{u} = \tilde{f}$ is now uniquely solvable for \tilde{u} .

CEM FE approximation

The CEM applies physically more realistic boundary conditions to the EIT problem given by (2.5). In this model an approximate solution for the interior potentials is

sought as well as an approximation to the potentials on the electrodes $U \in \mathbb{R}^L$. Following the method first described by Vauhkonen [47], the finite element approximation to the potential (2.16) is substituted into the weak form (2.14), where the test functions v are chosen as the shape functions $v = \psi_i, i = 1, \dots, N_n$, yielding

$$\sum_{j=1}^{N_n} \left\{ \int_{\Omega} (\sigma \nabla \psi_i) \cdot \nabla \psi_j + \sum_{l=1}^L \int_{E_l} \psi_i \psi_j \right\} u_j - \sum_{l=1}^L \int_{E_l} \frac{1}{z_l} \psi_i U_l = 0. \quad (2.23)$$

Substituting the finite element approximation (2.16) into equation (2.5) yields

$$I_l = \int_{E_l} \frac{1}{z_l} U_l - \sum_{i=1}^{N_n} \left\{ \int_{E_l} \frac{1}{z_l} \psi_i \right\} u_i,$$

and assuming z_l is constant on electrode l , we have the expression

$$I_l = \frac{1}{z_l} |E_l| U_l - \frac{1}{z_l} \sum_{i=1}^{N_n} \left\{ \int_{E_l} \psi_i \right\} u_i, \quad (2.24)$$

where $|E_l|$ is the area of the l^{th} electrode. Combining equations (2.23) and (2.24) leads to the linear system of equations

$$S \begin{pmatrix} u \\ U \end{pmatrix} := \begin{pmatrix} A + B & C \\ C^T & D \end{pmatrix} \begin{pmatrix} u \\ U \end{pmatrix} = \begin{pmatrix} 0 \\ I \end{pmatrix}, \quad (2.25)$$

where u is a vector of the values of the potential at the nodes, U is a vector of the voltages on the electrodes and I is the vector of currents supplied to the electrodes. The matrix A is given by (2.22) and the matrices B , C and D by

$$B_{ij} = \sum_{l=1}^L \frac{1}{z_l} \int_{E_l} \psi_i \psi_j dS \quad C_{jl} = -\frac{1}{z_l} \int_{E_l} \psi_j dS \quad D_{ll} = \frac{|E_l|}{z_l}, \quad (2.26)$$

where $i, j = 1, \dots, N_n$ and $l = 1, \dots, L$. This can be written compactly as

$$Sb = f \quad (2.27)$$

where $b = [u, U]^T$, $f = [0, I]^T$ and S is the block matrix in (2.25). Since the potential is only defined up to a constant, the g^{th} interior node, with coordinate x_g , is assumed to be at zero potential i.e. $u(x_g) = 0$. The g^{th} row and column of S and the g^{th} row of f and b are removed to generate \tilde{S} , \tilde{f} and \tilde{b} respectively. The $N_n + L - 1$ dimensional linear system $\tilde{S}\tilde{b} = \tilde{f}$ is now uniquely solvable for \tilde{b} .

2.2.1 Reference elements and boundaries

We first detail the classical computation of the stiffness matrix in (2.22) using a linear transformation to reference elements (see [53] for more details). It is instructive to detail this well-known computation because analogous transformations are required to compute the surface integrals appearing in the CEM.

Stiffness matrix

Using the piecewise-constant conductivity representation (2.18), (2.22) can be written

$$A_{ij} = \int_{\Omega} (\sigma \nabla \psi_i) \cdot \nabla \psi_j \, dV = \sum_{k=1}^{N_E} \int_{\Omega_k} (\sigma_k \nabla \psi_i) \cdot \nabla \psi_j \, dV, \quad (2.28)$$

where k is an index over the elements and A is the *stiffness* matrix. With the elemental shape functions the elemental stiffness matrices to be calculated in equation (2.28), are of the form

$$a_{ij}^k = \int_{\Omega_k} (\sigma_k \nabla \psi_i^{(k)}) \cdot \nabla \psi_j^{(k)} \, dV. \quad (2.29)$$

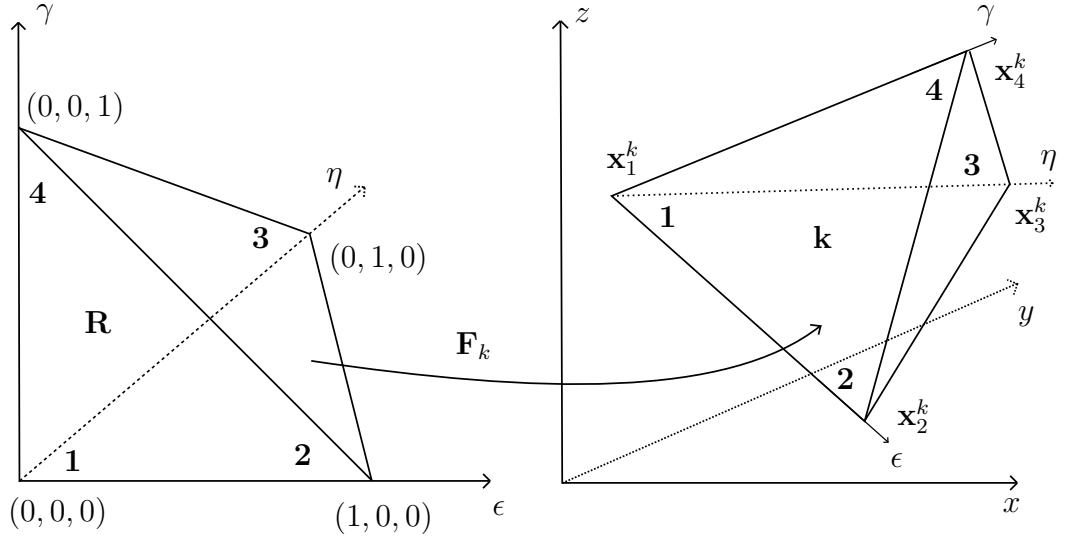
The stiffness matrix is then assembled from contributions from the elemental stiffness matrices. It is instructive to define a new mapping from a reference element to a global element allowing one to define arbitrary polynomial shape functions satisfying the interpolation property (2.17) in a simple geometry.

The linear mapping $\mathbf{F}_k : \mathbb{R}^3 \rightarrow \mathbb{R}^3$ from a reference element, R , chosen as the unit tetrahedron, to the k^{th} element, is illustrated in figure 2.1. It is useful to number the vertices in the local and reference element, by numbering the vertices 2 – 4 anti-clockwise looking into the element from vertex 1, as illustrated in figure 2.1. The k^{th} global element's vertex coordinates are specified as \mathbf{x}_1^k , \mathbf{x}_2^k , \mathbf{x}_3^k and \mathbf{x}_4^k , and the simplest mapping \mathbf{F}_k from the local element in coordinate system (ϵ, η, γ) to the global element k in (x, y, z) coordinate system is given by

$$(x, y, z) = \mathbf{F}_k(\epsilon, \eta, \gamma) = \sum_{i=1}^4 \mathbf{x}_i^k \chi_i(\epsilon, \eta, \gamma), \quad (2.30)$$

where χ_i is the linear basis function associated with the i^{th} vertex in the reference element. The basis functions χ_i above must satisfy the Lagrange interpolation property (2.17) and are uniquely determined as

$$\chi_1(\epsilon, \eta, \gamma) = 1 - \epsilon - \eta - \gamma, \quad \chi_2(\epsilon, \eta, \gamma) = \epsilon, \quad \chi_3(\epsilon, \eta, \gamma) = \eta, \quad \chi_4(\epsilon, \eta, \gamma) = \gamma.$$


 Figure 2.1: The mapping \mathbf{F}_k from a local element R to a general element k in 3D

This linear map sends a straight sided reference element to a straight sided global element. Equipped with this coordinate transformation, the derivatives of the shape functions with respect to global coordinates (x, y, z) must be converted to derivatives of the shape functions with respect to local coordinates (ϵ, η, γ) through the Jacobian matrix. This can be computed via the chain rule as

$$\begin{bmatrix} \frac{\partial \psi}{\partial \epsilon} \\ \frac{\partial \psi}{\partial \eta} \\ \frac{\partial \psi}{\partial \gamma} \end{bmatrix} = \begin{bmatrix} \frac{\partial x}{\partial \epsilon} & \frac{\partial y}{\partial \epsilon} & \frac{\partial z}{\partial \epsilon} \\ \frac{\partial x}{\partial \eta} & \frac{\partial y}{\partial \eta} & \frac{\partial z}{\partial \eta} \\ \frac{\partial x}{\partial \gamma} & \frac{\partial y}{\partial \gamma} & \frac{\partial z}{\partial \gamma} \end{bmatrix} \begin{bmatrix} \frac{\partial \psi}{\partial x} \\ \frac{\partial \psi}{\partial y} \\ \frac{\partial \psi}{\partial z} \end{bmatrix} = J \begin{bmatrix} \frac{\partial \psi}{\partial x} \\ \frac{\partial \psi}{\partial y} \\ \frac{\partial \psi}{\partial z} \end{bmatrix} = \begin{bmatrix} x_2^k - x_1^k & y_2^k - y_1^k & z_2^k - z_1^k \\ x_3^k - x_1^k & y_3^k - y_1^k & z_3^k - z_1^k \\ x_4^k - x_1^k & y_4^k - y_1^k & z_4^k - z_1^k \end{bmatrix} \begin{bmatrix} \frac{\partial \psi}{\partial x} \\ \frac{\partial \psi}{\partial y} \\ \frac{\partial \psi}{\partial z} \end{bmatrix} \quad (2.31)$$

where the matrix J is known as the *Jacobian* matrix, and the last equality follows from the definition of the linear coordinate transformation. Equipped with such a transformation, the elemental stiffness matrix can be written

$$\begin{aligned} a_{ij}^k &= \int_{\Omega_k} (\sigma_k \nabla \psi_i^{(k)}) \cdot \nabla \psi_j^{(k)} \, dx \, dy \, dz \\ &= \int_{\Omega_R} \left(\sigma_k \nabla (\psi_i^{(k)} \circ \mathbf{F}_k) \right) \cdot \left(\nabla (\psi_j^{(k)} \circ \mathbf{F}_k) \right) |J_k| \, d\epsilon \, d\eta \, d\gamma, \end{aligned} \quad (2.32)$$

where $|J_k|$ is the absolute value of the determinant of the Jacobian matrix, Ω_R is the reference element and $\int_{\Omega_R} = \int_0^1 \int_0^{1-\eta} \int_0^{1-\eta-\gamma} d\epsilon \, d\eta \, d\gamma$. Finally, using the definition of the Jacobian transformation (2.31), the gradient operator with respect to global

coordinates, $\nabla = (\frac{\partial}{\partial x}, \frac{\partial}{\partial y}, \frac{\partial}{\partial z})$, can be written in terms of the gradient operator with respect to local coordinates, namely $\nabla^R = (\frac{\partial}{\partial \epsilon}, \frac{\partial}{\partial \eta}, \frac{\partial}{\partial \gamma})$, as $\nabla = J_k^{-1} \nabla^{(R)}$, and so the elemental stiffness matrix is given by

$$a_{ij}^k = \int_{\Omega_R} \left(\sigma_k J_k^{-1} \nabla^{(R)} \psi_i^{(R)} \right) \cdot \left(J_k^{-1} \nabla^{(R)} \psi_j^{(R)} \right) |J_k| \, d\epsilon \, d\eta \, d\gamma, \quad (2.33)$$

where $\psi_i^{(R)} := \psi_i^{(k)} \circ \mathbf{F}_k$, the basis functions on the reference element.

CEM matrices

The forward problem for the CEM requires the additional computation of the matrices B , C , and D in equation (2.26) which are surface integrals for a 3D problem. During the meshing process it is convenient for electrodes to be the union of some tetrahedral element faces in 3D, so that the integrals can be written as the sum over faces of some boundaries. This means that we can write integrals of some function g over an electrode as

$$\int_{E_l} g \, dS = \sum_{p=1}^{n_l} \int_{l(b_p)} g \, dS, \quad (2.34)$$

where n_l is the number of faces that the l^{th} electrode contains, and $l(b_p)$ denotes the integral over the p^{th} face of the l^{th} electrode. With this notation, we can write the matrix entries of B and C in (2.26) as

$$B_{ij} = \sum_{l=1}^L \frac{1}{z_l} \int_{E_l} \psi_i \psi_j \, dS = \sum_{l=1}^L \frac{1}{z_l} \sum_{p=1}^{n_l} \int_{l(b_p)} \psi_i \psi_j \, dS, \quad (2.35)$$

and

$$C_{lj} = -\frac{1}{z_l} \int_{E_l} \psi_j \, dS = -\frac{1}{z_l} \sum_{p=1}^{n_l} \int_{l(b_p)} \psi_j \, dS, \quad (2.36)$$

respectively. The integrals over the electrodes have been split to surface integrals over individual boundaries $l(b_p)$. The contribution from each boundary can then be assembled to form B and C . The matrix D is independent of the choice of basis functions and is trivial to compute.

The surface integral of some scalar field $g : \mathbb{R}^3 \rightarrow \mathbb{R}$ over a surface S , is given by

$$\int_S g \, dS = \int_T g(\mathbf{h}(\epsilon, \eta)) |\partial_\epsilon \mathbf{h}(\epsilon, \eta) \times \partial_\eta \mathbf{h}(\epsilon, \eta)| \, d\epsilon \, d\eta, \quad (2.37)$$

where $\mathbf{h}(\epsilon, \eta)$ is a parametrization of the surface S and (ϵ, η) vary in a region T of the plane. Using the notation in equation (2.34), the p^{th} boundary of the l^{th} electrode is assumed to be a face of the k^{th} element as illustrated in figure 2.1. Let $\mathbf{G}_k(\epsilon, \eta) = \mathbf{F}_k(\epsilon, \eta, 0)$, where $\mathbf{F}_k(\epsilon, \eta, 0)$ is defined in (2.30), and $\partial_\epsilon \mathbf{G}_k, \partial_\eta \mathbf{G}_k$ be vectors of partial derivatives of this mapping. The surface integrals in equation (2.34) can be written as

$$\int_{l(b_p)} g \, dS = \int_T (g \circ \mathbf{G}_k(\epsilon, \eta)) |\partial_\epsilon \mathbf{G}_k(\epsilon, \eta) \times \partial_\eta \mathbf{G}_k(\epsilon, \eta)| \, d\epsilon \, d\eta, \quad (2.38)$$

where $\int_T = \int_0^1 \int_0^{1-\eta}$. So the p^{th} boundary of the l^{th} electrode has been parametrized by a plane $\mathbf{G}_k(\epsilon, \eta)$. The partial derivatives of the mapping \mathbf{G}_k are given by

$$\partial_\epsilon \mathbf{G}_k(\epsilon, \eta) = \mathbf{x}_3^k - \mathbf{x}_1^k, \quad \partial_\eta \mathbf{G}_k(\epsilon, \eta) = \mathbf{x}_2^k - \mathbf{x}_1^k,$$

and so magnitude of the cross product is given by

$$|\partial_\epsilon \mathbf{G}_k(\epsilon, \eta) \times \partial_\eta \mathbf{G}_k(\epsilon, \eta)| = |(\mathbf{x}_3^k - \mathbf{x}_1^k) \times (\mathbf{x}_2^k - \mathbf{x}_1^k)|.$$

It can be seen that the magnitude is independent of the parameters ϵ and η and physically is twice the total area of the p^{th} boundary of the l^{th} electrode. We now have to evaluate integrals along the unit triangle, T , of the form

$$\int_{l(b_p)} g \, dS = \int_T (g \circ \mathbf{G}_k(\epsilon, \eta)) |(\mathbf{x}_3^k - \mathbf{x}_1^k) \times (\mathbf{x}_2^k - \mathbf{x}_1^k)| \, d\epsilon \, d\eta.$$

The only contributions to the matrices (2.26) will be from basis functions ψ_i whose defining node, \mathbf{x}_i , lies on the boundary, since the product of all other basis functions along the boundary are identically 0. Thus instead of performing integration over the boundary of an element k , it is simplest just to integrate over the boundary $l(b_p)$. We define a reference boundary as the unit triangle, T , (see appendix B.3) define our local shape functions on this, and then map to the true boundary $l(b_p)$ as illustrated in figure 2.2. The surface integrals along a boundary $l(b_p)$ are now of the form

$$\int_{l(b_p)} g \, dS = \int_T (g \circ \mathbf{G}_{b_p}(\epsilon, \eta)) |(\mathbf{x}_3^{b_p} - \mathbf{x}_1^{b_p}) \times (\mathbf{x}_2^{b_p} - \mathbf{x}_1^{b_p})| \, d\epsilon \, d\eta,$$

and using the notation above, and defining $J_{b_p} = (\mathbf{x}_3^{b_p} - \mathbf{x}_1^{b_p}) \times (\mathbf{x}_2^{b_p} - \mathbf{x}_1^{b_p})$ the surface integrals appearing in the matrix entries of B in equation (2.35) can be written as

$$\int_{l(b_p)} \psi_i \psi_j \, dS = \int_T (\psi_i^{(b_p)} \circ \mathbf{G}_{b_p}(\epsilon, \eta)) (\psi_j^{(b_p)} \circ \mathbf{G}_{b_p}(\epsilon, \eta)) |J_{b_p}| \, d\epsilon \, d\eta. \quad (2.39)$$

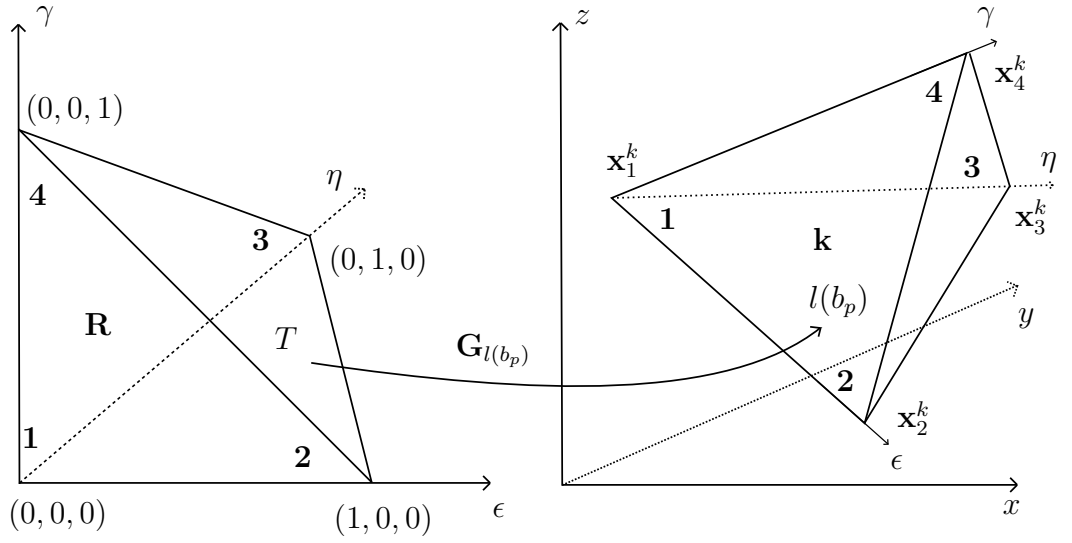


Figure 2.2: The mapping $\mathbf{G}_{l(b_p)}$ from a local boundary T , the unit triangle 123, to a general boundary $l(b_p)$ in 3D.

Similarly the integrals appearing in the entries of C in equation (2.36) can be written

$$\int_{l(b_p)} \psi_i \, dS = \int_T (\psi_i^{(b_p)} \circ \mathbf{G}_{b_p}(\epsilon, \eta)) |J_{b_p}| \, d\epsilon \, d\eta. \quad (2.40)$$

The shape functions on the unit triangle for a quadratic approximation in 3D are illustrated in appendix B.3. After the integrals have been evaluated, the matrices B and C are then assembled in an analogous manner to the stiffness matrix.

2.2.2 Polynomial approximation

It remains now to choose the shape functions $\psi_i^{(R)}$ on the reference element to interpolate the solution within the reference.

Global piecewise linear approximation

In three dimensions, the general form of linear approximation to the potential within element k is given by

$$u_h^k(x, y, z) = a + bx + cy + dz.$$

The coefficients are uniquely determined from the shape function interpolation property at the nodes (2.17), and so we can take the mapping basis functions as the local

basis functions for the potential on the element, that is $\psi_i^{(R)} = \chi_i$ in (2.30). The total finite element approximation is also continuous (C^0) since there is a unique linear polynomial that takes values at the three points along each element's faces [53].

Global piecewise polynomial approximation

For arbitrary order polynomials, the number of unknown coefficients to be determined equates to the number of nodes required on a given element. For example for quadratic approximation in three dimensions the general form of the approximation is given by

$$u_h^k(x, y, z) = a + bx + cy + dz + ex^2 + fy^2 + gz^2 + hxy + ixz + jyz,$$

and so there are 10 unknown coefficients and thus 10 shape functions that are not exactly 0 on each element. There is now freedom to choose the positions of nodes within the element to satisfy the interpolation property (2.17). In this thesis we position the nodes equispaced within an element (see appendix B.3 for basis functions for a quadratic element in 3D). The total finite element approximation is again C^0 since there is a unique quadratic polynomial that takes values at the six points along each element's faces.

Numerical quadrature

Gauss quadrature is used to evaluate the integrals appearing in (2.33), (2.39) and (2.40). Defining a function g as

$$g = \left(\sigma_k J_k^{-1} \nabla^{(R)} \psi_i^{(R)} \right) \cdot \left(J_k^{-1} \nabla^{(R)} \psi_j^{(R)} \right) |J_k|,$$

then we can write

$$a_{ij}^k = \int_R g \, dV,$$

where $dV = d\epsilon d\eta d\gamma$ in 3D. It is important to note that since a linear mapping is used from the reference element to the true element, the Jacobian determinant, $|J_k|$, is independent of ϵ, η, γ . If the polynomial approximation used in element k is of degree p , the integrand is a polynomial of degree $2(p-1)$. Similarly we can deduce that the matrices B and C in (2.39) and (2.40) require integration rules for polynomials of degree $2p$ and p respectively, although only $(n-1)$ D rules are required.

An N point quadrature rule for the approximate integral of a function $p : \mathbb{R}^n \rightarrow \mathbb{R}$ over a region R consists of a set of weights, w_i , and Gauss points, $\mathbf{x}_i \in \mathbb{R}^n$, where $i = 1, \dots, N$. Let \mathbb{P}_k denote the set of polynomials of degree k . The smallest integer k_n such that

$$\int_R p \, dV = \sum_{i=1}^{k_n} \omega_i p(\mathbf{x}_i) \quad \forall p \in \mathbb{P}_k$$

is the quadrature order. Quadrature rules are available to integrate polynomials of a given degree on triangles and tetrahedra, and the weights and Gauss points required to perform the numerical integration of the elemental stiffness matrix are listed in appendix B.4. We note that the quadrature order increases with increasing polynomial approximation order. For information on the numerical implementation of the forward problem in the open source reconstruction software EIDORS [62], see appendix B.1.

2.2.3 Convergence study

In the following section we perform a convergence study for the forward problem in 2D under uniform refinement of a square domain. In particular we are interested in L^2 convergence of the boundary voltages for the forward problem and H^1 convergence for the Fréchet derivative (see section 3.2.2) for the inverse problem. For the inverse problem, we are also interested in determining how accurately the forward problem can be solved for a given finite element triangulation. This is because a piecewise constant representation of the conductivity on finite elements is typically deployed leading to a single degree of freedom per triangle (2D) or tetrahedron (3D) for the inverse problem. Secondly a convergence study under different electrode models is performed to observe how the convergence rate changes to understand how effective high order FEM is at generating more accurate solutions for the forward problem.

There are well known error estimates for high order FE approximations for elliptic problems [61]. Let Ω be a polygonal domain, and assume the solution of an elliptic problem $u \in H^1(\Omega) \cap H^{k+1}(\Omega)$ with k an integer. Let u_h^k be the k^{th} order finite element approximation to u , then

$$\|u - u_h^k\|_{L^2} \leq C_1 h^{k+1} |u|_{k+1}, \quad \|\nabla(u - u_h^k)\|_{L^2} \leq C_2 h^k |u|_{k+1}, \quad (2.41)$$

where h is the length of the largest edge in the finite element mesh, k is the degree of polynomial approximation, C_1, C_2 are constants and the semi-norm $|\cdot|_{k+1}$ is defined

as

$$|u|_{k+1} = \left(\sum_{|\alpha|=k+1} \int_{\Omega} |D^{\alpha} u|^2 \right)^{\frac{1}{2}}.$$

If the solution u *a-priori* has high regularity, for example $u \in C^{\infty}(\Omega)$, we can deduce that exponential convergence is guaranteed in the H^1 and L^2 norm, for increasing p at a fixed h . Such regularity is true if $\partial\Omega$ is smooth, and the boundary conditions and conductivity are smooth functions. The forward problem in EIT with realistic electrode models does not have smooth prescribed boundary data, and so it is not obvious that such regularity will be present. From section 2.1.2 the solutions to the point and complete electrode models are known to have regularity $u \in H^{1-\epsilon}(\Omega)$ (in 2D) and $u \in H^{2-\epsilon}(\Omega)$ respectively for all $\epsilon > 0$, when $\sigma \in C^{\infty}(\Omega)$. Convergence results have been extended to solutions with fractional Sobolev regularity [63]. In particular let $u \in H^s(\Omega)$ and $s \in \mathbb{R}$ with $k + 1 \geq s \geq 1$, then

$$\|u - u_h^k\|_{L^2} \leq C_3 |u|_s h^s, \quad \|\nabla(u - u_h^k)\|_{L^2} \leq C_4 |u|_s h^{s-1},$$

where C_3, C_4 are constants. The power of h is independent of the approximation order. In particular for the CEM we can predict convergence at rate $h^{1-\epsilon}$ and $h^{2-\epsilon}$ in the H^1 and L^2 norms respectively for *all* approximation orders, and for the point electrode model ($u \in H^{1-\epsilon}(\Omega)$), convergence is not guaranteed in either norm.

We exhibit convergence results of high order FEM under different electrode models for each order of approximation under uniform refinement of a given finite element triangulation. In particular we consider convergence of FE solutions to the Laplacian ($\sigma = 1$) on a square domain $\Omega = [0, \pi]^2$. In doing so a novel analytic solution to the CEM is computed to test convergence. In all cases we consider Neumann zero boundary conditions on the $y = 1$, $x = 0$ and $x = 1$ boundaries of the square. Convergence is studied by computing a sequence of finite element triangulations, $T^{(i)}$, indexed by an integer $i \geq 1$, (see figure 2.3). Each finite element triangulation has a maximum associated element length h^i , where h is the maximum length in the coarsest mesh, $T^{(1)}$. The global linear, quadratic and cubic finite element errors are computed as a function of the refinement level, i , by calculating the L^2 norm and H^1 energy norm of the difference between analytic and FE solutions, $\|u - u_h\|_{L^2}$ and $\|u - u_h\|_{H^1} = \|\nabla(u - u_h)\|_{L^2}$. To approximate these integrals the same quadrature rule is used as to integrate the products of basis functions exactly over each element.

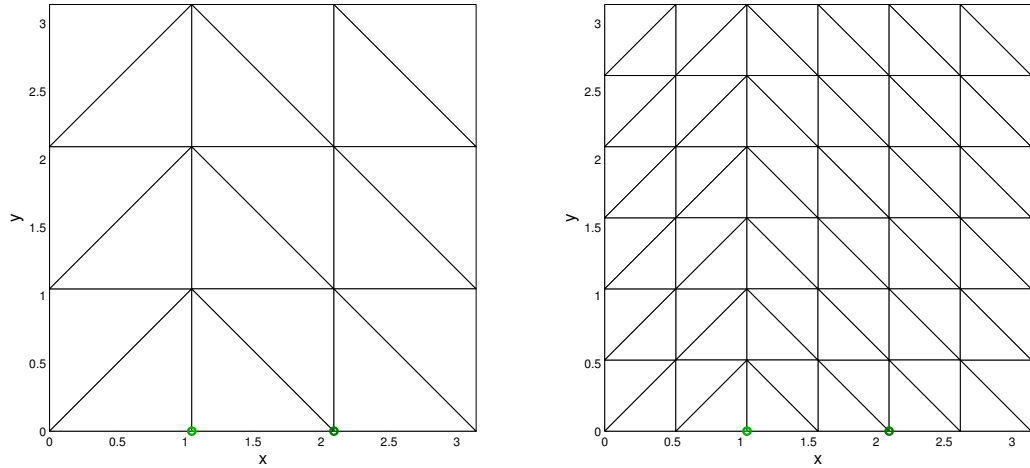


Figure 2.3: Uniform triangulations of square domain. The left and right hand figure represent the $T^{(1)}$ and $T^{(2)}$ triangulations respectively with point electrode model.

To demonstrate convergence $\log(\|u - u_h\|)$ is plotted against $-\log(h)$. Asymptotic convergence of the form Ch^k , as $h \rightarrow 0$, would give approximate straight lines of gradient $-k$, which we estimate through a Least-Squares fit.

Continuum model

We first consider the continuum models with a non-zero Neumann condition given by a function $f = \cos(x)$ on $y = 0$. After separation of variables, and using the Neumann zero boundary conditions on the $x = 0$ and $x = \pi$ boundary, we arrive at an analytic expression for the solution u of the Laplacian

$$u(x, y) = A_0 + \sum_{n=1}^{\infty} A_n \cos(nx) \cosh(n(\pi - y)), \quad (2.42)$$

where the coefficients A_n , $n \geq 1$, are given by

$$A_n n \sinh(n\pi) = \frac{2}{\pi} \int_0^{\pi} f(x) \cos(nx) dx, \quad (2.43)$$

and A_0 is a constant determined by choice of a ground point. Given the Neumann condition $f(x) = \cos(x)$, only 1 non-zero Fourier coefficient, $A_1 = \frac{1}{\sinh(\pi)}$, is retained. We note also that the solution is smooth, $u \in C^\infty(\Omega)$. Figure 2.4 demonstrates the convergence of the continuum model. We observe errors approximately of the form Ch^{p+1} and Ch^p in the L^2 and H^1 norm respectively, where p is the polynomial approximation degree. These results demonstrate that global high order finite element approximations are more accurate at a given triangulation, for this smooth boundary condition, and are in agreement with the classical error estimate (2.41).

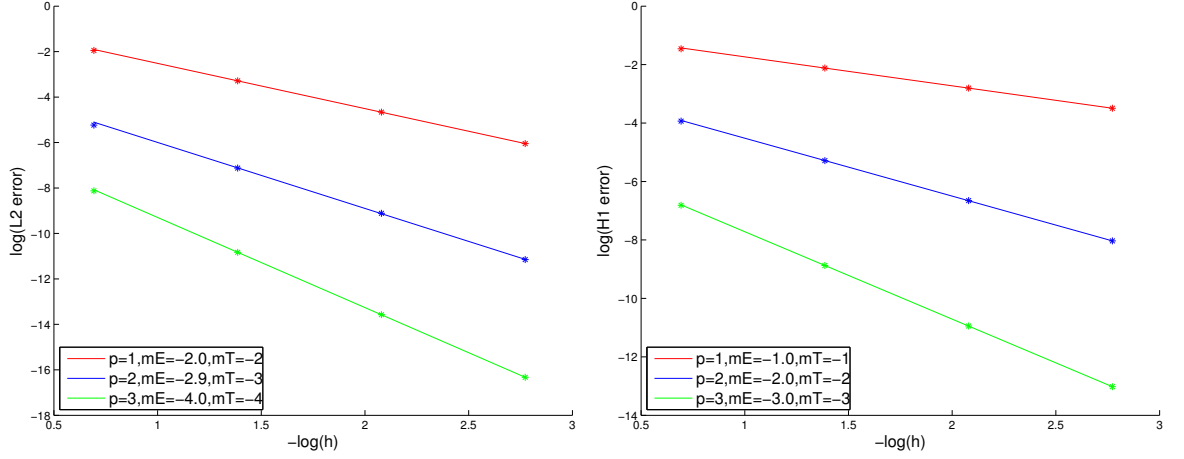


Figure 2.4: Convergence for the continuum model in the L^2 and H^1 norm. p is the polynomial approximation degree and mE and mT are the estimated and theoretical convergence rates respectively. We observe convergence of the form Ch^{p+1} and Ch^p in the L^2 and H^1 norm respectively.

Point electrode model

We consider a current function $f(x) = \delta(x - \frac{\pi}{3}) - \delta(x - \frac{2\pi}{3})$ and arrive at an expression for the coefficients as

$$A_n = \frac{2}{n \sinh(n\pi)} \left(\cos\left(\frac{n\pi}{3}\right) - \cos\left(\frac{2n\pi}{3}\right) \right).$$

The solution to the point electrode model is unbounded in the global H^1 -norm because of the Dirac delta Neumann conditions. To efficiently compute the infinite series we split into the interior and boundary nodes. On the $y = 0$ boundary we have

$$u(x, 0) = A_0 + \sum_{n=1}^{\infty} \frac{2}{n \tanh(n\pi)} \left(\cos\left(\frac{n\pi}{3}\right) - \cos\left(\frac{2n\pi}{3}\right) \right) \cos(x).$$

As $n \rightarrow \infty$, $\tanh(n\pi) \rightarrow 1$ and the series is a slowly converging harmonic-type series.

Away from the boundary $y > 0$

$$u(x, y) = A_0 + \sum_{n=1}^{\infty} \frac{2}{n \sinh(n\pi)} \left(\cos\left(\frac{n\pi}{3}\right) - \cos\left(\frac{2n\pi}{3}\right) \right) \cos(x) \cosh(n(\pi - y)),$$

which converges quickly as $n \rightarrow \infty$ because of the dominant $\sinh(n\pi)$ term. The L^2 and H^1 errors are plotted against the refinement level in figure 2.6. The point electrode model exhibits approximate $O(h)$ convergence in the L^2 norm independent of the polynomial approximation. Unsurprisingly there is effectively no convergence in the H^1 -norm because the analytic solution is unbounded in this norm, and this is an artefact of the series approximation to the gradient of the solution. These results are in agreement with theory, because in $2D$ the solution $u \in H^{1-\epsilon}(\Omega)$ for all $\epsilon > 0$ when

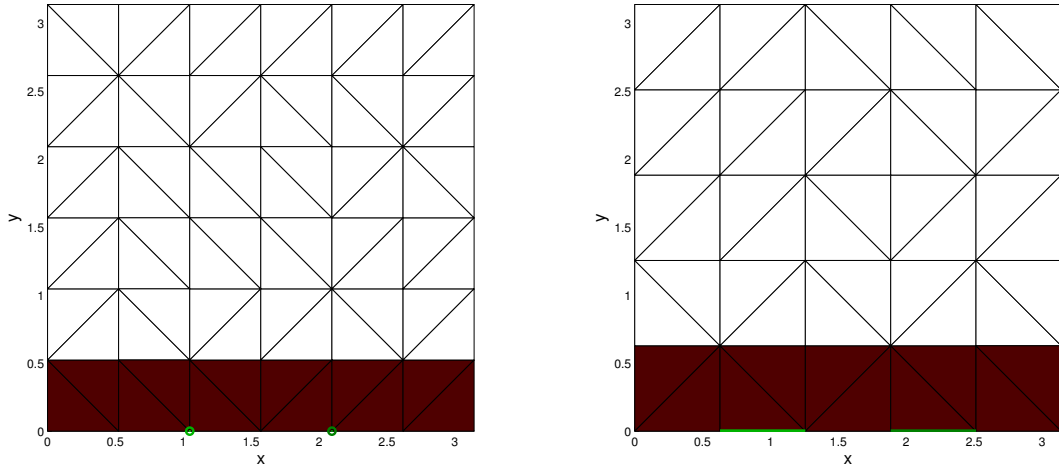


Figure 2.5: The left and right hand images are the square domain with point and complete electrode models. The red elements highlighted are the regions of the domain neglected for the convergence study away from the electrodes.

there are delta function current sources, and thus ∇u fails to be in L^2 . This example highlights the danger of the point electrode model, as a globally accurate sensitivity map can not be computed with this model.

Figure 2.7 illustrates convergence plots of the errors, neglecting a neighbourhood of elements near the boundary (see figure 2.5). In the interior there is convergence of the form Ch^{p+1} and Ch^p in both the L^2 and H^1 -norm. This can be explained because of elliptic regularity of the solution operator $T_\epsilon : H^s(\partial\Omega) \rightarrow C^\infty(\Omega \setminus \partial\Omega_\epsilon) : f \mapsto u_\epsilon$ for all $s \in \mathbb{R}$, mapping the boundary current density to interior potential, where $\partial\Omega_\epsilon$ is notation for an ϵ neighbourhood of the boundary. In particular the solution operator for an elliptic PDE preserves singular support [64], where the singular support is the complement of the smallest open set on which the function is smooth. In the interior of the domain, away from the point electrodes, the solution must be smooth. The solution to the discretised FEM solution also appears to retain this property to generate the h^p convergence observed. This is an interesting observation for the inverse problem if we consider the case when the conductivity is known in a neighbourhood of the boundary, because the results suggest that the sensitivity map is still accurately computed in the interior.

CEM

Semi-analytic solutions have been obtained for the CEM on the unit disc using Fourier decomposition methods [50, 65], the solutions being only semi-analytic because the

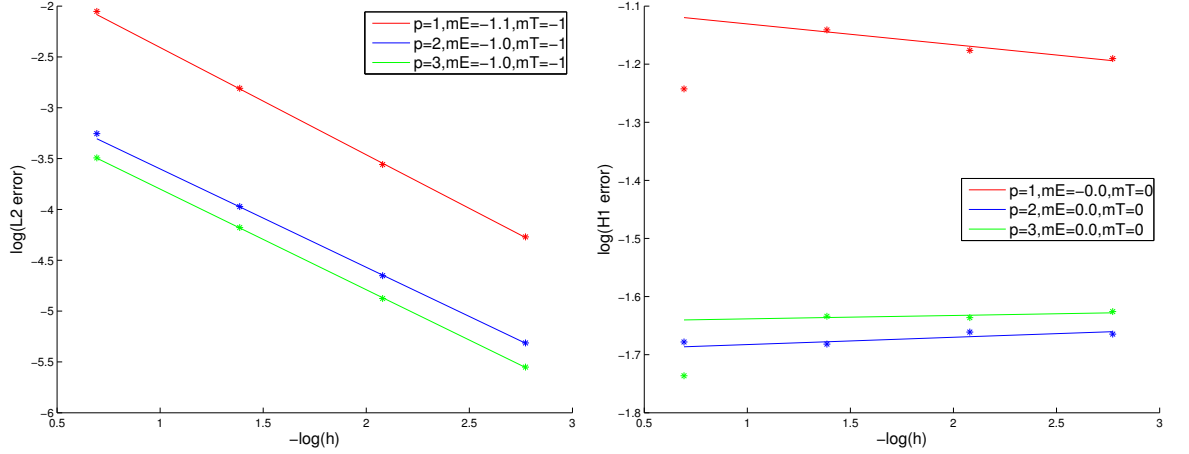


Figure 2.6: FEM convergence for the point electrode model. Convergence for the point electrode model in the L^2 and H^1 norm. p is the polynomial approximation degree and mE and mT are the estimated and theoretical convergence rates respectively. We observe convergence of the form Ch in the L^2 norm and no convergence in the H^1 norm, both independent of the polynomial approximation degree.

method results in an infinite dimensional system of equations to solve for the Fourier coefficients. We apply a similar technique to the CEM on the square domain with $\sigma = 1$. We consider the application of a potential vector $U \in \mathbb{R}^2$, $U = (1, -1)$, between two electrodes as opposed to a current vector $I \in \mathbb{R}^2$. The finite element system to solve for (u, I) in equation (2.44) becomes

$$\begin{pmatrix} A & 0 \\ B^T & -I \end{pmatrix} \begin{pmatrix} u \\ I \end{pmatrix} = \begin{pmatrix} -BU \\ CU \end{pmatrix}. \quad (2.44)$$

We denote the two electrodes on the $y = 0$ boundary as $E_1 = \{(x, y) | y = 0, \frac{\pi}{5} \leq x \leq \frac{2\pi}{5}\}$ and $E_2 = \{(x, y) | y = 0, \frac{3\pi}{5} \leq x \leq \frac{4\pi}{5}\}$ (see figure 2.5). We characterise the electrodes by their centre of mass, and width $(x_1, x_2, w) = (\frac{3\pi}{10}, \frac{7\pi}{10}, \frac{\pi}{5})$. The interior potential solves Laplace's equation, and the Neumann zero boundary conditions on the $x = 0$ and $x = \pi$ boundary imply that the solution again has the form (2.42). Substituting this into the Robin condition, we have for $x \in [0, \pi]$

$$\sum_{k=1}^{\infty} A_k k \sinh(k\pi) \cos(kx) = \begin{cases} \frac{1}{z_l}(U_l - A_0 - \sum_{k=1}^{\infty} A_k \cosh(k\pi) \cos(kx)) & \text{if } x \in E_l \\ 0 & \text{otherwise} \end{cases}$$

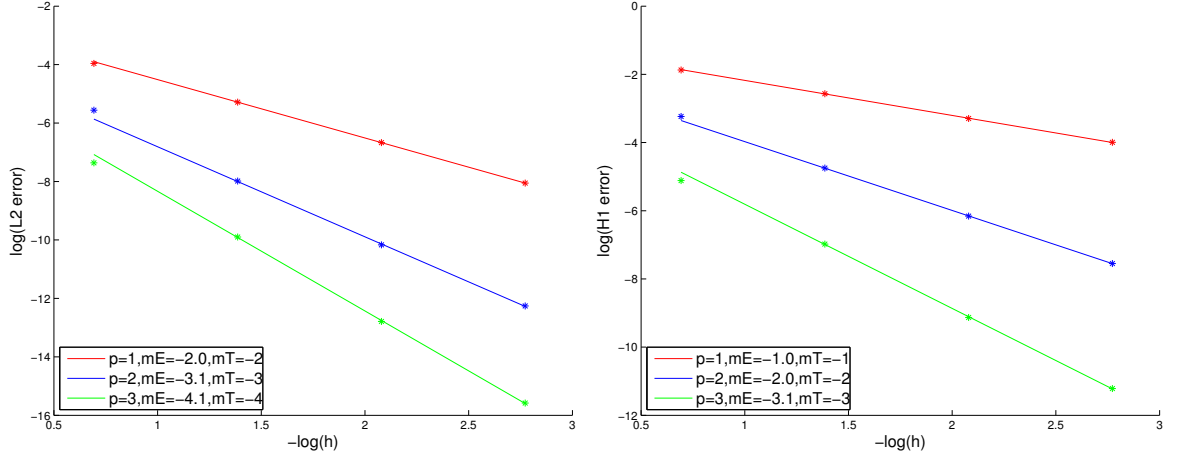


Figure 2.7: FEM convergence for the point electrode model in the L^2 and H^1 norm away from the driven electrodes. p is the polynomial approximation degree and mE and mT are the estimated and theoretical convergence rates respectively. We retain convergence observed with smooth boundary conditions of the form Ch^{p+1} and Ch^p in the L^2 and H^1 norm respectively (see figure 2.4).

We extend this to an even function over $[-\pi, \pi]$, multiply by $\cos(nx)$ and integrate over $[-\pi, \pi]$ resulting in

$$\sum_{k=1}^{\infty} \int_{-\pi}^{\pi} A_k k \sinh(k\pi) \cos(kx) \cos(nx) dx = \sum_{l=1}^2 \frac{1}{z_l} \left(\int_{E_l} (U_l - A_0) \cos(nx) dx - \sum_{k=1}^{\infty} \int_{E_l} A_k \cosh(k\pi) \cos(kx) \cos(nx) dx \right)$$

The orthonormality of $\cos(kx)$ implies that the left hand side is $A_n n \sinh(n\pi)$. The last term on the right hand side is a linear combination of A_k weighted by integrals of cosine products which can be computed analytically. We have an infinite system of equations for the Fourier coefficients, $A = (A_0, A_1, \dots)$ of the form, $SA = U$, where

$$S_{nk} = \sum_{l=1}^2 \frac{1}{z_l} \int_{x_l-w_l}^{x_l+w_l} \cos(nx) \cos(kx) \cosh(k\pi) dx + \delta_{nk} \pi \sinh(k\pi) \cos(kx) \quad n, k = 0, 1, 2, \dots$$

and

$$U_n = \sum_{l=1}^2 \frac{U_l}{z_l} \int_{x_l-w_l}^{x_l+w_l} \cos(nx) dx \quad n = 0, 1, 2, \dots$$

The existence and uniqueness result for the CEM ensures a unique solution in $H^1(\Omega)$. The linear system of equations are inverted numerically by truncating to a system of N equations. The matrix S is ill-conditioned in practice as N increases, because of the increasing contributions from the $k \sinh(k\pi)$ and $\cosh(k\pi)$ terms. The matrix S can be factorized as $S = MD$, where D is diagonal with entries $D_{kk} = \cosh(k\pi)$, and the inverse is given by $S^{-1} = D^{-1}M^{-1}$, where the matrix M has improved conditioning.

The matrix D is still ill-conditioned, but is diagonal and thus has an explicit inverse of the form $(D^{-1})_{kk} = \frac{1}{\cosh(k\pi)}$. This diagonal matrix acts to dampen high frequency coefficients in U .

Figure 2.8 shows convergence plots for the CEM under uniform refinement with a contact impedance on each electrode of $z = 1000$. The convergence in the L^2 -norm is approximately $O(h^2)$ and the convergence in the H^1 norm $O(h)$, both independent of the approximation degree, although higher order finite elements have a smaller associated constant. This is also in agreement with the theory, because for smooth conductivities we have regularity of the solution $u \in H^{2-\epsilon}(\Omega)$, for all $\epsilon > 0$, and the gradient $\nabla u \in H^{1-\epsilon}(\Omega)$ (see section 2.1.2). Figure 2.9 illustrates the error convergence away from the boundary with $z = 1000$. As with the point electrode model we again observe fast h^p type convergence in the interior of the domain because of elliptic regularity. This highlights that the errors in the forward problem in EIT, with a constant conductivity, are heavily concentrated near the electrodes.

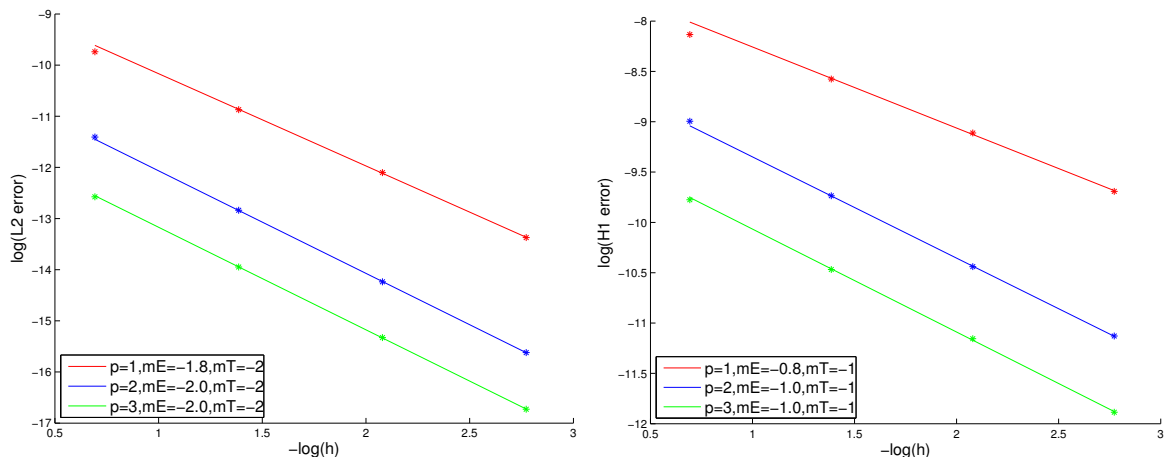


Figure 2.8: Convergence of the CEM with $z = 1000$. p is the polynomial approximation degree and mE and mT are the estimated and theoretical convergence rates respectively. We observe convergence of the form Ch^2 and Ch in the L^2 and H^1 norm respectively, independent of the polynomial approximation degree.

2.3 Conclusions

In this chapter the computation of global high order polynomial FE approximations to the CEM was outlined in 3D. The extension to arbitrary polynomial orders is conceptually straightforward, by first determining Lagrange interpolating basis functions

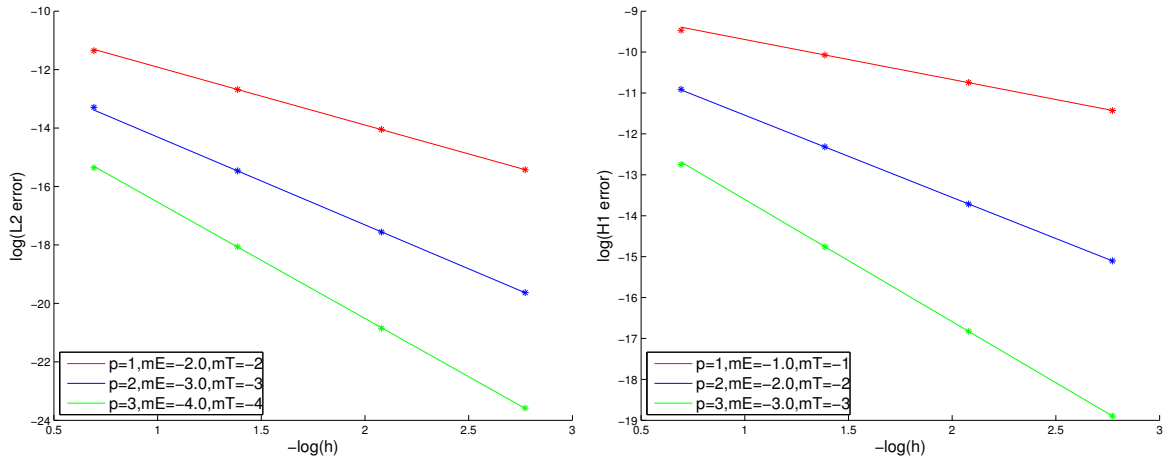


Figure 2.9: Convergence of the CEM with $z = 1000$ away from driven electrodes. p is the polynomial approximation degree and mE and mT are the estimated and theoretical convergence rates respectively. We retain convergence observed with smooth boundary conditions of the form Ch^{p+1} and Ch^p in the L^2 and H^1 norm respectively (see figure 2.4).

on the reference tetrahedron, and then using a quadrature rule consistent with the polynomial approximation degree.

A convergence study under different models was carried out in 2D on square domains. It was found that using high order FEM increased the accuracy of the forward problem in all models for a given finite element triangulation. However the global convergence rate was approximately independent of the polynomial degree for the point and complete electrode models. Any additional accuracy comes at the expense of the increased computational complexity with the additional degrees of freedom required for the solution. The solutions to the point electrode model are just short of H^1 regularity, and thus global convergence is not observed in this norm. For the complete electrode model, with a potential applied between two electrodes on a single side and Neumann zero conditions on the other three sides, approximately $O(h^2)$ and $O(h)$ global convergence in the L^2 and H^1 norm respectively was observed, and independent of the approximation order. An interesting observation was that away from the driven electrodes $O(h^{p+1})$ and $O(h^p)$ convergence to the analytic solution in the L^2 and H^1 norm respectively was observed for both the point and complete electrode models. These results strengthen the intuition that errors in the forward problem are heavily concentrated near electrodes and why finite element meshes are usually more refined near electrodes to compensate for this.

More advanced numerical methods to achieve exponential convergence of solutions

to PDE, such as hp-adaptive methods, are becoming increasingly popular in the literature. In these methods, the solution can be updated locally both through a spatial refinement of the elements (h-refinement), most useful where there are discontinuities present in the solution, or through an increase of the approximating polynomial degree (p-refinement), where the solution is smoother. Such methods aim to achieve exponential convergence as a function of the total degrees of freedom of the approximation. See [66, 67] for an application of hp-FEM for 2D EIT in the continuum model and CEM respectively.

2.3.1 Modelling errors and lung EIT

It is clearly important to solve the forward problem sufficiently accurately during an iterative reconstruction algorithm in EIT. How accurately the forward problem needs to be solved for the inverse problem is unclear though. The modelling error in the forward problem depends on the type of finite element approximation as discussed in this chapter. The inverse problem modelling error depends on the regularisation scheme and parameters used during a given inversion algorithm. In practical lung EIT it is also apparent that the boundary shape and electrode positions are inaccurately known. We will observe in section 4.1 that an inaccurately known boundary shape and electrode positions creates a much larger source of error in the forward problem solution than a sub optimal finite element method. In order for absolute lung EIT to become practically realisable it will require the systematic minimisation of modelling error i.e. determining the current dominant source of modelling error, improving the modelling to decrease the error until it does not dominate, and repeating until all sources of modelling error are negligible compared to measurement noise. It is of the author's opinion that accurately determining the external shape and electrode positions of a subject is currently the largest source of modelling error that needs to be reduced in lung EIT.

Chapter 3

Inverse problem in EIT

This chapter is largely theoretical and serves to outline general inverse problem theory, theory specific to EIT, as well as a novel discussion of EIT with eigenspace constraints on the conductivity. In section 3.1 we outline some general inverse problem theory that will be used in the subsequent chapters. This includes a discussion of mild and severe ill-posed problems, the singular value decomposition and reconstruction algorithms. In section 3.2 the Dirichlet-to-Neumann map is defined and Fréchet differentiability with respect to conductivity changes is demonstrated. We show that the derivative and discretisation commute which is not clearly stated in the literature. This is also related to the Fréchet derivative with respect to external boundary shape, because it is not clear whether the discretisation and derivative commute in this case. In section 3.3 we outline uniqueness results for the non-linear isotropic inverse conductivity problem. In section 3.3.1 we outline identifiability of $\sigma|_{\partial\Omega}$ from the DtN map by highlighting that the DtN map is a pseudo-differential operator. This will give us some insight into why EIT is ill-posed, and is also used to understand the problem with an inaccurately known external shape in sections 4.2.2 and 4.3.4. In section 3.3.2 we outline the use of complex geometric optics to determine the conductivity in the interior of Ω . This is used in our novel discussion of exact methods in lung EIT in section 3.3.3, where we highlight why accurate forward modelling, such as the correct number of spatial dimensions (three) and accurate boundary shape, should be used on a reconstruction model.

In section 3.4 we discuss the anisotropic inverse conductivity problem. In section 3.4.1 we outline the natural generalisation of the inverse conductivity problem to the

determination of a Riemannian metric on a manifold M as well as the non-uniqueness result in section 3.4.2. This is used in the remainder of this chapter as well as in the boundary shape chapter in 4.2.2. In section 3.4.3 we digress to discuss some problems in theoretical elasticity. We discuss the Saint-Venant compatibility condition, which is analogous to the Cotton-York integrability condition in section 4.2.2. We outline in detail two problems from theoretical elasticity that are directly used when discussing the anisotropic problem with constraints on the conductivity eigenspace. We outline a theorem stating the recovery of the deformation field from principal strains and a theorem on the existence of orthogonal coordinates on 3-dimensional Riemannian manifolds. These two problems are analogous to the anisotropic inverse conductivity problem with prescribed eigenvalues and eigenvectors respectively.

In section 3.4.4 we perform a novel discussion of the anisotropic inverse conductivity problem with constraints on the eigenspace of the metric. We define subclasses of anisotropic conductivity with eigenspace constraints: *prescribed eigenvalues*, *prescribed orthogonal coordinates*, *prescribed eigenvectors*, *fibrous* and *layered* conductivities, and by drawing analogies with the elasticity theory in the previous section we explain how such constraints restrict the set of diffeomorphisms fixing points on the boundary. We prove two uniqueness results. Firstly a local uniqueness result (in an ϵ -neighbourhood of the boundary) with a conductivity with prescribed eigenvalues is shown. Secondly a uniqueness results with prescribed eigenvectors is shown, assuming a globally defined coordinate system.

3.1 Ill-posed inverse problems

Let M and D be abstract spaces in which our solution and data lie respectively and consider an operator $F : M \rightarrow D, m \mapsto d = F(m)$. Hadamard [68] defined such a problem to be well-posed if (i) for any $d \in D$ there exists a solution $m \in M$, (ii) for any $d \in D$ the solution is unique (there exists an inverse, F^{-1}), and (iii) if the solution depends continuously on the data (F^{-1} is continuous). Hadamard further defined a problem to be *ill-posed* if any of the three criteria are not satisfied. In an inverse problem, we wish to determine some model parameters $m \in M$ from some data $d \in D$. A typical ill-posed inverse problem may satisfy the existence and uniqueness

criteria, but the inverse will be discontinuous. Small experimental errors in the data can lead to unbounded errors in the solution, and can also result in data that may not lie in the range of the forward operator F anymore, bringing into question the existence of a solution.

An archetypal linear ill-posed inverse problem is the inversion of a compact operator. Consider two Hilbert spaces X and Y , and denote $\{x_n\}_{n=1}^{\infty}$ and $\{y_n\}_{n=1}^{\infty}$ as orthogonal bases for X and Y respectively. Let $\sigma_n \in \mathbb{R}, n = 1, \dots, \infty$, and define two operators $F, F_N : X \rightarrow Y$ by

$$F : x \mapsto \sum_{n=1}^{\infty} \sigma_n \langle x, x_n \rangle y_n, \quad F_N : x \mapsto \sum_{n=1}^N \sigma_n \langle x, x_n \rangle y_n. \quad (3.1)$$

If $\sigma_n \rightarrow 0$ as $n \rightarrow \infty$, then $\|F - F_N\| \rightarrow 0$ as $N \rightarrow \infty$. In this case the operator F is the norm limit of a finite rank operator and so is compact. Conversely, any compact operator between two Hilbert spaces can be written in the form (3.1) where $\sigma_n \rightarrow 0$ as $n \rightarrow \infty$ [69]. Let $g \in R(A)$, then $Ff = g$ if and only if $\sigma_n \langle f, x_n \rangle = \langle g, y_n \rangle$. We require $\|f\| < \infty$ which implies $\sum_{n=1}^{\infty} \frac{\langle g, y_n \rangle^2}{\sigma_n^2} < \infty$, and thus observe that $F^{-1} : Y \rightarrow X$

$$F^{-1} : g \mapsto \sum_{n=1}^{\infty} \frac{\langle g, y_n \rangle}{\sigma_n} x_n,$$

satisfies $Ff = g$, and is unique. However, if we take $g_m = g + \sqrt{\sigma_m} y_m$, then $\|g - g_m\| = \sqrt{\sigma_m} \rightarrow 0$, but $\|f - f_m\| = \frac{1}{\sqrt{\sigma_m}} \rightarrow \infty$, and hence the inverse is not continuous, and the inversion of a compact operator between two Hilbert spaces is an ill-posed problem. Regularisation and prior information are important tools to perform stable inversion in practice as we discuss in section 3.1.3. We now consider two classic examples of linear ill-posed problems that we will use in this thesis.

3.1.1 Mild and severe ill-posedness

We present two examples to classify the degree of ill-posedness of an inverse problem, namely *differentiation* and the *backwards heat equation*.

Differentiation

We consider integration of a function $f \in L^2[0, \pi]$ with $f(0) = f(\pi) = 0$, represented using a Fourier sine series as $f(x) = \sum_{n=1}^{\infty} f_n \sin(nx)$. We denote the integration

operation $F : L^2([0, \pi]) \rightarrow L^2([0, \pi])$ by $(Ff)(x) = \int_0^x f(x') dx'$

$$F : f(x) \mapsto \sum_{n=1}^{\infty} -\frac{1}{n} f_n \cos(nx) + C.$$

Now $\frac{1}{n} \rightarrow 0$ as $n \rightarrow \infty$, and we observe that F is a linear, compact operator on L^2 , and thus differentiation is a classical ill-posed problem on L^2 . We note that the singular values have *polynomial* type decay, which classifies this operation as *mildly ill-posed* and this class of inverse problem is relatively tame. When we outline a mechanical model of the lung in chapter 6, we treat numerical differentiation as an ill-posed inverse integration problem.

Backwards heat equation

Consider the solution $u(x, t)$ of the heat equation in one spatial dimension

$$\frac{\partial u}{\partial t} = \frac{\partial^2 u}{\partial x^2}, \quad x \in [0, \pi],$$

with initial condition $u(x, 0) = f(x) \in L^2([0, \pi])$ and Dirichlet boundary conditions $u(0, t) = u(\pi, t) = 0$. Using separation of variables the solution to this problem is

$$u(x, t) = \sum_{n=1}^{\infty} A_n \sin(nx) e^{-n^2 t},$$

where A_n are the Fourier sine coefficients of $f(x)$. This is in the form of the abstract framework with $x_n(x) = \sin(nx)$, forming an orthogonal basis of $L^2([0, \pi])$. The solution operator $F : L^2([0, \pi]) \rightarrow L^2([0, \pi])$ is given by

$$F_t : f \mapsto F_t f = \sum_{n=1}^{\infty} \sigma_n \langle f, x_n \rangle x_n,$$

where $\langle \cdot, \cdot \rangle$ denotes the L^2 inner product and $\sigma_n = e^{-n^2 t}$. Now $\sigma_n \rightarrow 0$ as $n \rightarrow \infty$ and so the solution operator F_t is compact. An ill-posed problem would then be, given some heat distribution at time $t > 0$, what was the initial heat distribution at $t = 0$? Given no error in the solution u_t , then the solution would be

$$u(x, 0) = \sum_{n=1}^{\infty} e^{n^2 t} \langle u_t, x_n \rangle x_n,$$

but because of the factor $e^{n^2 t}$, any high frequency noise in u_t would generate large errors in the solution rendering it meaningless. The singular values of F have exponential

decay, and inverse problems with this type of decay are known as *severely* ill-posed. This instability demonstrates that using the formal inverse operator, if it exists, can be inadequate in the presence of any noise. The inverse problem of EIT has features similar to the backwards heat equation as will be explained in this chapter.

3.1.2 Singular value decomposition

In a finite dimensional setting, the singular value decomposition (SVD) is an important computational tool to analyse ill-conditioning of a discretised linear inverse problem and will be used in the boundary shape sensitivity study in section 4.4. We consider a matrix $F : \mathbb{R}^m \supset M \rightarrow D \subset \mathbb{R}^d$, $m \mapsto d = Fm$ whose SVD is given by [70]

$$F = U\Sigma V^T = \sum_{i=1}^{\min(m,d)} u_i \lambda_i v_i^T$$

where $U = (u_1, \dots, u_d) \in \mathbb{R}^{d \times d}$, $V = (v_1, \dots, v_m) \in \mathbb{R}^{m \times m}$ are orthonormal matrices, and $\Sigma = \text{diag}(\lambda_1, \dots, \lambda_{\min(m,d)}) \in \mathbb{R}^{d \times m}$. The SVD is unique up to reordering and the singular values are ordered such that $\lambda_1 \geq \lambda_2 \geq \dots \geq \lambda_{\min(m,d)} \geq 0$. The u_i and v_i are the left and right singular vectors respectively and satisfy

$$Fv_i = \lambda_i u_i, \quad F^T u_i = \lambda_i v_i. \quad (3.2)$$

The null space of F is the set $N(F) = \{m \in \mathbb{R}^m : Fm = 0\}$. If F has rank r , with $r < \min(m, d)$, the singular values $\lambda_{r+1}, \dots, \lambda_{\min(m,d)}$ are zero, and the corresponding singular vectors span $N(F)$. Left and right multiplication of the equation $d = Fm$ by U^T and U respectively yields

$$\sum_{i=1}^r (u_i^T d) u_i = \sum_{i=1}^r \lambda_i (v_i^T m) u_i.$$

Any components of d that are parallel to the singular vectors with small singular values are attenuated resulting in a meaningless solution m . In practice the data is subject to some instrumentation error threshold, ϵ , as well as a numerical error threshold, μ . Singular vectors with singular values below the instrumentation threshold give rise to observations with smaller amplitude than the instrument noise, and below the numerical error threshold are effectively unobservable. Model vectors parallel to these singular vectors will hence be sensitive to data errors. Effectively the singular value

spectrum can be classified as

$$\lambda_1 \geq \dots \geq \lambda_z \geq \mu \geq \lambda_{z+1} \geq \dots \geq \lambda_w \geq \epsilon \geq \lambda_{w+1} \geq \lambda_r > 0 = \lambda_{r+1} = \dots = \lambda_D,$$

and this characterises M . The subspace of M spanned by singular vectors associated with the singular values $\lambda_1, \dots, \lambda_z$ are observable in practice. The subspace of M spanned by singular vectors associated with the singular values $\lambda_{z+1}, \dots, \lambda_w$ generate data with amplitudes smaller than the noise level. The subspace of M spanned by singular vectors associated with singular values $\lambda_{w+1}, \dots, \lambda_r$ generate data with amplitudes that are numerically unobservable. The subspace of M spanned by the singular vectors with the remaining singular values result in null observations and are undetectable.

We finish this section with a discussion of how ill-posed problems, after discretisation, can be reposed as a regularised optimisation problem which will be used in the remaining chapters of this thesis. A good resource for inversion algorithms specific to EIT include [48], and for generic inverse problems in [71, 72, 73].

3.1.3 Reconstruction algorithms for ill-posed problems

In this section we derive the maximum *a posteriori* (MAP) estimate for ill-posed problems, which will be used in the subsequent three chapters. In applied inverse problems we think of two spaces — the model and data space. The model space, possibly after discretisation, consists of vectors $m \in \mathbb{R}^m$ of model parameters taking values in a discrete or continuous set. The data space consists of vectors $d \in \mathbb{R}^d$, taking values in some instrument responses. There are three sources of information in inverse problems: physical laws, results of measurements and prior information. The forward model sends the model parameters m to the data d , $F : m \mapsto d$, usually through some well understood physical law. Given some model parameters m we can assign a probability density $P_L(d|m)$ called the *likelihood*. Physical measurements give information about the true values of observable parameters, d . We can assign this probability density $P_D(d)$. If we have prior information of the model parameters we denote this with a probability density $P_M(m)$, called the *prior* distribution. If no prior information is given this implies $P_M(m)$ is a constant whereas perfect knowledge of the parameters implies $P_M(m)$ is a delta function. Using Bayes' theorem, the conditional

probability density, $P_C(m|d)$, is given by

$$P_C(m|d) = \frac{P_L(d|m)P_M(m)}{P_D(d)}.$$

In the Bayesian viewpoint, the conditional probability distribution of the parameters given the data is interpreted as the solution of the inverse problem, as opposed to a single set of physical values. Point estimates relate to the most probable values of the parameters, and dispersion estimates relate to the confidence levels we have of the parameters. The most common point estimate is the MAP estimate

$$m_{\text{MAP}} = \max_{m \in M} P_C(m|d). \quad (3.3)$$

This is the most probable configuration of the model given the measurements and prior information. Assuming the prior and likelihood distributions are Gaussian, we can form an expression for m_{MAP} . We assume the errors are additive, $d = F(m) + n$, where n is the measurement noise and Gaussian distributed with zero mean and covariance C_v , then

$$P_L(d|m) \propto \exp\left\{-\frac{1}{2}\|d - F(m)\|_{C_v^{-1}}^2\right\}$$

where $\|x\|_A := \sqrt{x^T A x}$. Similarly if the prior distribution is Gaussian with mean m_0 and covariance C_m , then

$$P_C(m|d) \propto \exp\left\{-\frac{1}{2}\|d - F(m)\|_{C_v^{-1}}^2\right\} \cdot \exp\left\{-\frac{1}{2}\|m - m_0\|_{C_m^{-1}}^2\right\},$$

and hence the MAP estimate is given by

$$m_{\text{MAP}} = \arg \min_{m \in M} \{\|d - F(m)\|_{C_v^{-1}}^2 + \|m - m_0\|_{C_m^{-1}}^2\}, \quad (3.4)$$

and we arrive at an output Least-Squares optimisation problem. This can be generalised to non Gaussian hypothesis and non-smooth norms [71, 74] and in general the MAP estimate can be written

$$m_{\text{MAP}} = \arg \min_{m \in M} \{\|d - F(m)\|_{C_v^{-1}}^2 + \alpha^2 P(m)\}.$$

The first term is the *data misfit* functional, and this is minimised because we want model parameters that accurately match the experimental data. The second term is the *prior* functional, or penalty term, and is included to enforce stability. A number of choices for the penalty term exist that enforce different smoothness properties on

the resulting reconstruction. The simplest choice is Tikhonov regularisation, $P(m) = \|m\|_2^2$, where the hyperparameter α dampens large values in the solution. An obvious extension of this penalty term is Generalised Tikhonov regularisation,

$$P(\sigma) = \|L(m - m_r)\|_2^2, \quad (3.5)$$

where L is a symmetric positive definite matrix and m_r is the prior mean. Choosing L as a discrete approximation to the Laplacian, for example, will promote differentiability of the solution. Other popular choices of penalty term include the total variation (TV) semi-norm, which is used when jump discontinuities are expected in parameter space [73, 75, 76], and sparsity and Besov space regularisation [77].

3.2 The Dirichlet-to-Neumann map

We consider two applied boundary voltages $u|_{\partial\Omega} = f \in H^{\frac{1}{2}}(\partial\Omega)$ and $v|_{\partial\Omega} = g \in H^{\frac{1}{2}}(\partial\Omega)$ to the PDE (2.1). The Dirichlet-to-Neumann (DtN) map, $\Lambda_\sigma : H^{\frac{1}{2}}(\partial\Omega) \rightarrow H^{-\frac{1}{2}}(\partial\Omega)$, is defined weakly through the equation

$$\int_{\Omega} \sigma \nabla u \cdot \nabla v = \int_{\partial\Omega} f \sigma \frac{\partial v}{\partial \nu} =: \int_{\partial\Omega} f \Lambda_\sigma(g) =: Q_\sigma(f, g).$$

This map takes as an input an applied boundary voltage and the resulting (unique) output as the boundary current density. $Q_\sigma(f, g)$ is the quadratic form associated with the DtN map, and in particular on the diagonal we have

$$Q_\sigma(f, f) = \int_{\Omega} \sigma \nabla u \cdot \nabla u = \int_{\partial\Omega} \Lambda_\sigma(f) f,$$

which is the power necessary to maintain the potential f on the boundary. To know $Q_\sigma(f, f)$ or $\Lambda_\sigma(f)$ for all $f \in H^{\frac{1}{2}}(\partial\Omega)$ is equivalent. In his seminal work [78], Alberto Calderón considered the map

$$\psi : \sigma \mapsto Q_\sigma, \quad (3.6)$$

and asked whether ψ is injective, that is, does $Q_{\sigma_1} = Q_{\sigma_2} \Rightarrow \sigma_1 = \sigma_2$? Calderón proved that the Fréchet derivative of ψ at a constant conductivity is in fact injective using a class of solutions to Laplace's equation known as complex geometric optics (CGO).

3.2.1 Fréchet differentiability

Calderón demonstrated Fréchet differentiability at a constant conductivity, but this is also true for any feasible conductivity [79]. We consider the Neumann-to-Dirichlet (NtD) map, N_σ , taking a boundary current density, $\sigma \frac{\partial u}{\partial \nu}|_{\partial\Omega} = f$ to boundary potential

$$N_\sigma : f \mapsto u|_{\partial\Omega}.$$

Analogously to the DtN map the NtD map is defined weakly through

$$\int_{\Omega} \sigma \nabla u \cdot \nabla u = \int_{\partial\Omega} f N_\sigma(f).$$

We denote the solution operator mapping a boundary current density to interior potential as $TN_\sigma : H^{-\frac{1}{2}}(\partial\Omega) \rightarrow H^1(\Omega)$. We have the following theorem, expressed in the form given by Lechleiter *et al.* [80]:

Theorem 3.2.1 (Fréchet derivative of continuum model: Conductivity). *Let $\sigma \in L_+^\infty(\Omega)$. The forward operator TN_σ is Fréchet differentiable with derivative TN'_σ*

$$TN'_\sigma(h)f = u^F,$$

where $u^F \in H^1(\Omega)$ solves

$$a_\sigma(u^F, v) = -a_h(u, v) \quad \forall v \in H^1(\Omega).$$

Furthermore N_σ is Fréchet differentiable with the derivative, DN_σ , satisfying

$$\int_{\partial\Omega} g DN_\sigma[h]f = - \int_{\Omega} h \nabla u \cdot \nabla v, \quad (3.7)$$

where u and v are solutions to the Neumann problems $\sigma \frac{\partial u}{\partial n}|_{\partial\Omega} = f$ and $\sigma \frac{\partial v}{\partial n}|_{\partial\Omega} = g$ of the conductivity equation respectively.

The continuum model is by far the most studied in terms of uniqueness and stability results in EIT, although is clearly not an accurate description of physical measurements, the most striking difference being that we can only inject a finite number of currents, at a finite number of locations, into the domain. Let $\sigma \in L_+^\infty(\Omega)$ and $z \in \mathbb{R}^L$, $z_l > 0$, we say the matrix, $R_{\sigma,z} \in \mathbb{R}^{L \times L}$, called the *transfer impedance* matrix satisfies

$$U = R_{\sigma,z}I.$$

If we have full knowledge of the transfer impedance matrix, then we can determine the boundary potential for any current injection. It turns out that the CEM is also Fréchet differentiable with respect to the interior conductivity and contact impedance changes. This is important for non-linear reconstruction algorithms that use a linear approximation to the forward problem at each iteration. The following theorem is due to Kaipio *et al.* [71]:

Theorem 3.2.2 (Fréchet derivative of complete electrode model: Conductivity). *Let $\sigma \in L_+^\infty(\Omega)$, the forward operator $T : (\sigma, z) \mapsto (u, U)$ is Fréchet differentiable, with derivative $T' : (h, \eta) \mapsto (u^F, U^F)$ satisfying $(u^F, U^F) = T'_{\sigma, z}(h, \eta)$, where (u^F, U^F) is defined*

$$B_{\sigma, \frac{1}{z}}((u^F, U^F), (v, V)) = - \int_{\Omega} h \nabla u \cdot \nabla v - \sum_{l=1}^L \eta_l \int_{E_l} (u - U_l)(v - V_l). \quad (3.8)$$

for all $(v, V) \in \dot{H}(\Omega)$, where (u, U) is the unique solution to (2.14).

The Fréchet derivative has the same form as in the continuum model i.e. the inner product of gradients of solutions are the kernel of the derivative in integral form. It is thus important for the inverse problem to have accurate solutions to the forward problem as measured in the H^1 -norm to ensure the derivative is accurately computed. The Fréchet derivative is also shown to be a compact operator in [79], and so the linearised inverse problem is severely ill-posed. The map $\sigma \mapsto \Lambda_\sigma$ is also non-linear, hinting at why fully non-linear inversion is so difficult in practice.

3.2.2 Numerical approximation

There are two methods to compute the Fréchet derivative numerically. Firstly the Fréchet derivative in integral form (3.7) can be discretised, or secondly the discretised (FEM) forward problem can be differentiated with respect to conductivity [81, 82, 83]. We show that these operations commute which is not clearly stated in the literature.

The FEM system matrix, S , maps a specific potential to the current density, and because the forward problem is well posed the inverse, S^{-1} , exists. We denote a linear operator Z mapping the electrode voltages to the specific measurement protocol (over all current excitations and voltage measurements). In particular for the m^{th}

measurement, V_m , $Z^{(m)}$ is a row vector and

$$V_m = Z^{(m)} S^{-1} f^{(m)}.$$

The vector $f^{(m)}$ is the discretised input current corresponding to the m^{th} measurement, and the matrix S depends on the specific electrode model used.

Continuum model

For the continuum model, the system matrix has the form

$$S_{ij} = A_{ij} = \int_{\Omega} \sigma \nabla \psi_i \cdot \nabla \psi_j,$$

where i, j are indices running over the number of nodes. If we have a piecewise constant discretisation of the conductivity on elements, $\sigma = \sum_{l=1}^{N_E} \sigma_l \chi_l$, then the derivative of the m^{th} measurement with respect to the l^{th} coefficient, σ_l , is

$$J_{ml} = \frac{\partial V_m}{\partial \sigma_l} = \frac{\partial}{\partial \sigma_l} (Z^{(m)} A^{-1} f^{(m)}) = -Z^{(m)} A^{-1} D A_{\sigma_l} u^{(m)}, \quad (3.9)$$

where we have used $D(A^{-1}) = -(A^{-1})(DA)(A^{-1})$. The matrix $J_c := J$ is called the *Jacobian* matrix and the matrix $D A_{\sigma_l}$ has components

$$[D A_{\sigma_l}]_{ij} = \int_{\Omega_l} \nabla \psi_i \cdot \nabla \psi_j \quad 1 \leq i, j \leq N_n. \quad (3.10)$$

The discretisation and the derivative commute which is important numerically, which we demonstrate by showing that the FEM approximation to the Fréchet derivative in (3.7) agrees with the Jacobian matrix. Consider a perturbation in the direction of the l^{th} characteristic function, $h = \alpha_l \chi_l$, and consider the finite element solution u_h, v_h with $\sigma \frac{\partial u}{\partial n}|_{\partial \Omega} = f$ and $\sigma \frac{\partial v}{\partial n}|_{\partial \Omega} = g$, then

$$\begin{aligned} \int_{\partial \Omega} g D N_{\sigma}[h] f &= - \int_{\Omega} h \nabla v_h \cdot \nabla u_h = - \int_{\Omega_l} \alpha_l \nabla (v^i \psi_i) \cdot \nabla (u^j \psi_j) \\ &= (v^i)^T \left(- \int_{\Omega_l} \alpha_l \nabla \psi_j \cdot \nabla \psi_j \right) u^j. \\ &= -\alpha_l Z^{(m)} A^{-1} D A_{\sigma_l} u^{(m)}, \end{aligned}$$

and differentiating with respect to α_l , we arrive at the Jacobian matrix (3.9).

Complete electrode model

For the complete electrode model the system matrix is slightly larger due to the boundary terms (2.44), although the derivative has a similar format and is given by

$$\frac{\partial V_m}{\partial \sigma_l} = \frac{\partial}{\partial \sigma_l} (Z^{(m)} S^{-1} f^{(m)}) = -Z^{(m)} S^{-1} DS_{\sigma_l} (u, U)^{(m)},$$

where V_m is the m^{th} voltage measurement, $(u, U)^{(m)}$ the vector of nodal and electrode potentials for the m^{th} measurement and DS_{σ_l} is given by

$$DS_{\sigma_n} = \begin{bmatrix} DA_{\sigma_n} & 0 \\ 0 & 0 \end{bmatrix}.$$

For details on the numerical implementation of the Jacobian see appendix B.2.

3.2.3 Calderón fields

In Calderón's seminal paper the derivative at a constant conductivity was calculated, and shown to be injective using specially constructed CGO solutions, which are harmonic functions with a highly oscillatory spatial dependence. To show the Fréchet derivative is injective at a constant conductivity, we need to show that $D\Lambda_1[h_1] = D\Lambda_1[h_2] \Rightarrow h_1 = h_2$. From (3.7) we thus need to show that if

$$\int_{\Omega} h \nabla u[f] \cdot \nabla u[g] = 0$$

for all harmonic functions $\Delta u[f] = \Delta u[g] = 0$ then $h = 0$. We introduce harmonic functions of the form $u = e^{a \cdot x}$ with $a \in \mathbb{C}^n$ with $a \cdot a = 0$, where \cdot denotes the *real* inner product. The condition $a \cdot a = 0$ implies $|\operatorname{Re}(a)| = |\operatorname{Im}(a)|$ and $\operatorname{Re}(a) \cdot \operatorname{Im}(a) = 0$. We introduce two fields $a = u + vi$ and $b = -u + vi$. Let $u_1 = e^{a \cdot x}$ and $u_2 = e^{b \cdot x}$, then

$$\int_{\Omega} ha \cdot be^{(a+b) \cdot x} = \int_{\Omega} -2h|u|^2 e^{2v \cdot xi}.$$

If we extend $h = 0$ outside of Ω , then

$$\int_{\mathbb{R}^n} h e^{2v \cdot xi} = 0$$

and thus by the Fourier transform inversion formula $h = 0$ if we perform this for all v . Consider the unit disc $D \subset \mathbb{R}^2$ and a complex frequency $\omega \in \mathbb{C}^2$, $\omega = a + zi$, where $a, z \in \mathbb{R}^2$ with $z = (z_1, z_2)$ and $a = (z_2, -z_1)$. Let $u = e^{\omega \cdot x}$, then for $x \in \partial D$

$$u(1, \theta) = e^{(a+zi) \cdot x} = e^{z_2 \cos(\theta) + iz_1 \cos(\theta) - z_1 \sin(\theta) + iz_2 \sin(\theta)} = e^{(iz_1 + z_2)e^{i\theta}} = \sum_{k=0}^{\infty} \frac{(iz_1 + z_2)^k}{k!} e^{ik\theta}.$$

In figure 3.1 we construct CGO solutions with trigonometric current patterns of the form $e^{ik\theta}$. The large complex frequencies, corresponding to finer spatial information of the conductivity, require many Fourier modes because of increasing contributions from the $(iz_1 + z_2)^k$ term. The problem is amplified in lung EIT when only a discrete, band limited, approximation to trigonometric patterns is available.

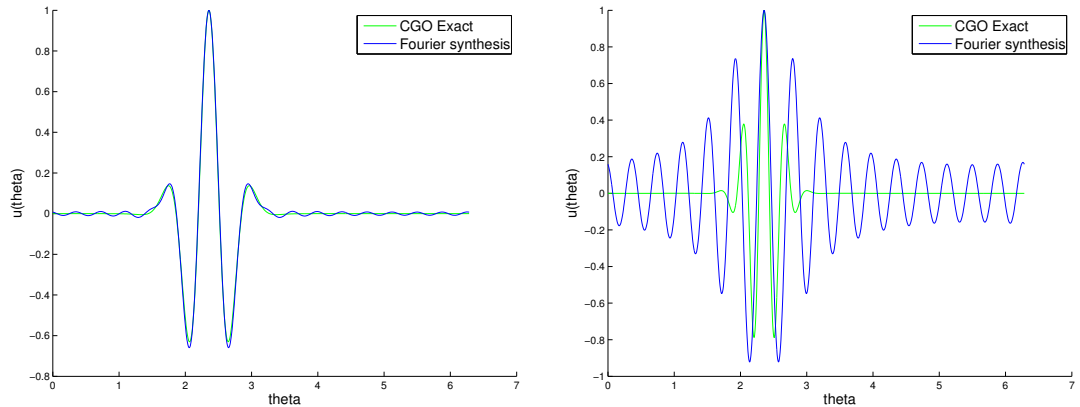


Figure 3.1: Construction of CGO solution at complex frequencies $\omega = 7 + 7i$ and $\omega = 14 + 14i$ respectively from a basis of 16 trigonometric patterns. The smaller complex frequency is resolved well with the Fourier basis, but the larger complex frequency, corresponding to the higher spatial frequency and hence spatial resolution, is not.

The CEM results in a finite dimensional transfer impedance matrix $R_\sigma \in \mathbb{R}^{n \times n}$. R_σ is self-adjoint, and because the potential is defined up to a constant there are only $\frac{1}{2}n(n-1)$ independent entries. There is no hope that a generic L^∞ conductivity distribution can be determined from this finite dimensional impedance matrix. However in [80] it has been shown that the derivative is injective for piecewise polynomial conductivities when the number of electrodes is sufficiently large.

3.3 Non-linear inverse conductivity problem

Calderón's paper has initiated much research on the uniqueness of the fully non-linear inverse conductivity problem. The uniqueness results can roughly be split into the determination of σ on the boundary and interior of Ω .

3.3.1 Boundary identifiability

We briefly review boundary identifiability results as this is important for our discussion on anisotropic media in section 3.4, the boundary shape problem in section 4.2.2, as

well as an important step for interior uniqueness results in dimension $n \geq 3$.

The first uniqueness result was proved by Kohn and Vogelius in [84], who showed that the Taylor series of an isotropic real-analytic conductivity is uniquely determined from Λ_γ on $\partial\Omega$, and was later extended by the same authors to piecewise real-analytic conductivities [85]. An alternative proof by Lee and Uhlmann [86] demonstrates that the DtN map is an elliptic *pseudo-differential* operator (PSDO) of order 1, which we briefly explain (for a much more rigorous treatment of PSDOs see [87, 88].)

Let L be a differential operator with constant coefficients, $L(D)u = \sum_\alpha a_\alpha D^\alpha u$. From the definition of the Fourier Transform (A.3), and applying L to $u(x)$ we obtain

$$(Lu)(x) = \frac{1}{(2\pi)^n} \int \int e^{i(x-y)\cdot\xi} L(\xi)u(y) dy d\xi,$$

where the *symbol* of the operator, $L(D)$, is defined as $L(\xi) = \sum_\alpha a_\alpha L(\xi^\alpha)$, by replacing partial derivatives $\frac{\partial}{\partial x_n}$ by ξ_n . Very loosely speaking, a PSDO, $\Psi(x, D)$, is an operator whose operation on the function $u(x)$ is another function of x given by

$$\Psi(x, D)u(x) = \frac{1}{(2\pi)^n} \int \int e^{i(x-y)\cdot\xi} \Psi(x, \xi)u(y) dy d\xi.$$

We consider the half-space $\Omega = \mathbb{R}_+^n = \{x = (x', x_n) : x_n > 0\}$ with $\partial\Omega = \mathbb{R}^{n-1}$. Let $f \in H^{\frac{1}{2}}(\mathbb{R}^{n-1})$ and let $v \in H^1(\mathbb{R}_+^n)$ be unique solution of

$$\Delta u = 0 \quad x \in \mathbb{R}_+^n,$$

with associated DtN map $f \mapsto -\frac{\partial u}{\partial x_n}|_{\mathbb{R}^{n-1}}$. The Laplacian can be factorized as

$$\Delta = (D_{x_n} - i\sqrt{-\Delta'})(D_{x_n} + i\sqrt{-\Delta'}),$$

where $D_{x_j} = \frac{1}{i} \frac{\partial}{\partial x_j}$, $-\Delta' = -\sum_{j=1}^{n-1} \frac{\partial^2}{\partial x_j^2}$ and

$$(\sqrt{-\Delta'}f)(x') := \frac{1}{(2\pi)^{n-1}} \int_{\mathbb{R}^{n-1}} e^{ix'\cdot\xi'} |\xi'| \tilde{f}(\xi') d\xi'.$$

Thus $\sqrt{-\Delta'}$ is a PSDO of order 1 with full symbol $|\xi'|$. The Laplacian, $-\Delta'$ has full symbol ξ'^2 , and hence $\sqrt{-\Delta'}$ and $-\Delta'$ are both elliptic and exhibit similar qualitative behaviour. We write the Laplacian as a coupled system of PDE

$$(D_{x_n} - i\sqrt{-\Delta'})v = 0, \quad (D_{x_n} + i\sqrt{-\Delta'})u = v, \quad u|_{\partial\Omega} = f.$$

The operator $(D_{x_n} - i\sqrt{-\Delta'})$ behaves like a forwards heat equation and is smoothing, so $v \in C^\infty(\Omega)$. The operator $(D_{x_n} + i\sqrt{-\Delta'})$ behaves like a backwards heat equation

which is severely ill-posed as we observed in section 3.1.1. Let $Rf = v|_{\partial\Omega}$, then R is a smoothing operator and

$$D_{x_n} u|_{\partial\Omega} = -i\sqrt{-\Delta'} u|_{\partial\Omega} + Rf.$$

The left hand side is essentially Neumann boundary data and hence

$$\Lambda_\sigma f := -iD_{x_n} u|_{\partial\Omega} = -\sqrt{-\Delta'} u|_{\partial\Omega} \quad \text{mod smoothing.}$$

The DtN map on the half space with $\sigma = 1$ is thus a PSDO of order 1 with full symbol $|\xi'|$. This result is a simplification of [86] where C^∞ conductivity metrics are considered. The DtN map is still a PSDO of order 1, although the full symbol is now given by an asymptotic series, $a(x, \xi) = \sum_{j \leq 1} a_j(x, \xi)$. The result shows that

$$\Lambda_\sigma f = \delta^{\frac{1}{2}} A f dx^1 \wedge \cdots \wedge dx^{n-1}|_{\partial M} \quad \text{mod smoothing operator} \quad (3.11)$$

where $\{x_i\}_{i=1}^{n-1}$ are boundary normal coordinates. The full symbol of $\delta^{\frac{1}{2}} A$ is clearly determined by Λ_g and it is further shown that the complete Taylor series of g at any boundary point is determined by the full symbol of $\delta^{\frac{1}{2}} A$.

As well as providing boundary determination, the result sheds light on why EIT is so challenging. The symbol expansion of Λ_σ only depends on the Taylor series of the conductivity on $\partial\Omega$ whilst interior conductivity changes are in the smoothing part of Λ_σ and hence very difficult to detect in practice. The fact that the DtN map is an elliptic PSDO of order 1 implies that it can be written as an integral operator with a distributional kernel $G(x, y)$ [87] and because the DtN map is elliptic the kernel is smooth ($C^\infty(\partial\Omega \times \partial\Omega)$) at least off the leading diagonal. The kernel can be computed explicitly for simple geometries and conductivities using classical applications of Green's theorem. The kernel of the DtN map is a function of $2(n - 1)$ variables, and the objective of the (isotropic) inverse conductivity problem is to determine a function of n variables from this information. Thus for $n \geq 3$ the inverse problem is, at least formally, overdetermined from a dimension counting argument.

3.3.2 Interior determination

Sylvester and Uhlmann [89] proved global uniqueness in three spatial dimensions for $\sigma \in C^\infty(\bar{\Omega})$ and smooth boundary $\partial\Omega$. We outline this result through the transformation to Schrödinger's equation in a similar spirit to [90]. This is useful for the

discussion of exact reconstruction algorithms in section 3.3.3.

A fundamental step is to transform the conductivity equation to a Schrödinger equation. By direct computation, if $\sigma^{-\frac{1}{2}}u$ solves the conductivity equation, then u solves the Schrödinger equation, $(-\Delta + q)u = 0$, with potential $q = \Delta(\sigma^{\frac{1}{2}})/\sigma^{\frac{1}{2}}$. Let $u \in H^1(\Omega)$, with $u|_{\partial\Omega} = f$, then the DtN map associated with Schrödinger's equation, $\Lambda_q : H^{\frac{1}{2}}(\partial\Omega) \rightarrow H^{-\frac{1}{2}}(\partial\Omega)$, $f \mapsto \frac{\partial u}{\partial\nu}|_{\partial\Omega}$, is defined weakly through

$$\int_{\Omega} (\nabla u \cdot \nabla v + quv) = \int_{\partial\Omega} v \Lambda_q f \quad \forall v \in H^1(\Omega).$$

Λ_q is a bounded linear map from $H^{\frac{1}{2}}(\partial\Omega)$ to $H^{-\frac{1}{2}}(\partial\Omega)$ and can be computed from the conductivity equation DtN map, Λ_{σ} . In particular let u solve $(-\Delta + q)u = 0$, $u|_{\partial\Omega} = f$, and $v = \sigma^{-\frac{1}{2}}u$ solve $-\nabla \cdot (\sigma \nabla v) = 0$, $v|_{\partial\Omega} = \sigma^{-\frac{1}{2}}f$ then it can be shown that $\Lambda_q f = \sigma^{-\frac{1}{2}}\Lambda_{\sigma}(\sigma^{-\frac{1}{2}}f) + \frac{1}{2}\sigma^{-1}\frac{\partial\sigma}{\partial\nu}|_{\partial\Omega}f$. We are now in a position to understand the uniqueness results for the Schrödinger potential. We loosely follow Salo [90] by stating two theorems:

Theorem 3.3.1 (Sylvester and Uhlmann). *Let $\Omega \subset \mathbb{R}^n$, with $n \geq 3$ and $\sigma_1, \sigma_2 \in C^2(\Omega)$. If $\Lambda_{\sigma_1} = \Lambda_{\sigma_2}$ then $\sigma_1 = \sigma_2$.*

Theorem 3.3.2 (Salo). *Let $\Omega \subset \mathbb{R}^n$, with $n \geq 3$ and $q_1, q_2 \in L^{\infty}(\Omega)$. If $\Lambda_{q_1} = \Lambda_{q_2}$ then $q_1 = q_2$.*

Theorem 3.3.2 implies theorem 3.3.1 as demonstrated in [90]. Interestingly this result hinges on σ having C^2 regularity and from boundary determination of the conductivity. By proving theorem 3.3.2 a uniqueness result for the inverse conductivity problem can be deduced, which we briefly outline. CGO solutions were used to demonstrate injectivity of the linearised problem and were extended to the fully non-linear problem by Sylvester and Uhlmann in [89]. Let $q = 0$, then $u = e^{ix \cdot \xi}$, $\xi \in \mathbb{C}^n$, solves the Schrödinger equation if and only if $\xi \cdot \xi = 0$. For $q \neq 0$ consider CGO solutions of the form $u(x) = e^{i\xi \cdot x}(1 + r(x))$, where r is a correction term. This solves Schrödinger's equation if and only if $e^{-i\xi \cdot x}(-\Delta + q)e^{i\xi \cdot x}(1 + r) = 0$ if and only if $(D^2 + 2\xi \cdot D + q)r = -q$, where $D_i = \frac{1}{i}\frac{\partial}{\partial x_i}$. The following lemma, on regularity of r , is due to Salo [90]:

Lemma 3.3.3. *Let $q \in L^{\infty}(\Omega)$. There is constant C such that for $\xi \in \mathbb{C}^n$, with $\xi \cdot \xi = 0$, and $|\xi| \geq \max(C\|q\|_{L^{\infty}}, 1)$, and for $a \in H^2$ with $\xi \cdot \nabla a = 0$, the equation $(-\Delta + q)u = 0$*

has a solution $u(x) = e^{i\xi \cdot x}(a + r)$, where $r \in H^1$ satisfies $\|r\|_{L^2} \leq \frac{C}{|\xi|} \|(-\Delta + q)a\|_{L^2}$ and $\|\nabla r\|_{L^2} \leq C \|(-\Delta + q)a\|_{L^2}$

We now consider two solutions satisfying $(-\Delta + q_i)u_i = 0$. We have

$$\begin{aligned} \int_{\partial\Omega} (\Lambda_{q_1} - \Lambda_{q_2})u_1u_2 &= \int_{\Omega} (\Delta u_1)u_2 - \nabla u_1 \cdot \nabla u_2 - (\Delta u_2)u_1 + \nabla u_1 \cdot \nabla u_2 \\ &= \int_{\Omega} (q_1 - q_2)u_1u_2. \end{aligned}$$

Thus $\Lambda_{q_1} = \Lambda_{q_2}$ implies $\int_{\Omega} (q_1 - q_2)u_1u_2 = 0$. If we let $u_1 = e^{i\xi \cdot x}(e^{ix \cdot b} + r_1)$ and $u_2 = e^{-i\xi \cdot x}(1 + r_2)$, these both satisfy the conditions in theorem 3.3.3 if $b \cdot \xi = 0$ then

$$\int_{\Omega} (q_1 - q_2)(e^{ix \cdot b} + r_1)(1 + r_2) = 0.$$

Let $\xi = s(\omega_1 + i\omega_2)$, where ω_1, ω_2 must be orthogonal by construction. So ω_1, ω_2, b must form an orthogonal set (and so this only works for $n \geq 3$). Since $\|r_j\|_{L^2} \leq \frac{C}{|s|}$ this can be chosen arbitrarily small for large enough spatial frequencies s , hence

$$\int_{\Omega} (q_1 - q_2)e^{ix \cdot b} = 0$$

holds for every $b \in \mathbb{R}^n$. Let $\bar{q} = q_1 - q_2$ inside Ω , and extend to 0 outside Ω , then the last identity implies the Fourier Transform of \bar{q} vanishes for every frequency $b \in \mathbb{R}^n$, and hence $\bar{q} = 0$.

Optimal uniqueness results

Identifying uniqueness in two spatial dimensions initially proved more difficult until Nachman [91] showed uniqueness of solution for $\sigma \in W^{2,p}(\Omega)$, with $p > 1$, with a positive lower bound and a Lipschitz boundary. In two spatial dimensions, the uniqueness problem was fully solved by Astala and Päivärinta [92] for $\sigma \in L^\infty(\Omega)$. In three dimensions, uniqueness has been proved for $\sigma \in W^{1,\infty}(\Omega)$ and $C^1(\Omega)$, as well as Lipschitz conductivities close to the identity in [93]. Unique identifiability for $\sigma \in L^\infty(\Omega)$ is still an open problem when $n \geq 3$.

3.3.3 Exact reconstruction methods and lung EIT

The original uniqueness result using CGO solutions outlined for the non-linear problem only worked in dimensions $n \geq 3$. Nachman [91] eventually extended uniqueness to

2D *constructively*, in that the proof gives rise to a practical reconstruction algorithm. We briefly explain the d-bar algorithm following Siltanen and Mueller [77] assuming that $\sigma = 1$ in a neighbourhood of $\partial\Omega$. The d-bar method works by constructing CGO solutions from Λ_σ by solving for $\psi(\cdot, k)$ for every $k \in \mathbb{C}^n$

$$\psi(\cdot, k)|_{\partial\Omega} = e^{ik \cdot x} - S_k(\Lambda_\sigma - \Lambda_1)\psi(\cdot, k) \quad \text{where} \quad (S_k f)(x) = \int_{\partial\Omega} G_k(x-y)f(y) dy$$

and G_k is the Fadeev Green's function [94]. Nachman [91] proved that the operator $I + S_k(\Lambda_\sigma - \Lambda_1)$ is invertible on $H^{\frac{1}{2}}(\partial\Omega)$ and thus $\psi(\cdot, k)|_{\partial\Omega}$, can be recovered for any complex frequency k . This step is severely ill-posed for large $|k|$ as figure 3.1 suggests. The *scattering transform* $t(k)$ is computed through

$$t(k) = \int_{\partial\Omega} e^{ik \cdot x}(\Lambda_\sigma - \Lambda_1)\psi(x, k) dx.$$

For $n = 2$ the d-bar equation is given by

$$\frac{\partial}{\partial \bar{k}} \mu(x, k) = \frac{1}{4\pi \bar{k}} t(k) e^{-i(kx + \bar{k}\bar{x})} \mu(\bar{x}, k), \quad (3.12)$$

and is uniquely solvable for μ given t [91]. Moreover the conductivity can be recovered from $\mu(x, k)$, as $\sigma(x) = \lim_{k \rightarrow 0} (\mu(x, k))^2$. The d-bar method was first translated to a practical algorithm by Siltanen *et al.* [95] for $\sigma \in C^2(\bar{\Omega})$ and has been applied with real chest data in [96] and to determine boundary conductivity in [97].

Reconstruction algorithms for non-linear inverse problems often rely on iterative gradient based methods to estimate parameters. Iterative reconstruction algorithms can be highly sensitive to initial guesses and can get stuck in local minima especially if under regularized. Exact reconstruction algorithms bypass such problems with local minima. There are still a number of challenges before exact reconstruction methods can be applied with confidence in lung EIT. Firstly d-bar methods are only completely understood in 2D because there is no analogous d-bar equation known in 3D. The scattering transformation can still be computed in 3D, and the high frequency limit of the scattering transform is the Fourier Transform of the potential q . The Schrödinger potential q satisfies $(-\Delta + q)\sigma^{\frac{1}{2}} = 0$, which is a well-posed problem given q and $\sigma|_{\partial\Omega}$ to compute σ [90]. This approximation has formed the basis of recent exact d-bar type methods in 3D in [98, 99]. Such high frequency scattering data, however, is very difficult to obtain in practice when only a relatively small number of electrodes are

used, and the number of electrodes is typically limited in order to obtain a full set of measurements quick enough before breathing effects become important. An analogy can also be drawn between the d-bar methods and the exact Katsevitch reconstruction algorithm in X-ray CT [100, 101]. In an implementation of the Katsevitch algorithm in micro-CT [102], it is noted that small errors in the forward problem e.g. the axis of rotation, can generate images that appear reasonable but with features at the incorrect spatial location, whereas iterative methods tend to compute the spatial location of features correctly at the expense of significant blurring. Features at incorrect spatial locations is clearly a dangerous property for an algorithm to have if EIT is to be used in clinical diagnosis. Hence an accurate forward problem, including parameters such as the correct boundary shape and electrode positions is still of paramount importance before we can use exact methods with confidence in lung EIT.

3.4 Anisotropic media

The uniqueness results discussed in this chapter so far are for a Euclidean domain, $\Omega \subset \mathbb{R}^n$, with an isotropic conductivity, $\sigma : \Omega \rightarrow \mathbb{R}^+$. We have demonstrated that, under certain regularity requirements, the map $\psi : \sigma \mapsto \Lambda_\sigma$ is injective. If σ is *anisotropic*, that is $\sigma : \Omega \rightarrow \mathbb{R}^{d \times d}$ is a symmetric positive definite matrix valued function of Ω , there is a well known obstruction to uniqueness — every diffeomorphism fixing points on the boundary, which we abbreviate as a *distortion*, gives rise to a conductivity producing the same electrical measurements on $\partial\Omega$ [103, 104, 105]. In other words, there is a large equivalence class of conductivities that all give rise to the same boundary measurements. Anisotropic conductivities are certainly present in nature in various forms, for example in medical applications muscle tissue has a preferred direction ($1/\sigma \approx 240$ and $675 \text{ } \Omega\text{cm}$ in longitudinal and transverse directions respectively [4]), similar to rock strata in geophysical applications. Improving our understanding of what information can be obtained about anisotropic conductivities from the DtN map is thus very important. Another interesting source of anisotropy arises from the low spatial resolution of EIT. For example if we have microscale layers of alternating conductivity, we would only reconstruct an homogenised average of the conductivity which will in general be anisotropic [106]. A practical question that

arises is given *a-priori* knowledge of the microscale anisotropy, for example the ratio of the principal eigenvalues, is it possible to invert the reconstructed homogenized conductivity to determine some microscale parameters?

In this section we demonstrate the non-uniqueness result for fully anisotropic conductivities and summarise uniqueness results that have been obtained for subclasses of fully anisotropic conductivities. We further define five classes of anisotropic conductivity: *prescribed eigenvalues*, *prescribed orthogonal coordinates*, *prescribed eigenvectors*, *fibrous* and *layered*, and discuss potential unique identifiability results for these. We begin by posing the geometric form of the inverse conductivity problem.

3.4.1 Geometric problem

We now state the geometric problem in EIT based on [31]. We first review a few key definitions and results on coordinates and mappings between Riemannian manifolds explicitly (see appendix A.2 for relevant notation) which will be used later in this chapter and in section 4.2 of the subsequent chapter when discussing the problem with an inaccurately known external boundary shape. Unless otherwise stated, M is assumed to be an oriented, compact, Riemannian manifold of dimension $n \geq 3$ with smooth boundary ∂M and metric, $g = g_{ij}dx^i \otimes dx^j$, with arbitrary coordinates $\{x^i\}_{i=1}^n$, and volume form $\mu_g = \sqrt{|g|}dx^1 \wedge \dots \wedge dx^n$.

Coordinate systems

Let $p \in U \subset M$ have local coordinates $x : U \rightarrow \mathbb{R}^n$ given by functions $\{x^i\}_{i=1}^n$ and we consider the same point $p \in V \subset M$ with local coordinates $y : V \rightarrow \mathbb{R}^n$. The metric transforms as $g_{ij}^x = g_{kl}^y \frac{\partial y^k}{\partial x^i} \frac{\partial y^l}{\partial x^j}$ under a change of coordinates. A metric g is said to be *flat* if in some (local) coordinate system it is given by δ_{ij} , the Euclidean metric. This is exactly equivalent to the Riemann curvature tensor being zero [107].

Given any Riemannian 2-manifold there exists, at least locally, *isothermal* coordinates such that the components of the metric is diagonal. In fact the metric tensor can be written in the form $g_{ij}(x) = \lambda(x)\delta_{ij}$, where $\lambda : M \rightarrow \mathbb{R}^+$ is a positive function, and so the matrix associated with the metric is a multiple of the identity. This is reasonable because the metric in general consists of 3 independent functions and there are 2 functions available to change coordinates. There is an extension to this result

for any Riemannian 3-manifold known classically as triply orthogonal systems (see, for example, [108].) In particular DeTurck and Yang [109] demonstrated that for such a 3-manifold there exists an atlas of C^∞ coordinate charts for M such that, in each chart, the metric has the form $g = \lambda_1(x, y, z)dx^2 + \lambda_2(x, y, z)dy^2 + \lambda_3(x, y, z)dz^2$, where $\lambda_i : M \rightarrow \mathbb{R}^+$ are in general three different functions. We will outline this result in detail in section 3.4.3. We again note this existence is reasonable because the metric is composed of 6 independent functions and there are only 3 functions available to change coordinates.

Mappings between manifolds

We also outline some special maps between manifolds which will become relevant in the external shape problem in EIT in the subsequent chapter. Firstly two metrics g_1 and g_2 on M are *conformally equivalent* if $g_1 = \alpha g_2$ for some positive function $\alpha : M \rightarrow \mathbb{R}^+$. Let $\Psi : (M, g) \rightarrow (N, h)$ be a C^∞ diffeomorphism and $\lambda : M \rightarrow \mathbb{R}^+$ a positive function, then g and h are *conformally related* if

$$\Psi_*g = \lambda h \quad \text{or as matrices in coordinates} \quad (D\Psi)G(D\Psi)^T = \lambda H,$$

where G and H are matrices defined by $[G]_j^i = g_{ij}$, and $[H]_j^i = h_{ij}$, $(D\Psi)_j^i = \frac{\partial \Psi^i}{\partial x^j}$ is the matrix of partial derivatives of Ψ . Ψ is called a *conformal transformation* and furthermore if $h = g$ then Ψ is called a *conformal map*. A metric g is *conformally flat* if there is a map $\Psi : (M, g) \rightarrow (N, e)$ such that

$$\Psi_*g = \lambda e \quad \text{or as matrices in coordinates} \quad (D\Psi)G(D\Psi)^T = \lambda I.$$

where e is a flat metric. The existence of isothermal coordinates in 2D means that every compact Riemannian 2-manifold is conformally flat, but in 3 or more dimensions this is not true. In 3 dimensions a necessary and sufficient condition for a conformally flat metric is that the Cotton-York tensor is identically zero, and in 4 or more dimensions the Weyl tensor is zero (see appendix A). Given a vector field X , we can define a one-parameter family of diffeomorphisms, Ψ_t , for $t \in [-\epsilon, \epsilon]$, by solving the ODE $\frac{d\Psi_t}{dt}|_{t=0} = X$. The linearised version of the conformal mappings is then $\mathcal{L}_X g = \lambda g$, where \mathcal{L}_X is the Lie derivative (see (A.19)), and the X that satisfy this system of PDE are called *conformal Killing* vector fields.

Laplace-Beltrami operator

The electric field can be considered as a 1-form du , because the work done moving a test charge between two points is the integral of the electric field along a curve connecting these points. The current density J is an $(n-1)$ -form, since the total current crossing a surface is given by the integral of J over the surface. The conductivity, σ , maps the 1-form du to the $(n-1)$ -form J i.e. $\sigma : \Omega^1(M) \rightarrow \Omega^{n-1}(M)$ (or $\sigma \in \Omega^1(M) \otimes (\Omega^{n-1}(M))^*$), and thus is interpreted as the Hodge star map $\star : \Omega^k(M) \rightarrow \Omega^{n-k}(M)$ (with $k = 1$).

Kirchhoff's law states that the exterior derivative of the current density, $J = \sigma du$, is zero when no interior sources are present, so $(\star d \star d)u = 0$. This results in the Laplace-Beltrami equation

$$\Delta_g u = \text{Div}(\text{grad}_g u) = 0 \quad \text{or in coordinates} \quad \sum_{i,j=1}^n \frac{1}{\sqrt{|g|}} \frac{\partial}{\partial x_i} (\sqrt{|g|} g^{ij} \frac{\partial u}{\partial x_j}) = 0, \quad (3.13)$$

where $|g| = \det(g_{jk})$. If we set $\sigma^{ij} = \sqrt{|g_{kl}|} g^{ij}$ then we recover the original conductivity equation in Cartesian coordinates. Taking the determinant of both sides implies, $|\sigma^{ij}| = |g_{ij}|^{\frac{n-2}{2}}$, and since $g^{ij} = |g_{ij}|^{-\frac{1}{2}} \sigma^{ij}$, we have

$$g_{ij} = (g^{ij})^{-1} = \left(\frac{1}{\sqrt{|g_{ij}|}} \sigma^{ij} \right)^{-1} = |g_{ij}|^{\frac{1}{2}} \sigma_{ij} = |\sigma_{ij}|^{\frac{1}{n-2}} \sigma_{ij}.$$

We see that a (possibly anisotropic) conductivity determines a Riemannian metric when M is considered as a subset of \mathbb{R}^n . Denoting the conductivity σ^{ij} as a matrix in Cartesian coordinates and in 3D we have $g^{ij} = |\sigma|^{-1} \sigma^{ij}$.

Boundary conditions

Let $u|_{\partial M} = f \in H^{\frac{1}{2}}(\partial M)$. The Dirichlet problem to the Laplace-Beltrami operator is uniquely solvable on (M, g) [64], and we introduce a Dirichlet-to-Neumann map

$$\Lambda_g : H^{\frac{1}{2}}(\partial M) \rightarrow H^{-\frac{1}{2}}(\Omega^{n-1}(\partial M)), \quad \Lambda_g : f \mapsto \iota^*(\sigma du),$$

where ι is the inclusion operator, $\iota : \partial M \hookrightarrow M$, and ι^* is the pullback, which is independent of the embedding of M . In Euclidean space, it is normal to interpret the current density as a scalar field on the boundary, $f = \sigma \frac{\partial u}{\partial \nu}|_{\partial \Omega}$. On a general Riemannian manifold there is not necessarily an outward facing normal present unless the manifold is implicitly assumed embedded in a higher dimensional space.

3.4.2 Non-uniqueness result

The anisotropic inverse conductivity problem is not unique, a well known result attributed to Tartar in [84]. We demonstrate this result explicitly as this is important to understand constrained anisotropic media in the remainder of this chapter, as well as the problem with an inaccurately known external shape in the subsequent chapter.

We consider the conductivity equation (2.1) with Dirichlet data $u|_{\partial\Omega} = f$. Through an integration by parts, the DtN map $\Lambda_\sigma : f \mapsto (\sigma \nabla u) \cdot \nu|_{\partial\Omega}$, and associated quadratic form $Q_\sigma(f, f)$, are defined weakly through

$$\int_{\Omega} \sum_{i,j=1}^n \sigma^{ij}(x) \frac{\partial u}{\partial x_i} \frac{\partial u}{\partial x_j} = \int_{\partial\Omega} f \sum_{i,j=1}^n (\sigma^{ij} \frac{\partial u}{\partial x_j}) \nu_i =: \int_{\partial\Omega} f(\Lambda_\sigma f) =: Q_\sigma(f, f).$$

Let $\Psi : \Omega \rightarrow \Omega'$ be a C^∞ diffeomorphism with $\Psi|_{\partial\Omega} = \psi$, and let $y = \Psi(x)$, then

$$\begin{aligned} \int_{\Omega} \sum_{i,j=1}^n \sigma^{ij} \frac{\partial u}{\partial x_i} \frac{\partial u}{\partial x_j} &= \int_{\Omega'} \sum_{i,j,k,l=1}^n \frac{\partial \Psi_l}{\partial x_i} \frac{\partial u}{\partial \Psi_l} \sigma^{ij} \circ \Psi^{-1}(y) \frac{\partial \Psi_k}{\partial x_j} \frac{\partial u}{\partial \Psi_k} |\det(D\Psi)^{-1}| \\ &= \int_{\Omega'} (\Psi_*\sigma)^{ij} \frac{\partial \tilde{u}}{\partial y_i} \frac{\partial \tilde{u}}{\partial y_j}, \end{aligned} \quad (3.14)$$

where the pushforward conductivity, $\Psi_*\sigma$, is given by

$$(\Psi_*\sigma)(y) := \frac{(D\Psi)\sigma(D\Psi)^T \circ \Psi^{-1}(y)}{|\det D\Psi|} \quad \tilde{u}(y) = (u \circ \Psi^{-1})(y). \quad (3.15)$$

Using an integration by parts on the last term in (3.14), we have

$$\int_{\Omega'} \sum_{i,j=1}^n (\Psi_*\sigma)^{ij} \frac{\partial \tilde{u}}{\partial y_i} \frac{\partial \tilde{u}}{\partial y_j} = \int_{\partial\Omega'} \tilde{f}(\Lambda_{\Psi_*\sigma} \tilde{f}) = Q'_{\Psi_*\sigma}(f \circ \psi^{-1}, f \circ \psi^{-1}).$$

Denote $\tilde{f} = f \circ \psi^{-1}$, then \tilde{u} is the unique solution of $\frac{\partial}{\partial y_i} ((\Psi_*\sigma)^{ij} \frac{\partial \tilde{u}}{\partial y_j}) = 0$, with $\tilde{u}|_{\partial\Omega'} = \tilde{f}$, and $Q_\sigma(f, f) = Q'_{\Psi_*\sigma}(f \circ \psi^{-1}, f \circ \psi^{-1})$. For $h \in H^{\frac{1}{2}}(\partial\Omega')$ define

$$((\psi_*\Lambda_\sigma)h)(x) := (\Lambda_\sigma(h \circ \psi))(y)|_{y=\psi^{-1}(x)}. \quad (3.16)$$

Then we have $\int_{\partial\Omega} f(\Lambda_\sigma f) = \int_{\partial\Omega'} \tilde{f}(\Lambda_\sigma f) \circ \psi^{-1} = \int_{\partial\Omega'} \tilde{f}(\psi_*\Lambda_\sigma) \tilde{f}$, and hence

$$\Lambda_{\Psi_*\sigma} = \psi_*\Lambda_\sigma. \quad (3.17)$$

If the deformation Ψ fixes points on the boundary i.e. $\psi = id$ and $\Omega' = \Omega$, then this simplifies to $\Lambda_{\Psi_*\sigma} = \Lambda_\sigma$. Hence there are potentially a large class of anisotropic

conductivities generating the same electrical measurements on the boundary. We denote the distortions on M as $\text{Diff}_\partial(M)$

$$\text{Diff}_\partial(M) = \{\Psi : M \rightarrow M \mid \Psi|_{\partial M} = id\}.$$

This non-uniqueness observation has broadly generated two different approaches to understanding anisotropy in EIT. The first approach is to determine if the distortions are the only obstruction to uniqueness. Lee and Uhlmann [86] proved that the boundary fixing diffeomorphisms are the only obstruction to uniqueness for a compact manifold with real-analytic metric under topological assumptions about the manifold. This result essentially hinges on Λ_g being a PSDO which determines the full Taylor series of g at the boundary. Lassas, Taylor and Uhlmann [46] improved this result by replacing compactness with completeness and removing the topological assumptions. In particular they proved:

Theorem 3.4.1 (Lassas, Taylor and Uhlmann). *Let M_1 and M_2 be complete, connected, real-analytic Riemannian n -manifolds with boundary with $n \geq 3$. Assume the boundaries ∂M_j are compact and all boundary points are regular, in the sense of Wiener. Assume that ∂M_1 and ∂M_2 contain a non-empty open set $\Gamma_1 = \Gamma_2 = \Gamma$, which are identified by a diffeomorphism. Assume each boundary is real analytic, with the metric tensors analytic up to Γ_j . Assume Λ_{Γ, g_1} and Λ_{Γ, g_2} coincide. Then M_1 and M_2 are isometric.*

We note that the result for $n \geq 3$ assumes a high degree of regularity of the metric in that it is real analytic. For the case $n = 2$, Sylvester [103] proved distortions are the only obstruction for C^3 conductivities sufficiently close to the identity. Astala, Lassas and Päiväranta [45] effectively completed the problem for $n = 2$ in the sense that the DtN map determines L^∞ anisotropic conductivities up to a H^1 distortion.

The second approach is to determine if there is unique identifiability for certain classes of anisotropic media. For example in the isotropic case in Euclidean space, with dimension $n \geq 3$, the space of boundary fixing diffeomorphisms consists of conformal maps of Euclidean space that are the identity on $\partial\Omega$. For $n \geq 3$, the conformal maps are exactly the similarity transformations: rotations, scaling, translations and inversions (see section 4.2.1). An isotropic conductivity is locally invariant under the rotation group, and the translations, scalings and inversion can only be the identity

because of the condition $F|_{\partial\Omega} = id$. So the equivalence class in the isotropic case degenerates to exactly the identity diffeomorphism. This raises the question that when does the equivalence class of diffeomorphisms reduce to a single identity diffeomorphism? An early result by Kohn and Vogelius [84] demonstrated uniqueness if the entire eigenspace of the anisotropic conductivity is known apart from a single eigenvalue. In [31] uniqueness for the conformal inverse problem, that is the recovery of a function α on M given the metric has the form $g = \alpha g_0$, with g_0 known, was shown to hold. The isotropic problem is a special case of this result when g_0 is the Euclidean metric. In [110] it was shown that if the conductivity matrix $A(x)$ is assumed to have the structure $A(a(x))$, where $A(t)$ is a known matrix function and $a(x)$ is an unknown scalar field, then this is uniquely identifiable under the assumption of monotonicity, $A(t)' \geq CI > 0$. This was generalised in [111] to $A(x) = A(x, a(x))$, where again $a(x)$ is unknown and $A(x, t)$ is known still under the monotonicity assumption.

3.4.3 Elasticity

Before discussing the anisotropic inverse conductivity problem further, we discuss some problems in theoretical elasticity. Firstly the Saint-Venant consistency condition is analogous to the vanishing of the Cotton-York tensor when considering an inaccurately known external shape with isotropic conductivity in the subsequent chapter. Secondly two problems in theoretical elasticity will be outlined in detail as this will be directly used when discussing anisotropic conductivities with constrained eigendata.

Curvature and Saint-Venant's condition

We consider $\Omega \subset \mathbb{R}^n$ in Euclidean space endowed with Cartesian coordinates, and let $F : \Omega \rightarrow \Omega' : x \mapsto \Psi(x) = y$ represent a deformation. Let $\{\partial_i\}_{i=1}^n$ represent tangent vectors at x , then the orthonormal pair, ∂_i and ∂_j , are sent to $\Psi_*\partial_i, \Psi_*\partial_j$ under the differential of Ψ at x . At the deformation point x and y we have the metric ds^2 and dS^2 respectively given by

$$ds^2 = g_{ij}(x)dx^i \otimes dx^j = (dx^i)^2, \quad dS^2 = g_{ij}(y)dy^i \otimes dy^j = (dy^i)^2.$$

where the second equalities follow since we are in Euclidean space using Cartesian coordinates. The pullback of the metric under Ψ , Ψ^*dS^2 , is thus

$$\Psi^*(dS^2) = \sum_{i,j,k} \frac{\partial \Psi_k}{\partial x_i} \frac{\partial \Psi_k}{\partial x_j} dx^i \otimes dx^j.$$

The difference of the two metrics defines a non-linear strain tensor, ϵ_{ij} , through

$$2\epsilon_{ij}dx^i \otimes dx^j := \Psi^*(dS^2) - ds^2 = \left(\frac{\partial \Psi_k}{\partial x_i} \frac{\partial \Psi_k}{\partial x_j} - \delta_{ij} \right) dx^i \otimes dx^j.$$

Consider an infinitesimal strain field u , defined by $\Psi(x) = x + \epsilon u(x)$, with ϵ sufficiently small, then the linearised strain tensor (an order 2 symmetric tensor) is given by the symmetrized derivative of the deformation field

$$\mu_{ij} = \frac{1}{2} \left(\frac{\partial u^i}{\partial x^j} + \frac{\partial u^j}{\partial x^i} \right) =: \frac{1}{2} \nabla_S(u),$$

where ∇_S is the symmetrised derivative of u . The tensor μ_{ij} is in fact the Lie derivative of the Euclidean metric, e , with respect to u (A.19)

$$\mu = \frac{1}{2} \mathcal{L}_u e.$$

A question we can ask is given a rank 2 tensor field, μ_{ij} , how do we know if this is the strain tensor of some deformation field? There is a consistency condition that this is true if and only if $S_{ijkl} = 0$, where

$$S_{ijkl} = \frac{\partial^2 \mu_{jk}}{\partial x_i \partial x_l} + \frac{\partial^2 \mu_{li}}{\partial x_k \partial x_j} - \frac{\partial^2 \mu_{jl}}{\partial x_k \partial x_i} - \frac{\partial^2 \mu_{ik}}{\partial x_l \partial x_j},$$

known as the *Saint-Venant* tensor [112, 113]. The Riemann curvature tensor measures the deviation of choosing local coordinates at a point on a manifold such that the metric is flat, and is given by (A.21). The diffeomorphism Ψ is a map between Euclidean spaces and thus the Riemann tensor must vanish for both the original metric e and the perturbation $e + \mu$. Consider the perturbation of the Euclidean metric in the direction of the strain tensor i.e. $g = e + \epsilon \mu$. Amrouche *et al.* demonstrate in [113] that the Saint-Venant integrability condition is equivalent to the linearisation of the Riemann tensor of the perturbation of the Euclidean metric being zero

$$S_{ijkl} = \lim_{\epsilon \rightarrow 0} \frac{R_{ijkl}(\epsilon)}{\epsilon},$$

where $R(\epsilon)$ refers to the Riemann tensor with metric $g_{ij} = e_{ij} + \epsilon \mu_{ij}$. Ciarlet *et al.* show in [112] that the Saint-Venant condition is the extension of the Poincaré lemma for

vector fields to matrix fields. The classical Poincaré lemma asserts that, on a simply connected domain Ω , if $\nabla \times v = 0$ for a vector field v then $v = \nabla f$ for some scalar field f . In the language of differential forms, on a simply connected manifold M , if $dF = 0$, then $F = du$ for some u so that every closed form is exact. The extension to matrix fields is that if $\nabla \times (\nabla \times w) = 0$ for a matrix field w then $w = \nabla_S(v)$ for some vector field v , where $(\nabla \times w)_{ij} = \epsilon_{ilk} \partial_l w_{jk}$, where ϵ_{ilk} is the Levi-Civita symbol.

Recovering the deformation field from principal strains

In the same article DeTurck and Yang also consider the inverse problem of determining the deformation field given the eigenvalues of the strain tensor [109]. We outline this result as we will use this directly when discussing anisotropy with prescribed eigenvalues. The authors considered two Riemannian manifolds (M, g) and (N, h) . Let $\Psi : M \rightarrow N$ be a diffeomorphism, then $\lambda(x)$ is said to be an eigenvalue of Ψ at $x \in M$ if $\det(\Psi^*h - \lambda g)(x) = 0$. The goal is to recover Ψ given a set of positive C^∞ functions $\lambda_1, \lambda_2, \dots, \lambda_n$ on M that are the eigenvalues of Ψ . Let e_1, \dots, e_n be an orthonormal basis of vector fields with respect to g on M , if $\Psi : M \rightarrow N$, then we define $\langle e_i, e_j \rangle_{\Psi^*h} := \langle d\Psi(e_i), d\Psi(e_j) \rangle_h$. Let S map a symmetric matrix to its eigenvalues in increasing order, and consider the (non-linear) PDE

$$S(\langle e_i, e_j \rangle_{\Psi^*h}) = \lambda,$$

where λ is a vector valued function $\lambda \in C^\infty(M, \mathbb{R}^n)$. The authors show the linearisation is diagonal hyperbolic. They further consider submanifolds M' and N' of M and N respectively and let $\psi : M' \rightarrow N'$ be a diffeomorphism. The authors further show that if λ , M' , N' and ψ are known, then ψ can be extended, at least in a neighbourhood of M' , to the diffeomorphism Ψ provided the Cauchy data is *admissible*. They demonstrate that a sufficient condition for admissible Cauchy data is that the eigenvalues $\kappa_1, \dots, \kappa_{n-1}$ of ψ^*h' with respect to g' are positive, distinct and interlock,

$$\lambda_1 < \kappa_1 < \lambda_2 < \dots < \kappa_{n-1} < \lambda_n. \quad (3.18)$$

The admissibility condition for the Cauchy problem can be interpreted as meaning that the eigenvectors at $p \in M'$ can not lie in the tangent space $T_p M'$. Hence by theorems A.1.3 and A.1.4 the non-linear Cauchy problem is well-posed and it is possible to

solve for the interior diffeomorphism Ψ , given $\psi : M' \rightarrow N'$ and $\lambda \in C^\infty(M, \mathbb{R}^n)$ up to 2^n sign choices. These sign choice represent choices of the orientation of the flag, $d\psi(e_1), \dots, d\psi(e_n)$. To sum up DeTurck and Yang proved the following [109]:

Theorem 3.4.2. *Let (M, g) and (N, h) be C^∞ manifolds and $\lambda_1, \dots, \lambda_n$ be C^∞ functions from M to $(0, \infty)$ such that $\lambda_i(x) \neq \lambda_j(x)$ whenever $i \neq j$ for all $x \in M$. Then in a neighbourhood of any $p \in M$ there exists a C^∞ diffeomorphism Ψ such that Ψ^*h has eigenvalues $\lambda_1, \dots, \lambda_n$. The C^∞ Cauchy problem for Ψ given ψ is locally solvable and has 2^n solutions provided the non interlocking condition (3.18) is satisfied.*

Orthogonal coordinates

In section 3.4.1 it was stated there exists coordinates on a 3-manifold in which the metric is diagonal. We outline this result in detail as we will use this to understand anisotropic conductivities with prescribed orthogonal coordinates. The authors attempt to solve the non-linear system of PDE

$$\frac{\partial \Psi^i}{\partial x^k} \frac{\partial \Psi^j}{\partial x^l} g_{ij}(x) = 0, \quad k \neq l, \quad (3.19)$$

for the orthogonal coordinates $\{\Psi^i\}$ in terms of the original coordinates $\{x^l\}$. They demonstrate that although the first condition in theorem A.1.5 is satisfied, the second condition on the dimension of $\ker(\sigma_P(\xi))$ is not. Hence the linearisation is not symmetric hyperbolic and there is no obvious theory to deduce anything about the non-linear problem. This difficulty is a reflection of the fact that if (x, y, z) are orthogonal coordinates then so are $(f(x), g(y), h(z))$ for monotone functions f, g, h .

DeTurck and Yang demonstrate the existence of orthogonal coordinates in the C^∞ category of metrics using the technique of moving frames, which we outline in detail. Solving for an orthogonal frame, as opposed to the coordinates, bypasses the non-uniqueness due to the monotonic functions adressed above. Following Cartan [114], who proved this in the real-analytic category, we let $\{\bar{e}_1, \bar{e}_2, \bar{e}_3\}$ be an orthonormal frame of vector fields on M and $\{\bar{\omega}_1, \bar{\omega}_2, \bar{\omega}_3\}$ be the dual basis of 1-forms. They search for coordinate functions (x^1, x^2, x^3) so that $\langle \frac{\partial}{\partial x^i}, \frac{\partial}{\partial x^j} \rangle_g = 0$, with the orthonormal coframe associated to (x^1, x^2, x^3) being (not summing over repeated indices)

$$\omega^i = f^i dx^i \quad f^i = (\langle dx^i, dx^i \rangle_g)^{-\frac{1}{2}} \quad i = 1, 2, 3.$$

Three applications of Frobenius' theorem (A.33) for the existence of x^i given ω^i give

$$\omega^i \wedge d\omega^i = 0 \quad i = 1, 2, 3. \quad (3.20)$$

Now $\{\omega^i\}$ also satisfies the structure equations for Riemannian geometry (A.18)

$$d\omega^i = \sum_j \omega^j \wedge \omega_j^i \quad i = 1, 2, 3, \quad (3.21)$$

where ω_j^i is the skew-symmetric matrix of connection 1-forms (A.17). Substituting equation (3.21) in (3.20) and repeated use of the skew-symmetry of \wedge and ω_j^i in its indices, leads to three equations

$$\omega^1 \wedge \omega^2 \wedge \omega_2^1 = 0, \quad \omega^1 \wedge \omega^3 \wedge \omega_3^1 = 0, \quad \omega^2 \wedge \omega^3 \wedge \omega_3^2 = 0. \quad (3.22)$$

The unknown coframe $\{\omega^i\}$ is related to the reference coframe $\{\bar{\omega}^i\}$, through $\omega^i = \sum_j b_j^i \bar{\omega}^j$ and $\bar{\omega}^j = \sum_k b_j^k \omega^k$, where b is an orthogonal matrix valued function of M . DeTurck and Yang demonstrate that ω_j^i can be eliminated from (3.22) and can be written as three non-linear equations in terms of b_j^i . The authors demonstrate that the linearisation of these equations is symmetric hyperbolic. In particular choose the reference frame to be the frame we are linearising about, $b_j^i(x) = \delta_j^i$, and let β_j^i be the variation in b (which is skew-symmetric since b is orthogonal). To first order in β

$$\frac{\partial}{\partial \bar{x}^1}(\beta_3^2) = 0, \quad \frac{\partial}{\partial \bar{x}^2}(\beta_1^3) = 0, \quad \frac{\partial}{\partial \bar{x}^3}(\beta_2^1) = 0, \quad (3.23)$$

which is a diagonal, and hence symmetric, hyperbolic system of PDE (see section A.1.2.) They further demonstrate that Cauchy data can be specified on a surface $\Sigma \subset M^3$ in the following way: Admissible Cauchy data consists of the coframe $\{\omega^i\}$ on Σ and is admissible if

$$\omega^i(v) \neq 0 \quad \forall v \in T\Sigma, \quad (3.24)$$

which means that none of the vectors in the dual frame $\{e_i\}$ can be tangent to Σ . Hence, given non-characteristic Cauchy data, the non-linear problem is well-posed by theorems A.1.3 and A.1.4. We state DeTurck and Yang's result as a theorem:

Theorem 3.4.3 (Orthogonal coordinates). *Let (M^3, g) be a three dimensional C^∞ Riemannian manifold. Then there exists an atlas of C^∞ coordinate charts on M such that, in each chart, the metric has the form*

$$g = \lambda_1(x, y, z)dx^2 + \lambda_2(x, y, z)dy^2 + \lambda_3(x, y, z)dz^2, \quad (3.25)$$

where $\lambda_i : M \rightarrow \mathbb{R}^+$, $i = 1, 2, 3$, are, in general, three different functions.

3.4.4 Anisotropy with eigenspace constraints

Abascal *et al.* performed a computational sensitivity study of anisotropic conductivities in 3D with known eigenvectors in [115]. The study demonstrated that the conductivity Jacobian with respect to the unknown eigenvalues, with fixed eigenvectors, were full rank, suggesting that this constraint on the conductivity eigenspace allows unique recovery of the eigenvalues. When considering the eigenspace of the contravariant electrical metric g^{ij} , the eigenvalue equation $g^{ij}v_i = \lambda v_j$ does not make sense because the left and right hand side are contravariant and covariant vectors respectively. We instead consider eigenvalues of the metric g with respect to another metric, say, h (or more practically the Euclidean metric e). The eigenvalues are the solutions $\lambda(x)$ of $\det(g - \lambda h)(x) = 0$ for $x \in M$, which is invariant under a local coordinate change.

In this section, we propose a theoretical framework to demonstrate unique recovery with given constraints on the eigenspace of the metric g . Given a diffeomorphism $\Psi : \Omega \rightarrow \Omega$ with $\Psi|_{\partial\Omega} = id$, we know that σ and $\Psi_*\sigma$ defined by (3.15) have the same DtN maps (3.17). We want to prescribe certain structure to σ and $\Psi_*\sigma$. More precisely, let σ and σ' be matrix valued functions of the conductivity and its pushforward. We want to characterise solutions $\Psi \in \text{Diff}_\partial(\Omega)$ of the non-linear system of PDE

$$(D\Psi(x))\sigma(x)(D\Psi(x))^T = \det(D\Psi(x))\sigma'(\Psi(x)), \quad (3.26)$$

such that the matrix valued functions σ and σ' share a specific constraint on their eigenspace. This eigenspace constraint, and the additional constraint that Ψ is fixed at the boundary, will restrict the set of diffeomorphisms. The ideal case would be to show that the solution space of diffeomorphisms reduces to the identity, as is the case when σ and σ' are both *a-priori* assumed isotropic.

Prescribed eigenvalues

We first consider the situation when all the eigenvalues of g with respect to h are known, and the goal is to determine g given Λ_g . We call this the *prescribed eigenvalues* inverse conductivity problem. We begin with a conjecture for this problem followed by a local uniqueness result, and an explanation for why the conjecture may be true:

Conjecture 3.4.4 (Prescribed eigenvalues). *Let $(M, g_1), (M, g_2), (M, h)$ be complete, connected real-analytic manifolds of dimension $n \geq 3$ with compact boundary ∂M . Assume the eigenvalues of g_1 and g_2 with respect to the known metric h are $\lambda_1, \lambda_2, \dots, \lambda_n$, with $\lambda_i \neq \lambda_j$ everywhere in M , and the eigenvalues $\kappa_1, \kappa_2, \dots, \kappa_{n-1}$ of ι^*g_1 and ι^*g_2 with respect to ι^*h are given and satisfy the interlocking property (3.18), where $\iota : \partial M \hookrightarrow M$. If $\Lambda_{g_1} = \Lambda_{g_2}$, then $g_1 = g_2$.*

By drawing a direct analogy to the inverse deformation problem considered in section 3.4.3 we have the following local result:

Theorem 3.4.5 (Local prescribed eigenvalues). *Given all the conditions in conjecture 3.4.4 and that $\Lambda_{g_1} = \Lambda_{g_2}$, then $g_1 = g_2$ in an ϵ -neighbourhood of ∂M .*

Proof. We consider the identical embedding of (M, h) in (M, g_1) and (M, g_2) . We assume that the eigenvalues of g_1 and g_2 are known with respect to h and are the same, so we know $\lambda \in C^\infty(M, \mathbb{R}^n)$ satisfying

$$\det(g_1 - \lambda h)(x) = 0 \quad \det(g_2 - \lambda h)(x) = 0 \quad \text{for all } x \in M. \quad (3.27)$$

Theorem 3.4.1 asserts that if $\Lambda_{g_1} = \Lambda_{g_2}$ then $g_1 = \Psi^*g_2$ for some $\Psi \in \text{Diff}_\partial(M)$. Thus from the *a-priori* assumption on the eigenvalues of g_1 and g_2 we have

$$\det(\Psi^*g_2 - \lambda h)(x) = 0 \quad \det(g_2 - \lambda h)(x) = 0 \quad \text{for all } x \in M. \quad (3.28)$$

Theorem 3.4.2 states that Ψ is uniquely determined in an ϵ -neighbourhood of ∂M from the restriction $\psi : \partial M \rightarrow \partial M$, given the sufficient conditions on the eigenvalues in (3.18) up to 2^n sign choices. The sign choice is fixed by choosing an orientation for each of the vectors e_1, \dots, e_n for every $x \in \partial M$. In particular $\Psi = id$ is a solution in this ϵ -neighbourhood and, since Ψ is unique, we thus have $g_1 = g_2$ in this ϵ -neighbourhood. \square

There are a number of possible improvements to this result. Firstly we note that theorem 3.4.2 is true for C^∞ metrics, and so if the regularity of the metric in theorem 3.4.1 was improved from C^∞ to real-analytic, then the above would be true in the C^∞ category. Secondly, this result is only true in an ϵ -neighbourhood of ∂M due to theorem A.1.3, and it is clearly of interest to understand if this can be extended to a global result over M to prove conjecture 3.4.4. The conditions in theorem 3.4.1 are true for

a complete and hence compact manifold, and so given an open cover of orthogonal coordinate charts of the manifold there exists a finite subcover of orthogonal charts covering the manifold. We apply a frame in a neighbourhood of $b \in \partial M$ with the prescribed eigenvectors satisfying the conditions in (3.18) and apply theorem 3.4.2 to uniquely recover Ψ in this chart. We then consider a surface of intersection of the current chart with the next coordinate chart, which also satisfies the conditions in (3.18) and again apply theorem 3.4.2 to recover Ψ in this chart, and continue this until we reach an arbitrary interior point $p \in M$. It is unclear, however, if the ϵ -neighbourhood in theorem A.1.3 can be chosen large enough for this continuation argument to hold. It is worth pursuing further research into the validity of this argument, perhaps with some additional topological assumptions on M , to obtain a global result.

Prescribed eigenvectors

Theorem 3.4.3 states that on any 3-manifold there exists an atlas of charts in which the components of the metric are diagonal. We assume *a-priori* we are working in such a local orthogonal coordinate system, with the metric g having the form $g = \sum_i \lambda_i (dx^i)^2$ for positive coordinate functions $\lambda_i : M \rightarrow \mathbb{R}^+$ for $i = 1, 2, 3$ and $x \in M$. We denote this as the *prescribed orthogonal coordinates* problem. We define two metrics g_1 and g_2 to be in the same *orthogonal class* if $g_1 = \sum_i \lambda_i (dx^i)^2$ and $g_2 = \sum_i \lambda'_i (dx^i)^2$ for positive functions $\lambda_i, \lambda'_i : M \rightarrow \mathbb{R}^+$ for $i = 1, 2, 3$.

In the outline of the proof of theorem 3.4.3 the orthogonal coframe can be solved for uniquely in a given coordinate chart given admissible coframe Cauchy data satisfying (3.24) on a surface $\Sigma \subset M^3$. Let $\Omega \subset \mathbb{R}^3$ with Euclidean metric and Cartesian coordinates. If any $v \in T_x \partial \Omega$ at $x \in \partial \Omega$ are parallel to any of the Cartesian coordinate axes, then Cauchy data is inadmissible at this point. For example the boundary of a cubic domain aligned with the Cartesian coordinate axes has no admissible characteristics. A spherical domain, on the other hand, will only have exactly 3 non-characteristic equatorial lines in which there are no admissible characteristics.

There is a single obstruction to uniqueness due to any three monotone functions that rescale each of the coordinate functions. Theorem 3.4.3 is also strictly local because we can only guarantee to solve for the coframe uniquely in an ϵ -neighbourhood of Σ due to the conditions in theorem A.1.3. It is unknown whether we can continue

the orthogonal coframe uniquely to an arbitrary point $p \in M$, and further research in this continuation is worth pursuing.

The prescribed orthogonal coordinates problem can in fact be formulated as a prescribed eigenvectors problem. Let n_1, n_2, n_3 be orthonormal basis in the neighbourhood U of x such that $n_i(x)$ is an eigenvector of Ψ at x corresponding to the eigenvalue $\lambda_i(x)$, $i = 1, 2, 3$, we have $n_i = dx^i$. Given 3 vector fields everywhere orthogonal on M , then each vector field forms an integrable distribution whose integral curves are the orthogonal coordinate functions. We denote these vector fields as the eigenvectors of the system and the eigenvalues as the coordinate functions at each point $x \in M$.

The goal is to determine three eigenvalues of the conductivity field which we call the *prescribed eigenvectors* inverse conductivity problem given the eigenvectors. In particular the prescribed eigenvectors problem boils down to understanding the rigidity of rescaling the metric by monotone functions that fix points on the boundary. We state a conjecture on unique identifiability with prescribed eigenvectors, followed by a uniqueness result assuming a global orthogonal coordinate system and an explanation of why this may be true.

Conjecture 3.4.6 (Prescribed eigenvectors). *Let (M, g_1) , (M, g_2) and (M, h) be compact real-analytic Riemannian 3-manifolds with smooth boundary ∂M . Assume that the eigenvectors of g_1 and g_2 with respect to h are n_1, n_2, n_3 so that $g_1 = \sum_i \lambda_i(n_i)^2$ and $g_2 = \sum_i \lambda'_i(n_i)^2$, with the associated eigenvalues satisfying the admissibility condition (3.24). If $\Lambda_{g_1} = \Lambda_{g_2}$, then $g_1 = g_2$.*

Theorem 3.4.1 implies that if $\Lambda_{g_1} = \Lambda_{g_2}$ then $g_1 = \Psi^*g_2$ for $\Psi \in \text{Diff}_\partial(M)$. Thus if we can show $g_1 = \Psi^*g_2$ with $\Psi \in \text{Diff}_\partial(M)$ implies $\Psi = id$, when g_1 and g_2 are in the same orthogonal class, then the above conjecture is true. We demonstrate this result under the assumption of a global coordinate system. For $i = 1, 2, 3$, let $x_i^{-,\partial} = \min_{x \in \partial M}(x_i)$, $x_i^{+,\partial} = \max_{x \in \partial M}(x_i)$, $x_i^- = \min_{x \in M}(x_i)$ and $x_i^+ = \max_{x \in M}(x_i)$. Let $I_i^\partial = (x_i^{-,\partial}, x_i^{+,\partial})$ and $I_i = (x_i^-, x_i^+)$, then we say $I \subseteq I^\partial$ if $I_i \subseteq I_i^\partial$ for $i = 1, 2, 3$.

Theorem 3.4.7 (Prescribed global orthogonal coordinates). *Let (M, g_1) and (M, g_2) be C^∞ Riemannian 3-manifolds with smooth boundary in the same orthogonal class. Assume a global orthogonal coordinate system, with $I \subseteq I^\partial$, and M and ∂M satisfying the admissibility condition (3.24). Given $\Psi \in \text{Diff}_\partial(M)$ and $\Psi^*g_2 = g_1$, then $\Psi = id$*

in M .

Proof. By assumption $g_1 = \sum_i \lambda_i(n_i)^2$, $g_2 = \sum_i \lambda'_i(n_i)^2$ and hence $\Psi^*g_2 = \sum_i (\lambda'_i \circ \Psi)(n_i)^2$ preserves the orthogonal coordinates. Theorem 3.4.3 states that there exists an atlas of orthogonal coordinate charts and we assume there exists a single global coordinate chart. This assumption means that we do not have to consider any potential non-uniqueness of orthogonal coordinates arising from continuing the prescribed coframe on ∂M as Cauchy data into an arbitrary point in the interior.

Any potential non-uniqueness arises due to monotone functions f, g, h that preserve the orthogonal coordinate structure. We consider applying a distortion Ψ to M , with orthogonal coordinates (x_1, x_2, x_3) , and so the orthogonal coordinate preserving diffeomorphisms are of the form $\Psi(x_1, x_2, x_3) = (f(x_1), g(x_2), h(x_3))$ where f, g, h are the identity on ∂M . We thus want conditions such that f, g, h are the identity in the interior of M . If all the range of the coordinates are on the boundary, i.e. $I \subseteq I^\partial$, and we have global orthogonal coordinates, satisfying the condition (3.24), then clearly the rescaling must be fixed because we observe the range of all the coordinates at the boundary. Hence each of the monotone functions have to be the identity and so the diffeomorphism Ψ is uniquely $\Psi = id$.

□

If theorem 3.4.1 was strengthened to C^∞ metrics then the above theorem again would be true in the C^∞ category. It also appears unknown what conditions on a 3-manifold are required for the atlas of orthogonal coordinate charts to be extended to a global coordinate system as we assumed in theorem 3.4.7. If the manifold is considered as a simply connected domain in \mathbb{R}^3 this is clearly possible to do. For a general M , for example, is it true that if a manifold is parallelizable, that is there exists smooth vector fields X_1, \dots, X_n on M such that at any point p of M the tangent vectors $X_i(p)$ provide a basis for tangent space at p , then can local coordinates be extended to global coordinates?

Layered and fibrous media

We consider classes of anisotropic conductivities that have two eigenvalues the same $\lambda_2 = \lambda_3$, which would be appropriate for materials with a single preferred direction,

such as muscle tissue. We denote the preferred eigendirection as a vector field $N \in C^\infty(\Omega, \mathbb{R}^3)$. The conductivity can be written in the form $\sigma = \alpha NN^T + \beta I$, so that $\sigma N = (\alpha + \beta)N$ and $\sigma N^\perp = \beta N^\perp$, where N^\perp is a vector orthogonal to N . The goal is then to determine the two eigenvalues α and β and the eigendirection N (which is two degrees of freedom because the eigendirections are normalisable), which completely specifies the conductivity. We denote this problem as the *fibrous* inverse conductivity problem. The problem is now a mixture of the prescribed eigenvector and eigenvalue problem which in a sense would combine conjectures 3.4.4 and 3.4.6. We could relax one of the conditions so that the preferred eigendirection, N , is known for all $x \in M$, and thus only seek the two distinct eigenvalues α and β .

We further define a *layered* media to be fibrous but with N satisfying the integrability condition to be normal to a family of surfaces. From (A.33) the necessary and sufficient condition is that $w \wedge dw = 0$, where ω is the 1-form associated with the preferred eigendirection field, $\omega = \sum_i N_i dx^i$. Computing this condition we get

$$dw = \sum_{i < j} \left(\frac{\partial N_i}{\partial x_j} - \frac{\partial N_j}{\partial x_i} \right) dx^i \wedge dx^j \implies \omega \wedge d\omega = \sum_{i < j, k} N_k \left(\frac{\partial N_i}{\partial x_j} - \frac{\partial N_j}{\partial x_i} \right) dx^i \wedge dx^j \wedge dx^k.$$

Hence $dw \wedge w = 0$ implies $N \cdot (\nabla \times N) = 0$. Consider one such foliated surface, S , as an embedded submanifold of M , and denote the inclusion as $f : S \hookrightarrow M$ with the pulled back metric, $g|_S = f^*g$. Because S is a co-dimension 1 submanifold of M , there exists another diffeomorphism $r : S \rightarrow S$ such that $r^*(g|_S) = \gamma e$, where e is a flat metric (see section 3.4.1), and hence $g|_S$ is conformally flat. If the surface S further intersects with ∂M , and we knew the interior structure of S in M , then it is known that any distortion restricted to S , $\Psi|_S$, of a conformally flat metric must be the identity [31]. We can not deduce that the entire diffeomorphism is the identity because we can not *a-priori* assume that the structure of S in the interior of M is known. However this additional structure may prove useful when considering whether a layered material is uniquely determined from Λ_g , because M now has a product structure. That is the metric locally takes the form $g = g|_S \oplus g_N$, where $g|_S$ is conformally flat, and g_N is the metric associated with the normal eigendirection.

For such a material we want to characterise the solutions Ψ to

$$(D\Psi)^T(\alpha NN^T + \beta I)(D\Psi) = \alpha' N' N'^T + \beta' I \quad \Psi|_{\partial\Omega} = id. \quad (3.29)$$

Assume there are two diffeomorphisms Ψ and Φ with $\Psi|_{\partial\Omega} = \Phi|_{\partial\Omega} = id$, and consider difference between two diffeomorphisms. $h = \Psi - \Phi$, with $h|_{\partial\Omega} = 0$, we arrive at (keeping only first order terms in h)

$$(Dh)^T(\alpha NN^T + \beta I)(D\Psi) + (D\Psi)^T(\alpha NN^T + \beta I)(Dh) = 0 \quad h|_{\partial\Omega} = 0. \quad (3.30)$$

This is clearly a more complicated system of PDE than when working with orthogonal coordinates. In particular the coefficients of the system depend on the unknowns α, β and N . The system, in general, is not symmetric hyperbolic and so we can not use the uniqueness results for such systems as presented in this chapter. Perhaps the technique of moving frames can be deployed to understand the rigidity of a layered conductivity under diffeomorphism. We leave this as an open question as to whether a fibrous or layered material is uniquely identifiable from the DtN map.

Chapter 4

Shape and electrode position corrections

This chapter will be organised as follows. Firstly a brief motivation for the shape problem will be discussed followed by a theoretical discussion of uniqueness results for the simultaneous reconstruction of the external shape and conductivity from the DtN map. Secondly, a novel calculation of the Fréchet derivative of the continuum model is presented with respect to the external shape and a novel numerical sensitivity study will be performed under different measurement strategies. Finally a novel algorithm is proposed for absolute conductivity and electrode position imaging with a fixed boundary shape and contact impedance in 3D and numerical results for spherical and cylindrical geometries presented. In the subsequent chapter, results from a shape correction algorithm on real human data using the fEITER instrument will be outlined.

4.1 Inaccurately known external shape

An inaccurate knowledge of the external boundary shape and electrode positions are known to create major artefacts in lung EIT [30, 32, 116]. In the ICU many patients often have MRI and CT scans during their course of treatment, and if these are available it is reasonable to use this as prior information to generate an external shape specific to the patient. A recent study on pig data, with external shapes informed from CT scans, has demonstrated that informing the shape from CT improves the quality of EIT reconstructions [117]. The authors define the mismatch ΔS between

a smooth extruded shape represented using a Fourier series and the original extruded shape (both normalised to π) as the area of symmetric difference between the two shapes divided by π . The study suggests that there is little difference in the quality of dynamic EIT reconstructions if the model shape is known within a mismatch of $\Delta S = 3.91\%$ of the exact shape. MRI and CT can additionally provide us with prior information of the interior conductivity distribution, which should further improve the quality of EIT reconstructions. An alternative method of shape capture could use optical tracking techniques as demonstrated for breast cancer detection in [34]. Even with informed FEM models, however, the shape problem is still present in lung EIT because when the patient breathes the external shape and the electrode positions change relative to a fixed geometrical model of the thorax.

To illustrate why boundary shape changes can be so important, the error in measured voltages on a unit disc with unit conductivity as a function of the standard deviation in electrode position perturbation are displayed in figure 4.1. In particular, 16 electrodes are placed equiangular on the unit circle, and the theta coordinate perturbed by adding normally distributed noise with mean 0 and standard deviation α . A nearest neighbour adjacent-adjacent drive-measurement strategy is used without measuring on driven electrodes. With a standard deviation of $\alpha \approx 0.17^\circ$ the total 2-norm voltage error due to incorrect positions of electrodes is approximately the same as measurement signal-to-noise ratio (SNR) level of 50, where the addition of SNR to measurements $V \in \mathbb{R}^m$ is defined through

$$V \mapsto \tilde{V} = V + \frac{\|V\|}{\|n\|\text{SNR}}n, \quad (4.1)$$

where $n \in \mathbb{R}^m$ is a vector with entries from the standard normal distribution, $n_i \in \mathcal{N}(0, 1)$. Relatively modest inaccuracies of the electrode position of less than a degree leads to voltage errors larger than a practical noise level. We observe that even with the relatively coarse finite element mesh, there is little difference in the measured voltages between linear, quadratic or cubic approximation, highlighting that shape changes can be a major source of error in the forward problem in lung EIT.

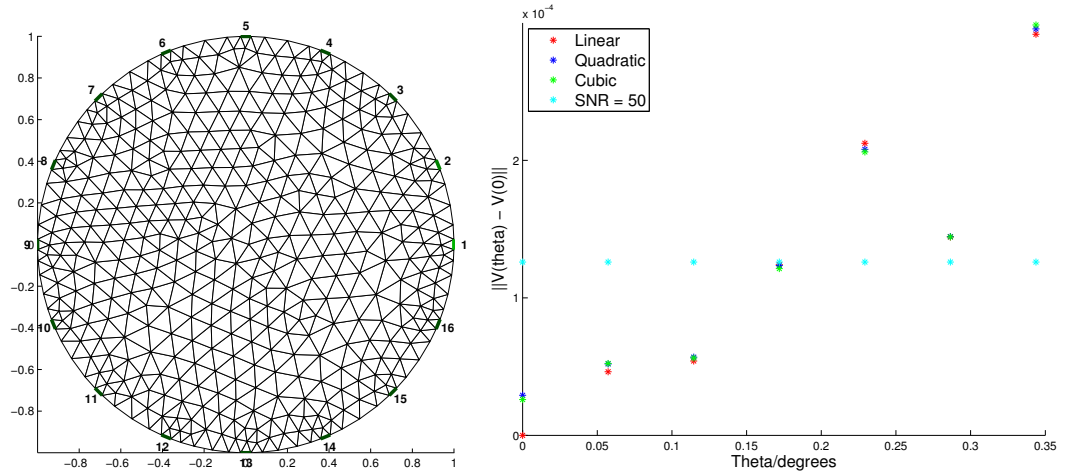


Figure 4.1: The figure illustrates the 2-norm error in measured voltages on a unit circle with $\sigma = 1$ as a function of the standard deviation in electrode angle perturbation, α . When $\alpha \approx 0.17^\circ$ the voltage error is larger than an SNR of 50 of the measurements. We also observe that even with a relatively coarse mesh (813 elements and 450 nodes), there is negligible difference in the measured voltages when using linear, quadratic or cubic approximation compared to an SNR of 50.

4.2 Global uniqueness

Lionheart [30, 31] demonstrated that assuming full knowledge of the DtN map and the conductivity is *a-priori* assumed isotropic, that if the boundary shape of the reconstruction model is inaccurately known, an isotropic conductivity can only be reconstructed if the thorax shape and model domain are related through a conformal map. In other words, if the model and exact shapes are not related conformally, then we can not find an isotropic conductivity consistent with the measurements in the model domain. In this section we review uniqueness results for an isotropic conductivity and an unknown shape.

4.2.1 Configuration manifolds

In section 3.4 we observed that an anisotropic conductivity determines a Riemannian metric, $g^{ij} = |\sigma|^{-1} \sigma^{ij}$ in 3D, and theorem 3.4.1 also states that Λ_g determines a real analytic metric g up to a distortion.

Lionheart [30] modelled the unknown shape problem, by considering the body as a manifold M with smooth boundary ∂M . A *configuration* is a smooth embedding $C : M \rightarrow \mathbb{R}^3$ with $C(M) = \bar{\Omega}$. Knowledge of the DtN map on ∂M corresponds to knowing the electrode positions and boundary in some coordinate system but not how this system is embedded in \mathbb{R}^3 . An anisotropic real-analytic metric g can be

determined on M up to a distortion $\Phi \in \text{Diff}_{\partial M}(M)$ by theorem 3.4.1. Given two configurations there exists a smooth invertible mapping $\Psi = C_2 \circ \Phi \circ C_1^{-1} : \bar{\Omega}_1 \rightarrow \bar{\Omega}_2$. We suppose that two electrical metrics g_1 and g_2 are found on Ω_1 and Ω_2 consistent with the measurements, then there must be such a Ψ satisfying $\Psi_*g_1 = g_2$. If the conductivity is *a-priori* assumed to be isotropic, $g_1 = \lambda_1 e$ and $g_2 = \lambda_2 e$, it is by definition conformally flat. We observe that Ψ must be a conformal map between Euclidean spaces, so that $\Psi^*e = \lambda e$ for some positive function λ .

If the underlying conductivity distribution is assumed to be anisotropic, there is no reason why Ψ must be conformal to preserve the isotropic structure. As with the anisotropic inverse conductivity problem, little is known about what information can be obtained with an incorrectly known external shape and anisotropic conductivity. For the rest of this section we will assume that the conductivity distribution *a-priori* is isotropic.

Conformal maps

Let $\Omega, \tilde{\Omega} \subset \mathbb{R}^n$. For $\Psi : \Omega \rightarrow \tilde{\Omega}$ to be a conformal map between Euclidean spaces, we require $\Psi^*e = \lambda e$ or as matrices in Cartesian coordinates

$$D\Psi^T D\Psi = \lambda I,$$

where $D\Psi$ is the Jacobian matrix of $\Psi = (\Psi_x, \Psi_y)$. Taking the determinant of both sides we find that the conformal factor, λ , must satisfy $\lambda = \det(D\Psi)^{2/n}$. The structure of the vector space of conformal maps is dependent on the dimension. In particular for the case $n = 2$, this condition is satisfied if and only if the two components of Ψ satisfy the Cauchy-Riemann equations

$$\frac{\partial \Psi_x}{\partial x} - \frac{\partial \Psi_y}{\partial y} = 0, \quad \frac{\partial \Psi_x}{\partial y} + \frac{\partial \Psi_y}{\partial x} = 0.$$

These are satisfied for any complex analytic function, Ψ , and hence the vector space of such functions is infinite dimensional. Figure 4.2 illustrates a conformal, Ψ^C , and non-conformal, Ψ^{NC} , map from the unit circle,

$$\Psi^C : (x, y) \mapsto \left(x + \frac{\epsilon}{2}(x^2 - y^2 - 1), y + \epsilon xy\right), \quad \Psi^{NC} : (x, y) \mapsto \left(x, \left(1 - \frac{\epsilon}{2}\right)y\right), \quad (4.2)$$

parameterised by $\epsilon \in \mathbb{R}$. The boundary voltage data using an adjacent-adjacent drive-measurement strategy with point electrodes after a conformal distortion is the

same as without a distortion but the non-conformally mapped domain has noticeably different boundary data. This highlights how conformal changes in the shape can not be detected with EIT. In [118] it is further demonstrated experimentally that only the non-conformal component of the shape deformation can be recovered from the electrical data in 2D.

For the case $n \geq 3$, the space of conformal maps is a finite dimensional Lie group of dimension $(n+1)(n+2)/2$ [30]. Specifically, up to similarity transformations (translations, dilations and rotations), conformal maps are the identity map or a *Kelvin* transformation. This is known as Liouville's theorem [119] (see [120] for a proof):

Theorem 4.2.1 (Liouville). *Let $\Omega, \tilde{\Omega} \subset \mathbb{R}^n$ with $n \geq 3$. An orientation preserving diffeomorphism $\Psi : (\Omega, e) \rightarrow (\tilde{\Omega}, e)$ is conformal if and only if*

$$\Psi(x) = \alpha Ah(x - x_0) + b$$

where $\alpha \in \mathbb{R}$, $x_0 \in \mathbb{R}^n \setminus \Omega$, $b \in \mathbb{R}^n$, A is an $n \times n$ orthogonal matrix and $h(x) = x$ or $h(x) = \frac{x}{|x|^2}$, a *Kelvin* transformation.

Lionheart [30] uses this result to demonstrate that in 3D the conformal maps can be fixed (up to similarity) by explicitly measuring three non co-linear coordinates on the boundary. These measurements fix the vector $x_0 \in \mathbb{R}^3$ above corresponding to Kelvin transformations and implies that the shape and an isotropic conductivity can be recovered from the electrical data up to similarity. The dilation can be fixed with some additional *a-priori* information of the conductivity and/or contact impedances, and we can never expect to determine, nor are interested in, the exact orientation or position of the subject from electrical data.

In three dimensional respiratory EIT, when a generic thorax cross section is used for the computational domain, it is highly unlikely that this can be mapped to the exact domain by a conformal map. It is apparent that a good approximation to the exact shape should be used initially if available, as well as accounting for any discrepancy explicitly in a reconstruction algorithm if required.

4.2.2 Conformal flatness

In this section we will describe in detail a constructive uniqueness result for the external shape in 3D. We note different reconstruction algorithms in 2D have been proposed

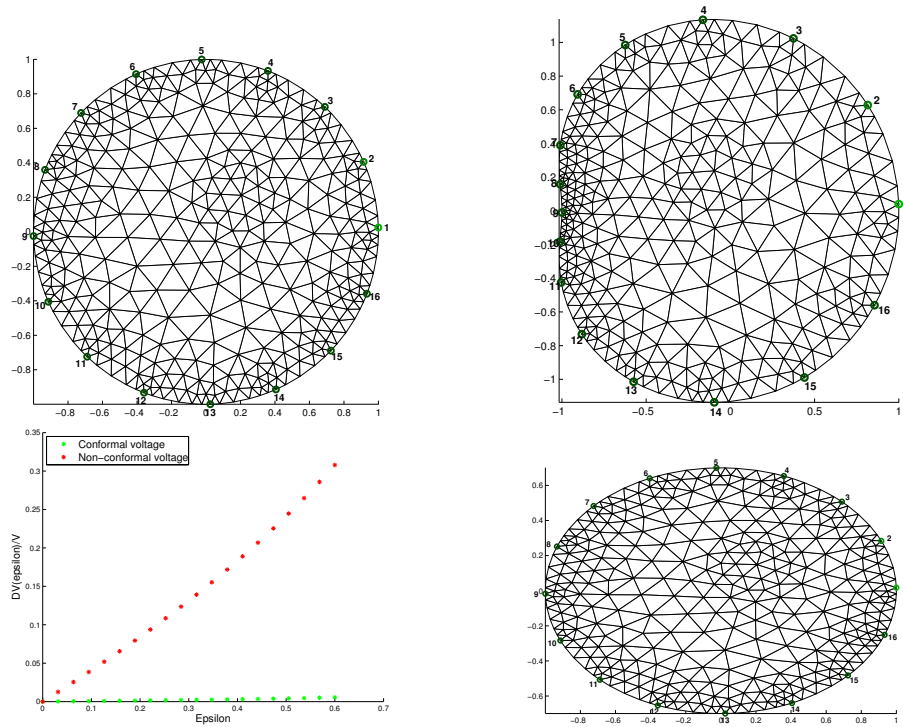


Figure 4.2: The top left figure illustrates a unit disc with unit conductivity and the top right and bottom right illustrates a conformal and non-conformal distortion as a function of ϵ given by (4.2). The 2-norm voltage error is plotted in the bottom left figure as a function of ϵ . The error diverges for a non-conformal change as ϵ increases, but is approximately zero for conformal changes. This highlights that conformal distortions can not be detected from electrical boundary measurements.

by Kolehmainen *et al.* using minimally anisotropic conductivities and Teichmüller mappings (see [121, 122, 123, 124].)

In [57] a reconstruction algorithm was proposed to reconstruct the shape and an isotropic conductivity in three or more dimensions from the observation that a deformed conductivity is conformally flat. The Robin boundary value problem (2.15) is considered, where the data for the inverse problem consists of the Robin-to-Neumann (RtN) map, $R_\eta : H^{-\frac{1}{2}}(\partial\Omega) \rightarrow H^{-\frac{1}{2}}(\partial\Omega)$, $h \mapsto \sigma \frac{\partial u}{\partial \nu} |_{\partial\Omega}$, defined weakly through

$$R(h, h) := \int_{\partial\Omega} (R_\eta h) h := \int_{\partial\Omega} \sigma \frac{\partial u}{\partial \nu} (u + z\sigma \frac{\partial u}{\partial \nu}) = \int_{\Omega} \sigma \nabla u \cdot \nabla u + \int_{\partial\Omega} z |\sigma \frac{\partial u}{\partial \nu}|^2, \quad (4.3)$$

where $R : H^{-\frac{1}{2}}(\partial\Omega) \times H^{-\frac{1}{2}}(\partial\Omega) \rightarrow \mathbb{R}$ is the bilinear form associated with R_η .

Deformation by a diffeomorphism

An incorrect model domain $\tilde{\Omega}$ can be viewed as a deformation of the true domain Ω , through a diffeomorphism $\Psi : \Omega \rightarrow \tilde{\Omega}$, with inverse $\Psi^{-1} : \tilde{\Omega} \rightarrow \Omega$. We denote $\psi = \Psi|_{\partial\Omega}$ as the restriction of Ψ to the boundary. When u solves $\nabla \cdot (\sigma \nabla u) = 0$ in Ω ,

then $\tilde{u}(\tilde{x}) = u(\Psi^{-1}(\tilde{x}))$ and $\tilde{h}(\tilde{x}) = h(\psi^{-1}(\tilde{x}))$ satisfy the conductivity equation

$$\nabla \cdot (\tilde{\sigma} \nabla \tilde{u}) = 0 \quad \text{in } \tilde{\Omega} \quad (\tilde{z} \tilde{\nu} \cdot \tilde{\sigma} \nabla \tilde{u} + \tilde{u})|_{\partial \tilde{\Omega}} = \tilde{h}$$

where $\tilde{\nu}$ is the unit normal vector of $\partial \tilde{\Omega}$, \tilde{z} is the deformed contact impedance and $\tilde{\sigma}$ is the pushforward conductivity

$$\tilde{\sigma}(\tilde{x}) = \frac{(D\Psi(x))\sigma(x)(D\Psi(x))^T}{|\det D\Psi(x)|} \Big|_{x=\Psi^{-1}(\tilde{x})}$$

where $D\Psi$ is the Jacobian of the map Ψ . As described in the previous section an isotropic conductivity can be pushed-forward to an anisotropic conductivity if Ψ is not conformal. The current flux, J , across the boundary is considered as an invariant $(n-1)$ -form, $J = \nu \cdot \sigma \nabla u dS_E \in \Omega^{n-1}(\partial \Omega)$ where dS_E is the Euclidean volume form of the boundary, or $J = i^*(\star du)$. The contact impedance is interpreted as a density

$$\tilde{z}(\tilde{x}) = (\det D\psi(x))z(x), \tag{4.4}$$

so that $z\nu \cdot \nabla u$ transforms invariantly under Ψ . This rule in turn implies that if $\psi : \partial \Omega \rightarrow \partial \tilde{\Omega}$, the map $\tilde{R} = \psi_* R$, defined by $\psi_* R(h)(\tilde{x}) = R(h \circ \psi)(x)|_{x=\psi^{-1}(\tilde{x})}$, satisfies $R[h, h'] = \tilde{R}[h \circ \psi^{-1}, h' \circ \psi^{-1}]$ and the measurements are invariant (see section 3.4.2). We have the following theorem due to Kolehmainen *et al.* [57].

Theorem 4.2.2. *Let $\Omega \subset \mathbb{R}^3$ be a bounded, convex C^∞ domain, and assume an isotropic and smooth conductivity σ . Let $\tilde{\Omega}$ be a model of the domain and $\psi : \partial \Omega \rightarrow \partial \tilde{\Omega}$ be an orientation preserving diffeomorphism. Assuming complete knowledge of $\partial \tilde{\Omega}$, the contact impedance $z \circ \psi^{-1}$ and the map $\tilde{R} = \psi_* R$, then Ω can be determined up to a rigid transformation T and the conductivity $\sigma \circ T^{-1}$ on the reconstructed domain $T(\Omega)$.*

We briefly outline this result to understand why we have uniqueness up to a rigid transformation. Firstly the RtN map determines the DtN map since from equation (4.3), $Rz\Lambda_\sigma + R = \Lambda_\sigma$ and so $\Lambda_\sigma = (R^{-1} - z)^{-1}$ and $R = (z + \Lambda_\sigma^{-1})^{-1}$. Given two PSDOs A and B with principal symbols of order a and b respectively then the composition AB is a PSDO of order $a + b$ [87]. Λ_σ is a PSDO of order 1 (see section 3.3.1) and so Λ_σ^{-1} is a PSDO of order -1 . Using a formal Neumann series we also have

$$R = z^{-1} \sum_{m=0}^{\infty} (-z^{-1} \Lambda_\sigma^{-1})^m,$$

and thus R is a PSDO of order 0 with principal symbol $1/z$. Now $\tilde{R} = R_{\tilde{z}, \tilde{\sigma}}$, where $\tilde{z}(x) = \det(D\psi)z(\psi^{-1}(x))$ and $\tilde{\sigma}$ is the pushforward conductivity and so \tilde{R} determines \tilde{z} , and thus also $\det(D\psi)$. Λ_σ can be determined from $R_{\sigma, z}$, and thus from (3.11), $R_{\tilde{\sigma}, \tilde{z}}$ determines the Taylor series of \tilde{g}_{jk} in boundary normal coordinates [86]. Kolehmainen *et al.* use the recovered $\tilde{g}_{jk}|_{\partial\tilde{\Omega}}$ and $\det(D\Psi|_{\partial\Omega})$ to prove that the metric tensor on $\partial\tilde{\Omega}$ corresponding to the Euclidean metric of $\partial\Omega$ can be determined. The authors further use a classical result from the geometry of surfaces which states that intrinsically isometric C^2 smooth surfaces that are boundaries of a *strictly convex* body are congruent in a rigid motion, and so the boundary data uniquely determines the map $T \circ \psi^{-1}$ where T is a rigid motion. Hence we can find the surface $T(\partial\Omega)$ and on it the map $T_*\Lambda_{\tilde{\sigma}} = T_*\Lambda_\sigma$. Hence from the uniqueness of the isotropic inverse conductivity problem then we can determine $\sigma \circ T^{-1}$.

Construction of the surface $T(\partial\Omega)$ from the recovered metric $\tilde{g}_{jk}|_{\partial\tilde{\Omega}}$ is a difficult task numerically. However we have already observed that an isotropic conductivity pushed-forward by a diffeomorphism is conformally flat. Let $\eta = (\Psi_m)_*\sigma$ be a possibly anisotropic conductivity in $\tilde{\Omega}$ such that σ is isotropic. As observed in section 3.4, this determines a Riemannian metric $g^{jk} = \det(\eta)^{-1}\eta^{jk}$, and in some coordinates the metric g is a scalar function times the Euclidean metric, that is g is conformally flat i.e. $g_{ij}(x) = e^{-2\alpha(x)}\bar{g}_{ij}(x)$, where $\bar{g}_{ij}(x)$ is a metric with zero curvature tensor and $\alpha : \Omega \rightarrow \mathbb{R}$. The necessary and sufficient integrability conditions for g to be conformally flat are that the Cotton-York tensor (A.30) vanishes. A penalty term on the Cotton-York tensor can be included in the reconstruction algorithm.

Conformal map to rigid transformation

We note that this result means that the shape of a convex body can be recovered up to a rigid transformation for the RtN map as opposed to a more general conformal transformation for the DtN map. The transformation rule for the contact impedance, and hence the recovery of $\det(D\psi)$, has pinned down the surface area change at every point on the boundary which fixes the scaling and Kelvin transformation. Intuitively since the surface metric can be recovered this determines the curvature of the surface and because the surface is assumed convex, and has for example no saddle points, there is no ambiguity in the embedding of the surface in \mathbb{R}^3 up to a rigid transformation.

4.3 Reconstruction algorithms

In the previous section it was demonstrated that the shape and an isotropic conductivity can be determined from electrical data, but the conformal flatness approach has some computational difficulties. Firstly to determine the deformed contact impedance we need to calculate the principal symbol of the RtN map using highly oscillatory boundary data, which is impractical with a realistic number ($16 - 128$) of electrodes. Secondly the more poignant issue is the use of a minimisation term on the Cotton-York tensor as part of a reconstruction algorithm. The tensor requires the computation of the derivative of the Ricci tensor, which itself involves second derivatives of the metric tensor. If the conductivity is assumed to be at least three times continuously differentiable, then this in principle is possible, but this imposes quite a large smoothness assumption on the conductivity. Piecewise constant conductivities, which are often used in practice in finite element methods are not even continuous, let alone differentiable. It may be possible to define these derivatives in a weak sense but we will leave this uniqueness result as simply a theoretical note — in principle, the full data are sufficient to estimate the shape and isotropic conductivity uniquely up to a rigid motion. It is of interest from a theoretical perspective to determine if this result can be generalised to non-convex shapes, because a typical human body will not satisfy the convexity condition.

A number of alternative reconstruction algorithms to estimate the shape and conductivity from knowledge of the NtD map have recently been proposed in the literature. A Bayesian approximation error approach [36] has been proposed to reconstruct the conductivity and a low rank estimate of the shape. This approach treats all sources of modelling error such as the FE discretisation and the boundary shape, but not the unknown conductivity, as ‘nuisance’ parameters. The modelling error covariance is estimated from an ensemble of 150 CT images of thorax shapes and this covariance is then incorporated into a standard regularised Gauss-Newton method to reconstruct the conductivity.

Other reconstruction algorithms include calculating the derivative of the data with respect to shape, in effect to determine the embedding of $\partial\Omega$ in \mathbb{R}^n . In GREIT [23] a

Jacobian with respect to electrode movement is calculated and used as part of a regularised Least-Squares algorithm to explicitly account for patient's breathing movement. The perturbation Jacobian used in GREIT stems from the work in [125, 126]. The shape correction work has been extended in [33] [118] where it is demonstrated that the electrode positions can be reconstructed up to a conformal deformation of the domain.

In the following two sections we firstly perform a novel calculation of the Fréchet derivative with respect to boundary shape for the continuum model. Secondly we outline the calculation of the Fréchet derivative for the CEM with respect to boundary shape as demonstrated by Dardé *et al.* [56, 127].

4.3.1 Fréchet differentiability: Continuum model

In this section we perform a novel calculation of the Fréchet derivative of the NtD map with respect to the boundary shape and electrode position. We consider the NtD map as depending on a vector field mapping the boundary of the domain to \mathbb{R}^3 . Let $\Psi[h](x) = x + h(x)$, for $x \in \partial\Omega$, and $\partial\Omega_h$ represent the perturbed boundary

$$\partial\Omega_h = \Psi[h](\partial\Omega) = \{y \in \mathbb{R}^n | y = \Psi[h](x) \text{ for some } x \in \partial\Omega\}.$$

We assume that $\partial\Omega$ and $\partial\Omega_h$ are both smooth, and define an origin-centred ball of radius $d > 0$, in $C^1(\partial\Omega, \mathbb{R}^n)$, denoted B_d . We firstly extend the domain of definition of Ψ to the whole of Ω , so that $\Psi : \Omega \rightarrow \Omega_h$, and at the end of the calculation we show that this can be converted back to a vector field h mapping $\partial\Omega$ to $\partial\Omega_h$.

We consider the NtD map as a linear operator $N_h \in L(H^{-\frac{1}{2}}(\partial\Omega_h), H^{\frac{1}{2}}(\partial\Omega_h))$, with the associated quadratic form

$$\int_{\Omega_h} \sigma \nabla u_h \cdot \nabla v_h =: \int_{\partial\Omega_h} f_h N_h g_h =: Q_h(f, g), \quad (4.5)$$

which includes the functional dependence of the perturbation field h , f_h and g_h are deformed current densities defined below and u_h is the solution of the conductivity equation when Ω is replaced by Ω_h . The domain of the conductivity is extended to be defined over the whole of \mathbb{R}^n , so that $\sigma : \mathbb{R}^n \rightarrow \mathbb{R}^+$. In effect this assumption implies that σ is known within a neighbourhood of the boundary. We consider the map $\psi : h \rightarrow Q_h$ and we wish to determine the formal derivative of this at the origin

i.e. at $\partial\Omega$ in the direction h . We denote two applied current densities $f = \sigma \nabla u \cdot \nu|_{\partial\Omega}$ and $g = \sigma \nabla v \cdot \nu|_{\partial\Omega}$. We have the usual weak formulation for the continuum model: Given $f \in H^{-\frac{1}{2}}(\partial\Omega)$, find $u \in H^1(\Omega)$ such that

$$a(u, v) = f(v) = \int_{\partial\Omega} f(Ng) \quad \forall v \in H^1(\Omega),$$

where $a(u, v)$ and $f(v)$ are defined in (2.11).

We now need to define the current density in the perturbed domain. The obvious candidate would be, $f_h = f \circ \Psi|_{\partial\Omega}^{-1}$, which preserves the *current density* at a point in the undeformed region to the same point mapped to the deformed boundary. However, in the case that the electrodes are elastic and can deform, this density would not necessarily preserve the consistency condition (2.2) that the integral of the current density is zero across the deformed boundary. Instead we consider the current density, $f_h = f \circ \Psi|_{\partial\Omega}^{-1} / \det(J^S\Psi)$, where $J^S\Psi$ is the surface Jacobian defined below. This preserves the *total current* over a given region in the undeformed region to the same region mapped to the deformed boundary, and automatically satisfies the consistency condition (2.2). The surface Jacobian effectively measures the area change of a given undeformed region to the deformed region, and so in the event that the electrode shapes are rigid these two densities would be the same.

We consider two applied current densities $f_h = f \circ \Psi|_{\partial\Omega}^{-1} / \det(J^S\Psi)$ and $g_h = g \circ \Psi|_{\partial\Omega}^{-1} / \det(J^S\Psi)$. We have the weak formulation for the perturbed problem: Given $f_h \in H^{-\frac{1}{2}}(\partial\Omega_h)$, find $u_h \in H^1(\Omega_h)$ such that

$$a_h(u_h, v_h) = f_h(v_h) = \int_{\partial\Omega_h} f_h(N_h g_h) \quad \forall v_h \in H^1(\Omega_h)$$

where

$$a_h(u, v) = \int_{\Omega_h} \sigma \nabla u \cdot \nabla v, \quad f_h(v) = \int_{\partial\Omega_h} f_h v.$$

Since this is true for all $v \in H^1(\Omega_h)$, then through a change of variables we can write the integral as

$$\begin{aligned} a_h(u_h, v \circ \Psi^{-1}) &= \int_{\Omega} |J_{\Psi}| J_{\Psi}^{-1} (\sigma \circ \Psi) (J_{\Psi}^{-1})^T \nabla (\Psi^* u_h) \cdot \nabla v \\ &= \int_{\partial\Omega} (\Psi^* f_h) v |J^S\Psi| = \int_{\partial\Omega} f v = a(u, v), \end{aligned}$$

where $\Psi^* u = u \circ \Psi$, J_{Ψ} is the Jacobian of Ψ and $|J^S\Psi|$ is the determinant of the Jacobian of the restriction $\psi := \Psi|_{\partial\Omega}$. This equation states that the total power

dissipation of the two boundary value problems is the same. We also deduce

$$a_h(u_h, v_h) = a(\Psi^* u_h, v).$$

Through a change of variables we also have

$$a_h(u_h, v \circ \Psi^{-1}) = a_{(\Psi^{-1})_* \sigma}(\Psi^* u_h, v).$$

To calculate the Fréchet derivative at the origin in the direction h we estimate $(Q_h - Q_0)(f, g)$, and thus

$$\begin{aligned} (Q_h - Q)(f, g) &= a_h(u_h, v_h) - a(u, v) = a(\Psi^* u_h, v) - a_{(\Psi^{-1})_* \sigma}(\Psi^* u_h, v) \\ &= \int_{\Omega} (\sigma - |J_{\Psi}| J_{\Psi}^{-1} (\sigma \circ \Psi) (J_{\Psi}^{-1})^T) \nabla(\Psi^* u_h) \cdot \nabla v. \end{aligned}$$

The vector field h on $\partial\Omega$ can be split into normal and tangential components, $h_{\nu} = (h|_{\partial\Omega} \cdot \nu)$ and $h_t = h|_{\partial\Omega} - h_{\nu} \nu$. To calculate the formal derivative to this problem, we linearise the three terms J_{Ψ}^{-1} , $|J_{\Psi}|$ and $\sigma \circ \Psi$ on the right hand side to first order in $\|h\|_{C^1}$. Firstly, for the Jacobian matrix J_{Ψ} we have

$$(J_{\Psi})_{ij} = \frac{\partial \Psi(x)_i}{\partial x_j} = \delta_{ij} + \frac{\partial h_i}{\partial x_j},$$

and so $J_{\Psi} = I + J_h$, where $(J_h)_{ij} := \frac{\partial h(x)_i}{\partial x_j}$, and thus

$$J_{\Psi}^{-1} = I - J_h + O(\|h\|_{C^1}^2). \quad (4.6)$$

Secondly, for the composition term $\Psi^* \sigma$

$$(\Psi^* \sigma)(x) = (\sigma \circ \Psi)(x) = \sigma(x + h(x)) = \sigma(x) + h \cdot \nabla \sigma(x) + O(\|h\|_{C^1}^2) \quad (4.7)$$

Thirdly, for the determinant of the Jacobian $\det(J_{\Psi})$, the determinant of a matrix is the product of its eigenvalues, which implies $\det(I + A) = \prod_{i=1}^n (1 + a_i) = 1 + \sum_i a_i + O(a_i^2)$, where $\{a_i\}_{i=1}^n$ are the eigenvalues of A . Hence

$$\det(J_{\Psi}) = \det(I + J_h) = 1 + \text{tr}(J_h) + O(\|h\|_{C^1}^2) = 1 + \nabla \cdot h + O(\|h\|_{C^1}^2), \quad (4.8)$$

For the Fréchet derivative for the CEM we also require the linearisation of $|J_S \Psi|$ to first order in $\|h\|_{C^1}$ so also calculate this. Firstly we note that the boundary can be considered as a two dimensional Riemann surface, M^2 , embedded in \mathbb{R}^3 . We consider a point $x = (x^1, x^2, x^3)$ on the surface, and let $\Psi : U \subset \mathbb{R}^2 \rightarrow M^2, (u^1, u^2) \mapsto$

$(x^1, x^2, x^3) = \Psi(u^1, u^2)$, where $u \in U \subset \mathbb{R}^2$. The ambient metric in \mathbb{R}^3 is simply δ_{ij} , and thus $ds^2 = dx^i \otimes dx^i$. Pulling the metric back under Ψ , $\Psi^* ds^2$,

$$\Psi^* ds^2 = \sum_{i=1}^3 \sum_{\alpha, \beta=1}^2 \frac{\partial x^i}{\partial u^\alpha} \frac{\partial x^i}{\partial u^\beta} du^\alpha du^\beta = \sum_{\alpha, \beta=1}^2 g_{\alpha\beta} du^\alpha \otimes du^\beta$$

The volume form for the surface, dS , is given by $\sqrt{\det g} du^1 \wedge du^2$. If we denote the vector $e_i = \frac{\partial x}{\partial u^i}$, and remembering $g_{\alpha\beta} = \langle \frac{\partial x}{\partial u^\alpha}, \frac{\partial x}{\partial u^\beta} \rangle$, then

$$\det g = (e_1 \cdot e_1)(e_2 \cdot e_2) - (e_1 \cdot e_2)^2 = |e_1|^2 |e_2|^2 \sin^2(\theta) = |e_1 \times e_2|^2.$$

Choose e_1 and e_2 so they are orthogonal and tangential to the surface, and denote the outer unit normal by $\nu = e_1 \times e_2$. We consider the perturbation $\Psi_h|_{\partial\Omega} : x \mapsto \tilde{x} = x + h_t + h_\nu \nu$, where we have resolved into tangential and normal components.

$$\det \tilde{g} = |\tilde{e}_1 \times \tilde{e}_2| = |e_1 \times e_2 + e_1 \times \frac{\partial h}{\partial u_2} + \frac{\partial h}{\partial u_1} \times e_2 + \frac{\partial h}{\partial u_1} \times \frac{\partial h}{\partial u_2}|^2 = |\nu + b|^2 = 1 + 2\nu \cdot b + b \cdot b.$$

where

$$b = e_1 \times \frac{\partial h}{\partial u_2} + \frac{\partial h}{\partial u_1} \times e_2 + \frac{\partial h}{\partial u_1} \times \frac{\partial h}{\partial u_2}.$$

Using the vector identity $(a \times b) \cdot (c \times d) = (a \cdot c)(b \cdot d) - (a \cdot d)(b \cdot c)$ (for arbitrary vectors $a, b, c, d \in \mathbb{R}^3$) yields

$$\nu \cdot b = \sum_{i=1}^2 e_i \cdot \frac{\partial h}{\partial u_i} = \text{Div}_g h = \text{Div}_g(h_t) + h_\nu \text{Div}_g(\nu),$$

where the second equality follows by definition of Div_g , the divergence with respect to the surface metric g , and the last equality by splitting the h field explicitly into normal and tangential components, $h = h_t + h_\nu \nu$. The first term on the right is the surface divergence of the vector field h_t . The last term is equal to $2Hh_\nu$, where $H := \text{Div}_g(\nu)$ is the mean surface curvature [128]. For a two-dimensional surface, this equals the addition of the maximum and minimum curvatures at a given point. Thus

$$\det \tilde{g}_{ij} = 1 + 2(\text{Div}_g(h_t) + 2Hh_\nu) + O(\|h\|_{C^1}^2).$$

If we consider a tangential vector field on $\partial\Omega$, this will give us the divergence of the tangential vector field, $\text{Div}h_t$, we thus have

$$|J^S \Psi| = \sqrt{\det \tilde{g}_{ij}} = 1 + \text{Div}h_t + 2Hh_\nu + O(\|h\|_{C^1}^2), \quad (4.9)$$

Using the three estimates for J_Ψ^{-1} , $\Psi^*\sigma$ and $\det(J_\Psi)$ in (4.6), (4.7) and (4.8) we have

$$a(\Psi^*u_h - u, v) = \int_{\Omega} (\sigma J_h^T + J_h\sigma - (h \cdot \nabla + \nabla \cdot h)\sigma) \nabla(\Psi^*u_h) \cdot \nabla v.$$

From the above equation, and ellipticity of $a(\cdot, \cdot)$ (2.12), we have two estimates for some constants A, B

$$A \|\Psi^*u_h - u\|_{H^1} \|v\|_{H^1} \leq |a(\Psi^*u_h - u, v)| \leq B \|h\|_{C^1} \|v\|_{H^1}.$$

Choosing $v = \Psi^*u_h - u$, implies continuity of $h \mapsto (\Psi^*u_h - u)$,

$$\|\Psi^*u_h - u\|_{H^1} \leq C \|h\|_{C^1}.$$

Consider the problem: Find $w \in H^1(\Omega)$ such that

$$a(w, v) = s_h(v) \quad \forall v \in H^1(\Omega),$$

where

$$s_h(v) = \int_{\Omega} (\sigma J_h^T + J_h\sigma - (h \cdot \nabla + \nabla \cdot h)\sigma) \nabla u \cdot \nabla v. \quad (4.10)$$

We have

$$a(\Psi^*u_h - u - w, v) = \int_{\Omega} (\sigma J_h^T + J_h\sigma - (h \cdot \nabla + \nabla \cdot h)\sigma) \nabla(\Psi^*u_h - u) \cdot \nabla v.$$

Let $v = \Psi^*u_h - u - w$, then the above equation, (2.12), and the continuity of $h \mapsto (\Psi^*u_h - u)$ implies

$$\|\Psi^*u_h - u - w\|_{H^1(\Omega)} \leq C \|h\|_{C^1}^2.$$

Denote u and v as solutions of the conductivity equation (2.1) with boundary currents $f_1 = \sigma \frac{\partial u}{\partial \nu}|_{\partial\Omega}$ and $f_2 = \sigma \frac{\partial v}{\partial \nu}|_{\partial\Omega}$ respectively, and we call these solutions the *forward* and *adjoint* field respectively. We thus have the solution w is the Fréchet derivative of $h \mapsto Q_h$ at the origin (i.e. $\partial\Omega$) in the direction h .

Geometric interpretation

The geometric interpretation of the linear functional (4.10) is that it is the Lie derivative of the conductivity tensor with respect to the vector field h ,

$$s_h(v) = \int_{\Omega} (\mathcal{L}_h\sigma) \nabla u \cdot \nabla v,$$

see equation (A.19). Assume the metric is preserved under the flow induced from the perturbation vector field h , that is $\mathcal{L}_h\sigma = \lambda\sigma$ for some positive function λ . The h that satisfy these are exactly the conformal Killing vector fields (see section 3.4.1) which are the linearised version of the conformal mappings discussed in section 4.2. Hence the linearised version of the non-uniqueness due to an inaccurately known boundary shape is that a change in N_σ can be attributed to either an isotropic conductivity change $\lambda\sigma$ or a conformal Killing vector field h .

Electrode and boundary movement - tangential and normal components

The expression for the linear functional s_h in (4.10) is defined over Ω , but can be simplified to an integral over $\partial\Omega$. In particular the integrand can be written in the form $\text{div}(a) + b$ for a given vector field a and scalar field b through the identity

$$\begin{aligned} ((\sigma J_h^T + J_h\sigma - (h \cdot \nabla + \nabla \cdot h)\sigma)\nabla u) \cdot \nabla v &= -(h \cdot \nabla v)\nabla \cdot (\sigma\nabla u) - (h \cdot \nabla u)\nabla \cdot (\sigma\nabla v) \\ &+ \nabla \cdot \left((h \cdot \nabla u)\sigma\nabla v + (h \cdot \nabla v)\sigma\nabla u - ((\sigma\nabla u) \cdot \nabla v)h \right). \end{aligned} \quad (4.11)$$

The key point is that if u and v solve the conductivity equation, the first two terms on the right are zero, and so the linear functional is really an integral of the form $\int_\Omega \text{div}(a)$, which can be simplified through the divergence theorem. We find that

$$s_h(v) = \int_{\partial\Omega} (h \cdot \nabla u)\sigma \frac{\partial v}{\partial \nu} + (h \cdot \nabla v)\sigma \frac{\partial u}{\partial \nu} - h_\nu((\sigma\nabla u) \cdot \nabla v). \quad (4.12)$$

The tangential components move the electrodes around a fixed boundary, whereas the normal components move the boundary, and we consider these separately. Given a vector field $a : \partial\Omega \rightarrow \mathbb{R}^3$, we denote the component normal to $\partial\Omega$ as $a_\nu = (a \cdot \nu)$ and the component tangential to $\partial\Omega$ as $a_t = a - a_\nu\nu$. We consider a perturbation vector field in the tangent bundle of $\partial\Omega$, that is $h \cdot \nu = 0$ i.e. $h = h_t$, which are exactly the vector fields that move the electrodes along the boundary with the external shape fixed. From (4.10) and the divergence theorem, we have that

$$\int_{\partial\Omega} (DN_0[h]f_1)f_2 = \int_{\partial\Omega} (h_t \cdot (\nabla v)_t)f_1 + (h_t \cdot (\nabla u)_t)f_2. \quad (4.13)$$

The derivative consists of two terms and it is instructive to explain their physical significance. The first term is the drop in power at the measurement electrodes from stimulating at the wrong location and is proportional to the product of the (tangential)

gradient of the measurement adjoint field, the tangential perturbation vector field and the forward field current density. The second term is the drop in power at the measurement electrodes from measuring at the wrong location and is proportional to the product of the (tangential) gradient of the excitation forward field, the tangential perturbation vector field and the adjoint field current density. The formula is useful as it predicts which drive and measurement strategies are best to determine the shape. For example if measurements are recorded near drive electrodes, we expect the gradient of the forward and adjoint fields to be large and hence measurements there will have a high sensitivity to boundary shape changes.

For boundary movement we only consider the normal component of h , $h = h_\nu \nu$, and we obtain

$$\int_{\partial\Omega} (DN_0[h]f_1)f_2 = \int_{\partial\Omega} (h_\nu \nu \cdot (\nabla u)_\nu) f_2 - h_\nu \sigma (\nabla u)_t \cdot (\nabla v)_t. \quad (4.14)$$

The first term is the drop in power at the measurement electrodes from measuring at the wrong location and is proportional to the product of the (normal) gradient of the excitation forward field, the normal perturbation vector field and the adjoint field current density. We note that in the limit of point measurements this term becomes unbounded because of the singularity in the normal derivative at the drive location, however this does predict that there should be very high sensitivity to normal changes when measurements are recorded at driven electrodes. The second term is the drop in power at the measurement electrodes from a normal perturbation of the boundary away from driven electrodes and is proportional to the product of the normal perturbation field and inner product of the (tangential) gradient of the excitation forward field multiplied by the (tangential) gradient of the measurement adjoint field. This takes the same form as the Fréchet derivative for conductivity changes (3.7), with $\delta\sigma$ replaced with $h_\nu \sigma$, and predicts that away from measurement electrodes the normal changes are of a similar difficulty to detect as interior conductivity changes. Hence the NtD map should be very insensitive to normal changes away from the electrodes.

We summarise the differentiability result of this section as a theorem.

Theorem 4.3.1 (Fréchet derivative of continuum model: Shape). *Let $h \in C^1(\partial\Omega, \mathbb{R}^n)$, then N_0 is Fréchet differentiable at the origin 0 (i.e. $\partial\Omega$) in the direction h , with the*

derivative $DN_0 : C^1(\partial\Omega, \mathbb{R}^n) \times H^{-\frac{1}{2}}(\partial\Omega) \rightarrow H^{\frac{1}{2}}(\partial\Omega)$ satisfying

$$\int_{\partial\Omega} f_2 DN_0[h] f_1 = \int_{\partial\Omega} (h_\nu \nu \cdot (\nabla u)_\nu) f_2 - h_\nu \sigma (\nabla u)_t \cdot (\nabla v)_t + (h_t \cdot (\nabla v)_t) f_1 + (h_t \cdot (\nabla u)_t) f_2,$$

where u and v are the solutions to Neumann problems $\sigma \frac{\partial u}{\partial \nu}|_{\partial\Omega} = f_1$ and $\sigma \frac{\partial v}{\partial \nu}|_{\partial\Omega} = f_2$ respectively.

4.3.2 Fréchet differentiability: CEM

We now outline the calculation of the Fréchet derivative for the CEM as calculated by Dardé *et al.* [56, 127]. We again consider the CEM including the functional dependence of the perturbation of the boundary, $R : B_d \times \mathbb{R}^L \rightarrow \mathbb{R}^L$, $(h, I) \rightarrow U[h]$. $(u[h], U[h])$ is the solution of the complete electrode model when Ω is replaced by Ω_h and the electrodes E_l to $\Psi(E_l) =: E_l[h]$. The weak formulation of the CEM is to find $(u, U) \in \dot{H}(\Omega)$ such that

$$B((u, U), (v, V)) = \sum_{l=1}^L I_l V_l \quad \text{for all } (v, V) \in \dot{H}(\Omega)$$

where $B((u, U), (v, V))$ is defined in (2.13). The weak formulation of the CEM in the perturbed domain is to find $(u[h], U[h]) \in \dot{H}(\Omega_h)$

$$B_h((u[h], U[h]), (w, W)) = \sum_{l=1}^L I_l W_l \quad \text{for all } (w, W) \in \dot{H}(\Omega_h)$$

where $B_h((u, U), (v, V))$ is defined in (2.13) with Ω and E_l replacted with Ω_h and $E_l[h]$ respectively. Let $(w, W) = (v \circ \Psi^{-1}, V)$, changing variables in the integral we have

$$\begin{aligned} B_h((u[h], U[h]), (v \circ \Psi^{-1}, V)) &= \int_{\Omega} J_{\Psi}^{-1}(\Psi^* \sigma) (J_{\Psi}^{-1})^T |J_{\Psi}| \nabla(\Psi^* u[h]) \cdot \nabla v \\ &\quad + \sum_{l=1}^L \frac{1}{z_l} \int_{E_l} (U_l[h] - \Psi^* u[h]) (V_l - v) |J^S \Psi| \end{aligned}$$

where $\Psi^* u[h] = u[h] \circ \Psi$, J_{Ψ} is the Jacobian of the mapping and $|J^S \Psi|$ is the determinant of the surface Jacobian restriction $\Psi|_{\partial\Omega} : \partial\Omega \rightarrow \partial\Omega_h$. $B((u, U), (v, V)) = B_h((u[h], U[h]), (v \circ \Psi^{-1}, V))$, and we deduce that the difference between the perturbed solution $(\Psi^* u[h], U[h])$ and the unperturbed solution (u, U) satisfies

$$\begin{aligned} B((\Psi^* u[h] - u, U[h] - U), (v, V)) &= \int_{\Omega} (\sigma - |J_{\Psi}| J_{\Psi}^{-1}(\Psi^* \sigma) (J_{\Psi}^{-1})^T) \nabla(\Psi^* u[h]) \cdot \nabla v \\ &\quad + \sum_{l=1}^L \frac{1}{z_l} \int_{E_l} (U_l[h] - \Psi^* u[h]) (V_l - v) (1 - |J^S \Psi|) \end{aligned}$$

To calculate the Fréchet derivative we linearise the terms on the right hand side of the above expression to first order in h , as we did for the continuum model using the expressions (4.6), (4.7), (4.8) and (4.9), which yields

$$B((\Psi^*u[h] - u, U[h] - U), (v, V)) = \int_{\Omega} (\sigma J_h^T + J_h \sigma - (h \cdot \nabla + \nabla \cdot h) \sigma) \nabla (\Psi^*u[h]) \cdot \nabla v \\ - \sum_{l=1}^L \frac{1}{z_l} \int_{E_l} (U_l[h] - \Psi^*u[h])(V_l - v) (\text{Div} h_t + 2Hh_\nu) + O(\|h\|_{C^1}^2).$$

We consider a sesquilinear functional by replacing $(\Psi^*u[h], U[h])$ by (u, U) in the above expression

$$s_h(v, V) = \int_{\Omega} (\sigma J_h^T + J_h \sigma - (h \cdot \nabla + \nabla \cdot h) \sigma) \nabla u \cdot \nabla v \\ - \sum_{l=1}^L \frac{1}{z_l} \int_{E_l} (U_l - u)(V_l - v) (\text{Div} h_t + 2Hh_\nu)$$

and consider the variational problem: Find $(w, W) \in \dot{H}(\Omega)$

$$B((w, W), (v, V)) = s_h(v, V) \quad \text{for all } (v, V) \in \dot{H}(\Omega).$$

In a similar manner to the continuum case it is shown in [127] that

$$\|(\Psi^*u[h] - u, U[h] - U) - (w[h], W)\| \leq C|I| \|h\|_{C^1}^2,$$

and so defines a formal Fréchet derivative for the problem for a vector field h whose domain is Ω . The above expression for the linear functional for the Fréchet derivative can be simplified to an integral over $\partial\Omega$ using the identity (4.11), yielding

$$s_h(v, V) = \int_{\partial\Omega} ((h \cdot \nabla u) \sigma \nabla v + (h \cdot \nabla v) \sigma \nabla u - ((\sigma \nabla u) \cdot \nabla v) h) \cdot \nu \\ - \sum_{l=1}^L \frac{1}{z_l} \int_{E_l} (U_l - u)(V_l - v) (\text{Div} h_t + 2Hh_\nu)$$

Electrode movement - tangential component

We now consider the tangential component of the boundary vector field, h , so that $h \cdot \nu = 0$, which are the fields that move the electrodes around the boundary. We have

$$s_h(v, V) = \int_{\partial\Omega} ((h \cdot \nabla u) \sigma \nabla v \cdot \nu + (h \cdot \nabla v) \sigma \nabla u \cdot \nu - \sum_{l=1}^L \frac{1}{z_l} \int_{E_l} (U_l - u)(V_l - v) (\text{Div} h_t))$$

Following Dardé *et al.* [56, 127] we subtract the directional derivative of the unperturbed solution, u , in the direction h from the formal Fréchet derivative, $\tilde{w}[h] = w[h] - h \cdot \nabla u$. Then $B((\tilde{w}, W), (v, V)) = B((w - h \cdot \nabla u, W), (v, V))$ is given by

$$\begin{aligned} B((\tilde{w}, W), (v, V)) &= \int_{\partial\Omega} ((h \cdot \nabla u)\sigma \nabla v \cdot \nu + (h \cdot \nabla v)\sigma \nabla u \cdot \nu \\ &\quad - \sum_{l=1}^L \frac{1}{z_l} \int_{E_l} (U_l - u)(V_l - v)(\text{Div} h_t) \\ &\quad - \int_{\Omega} \sigma \nabla (h \cdot \nabla u) \cdot \nabla v - \sum_{l=1}^L \frac{1}{z_l} \int_{E_l} (-h \cdot \nabla u)(V_l - v). \end{aligned}$$

Using the divergence theorem on the 3rd term, that $(\sigma \nabla u) \cdot \nu$ is identically 0 off the electrodes and the impedance boundary condition, we can simplify to

$$\begin{aligned} B((\tilde{w}, W), (v, V)) &= - \sum_{l=1}^L \int_{E_l} \frac{1}{z_l} (U_l - u)(h \cdot \nabla (V_l - v))_t \\ &\quad - \sum_{l=1}^L \frac{1}{z_l} \int_{E_l} (U_l - u)(V_l - v)(\text{Div} h_t) \\ &\quad - \sum_{l=1}^L \frac{1}{z_l} \int_{E_l} h \cdot \nabla (U_l - u)_t (V_l - v). \end{aligned}$$

Collecting the right hand side terms into a surface divergence, Div_g , and using the divergence theorem on each electrode, we arrive at

$$B((\tilde{w}, W), (v, V)) = - \sum_{l=1}^L \frac{1}{z_l} \int_{\partial E_l} (h \cdot \nu|_{\partial E}) (U_l - u)(V_l - v)$$

Boundary movement - normal component

The boundary movement is composed of normal perturbations of the boundary i.e. with vanishing tangential components. The procedure is similar to the tangential perturbations if we let $h = h_n n$ denote a normal vector field, then

$$\begin{aligned} B((w, W), (v, V)) &= \int_{\partial\Omega} ((h \cdot \nabla u)\sigma \nabla v \cdot \nu + (h \cdot \nabla v)\sigma \nabla u \cdot \nu - ((\sigma \nabla u) \cdot \nabla v)h \cdot \nu \\ &\quad - \sum_{l=1}^L \frac{1}{z_l} \int_{E_l} (U_l - u)(V_l - v)(2Hh). \end{aligned}$$

As with the tangential case, we proceed again by subtracting the directional derivative of u in the direction of h from the formal Fréchet derivative, $B((\tilde{w}, W), (v, V)) =$

$B((w - h \cdot \nabla u, W), (v, V))$, resulting in

$$\begin{aligned} B((\tilde{w}, W), (v, V)) &= \int_{\partial\Omega} ((h \cdot \nabla u) \sigma \nabla v \cdot \nu + (h \cdot \nabla v) \sigma \nabla u \cdot \nu - (\sigma \nabla u \cdot \nabla v) h \cdot \nu) \\ &\quad - \sum_{l=1}^L \frac{1}{z_l} \int_{E_l} (U_l - u)(V_l - v)(2Hh) \\ &\quad - \int_{\Omega} \sigma \nabla (h \cdot \nabla u) \cdot \nabla v - \sum_{l=1}^L \frac{1}{z_l} \int_{E_l} (-h \cdot \nabla u)(V_l - v). \end{aligned}$$

We thus have

$$\begin{aligned} B((\tilde{w}, W), (v, V)) &= \int_{\partial\Omega} h \cdot (\sigma \nabla u \frac{\partial v}{\partial \nu} - \sigma \nabla u \cdot \nabla v \nu) - \sum_{l=1}^L \frac{1}{z_l} \int_{E_l} (U_l - u)(V_l - v)(2Hh) \\ &\quad - \sum_{l=1}^L \frac{1}{z_l} \int_{E_l} (-h \cdot \nabla u)(V_l - v). \end{aligned}$$

By considering normal and tangential components of ∇u and ∇v we then have

$$\begin{aligned} B((\tilde{w}, W), (v, V)) &= - \int_{\partial\Omega} h_\nu (\sigma \nabla u)_t \cdot (\nabla v)_t \\ &\quad - \sum_{l=1}^L \frac{1}{z_l} \int_{E_l} h_\nu (V_l - v)(2H(U_l - u) - \nu \cdot \nabla u) \end{aligned}$$

Electrode and boundary movement

We summarise the differentiability result of Dardé *et al.* [56, 127] outlined in this section as a theorem.

Theorem 4.3.2 (Fréchet derivative of complete electrode model: Shape). *Let $h \in C^1(\partial\Omega, \mathbb{R}^n)$, then the transfer impedance matrix $R_0 \in \mathbb{R}^{L \times L}$ is Fréchet differentiable at the origin 0 (i.e. $\partial\Omega$) in the direction h , with the derivative $W \in \mathbb{R}^{L \times L}$ satisfying*

$$\begin{aligned} \sum_{m=1}^M (W[h]I)_m \tilde{I}_m &= - \sum_{l=1}^L \frac{1}{z_l} \int_{\partial E_l} (h \cdot \nu_{\partial E}) (U_l - u)(V_l - v) - \int_{\partial\Omega} h_\nu (\sigma \nabla u)_t \cdot (\nabla v)_t \\ &\quad - \sum_{l=1}^L \frac{1}{z_l} \int_{E_l} h_\nu ((U_l - u)2H - \nu \cdot \nabla u)(V_l - v). \end{aligned} \quad (4.15)$$

where (u, U) and (v, V) are the solutions to problems with currents I and \tilde{I} respectively.

The physical interpretation of the Fréchet derivative (4.15) is similar to the continuum case, although now we have additional terms if the electrodes are non rigid and can distort in shape.

Physical interpretation of formula

From the sampling form (4.15), we see the electrode movement term is incorporated via the tangential components of the distortion, and the boundary shape via the normal components of the distortion. We see that there are three contributing terms which we can briefly explain. The first term describe what happens when we consider distorting an electrode. If we increase the electrode size through a tangential vector field whose domain is the boundary of the electrode, then the electrode increases in size and there is a larger drop in potential over the deformed electrode. The second term is the sensitivity we would expect if we were performing EIT only on the surface $\partial\Omega$ with no interior changes, that is if we had a change in conductivity $h = h_\nu\sigma\delta_{\partial\Omega}$ in (3.8). Hence this again predicts that there will be a low sensitivity of the change in voltages to normal shape boundary changes away from electrodes, because of the ill-posed nature of the inverse conductivity problem. The last integral consists of two different terms. The term with normal derivative of u is where we have a drop in potential from the extra piece of conductive material added at the electrode. The term with the mean curvature, H , does not appear in the continuum model Fréchet derivative but appears here because of the impedance boundary condition. If the surface has positive curvature with respect to the outward pointing normal, and we distort in this direction, the electrode increases in size and so there is a larger drop in potential over the electrode. The opposite effect occurs if the surface is negatively curved. If the surface has a saddle point then $H = 0$, the electrode does not change size and this term is identically zero.

4.3.3 Shape derivative calculation

In this section we will describe a novel non-linear reconstruction algorithm to perform simultaneous reconstruction of the electrode positions and conductivity in 3D. We consider a subset of the shape determination problem, where the external boundary shape is fixed but the electrodes are inaccurately known. Circular electrodes of fixed diameter are used which ensures that boundary surface area change, $\det(D\psi)$, is constant which fixes the scaling and Kelvin transformation. The shape derivative is only computed at the electrode locations, and not for other nodes on the boundary, and so

the translational null space is fixed. We illustrate the algorithm with results obtained with simulated data from spherical and cylindrical geometries. The next chapter will in part be devoted to shape correction results from real biomedical EIT data obtained from a healthy subject as part of a pilot study at the University of Manchester.

In section 4.3.1 we outlined the calculation of the Fréchet derivative of the measurement map with respect to external boundary shape for the continuum model. With the external boundary shape and shapes of electrodes fixed, then only two tangential vector fields forming a basis for the tangent space of an electrode are required for the shape derivative. Given a tangential perturbation of the electrode position of the form (4.17), the Fréchet derivative for the CEM (4.15) can be computed by differentiating with respect to α . In 3D this would require the computation of a line integral along the boundary of the electrode and for normal shape changes this would also require the computation of the mean surface curvature H . The Fréchet derivative with respect to conductivity changes and the discretisation commute with one another as presented in section 3.2.2. It is not clear that this is true for the Fréchet derivative with respect to boundary shape with straight sided finite elements, because there is no consistent notion of curvature for piecewise linear boundary triangles. Instead of discretising the formal Fréchet derivative we differentiate the discretisation with respect to electrode position using a finite difference approximation of the Jacobian $J_m : \mathbb{R}^{3L} \rightarrow \mathbb{R}^N$

$$(J_m)_{i,3(j-1)+k} = \lim_{\epsilon \rightarrow 0} \frac{V_i(x_j + \epsilon e_k) - V_i(x_j)}{\epsilon} \quad j = 1, \dots, L, \quad k = 1, 2, 3 \quad (4.16)$$

using EIDORS¹. The index i corresponds to the i^{th} voltage measurement over all simulations, x_j is the j^{th} Cartesian coordinate of the centre-of-mass of the electrode and e_k is the k^{th} Cartesian unit vector field. The perturbation size was chosen as $\epsilon = 10^{-6}$ sufficiently small so that the linear approximation is valid but large enough to avoid floating point arithmetic errors [125, 129]. This can be considered as the first partial derivative of the forward problem with respect to each coordinate of each electrode. To calculate this derivative we require some modelling assumptions on the behaviour of electrode movement. Firstly, the shape of the electrode can conceivably deform as it moves along the boundary if flexible ‘elastic’ electrodes were used. We use an identical perturbation for each node of a given electrode and so we are assuming the

¹The library function `jacobian_movement_perturb.m`

electrodes move along the boundary rigidly without changing shape. Secondly, to calculate the normal component of electrode movement in the finite difference approximation, a small piece of conductive material has to be added under each electrode. We assume the conductivity is constant in a neighbourhood of the electrode, and so the conductivity of the small additional piece is the same as under the unperturbed electrode.

The finite difference approximation to the Jacobian is further projected into normal and tangential components of the electrodes. It is assumed that each electrode is approximately flat, and we compute the unique outward pointing normal n , and two tangent vectors, $\{t^{(j)}\}_{j=1}^2$, chosen to form an orthogonal basis for the tangent space of the electrode. With an abuse of notation we denote the normal as $\nu_i = t_i^{(3)}$. The position of the m^{th} electrode on $\partial\Omega$ parameterised by a vector $\theta^m \in \mathbb{R}^2$ through

$$v_m(\theta) = v_m(0) + \sum_{i=1}^2 \theta_i^m t_i^m. \quad (4.17)$$

We aim to iteratively update the electrode positions during the algorithm from an initial guess of each electrode $v_m(0)$ by estimating $\theta := (\theta_1^1, \theta_2^1, \theta_1^2, \dots, \theta_2^L) \in \mathbb{R}^{2L}$.

The tangential movement Jacobian is calculated by projecting this onto each pre-computed tangential vector field on each electrode, to generate a tangential movement Jacobian $J_m^t : \mathbb{R}^{2L} \rightarrow \mathbb{R}^m$. Likewise the normal movement Jacobian can be calculated by projecting this onto each pre-computed normal vector fields on each electrode generating a normal movement Jacobian $J_m^\nu : \mathbb{R}^L \rightarrow \mathbb{R}^m$. This calculation can be repeated for b other boundary nodes that do not belong to an electrode, to generate a Jacobian $J_m^b : \mathbb{R}^b \rightarrow \mathbb{R}^m$. We then define three boundary shape Jacobians as

$$J_m^t, \quad J_m^{t,\nu} = [J_m^t, J_m^\nu], \quad J_m^{t,\nu,b} = [J_m^t, J_m^\nu, J_m^b].$$

4.3.4 Simultaneous retrieval procedure

A dual modelling approach is used requiring a coarse and fine discretisation of the domain denoted $\sigma_f \in \mathbb{R}^{N_E^f}$ and $\sigma_c \in \mathbb{R}^{N_E^c}$ respectively with $N_E^c \ll N_E^f$. We will discuss the dual modelling approach shortly. The vector of all the electrode centre-of-mass positions is denoted $v \in \mathbb{R}^{3L}$. We aim to recover σ and θ from the voltages and denote this as a vector $x = (\sigma, \theta) \in \mathbb{R}^{N_E^c + 2L}$. The MAP estimate of x is equivalent to

the minimisation problem

$$x = \arg \min_y \left\{ (ZF(y)I - V)^T \Gamma_e^{-1} (ZF(y)I - V) + (y - x_{(r)})^T \Gamma_x^{-1} (y - x_{(r)}) \right\}, \quad (4.18)$$

where Γ_e denotes the noise covariance, Γ_x the regularisation covariance operator and V is the vector of measured voltages. The inverse problem is highly non-linear and an iterative non-linear algorithm is used to compute the MAP estimate. This has the potential to be computationally intensive because at each iteration, and during a linesearch, a new finite element mesh must be generated from the updated electrode positions along with a new conductivity and movement Jacobian. Additionally a coarse-fine mapping must be computed to efficiently solve the inverse problem on a low resolution model as well as computing the forward problem sufficiently accurately on a higher resolution model.

To decrease the complexity, a two stage algorithm is deployed where the initial stage is solely to determine a good approximation to the electrode positions from the measured voltages. We *a-priori* assume the conductivity is known, and constant, in a neighbourhood of the boundary, and this constant background conductivity is set on the forward model when initially only determining the electrode positions. After the electrode positions have been determined sufficiently accurately, the second stage is to simultaneously determine the conductivity and the remaining small corrections to the electrode positions. In effect we assume that the ranges of the maps taking the boundary shape to the electrical data and conductivity to the electrical data do not intersect, and can thus be estimated separately. This is plausible because we know we can reconstruct both the conductivity and shape from the measurements, up to a rigid transformation for a convex body. We note that we should not expect to determine the conductivity first followed by the boundary shape. Firstly the DtN map from a deformed conductivity would most likely be consistent with an anisotropic conductivity in the undeformed domain as discussed in this chapter. Secondly the pushforward DtN map $\psi_* \Lambda_\sigma = \Lambda_{\Psi_* \sigma}$ on the deformed domain Ω_h will most likely have a different symbol to the DtN map Λ_{σ_r} associated with the prior conductivity on the undeformed domain. The difference between DtN maps with different symbols is not a smoothing operator, which means that the difference in electrical data arising from a deformed and undeformed conductivity would be significantly larger than the typical small differences associated with interior conductivity changes. The symbol only depends on

the conductivity and its derivatives at the boundary (see section 3.3.1) and so a conductivity reconstruction algorithm would most likely fit the conductivity changes near to the electrodes to compensate for any significant difference in the symbols. The over-fitting of the conductivity near the electrodes is a common observation with an inaccurately known shape in practice [32, 116].

Stage 1: Determining electrode positions

A Gauss-Newton method is deployed to the regularised tangential movement problem. The electrodes move tangentially to the domain at each iteration and so do not in general lie on the boundary of the domain after each iteration. These are thus projected back onto the fixed domain by computing the nearest boundary simplex of the finite element mesh. With the new electrode positions, a new finite element mesh is generated using the EIDORS function `ng_mk_gen_models.m`, and assigned the given *a-priori* conductivity. This is continued until the electrodes have been determined sufficiently accurately.

To determine the electrode positions, with the conductivity fixed, means that the degrees of freedom associated with the conductivity can be neglected. The inverse prior covariance matrix is given by $\Gamma_\theta^{-1} = \beta^2 L_\theta^T L_\theta$, and classical Tikhonov regularisation is used for the electrode positions. The i^{th} Gauss-Newton iteration is of the form

$$x_{(i+1)} = x_{(i)} - \mu_{(i)} H_{(i)}^{-1} g_{(i)}, \quad (4.19)$$

where $\mu_{(i)}$ is a linesearch parameter to ensure sufficient decrease of the functional (4.18), and $g_{(i)}$ and $H_{(i)}$ are the gradient and Hessian of the functional. To compute the gradient, $g_{(i)} \in \mathbb{R}^{2L}$, of the functional (4.18), at the point x_i , we need to calculate the first partial derivatives of the functional with respect to electrode positions, $g_{(i)} = 2J_m(x_{(i)})^T \delta V_{(i)} + 2\Gamma_\theta^{-1}(x_{(i)} - x_{(r)})$, where $\delta V_{(i)} = ZF(x_{(i)})I - V$ is the data misfit vector at each iteration. The Gauss-Newton method assumes all second order partial derivatives of the voltages with respect to v can be neglected. Classical Tikhonov regularisation is deployed, so that the prior covariance matrix is diagonal, which allows us to write the Hessian matrix of the functional (4.18) at the point $x_{(i)}$ as $H_{(i)} = 2J_m(x_{(i)})^T J_m(x_{(i)}) + \beta^2 2L_\theta^T L_\theta \in \mathbb{R}^{2L \times 2L}$. To avoid remeshing during the line-search, which is computationally expensive, the forward problem is linearised along the

particular descent direction, although remeshing is performed at each Gauss-Newton iteration.

Stage 2: Determining conductivity and electrode positions

After the electrode positions have been determined sufficiently accurately, the minimiser of the functional is again approached via a Gauss-Newton method to generate a sequence of iterations $x_{(i)}$. For simplicity we chose the initial guess as the prior distribution, $x_{(0)} = x_{(r)}$, and we assume that the conductivity and electrode position changes are independent, resulting in an inverse prior covariance matrix of the form

$$\Gamma_x^{-1} = \begin{bmatrix} \alpha^2 L_\sigma^T L_\sigma & 0 \\ 0 & \beta^2 L_\theta^T L_\theta \end{bmatrix}. \quad (4.20)$$

Laplace regularisation for the conductivity and Tikhonov regularisation for the electrode positions is deployed, which means that the $L_\theta^T L_\theta$ is the identity matrix and $L_\sigma^T L_\sigma$ is a discrete approximation to the Laplacian. The Laplace regularisation matrix has a null space spanned by constant vectors, and thus $L_\sigma^T L_\sigma$ is not strictly invertible. However determining a constant conductivity background from the voltages is well-posed and so this single rank deficiency does not create problems in practice. The Gauss-Newton iteration is again of the form (4.19). During the first stage of the algorithm it is assumed that the electrode positions have been found sufficiently well and so we do not remesh after each Gauss-Newton step. A linear approximation to movement is adopted so that the electrode Jacobian J_m is approximated as constant, although the conductivity Jacobian J_c is updated at each iteration. To compute the gradient, $g_{(i)} \in \mathbb{R}^{N_E^c + 2L}$, of the functional (4.18), at the point $x_{(i)}$, we need to calculate the first partial derivatives of the functional with respect to conductivity and electrode positions,

$$g_{(i)} = 2[J_c(x_{(i)})|J_m(x_{(i)})]^T \delta V_{(i)} + 2\Gamma_x^{-1}(x_{(i)} - x_{(r)}) \quad (4.21)$$

where $\delta V_{(i)} = ZF(x_{(i)})I - V$ is the data misfit vector at each iteration. The Gauss-Newton method assumes all second order partial derivatives of the voltages with respect to σ and v can be neglected. This, and the structure of the prior covariance matrix in (4.20) allows us to write the Hessian matrix, $H_{(i)} \in \mathbb{R}^{N_E^c + 2L \times N_E^c + 2L}$, of the

functional (4.18) at the point $x_{(i)}$, as a 2×2 block matrix of the form

$$H_{(i)} = 2 \begin{bmatrix} J_c(x_{(i)})^T J_c(x_{(i)}) + \alpha^2 L_\sigma^T L_\sigma & J_c(x_{(i)})^T J_m(x_{(i)}) \\ J_m(x_{(i)})^T J_c(x_{(i)}) & J_m(x_{(i)})^T J_m(x_{(i)}) + \beta^2 L_\theta^T L_\theta \end{bmatrix}. \quad (4.22)$$

Dual modelling

The quantities $ZF(x_{(i)})I$, $[J_c(x_{(i)})|J_m(x_{(i)})]$ and $H_{(i)}^{-1}$ must be computed for every iteration of the Gauss-Newton method as well as during the linesearch. Recomputing the Jacobians and inverting the Hessian matrix in 3D are computationally intensive tasks. A dual modelling approach is deployed, where the reconstructed conductivity is represented on a coarse finite element model, but a fine finite element model used for the forward problem [130]. The fine finite element mesh contains the electrode positions, with a high mesh density near the electrodes, whereas the coarse mesh is chosen to have approximately uniform density through the domain. This approach ensures that the forward problem can be solved sufficiently accurately on the fine mesh whilst only using a low dimensional representation of the reconstructed conductivity on the coarse mesh.

A coarse to fine projection matrix, $P : \mathbb{R}^{N_c^E} \rightarrow \mathbb{R}^{N_f^E}$, can be computed with these two discretisations using EIDORS², where P_{ij} represents the fraction of the i^{th} fine finite element contained within the j^{th} coarse finite element. This projection matrix allows one to efficiently calculate the coarse conductivity Jacobian columnwise through

$$[J_c]_{ij} = [J_f P]_{ij} = \sum_k \frac{\partial V_i}{\partial \sigma_k^f} P_{kj}.$$

The reconstruction model is also generated slightly larger than the forward model allowing one to project the coarse discretisation onto the fine discretisation through $\sigma_f = P\sigma_c$. This projection allows the forward problem to be resolved sufficiently accurately at each iteration as well as during the linesearch.

It was observed in numerical simulations that regenerating a finite element mesh with new electrode positions during linesearches in an iterative algorithm was slow. In order to speed up the algorithm, the updated electrode movement is assumed sufficiently small during the linesearch so that the voltages can be linearised through

$$ZF(\sigma + \delta\sigma, v + \delta v)I \approx ZF(\sigma + \delta\sigma, v)I + ZJ_m \delta v, \quad (4.23)$$

²The library function `mk_coarse_fine_mapping.m`

valid for small changes in the electrode positions. The electrode position Jacobian, J_m , is computed on the fine finite element discretisation.

Linesearches

The descent direction, $p_{(i)} = -H_{(i)}^{-1}g_{(i)}$, can be computed and we are left with a 1D minimisation problem at the i^{th} iteration for $t_{(i)}$

$$\min_t g(t) \quad \text{where} \quad g(t) = f(x_i + tp_i),$$

where $f : \mathbb{R}^{N_E+2L} \rightarrow \mathbb{R}$ is the functional in (4.18). A bracketing linesearch with quadratic polynomial interpolation is used to perform the linesearch. Since $p_{(i)}$ is a descent direction, then there must exist a μ such that $g(0) > g(\mu)$. Using such a μ , we then find $0 < s_1 < s_2 < s_3$ such that $g(s_2) < \min\{g(s_1), g(s_3)\}$. Once these three points are determined, a unique convex quadratic can be fit through the points and the linesearch parameter chosen as the unique minimiser of the given quadratic. The bracketing linesearch requires the recomputation of the forward problem with the new conductivity and electrode positions. Again the dual modelling approach is used to recompute the voltages at the new conductivity iteration and the voltages are linearised with respect to tangential changes as in (4.23).

Termination criterion

In the two stage algorithm outlined it is instructive to define a criterion to exit out of the initial stage of determining the electrode positions, especially in the practical situation of when the exact conductivity and electrode positions are not known. This initial stage is based on an iterative Gauss-Newton method, and as discussed in the results section, it was found numerically that the total 2-norm error in the voltage misfit generally converged in such a way that the misfit in voltages at the end of the first stage of the algorithm is largely associated with the unknown conductivity perturbation. Hence a tolerance could be pre-defined and when the error in voltages between successive iterates drops below this tolerance we terminate and move onto the second stage of the algorithm. For the numerical results in this chapter this termination criterion was not implemented and the number of iterates was chosen to give the best appearance of reconstructed conductivity images.

4.4 Numerical results

In this section numerical results are presented from a sensitivity study of the boundary shape Jacobians followed by reconstructions using the simultaneous conductivity and electrode position algorithm outlined in the previous section. All figures can be found on pg. 131-169 at the end of this chapter.

4.4.1 Sensitivity study

A sensitivity analysis is undertaken on the Jacobian with respect to boundary shape. A cylindrical domain of unit height and radius is constructed, with three rings of 16 electrodes placed about the axis of rotational symmetry approximately equidistant on each ring. The electrodes are all assumed to be circular with a fixed diameter of 0.05 and contact impedance of $z = 0.01$. A 3D finite element (FE) forward model extruded along the caudal-distal axis was generated using EIDORS³ calling the Netgen mesh generator [131] by supplying the external shape, the electrode positions and outward pointing normals, and a constant conductivity of $\sigma = 1$ assigned to the model.

As discussed in section 3.1.2, the right singular vectors, v_i , corresponding to the singular values below an experimental threshold, $\lambda_i < \epsilon$, effectively give no observational change in voltage data. We normalise the singular values relative to the largest singular value, and an SNR level of 50 (which is used in the numerical results of this section) corresponds to a signal-to-noise ratio of $316 \approx 10^{50/20}$. Hence singular vectors corresponding to singular values with $\lambda_i < 1/316$ are effectively unobservable.

The SVD is computed in MATLAB for a number of different excitation and measurement strategies and three different electrode position Jacobians — the tangential movement Jacobian $J_m^t : \mathbb{R}^{2L} \rightarrow \mathbb{R}^m$, the tangential-normal movement Jacobian, $J_m^{t,\nu} : \mathbb{R}^{3L} \rightarrow \mathbb{R}^m$, and a tangential-normal-boundary Jacobian, $J_m^{t,\nu,b} : \mathbb{R}^{3L+b} \rightarrow \mathbb{R}^m$. For the Jacobian $J_m^{t,\nu,b}$ three boundary nodes ($b = 3$) that are not a member of any of the electrodes were chosen on the curved surface of the cylinder. Different measurement strategies are also adopted, with traditional 2D data collection as well as more fully 3D data collection schemes used, to understand the sensitivity to electrode position changes with different measurement strategies. We label the electrodes on the

³The library function `ng_mk_gen_models.m`

cylinder from 1 – 16 on the top ring ($z = 0.75$), 17 – 32 on the middle ring ($z = 0.5$) and 33 – 48 on the bottom ring ($z = 0.25$), with electrodes i , $16 + i$ and $32 + i$ for $i = 1, \dots, 16$ on approximately the same vertical axis. Pseudo 2D current patterns were deployed where currents are injected between electrodes i and $i + A$ with an offset given by an integer A . For example $A = 1$ corresponds to an adjacent excitation strategy, $A = 8$ is an opposite excitation strategy and $A \geq 17$ corresponds to exciting current between different rings. For $A \leq 8$, voltage measurements are also recorded with the same offset on the driven ring as well as on the other two rings, but no measurements are recorded between different rings. For $A \geq 17$ measurements between different rings are included with the measurement offset given by A . Measurement strategies that include measurements recorded on driven electrodes, and those that reject these measurements, are both used in the following comparison.

From section 4.2 we know the electrical data determines the boundary shape up to a conformal map. In particular if three points on the boundary are fixed and known, or three or more shapes of the electrodes are fixed and known, then the Kelvin transformations reduces to the identity. We fix the electrode shapes, because these are known in practice, which eliminates these transformations from the null space of the Jacobian. We are left with three rotations and three translations which can potentially appear in the null space of the boundary shape Jacobian. The shape derivative is only sampled at the electrode positions, with the rest of the boundary fixed, and with this assumption the translations will disappear from the null space. We are left with rotational perturbations which will only appear in the null space if there is any rotational symmetry of the object.

In figure 4.3 the singular values of J_m^t and $J_m^{t,\nu,b}$ are plotted with an $A = 1$ measurement strategy. In particular $J_m^{t,\nu,b}$ was calculated with an additional three boundary nodes away from electrodes on the curved surface of the cylinder, and thus there are 96 and 147 degrees of freedom associated with each Jacobian respectively. The first observation is that the singular values do not decay rapidly to zero indicating that the problem is only mildly ill-posed. A selection of singular vectors of $J_m^{t,\nu,b}$ can be seen in figures 4.6 and 4.7, for the case when measurements from driven electrodes are included and not included respectively. In particular $J_m^{t,\nu,b} = U\Sigma V^T$, where $V \in \mathbb{R}^{147 \times 147}$, and each singular vector $v \in \mathbb{R}^{147}$ is of unit length. For a given singular

value, each singular vector corresponds to the weighting along each direction of each electrode ($3 \times 48 = 144$ components) and the normal direction of the three boundary nodes (3 components), giving a total of 147 components. The figure then displays, for a selection of singular values, the weighting along each direction of each electrode and the weighting along normal direction of boundary nodes. If measurements are not included on the driven electrodes, the singular vectors associated with the largest singular values ($i = 1, \dots, 48$) typically correspond to tangential perturbations parallel to the z-axis, and the next largest ($i = 49, \dots, 95$) to tangential perturbations in the azimuthal direction. The singular vectors associated with singular values ($i = 96, \dots, 143$) are typically associated with perturbations normal to the cylindrical boundary. The remaining four singular vectors are associated with the normal perturbation of the boundary nodes away from the electrodes, and the single rotational symmetry of the cylindrical object. If measurements are included on the drive electrodes, however, the singular vectors with the largest singular values typically had largest components corresponding to normal perturbations of the electrodes, although normal changes away from the electrodes always have a low sensitivity associated and highlights why the full boundary shape is difficult to determine.

In figure 4.4 the singular values of the tangential movement Jacobian are plotted for $A = 1, 7, 8$ and 23 measurement strategies. An interesting observation is the $A = 8$ strategy Jacobian is clearly rank deficient because of insufficiency of the data with this ‘opposite’ measurement strategy. The conditioning for the $A = 1, 7$ and 23 measurement strategies appear qualitatively similar which can be explained because these strategies all record measurements on electrodes adjacent to drive electrodes, where the sensitivity to tangential changes is largest. The conditioning is improved for different strategies when measurements are recorded on driven electrodes. A selection of singular vectors of $J_m^{t,\nu,b}$ can be seen in figures 4.8 and 4.9 for the $A = 23$ measurement strategy. The singular vectors exhibited qualitatively similar behaviour to the singular vectors for the $A = 1$ strategy. There is also only a mild decay of the singular values (apart from the three normal directions away from electrodes, and the singular vector associated with the rotational symmetry of the cylinder).

The SVD is also calculated for the conductivity Jacobian on the cylindrical domain over different measurement patterns. Figure 4.5 displays the singular values

exhibiting the well known exponential decay, highlighting the severely ill-posed nature of reconstruction. Given the SVD on this background image, it is instructive to also understand what information on the interior of the domain we can obtain from the boundary data. Given a conductivity perturbation, $\delta\sigma = \sum_{i=1}^{N_E^c} \delta_i \chi_i$, parameterised by the vector $\delta \in \mathbb{R}^{N_E^c}$, the change in voltages, $d \in \mathbb{R}^m$, satisfies (to first order in $\delta\sigma$)

$$d = U\Sigma V^T \delta + O(\|\delta\sigma\|_\infty^2) = \sum_{i=1}^{N_E^c} u_i \lambda_i (v_i^T \delta) + O(\|\delta\sigma\|_\infty^2).$$

The right singular vectors also form a basis for \mathbb{R}^N , and so we can write the conductivity perturbation vector as

$$\delta = \sum_{i=1}^{N_E^c} (\delta^T v_i) v_i.$$

By truncating the series at a measurement precision cut off, that is by rejecting v_i for $i > r$ with $\lambda_i \leq \epsilon$, we reject components of δ that are undetectable leading to a ‘SVD projection perturbation’, $\delta^{(r)}$, and corresponding image, $(\delta\sigma)^{(r)}$, given by

$$\delta^{(r)} = \sum_{i=1}^r (\delta^T v_i) v_i, \quad (\delta\sigma)^{(r)} = \sum_{i=1}^{N_E^c} \delta_i^{(r)} \chi_i,$$

respectively. Generating such images gives an indication of what information about the perturbation we can obtain with a practical EIT system operating at a given noise level, and also allow us to study what the effect of different measurement strategies is on the projected image. Two smooth conductivity perturbations are considered using a Gaussian perturbation of the form

$$\sigma_{inc}(x) = s \exp\left(-\frac{\|x - x_0\|^2}{v}\right), \quad (4.24)$$

where x_0 is referred to as the centre of the inclusion, v the variance and s is the conductivity perturbation magnitude.

Firstly a perturbation concentrated at the centre with $x_0 = (0, 0, 0.5)$, $v = 0.2$ and $s = 2$ is considered. Figure 4.10 displays $(\delta\sigma)^{(r)}$ over a range of r values in the xy plane. Figure 4.11 displays a central perturbation in the xz plane and we observe that the resolution in this direction is much worse because electrical measurements can not be recorded on the top and bottom of the cylinder. This highlights how resolving the conductivity in the z direction is inherently difficult in lung EIT. When $r \leq 100$ the $A = 23$ strategy appears to give more interior information than the $A = 1$ strategy

| r | $\frac{\lambda_r}{\lambda_1}$ | $\ \delta - \delta_r\ _2$ | $\frac{\lambda_r}{\lambda_1}$ | $\ \delta - \delta_r\ _2$ |
|-----|-------------------------------|---------------------------|-------------------------------|---------------------------|
| 50 | 3.6 | 15.6 | 4.7 | 12.3 |
| 100 | 8.9 | 14.5 | 12.3 | 10.9 |
| 200 | 52.7 | 7.1 | 88.1 | 8.0 |
| 300 | 285.3 | 5.9 | 501.2 | 6.0 |

Table 4.1: Errors of SVD image for central perturbation with $A = 1$ (second and third column) and $A = 23$ (fourth and fifth column) measurement strategy. The first column indicates the number of projections r . The norm of the central perturbation has $\|\delta\|_2 = 15.6$.

| r | $\frac{\lambda_r}{\lambda_1}$ | $\ \delta - \delta_r\ _2$ | $\frac{\lambda_r}{\lambda_1}$ | $\ \delta - \delta_r\ _2$ |
|-----|-------------------------------|---------------------------|-------------------------------|---------------------------|
| 50 | 3.6 | 3.9 | 4.7 | 3.4 |
| 100 | 8.9 | 2.8 | 12.3 | 2.5 |
| 200 | 52.7 | 1.7 | 88.1 | 1.6 |
| 300 | 285.3 | 1.2 | 501.2 | 1.2 |

Table 4.2: Errors of SVD image for boundary perturbation with $A = 1$ (second and third column) and $A = 23$ (fourth and fifth column) measurement strategy. The first column indicates the number of projections r . The norm of the boundary perturbation has $\|\delta\|_2 = 4.4$.

in both the xz and xy plane. The errors for the $A = 1$ and $A = 23$ strategy SVD images as a function of r can also be seen in table 4.1. The table demonstrates that when $r \leq 100$ the $A = 23$ strategy gives more information about the perturbation than the $A = 1$ strategy, but when $r = 300$ the $A = 1$ strategy gives marginally more information about the perturbation than the $A = 23$ strategy.

Secondly a perturbation concentrated near the boundary with $x_0 = (0.5, 0.5, 0.7)$, $v = 0.05$ and $s = 2$ is considered. Figure 4.12 displays $(\delta\sigma)^{(r)}$ over a range of r values in the xy plane. We get reasonable resolution of the perturbation with a lot less singular vectors than the central perturbation case, highlighting why EIT is good at detecting inclusions near the measurement locations. Figure 4.13 displays the boundary perturbation in the xz plane. We observe that the resolution in this direction is not as good as in the xy plane, although the resolution is still better in this direction for small cut-off values than the analogous figure with a central perturbation. The errors for the $A = 1$ and $A = 23$ strategy SVD images as a function of r can be seen in table 4.2. The table demonstrates that when $r < 300$ the $A = 23$ strategy gives more information about the perturbation than the $A = 1$ strategy.

4.4.2 Simultaneous reconstruction

For the spherical and cylindrical geometry we use a background conductivity of $\sigma = 1$, and an unknown conductivity of the form $1 + \sigma_{inc}(x)$, where $\sigma_{inc}(x)$ is given by (4.24). For the spherical external shape an inclusion with $x_0 = (0, 0.3, 0.3)$, $v = 0.1$ and $s = 2$ is chosen. For the cylindrical external shape three different inclusions are used. Firstly an extruded inclusion with centre at $x_0 = (0.2, 0.2, z)$, with $z \in [0, 1]$, $v = 0.15$ and $s = 2$. Secondly an inclusion with centre at $x_0 = (0.2, 0.2, 0.5)$, variance $v = 0.1$ and $s = 2$. Thirdly two Gaussian inclusions with centres at $x_0 = (0.5, 0.0, z)$ and $x_0 = (-0.5, 0, z)$, with $z \in [0, 1]$ and both with variances 0.15 and $s = -0.7$ are denoted $B1$ and $B2$ respectively. We denote these three cylindrical test domains as $C1$, $C2$ and $C3$ respectively.

The electrode position error was modelled by perturbing each coordinate of each electrode, parameterised by p . In particular the i^{th} electrode centre-of-mass coordinates are perturbed through, $v_i \mapsto \tilde{v}_i = v_i + pn_i$, where $n_i \in \mathbb{R}^3$ with each component sampled from the normal distribution with mean 0 and standard deviation 1. The new coordinates are then projected back onto the surface of the model sphere or cylinder. A $p = 0.1$ perturbation resulted in an average perturbation of the electrode of approximately $\approx 8\%$ of the geometry radius, corresponding to $\approx 1 - 2$ cm on a human body. We define the total 2-norm error, e , of the electrode centre-of-mass coordinates as

$$e := \left(\sum_{m=1}^L \|v_m^A - v_m^M\|_2 \right)^{\frac{1}{2}} \quad (4.25)$$

where $v_m^A, v_m^M \in \mathbb{R}^3$ are the actual and model coordinates of the m^{th} electrode. The current and voltage were simulated using pair current drives and pair voltage measurements. White Gaussian pseudo-random noise is added to the voltage data, parameterised by the SNR through (4.1). A noise level with an SNR of 50 is used throughout all the subsequent reconstructions in this chapter, which is of a similar order of accuracy of a typical EIT measurement system (see section 5.1.1).

The two stage algorithm is then deployed to firstly determine the approximate electrode positions and then simultaneously determine the conductivity and electrode positions. The scenario with the electrode positions fixed is also studied because this gives us an understanding of how well a standard Laplace regularised reconstruction performs. The degrees of freedom associated with electrode positions are removed from

the algorithm, and the algorithm degenerates to a classical Laplace regularised MAP estimate, solved using a non-linear Gauss-Newton method with dual modelling and a bracketing linesearch. This algorithm is referred to as the standard algorithm and the algorithm incorporating electrode movement as the shape correction algorithm. In all cases the regularisation parameters were chosen to give best appearance of the images.

Spherical geometry

A unit sphere and a cylinder with unit radius and height are used in the following simulations. Figure 4.15 illustrates the spherical model with spherical inclusion used with approximately 200000 elements and a $p = 0.1$ perturbation of the electrodes. Figure 4.14 displays the initial fine and coarse reconstruction models with approximately 32000 and 1100 finite elements respectively. The sphere is covered with 14 electrodes placed equidistantly around the equator, 9 electrodes equidistantly around the tropics and an electrode on the north and south pole, resulting in 34 electrodes. A nearest neighbour current injection and measurement protocol was deployed.

Figure 4.16 illustrates the reconstruction with the electrode positions known and fixed. This is the best case scenario when the electrode positions are known during the algorithm. All spherical reconstructions have hyperparameters of $\alpha = 10^{-5}$ and $\beta = 0.015$. Reconstructions with a perturbation of $p = 0.1$ can be seen in figure 4.17 and figure 4.18 for a standard and shape correction algorithm. The standard algorithm has distinctive artefacts in a neighbourhood of the boundary whereas the shape correction algorithm removes these artefacts. Figure 4.19 illustrates lineplots through the solutions with electrodes known and fixed, a shape correction algorithm and a standard algorithm with incorrect electrode positions. The shape correction algorithm generates images qualitatively similar to the standard algorithm with known electrode positions. Figure 4.20 illustrates the convergence of the voltage and electrode positions (which we do not know in practice) during the first stage of the algorithm. The first stage of the algorithm appears to converge in such a way that the difference in voltages by the end of the first stage of the algorithm is largely associated with the conductivity perturbation. This numerically suggests that we can first determine the electrode positions and then conductivity changes as we implicitly assume in this two stage algorithm. The initial and final total 2-norm errors in the electrode positions

are 0.463 and 0.150 respectively. Figure 4.21 illustrates the initial and final error in electrode positions at the end of the two stage algorithm, indicating that the electrode positions have been determined well.

Cylindrical $C1$ geometry

Figure 4.22 displays the initial fine and coarse reconstruction models used to solve the forward problem and inverse problem with approximately 37000 and 1300 finite element respectively. These initial fine and coarse discretisations were used for all the cylindrical simulations.

Figure 4.23 illustrates the cylindrical model with cylindrical inclusion, $C1$, used with approximately 168000 tetrahedral elements respectively with a $p = 0.1$ perturbation of the electrodes. All $C1$ reconstructions use hyperparameters of $\alpha = 2 \times 10^{-5}$ and $\beta = 0.08$. Figure 4.24 illustrates the reconstruction with the electrode positions known and fixed with an $A = 1$ measurement strategy. This is the best case scenario when the electrode positions are known during the algorithm. Reconstructions with a perturbation of $p = 0.1$ can be seen in figure 4.25 and figure 4.26 for a standard and shape correction algorithm. The shape correction algorithm again removes the boundary artefacts observed in the standard algorithm. Figure 4.27 illustrates line-plots through the solutions with electrodes known and fixed, a shape correction and non shape correction algorithm. Figure 4.28 illustrates the convergence of the voltage and electrode positions during the first stage of the algorithm. As with the spherical geometry the first stage of the algorithm appears to converge in such a way that the difference in voltages by the end of the first stage of the algorithm is largely associated with the conductivity perturbation. The initial and final total 2-norm errors in the electrode positions are 0.547 and 0.338 respectively. Figure 4.29 illustrates the initial and final error in electrode positions, highlighting that the electrode positions have been determined accurately.

Cylindrical $C3$ geometry

For the cylindrical domains with two cylindrical inclusions, $C3$, an $A = 1$ measurement strategy is deployed, and the figure cross-sections are displayed through the $B1$ inclusion. All cylindrical $C3$ reconstructions use hyperparameters of $\beta = 0.1$, and

$\alpha = 2 \times 10^{-5}$. Figure 4.30 illustrates the *C3* model used with approximately 166000 tetrahedral elements and a $p = 0.1$ perturbation of the electrodes.

Figure 4.31 illustrates the reconstruction with the electrode positions known and fixed. This is the best case scenario when the electrode positions are known during the algorithm. Reconstructions with a perturbation of $p = 0.1$ can be seen in figure 4.32 and figure 4.33 for a standard algorithm with incorrect electrode positions and shape correction algorithm. The standard algorithm has distinctive artefacts in a neighbourhood of the boundary whereas the shape correction algorithm removes these artefacts. Figure 4.34 illustrates lineplots through the solutions with electrodes known and fixed, a shape correction algorithm and standard algorithm with incorrect electrode positions. Figure 4.35 illustrates the convergence of the voltage and electrode positions during the first stage of the algorithm. Figure 4.36 illustrates the initial and final error in electrode positions, which are again estimated well (the initial and final total 2-norm errors in the electrode positions are 0.582 and 0.335 respectively.)

Cylindrical *C2* geometry

For the cylindrical domains with a single spherical inclusion, *C2*, an $A = 1$ and $A = 23$ measurement strategy is deployed. Figure 4.37 illustrates the cylindrical model *C2* with a spherical inclusion used with approximately 167000 tetrahedral elements respectively with a $p = 0.075$ perturbation of the electrodes. All cylindrical *C2* reconstructions use hyperparameters of $\beta = 0.075$, and $\alpha = 10^{-5}$ and $\alpha = 5 \times 10^{-5}$ for an $A = 1$ and $A = 23$ strategy respectively.

Figure 4.38 illustrates the reconstruction with the electrode positions known and fixed with an $A = 1$ strategy. This is the best case scenario when the electrode positions are known during the algorithm. Reconstructions with a perturbation of $p = 0.1$ can be seen in figure 4.39 and figure 4.40 for a standard and shape correction algorithm. The standard algorithm has distinctive artefacts in a neighbourhood of the boundary whereas the shape correction algorithm removes these artefacts. Figure 4.41 illustrates lineplots through the solutions with electrodes known and fixed, a shape correction and non shape correction algorithm. We observe good resolution in both directions transverse to the z -axis although the resolution parallel to the z -axis is much poorer. Figure 4.42 illustrates the convergence of the voltage and electrode

positions during the first stage of the algorithm. We again observe that the voltage error in the initial stage is converging to the voltage error with a homogeneous domain with the correct electrode positions. Figure 4.43 illustrates the initial and final error in electrode positions with an $A = 1$ strategy, and we again observe the electrode positions are determined well (the initial and final total 2-norm errors in the electrode positions are 0.413 and 0.200 respectively.)

Figure 4.44 illustrates the reconstruction with the electrode positions known and fixed with an $A = 23$ strategy. This is the best case scenario when the electrode positions are known during the algorithm. Reconstructions with a perturbation of $p = 0.075$ can be seen in figure 4.45 and figure 4.46 for a standard and shape correction algorithm. The standard algorithm has distinctive artefacts in a neighbourhood of the boundary whereas the shape correction algorithm removes these artefacts. Figure 4.47 illustrates lineplots through the solutions with electrodes known and fixed, a shape correction and non shape correction algorithm. We again observe good resolution in both directions transverse to the z -axis although the resolution parallel to the z -axis is much poorer. Figure 4.48 illustrates the convergence of the voltage and electrode positions during the first stage of the algorithm. Figure 4.49 illustrates the initial and final error in electrode positions, which are again estimated well (the initial and final total 2-norm errors in the electrode positions are 0.413 and 0.241 respectively.) The $A = 1$ strategy also appears to have slightly lower contrast in the reconstructed conductivity than the $A = 23$ strategy, although the benefits of this strategy are not entirely obvious.

4.5 Conclusions

The NtD map determines the boundary shape and an isotropic conductivity up to a conformal map which consists of rotations, translations, a scaling and a Kelvin transformation in 3D. The RtN map determines the boundary shape and an isotropic conductivity up to a rigid transformation for a convex domain in 3D. Further constraints can pin down the boundary shape exactly. If the shape change is only sampled at electrode positions, then the translations disappear from the null space of the map $\psi : h \mapsto Q_h$, and the null space associated with rotations has the same dimension

as the number of rotational symmetries of the domain. The scaling can be pinned down if, for example, the contact impedance or some *a-priori* knowledge of the interior conductivity is known. The Kelvin transformations disappear from the null space if three non co-linear points on the boundary are known exactly, or if the shapes of the electrodes are known and fixed.

A numerical and theoretical study of the linearised problem of determining electrode positions from the electrical data has been performed. In particular it is demonstrated that this is only a mildly ill-posed problem in comparison to the important internal conductivity changes which is severely ill-posed. There are a number of useful insights from this sensitivity study. Firstly if the external shape is fixed, the measurement strategies that measure near driven electrodes, where the electric field is largest, are the best at determining the electrode positions but purely opposite drive and measurement strategies are insufficient to determine the electrode positions uniquely. If the external shape is also unknown, and so the electrodes can move normally to the boundary, then if measurements are not recorded on drive electrodes, the electrical data is less sensitive to normal changes than tangential changes. However if recordings are taken on driven electrodes the electrical data is more sensitive to normal changes than tangential changes. The electrical data is very insensitive to normal changes away from drive and measurement electrodes, indicating that using the electrical measurements to determine the whole external boundary shape is more ill-posed than just determining the electrode positions on a fixed boundary shape. This highlights that using another technique to determine the boundary shape provides extremely useful *a-priori* information as we will observe in the subsequent chapter, as we can only realistically sample the normal shape change near current driven electrodes. Adjacent excitation and measurement patterns are thus good at determining the electrode positions, although are notoriously bad at determining interior conductivity changes [21] in 2D. Optimal measurement strategies to determine interior conductivity changes in 3D is an important topic for future research.

A novel two stage reconstruction algorithm to determine the electrode positions and conductivity, given that the external boundary shape is known, was implemented. In the first stage the electrode positions are found to a sufficient degree of accuracy using a non-linear regularised Gauss-Newton method using remeshing of the finite element

model at each iteration. The voltages by the end of the first stage of the algorithm appear to converge in such a way that the voltage discrepancy is largely associated with interior conductivity changes only. In the second stage a non-linear reconstruction algorithm to determine the conductivity, and linearised changes in the electrode positions, to reduce computational complexity of remeshing at every iteration, was implemented. It was observed numerically that the first stage of the algorithm did not fit electrode positions changes to potential conductivity changes, because the reconstructions when determining the shape and positions are of a similar quality to when the electrode positions are known and fixed. In particular numerical results suggested that shape and conductivity changes can be separated from the electrical data, and reinforces the theoretical discussion that the shape and isotropic conductivity can be uniquely determined from the electrical data.

There are a number of extensions to this work. Firstly different regularisation norms, such as Total Variation for discontinuous conductivities, could be used. This will require a significant change to the algorithm because a mixed regularisation scheme for the conductivity and electrode positions will be required. Secondly, we would like to extend this work to more generic 3D models with an arbitrary boundary $\partial\Omega$. Such an extension would not require substantial modification of the algorithm, although updated electrode positions will need to be projected on to the surface of the model, by computing the nearest boundary element to the updated electrode position. A mesh generator that can triangulate general surfaces with arbitrary electrode positions will suffice. A more difficult problem is when the external shape is also unknown so that normal changes of the boundary need to be incorporated. As we have demonstrated from the sensitivity study, these are only easy to detect at drive electrodes if measurements are recorded on drive electrodes, which is challenging with a practical EIT instrument, so we can only hope to obtain a low rank estimate of the external shape. It is thus important that non electrical methods should be used to capture the external shape if at all possible as demonstrated in the next chapter.

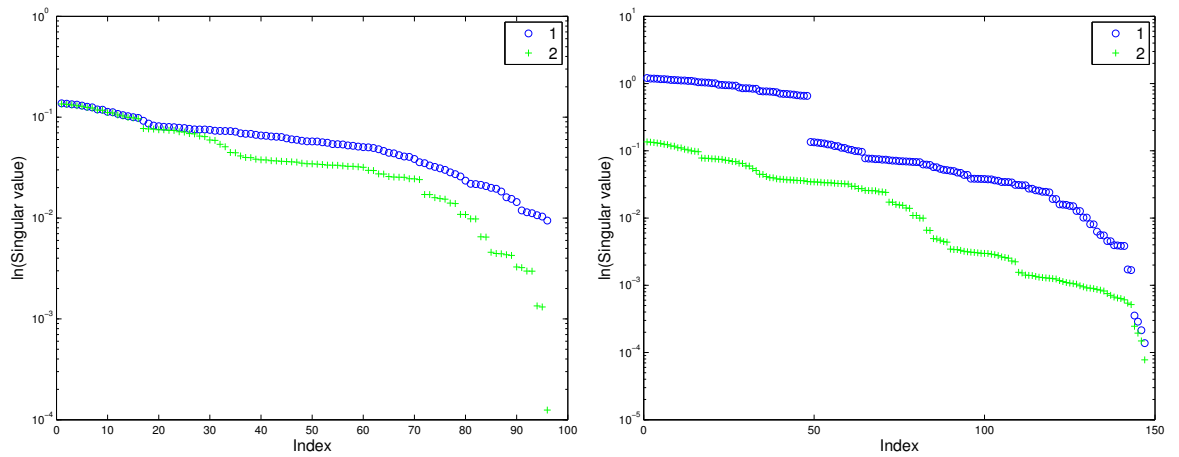


Figure 4.3: Singular value decay for boundary shape Jacobian on cylindrical domain with $A = 1$ measurement strategy. The blue and green line indicates that measurements on driven electrodes have and have not been recorded respectively. The left hand image indicates the singular values of J_m^t . Measuring on driven electrodes improves the conditioning of the tangential movement Jacobian. The right hand figure illustrates the singular values of $J_m^{t,\nu,b}$. If measurements are not included on driven electrodes, the singular vectors corresponding to normal changes are associated with the smallest singular values (see figures 4.6 and 4.7 for associated singular vectors.) The small group of three singular values correspond to normal changes away from electrodes. If measurements are included on driven electrodes the normal changes on electrodes correspond to the largest singular values, although normal changes away from electrodes still correspond to the smallest singular values.

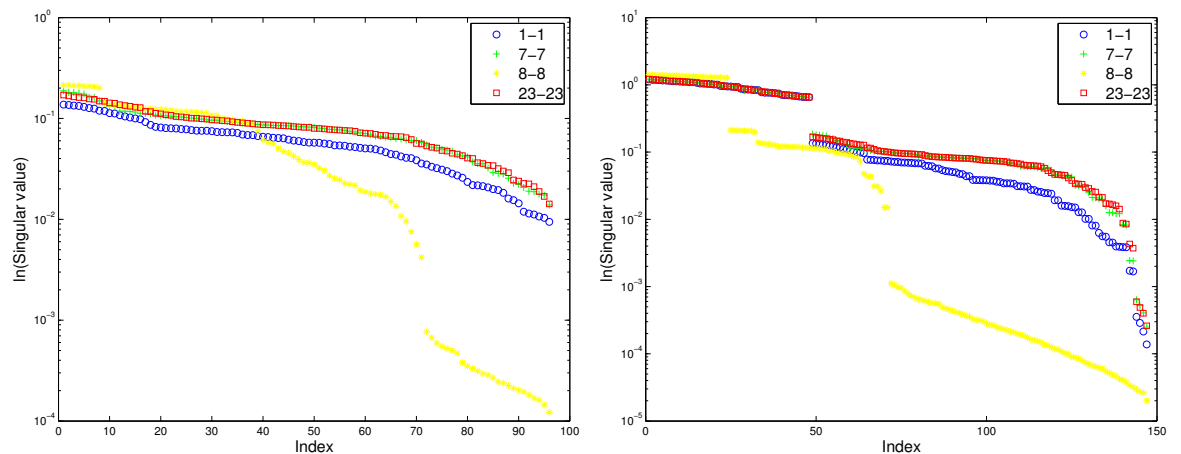


Figure 4.4: Singular value decay for J_m^t (left hand) and $J_m^{t,\nu,b}$ (right hand) boundary shape Jacobian respectively on cylindrical domain with measurement strategies $A = 1, 7, 8$ and 23 . The singular value decay for the $A = 1, 7, 23$ strategies have qualitatively similar behaviour, as do the associated singular vectors (see figures 4.6 - 4.9). A pure opposite ($8-8$) strategy has a particularly quick decay indicating an insufficiency in the data from this strategy to determine the electrode positions.

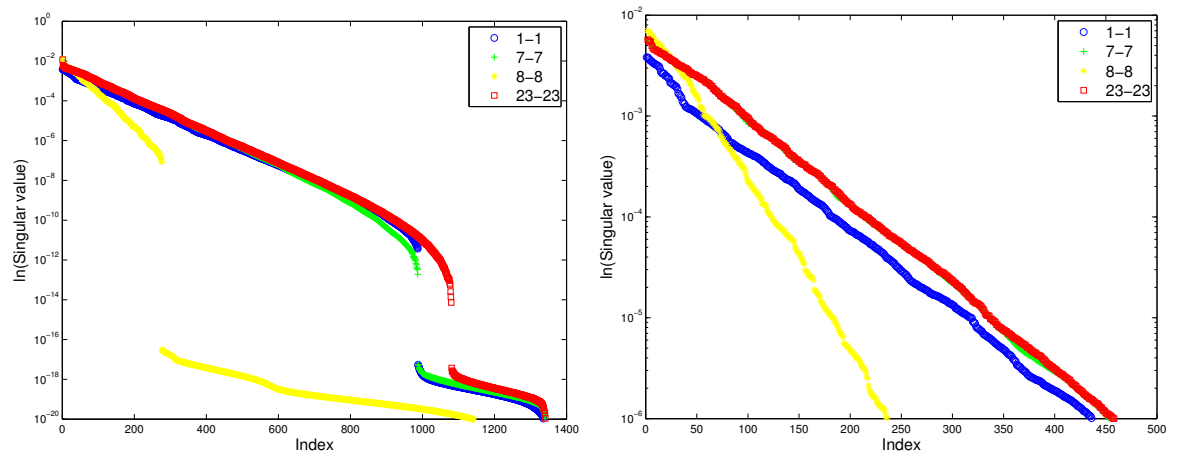


Figure 4.5: Singular value decay for conductivity Jacobian on cylindrical domain with measurement strategies $A = 1, 7, 8$ and 23 . The left hand figure represents the whole spectrum and the right hand figure a zoom on ‘observable’ singular values. The singular value decay for the $A = 1, 7, 23$ strategies have qualitatively similar behaviour, and exhibit the well known exponential decay indicating the severely ill-posed nature of the linearised reconstruction problem. There is an effective drop in rank at singular index $i \approx 1000$. A pure opposite ($8 - 8$) strategy has a particularly quick decay indicating an insufficiency in the data from this strategy to determine the electrode positions.

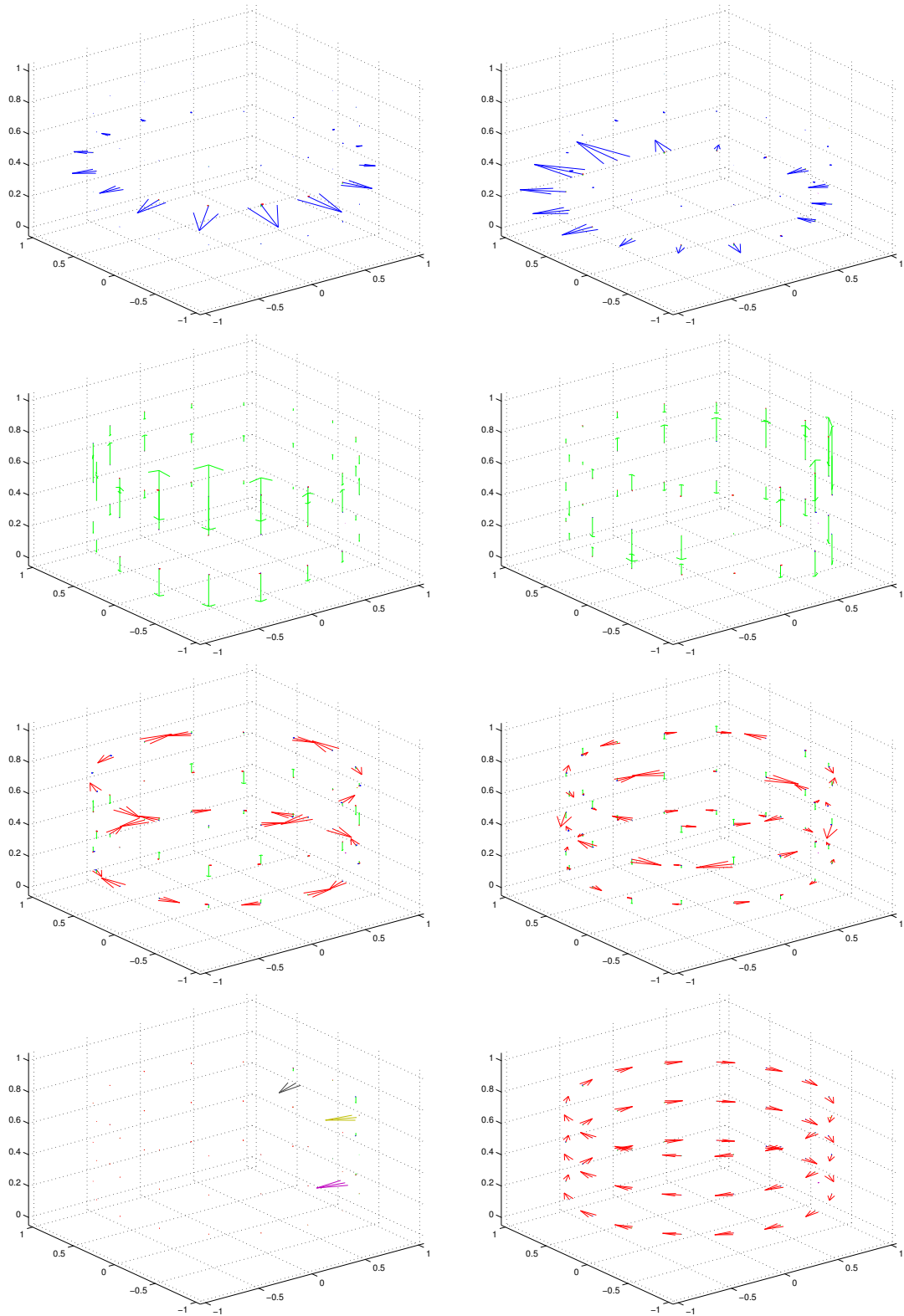


Figure 4.6: Singular vectors for boundary shape Jacobian on cylindrical domain with $A = 1$ measurement strategy and measurements recorded driven electrodes. Green indicates components of movement in z-direction, red in the angular direction and blue in the radial direction. The left hand column corresponds to singular values 1, 49, 91, 144 and the right hand column to singular values 8, 51, 97, 147. Singular vectors 1 – 48 are typically dominated by normal perturbations of the electrode e.g. 1 and 8 above. Singular vectors 49 – 96 are typically dominated by perturbations of the electrodes aligned with the z-axis. Singular vectors 97 – 143 typically dominated by azimuthal changes in the electrodes. The smallest singular vectors 144 – 146 are associated with normal changes of the boundary away from the driven electrode and the smallest singular vector 147 corresponds to the single rotational similarity transformation on the cylinder.

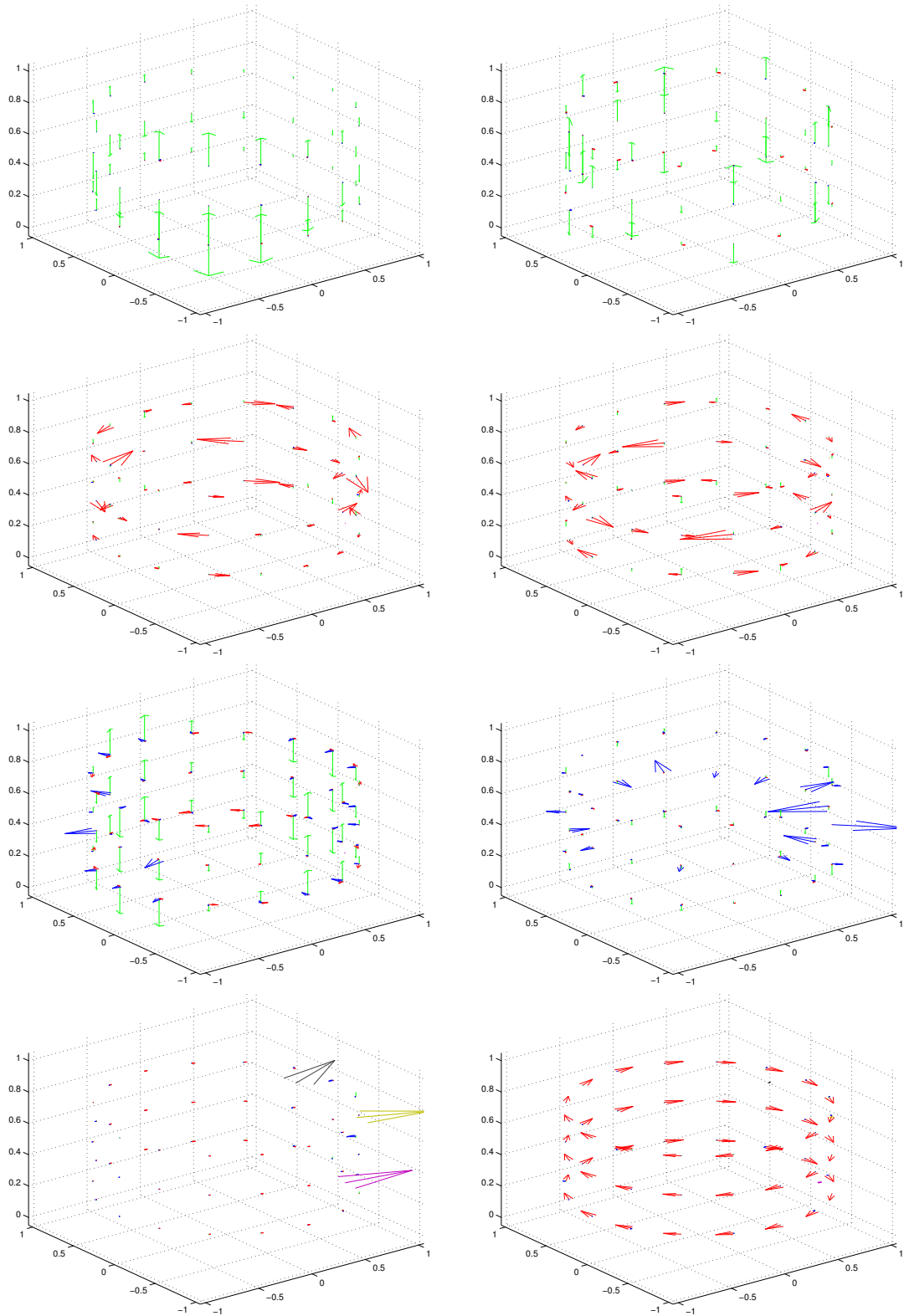


Figure 4.7: Singular vectors for boundary shape Jacobian on cylindrical domain with $A = 1$ measurement strategy with no measurements on driven electrodes. Green indicates components of movement in z -direction, red in the angular direction and blue in the radial direction. The left hand column corresponds to singular values 1, 49, 91, 144 and the right hand column to singular values 8, 51, 97, 147. We notice that in comparison to figure 4.6 the largest singular values 1 – 48 correspond to changes along the z -axis of the cylinder, and the singular values 97 – 144 now correspond to normal changes in the boundary at the electrodes. This highlights that measurements at the driven electrodes are best at determining the normal shape change, whereas measurements near to the driven electrodes are best at determining the tangential movement of electrodes.

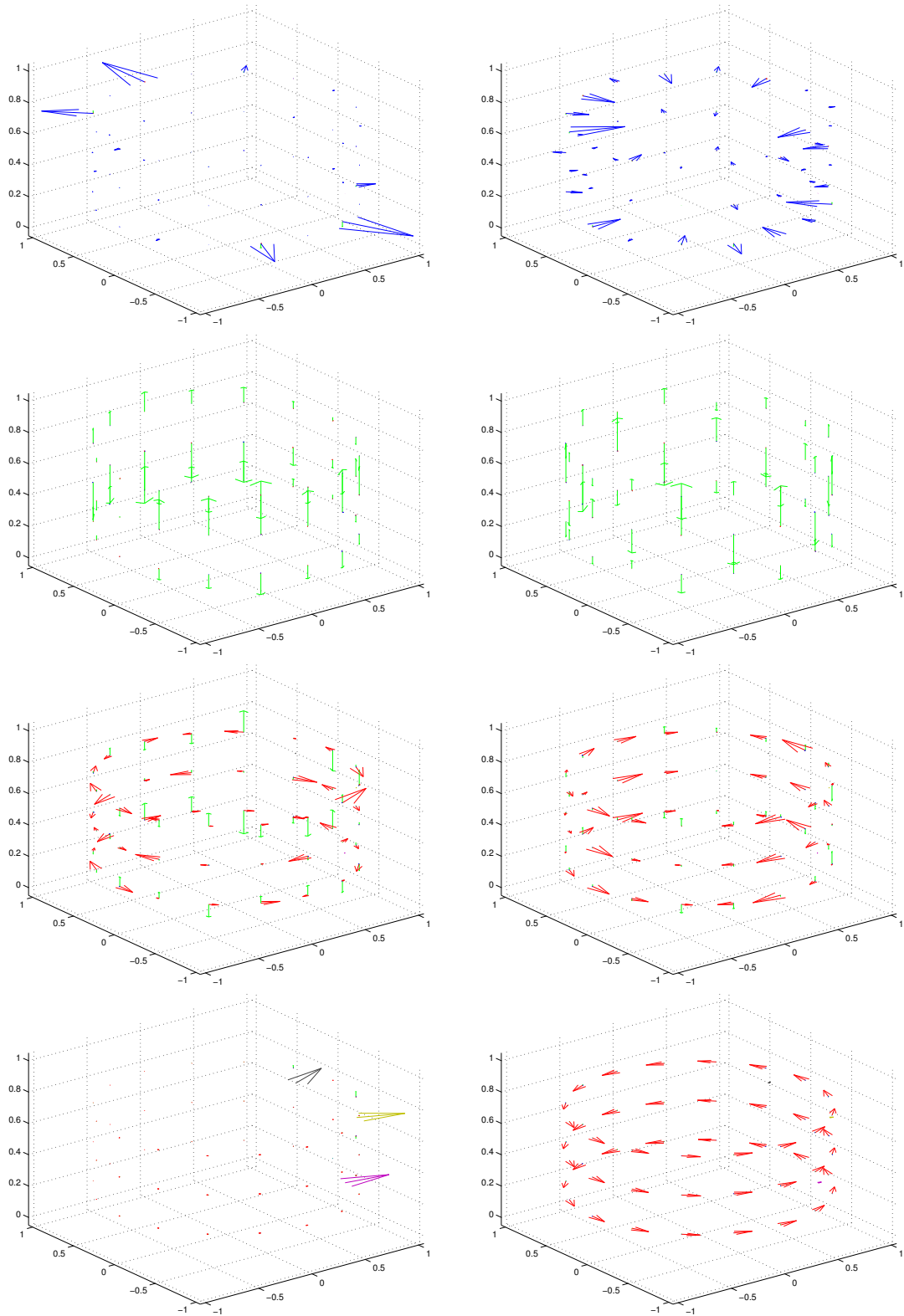


Figure 4.8: Singular vectors for boundary shape Jacobian on cylindrical domain with $A = 23$ measurement strategy with measurements recorded on driven electrodes. Green indicates components of movement in z -direction, red in the angular direction and blue in the radial direction. The left hand column corresponds to singular values 1, 49, 91, 144 and the right hand column to singular values 8, 51, 97, 147. Singular vectors 1 – 48 are typically dominated by normal perturbations of the electrode e.g. 1 and 8 above. Singular vectors 49 – 96 are typically dominated by perturbations of the electrodes aligned with the z -axis. Singular vectors 97 – 143 typically dominated by azimuthal changes in the electrodes. The smallest singular vectors 144 – 146 are associated with normal changes of the boundary away from the driven electrode and the smallest singular vector 147 corresponds to the single rotational similarity transformation on the cylinder. The singular vectors are qualitatively similar to the $A = 1$ strategy (see figure 4.6.)

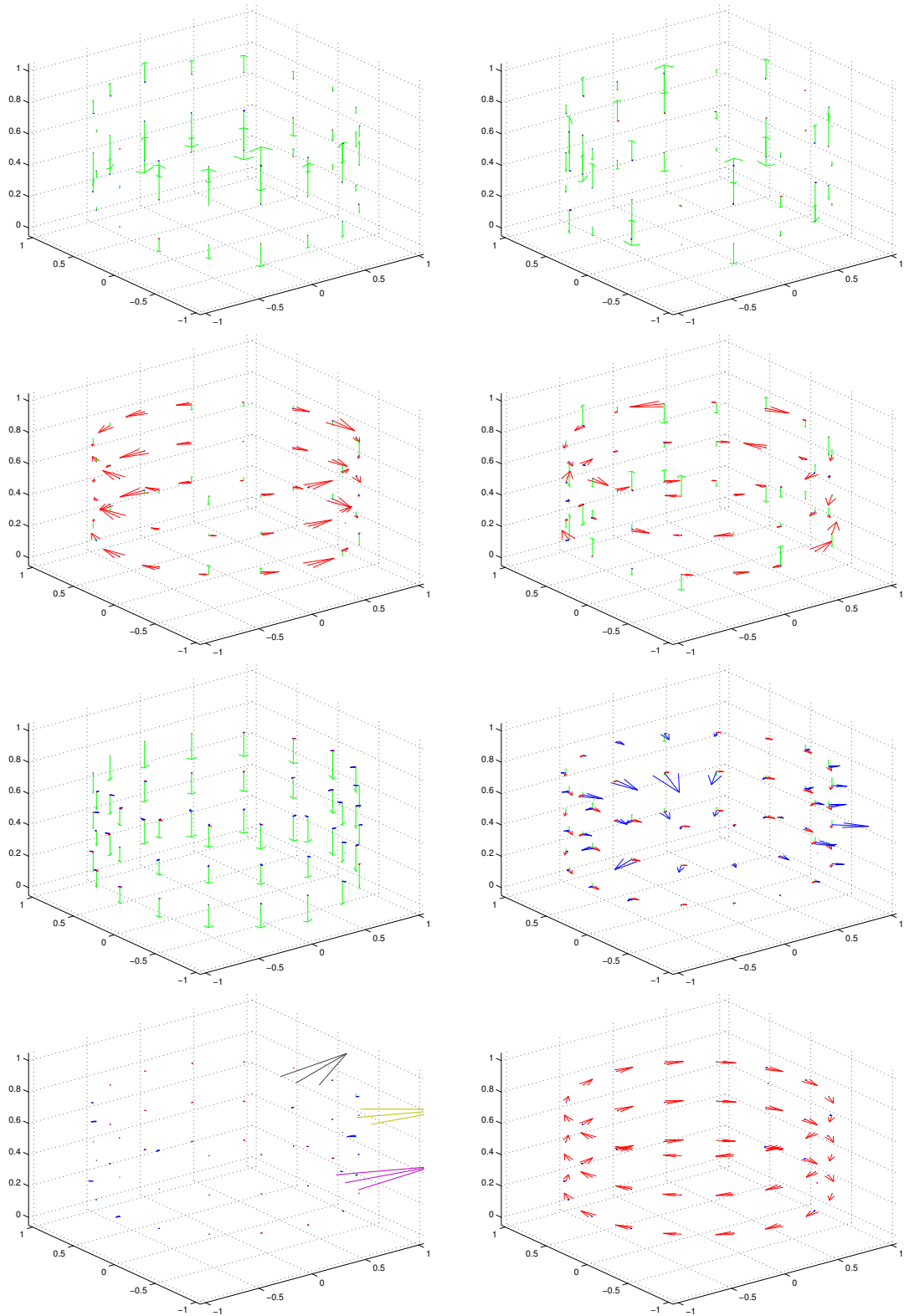


Figure 4.9: Singular vectors for boundary shape Jacobian on cylindrical domain with $A = 23$ measurement strategy and no measurements on driven electrodes. Green indicates components of movement in z -direction, red in the angular direction and blue in the radial direction. The left hand column corresponds to singular values 1, 49, 91, 144 and the right hand column to singular values 8, 51, 97, 147. We notice that in comparison to figure 4.8 the largest singular values 1 – 48 correspond to changes along the z -axis of the cylinder, and the singular values 97 – 144 now correspond to normal changes in the boundary at the electrodes. This highlights that measurements at the driven electrodes are best at determining the normal shape change, whereas measurements near to the driven electrodes are best at determining the tangential movement of electrodes. The singular vectors are qualitatively similar to the singular vectors of the $A = 1$ strategy (see figure 4.7.)

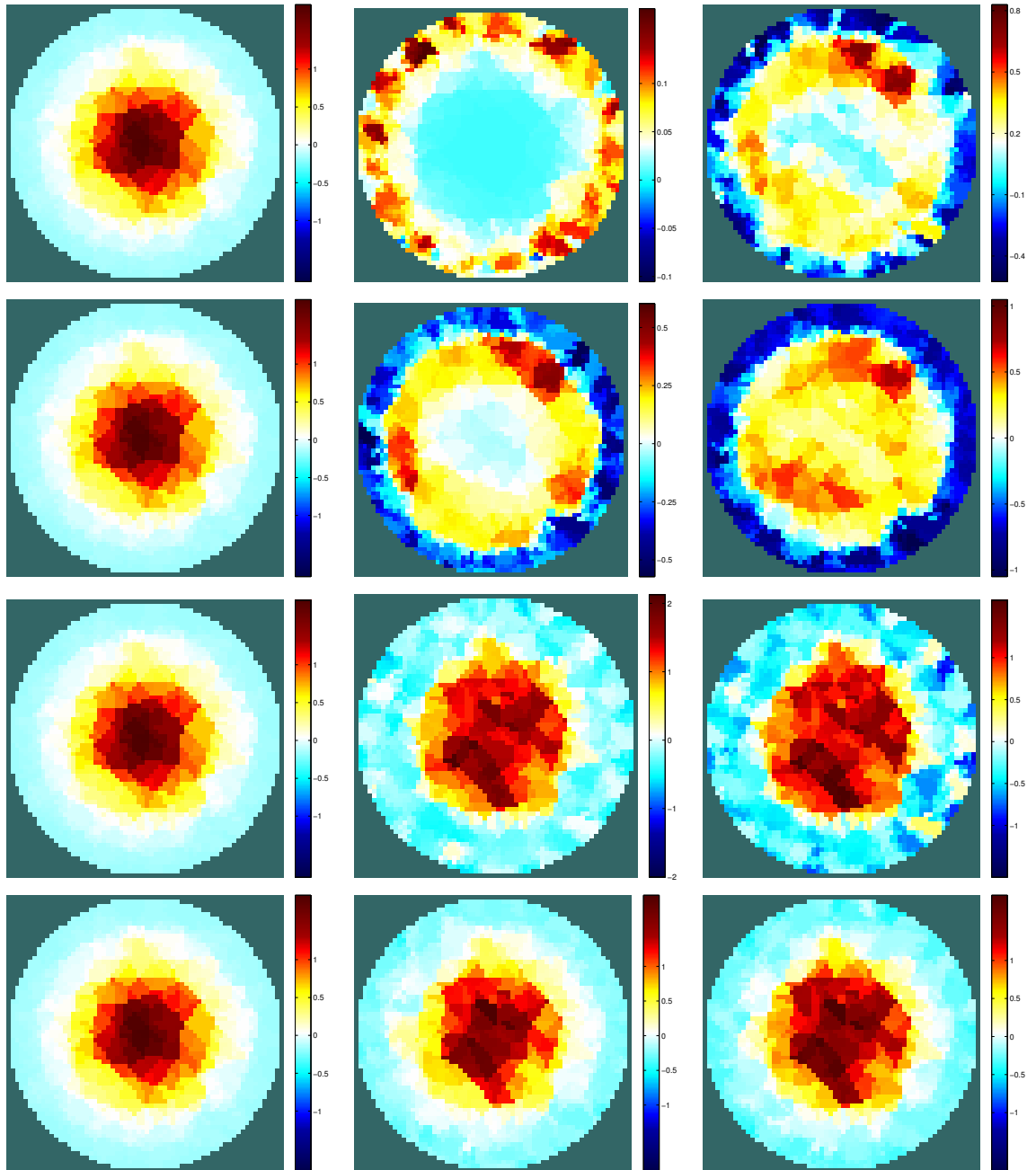


Figure 4.10: SVD projections on xy slice through the centre of spherical interior inclusion. The left, centre and right column indicate the true inclusion, the SVD projection with $A = 1$ measurement strategy and SVD projection with $A = 23$ measurement strategy respectively. Top row to bottom row indicates the projection with $N = 50, 100, 200$ and 300 singular vectors. See table 4.1 for the singular values and errors. We observe that singular vectors with large singular values largely contain information related to the boundary. The $A = 23$ strategy contains slightly more information about the inclusion at a low number ($N = 50, 100$) projections, indicating that this strategy has the potential to be more useful than the traditional $A = 1$ strategy.

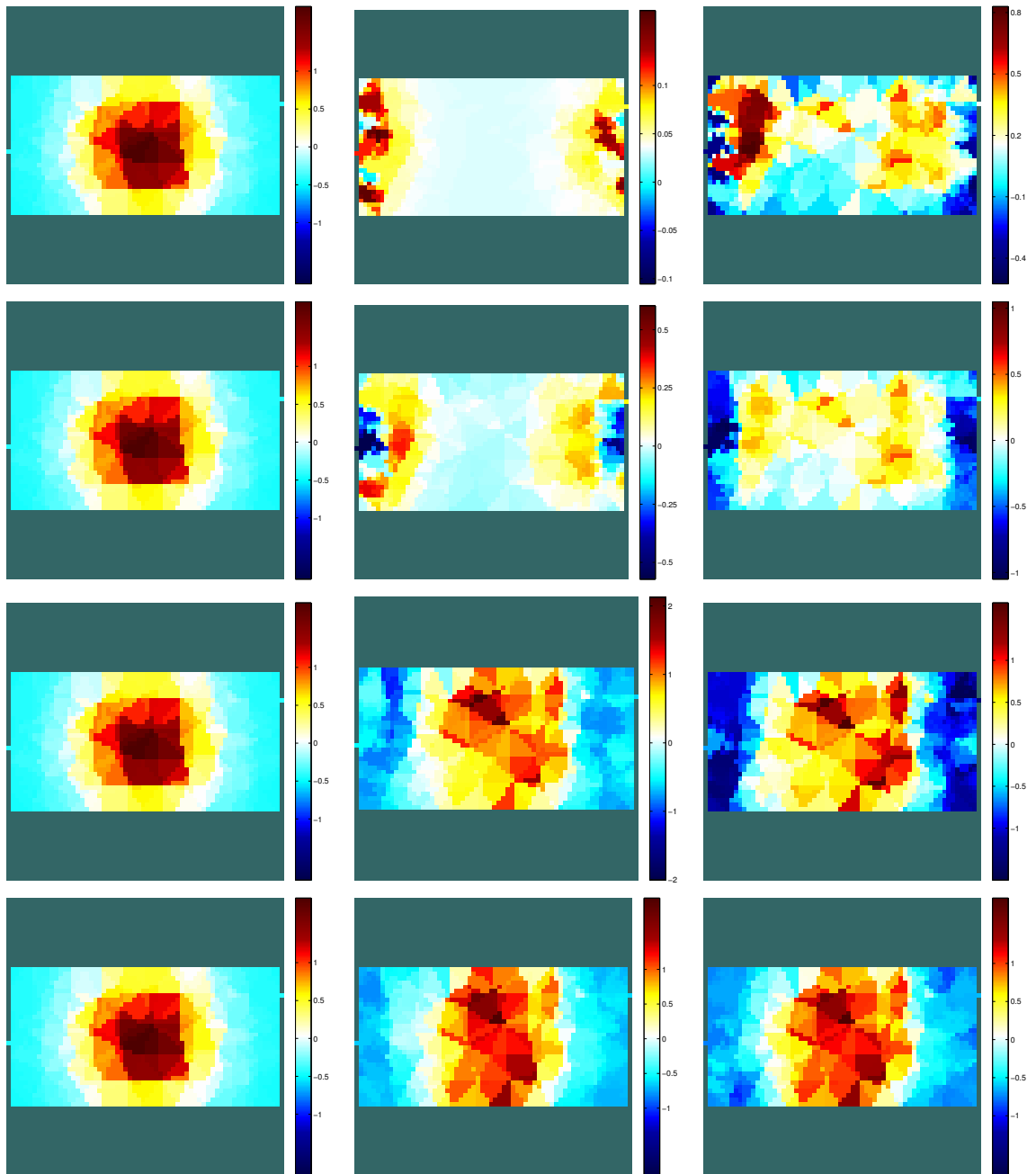


Figure 4.11: SVD projections on xz slice through the centre of spherical interior inclusion. The left, centre and right column indicate the true inclusion, the SVD projection with $A = 1$ measurement strategy and SVD projection with $A = 23$ measurement strategy respectively. Top row to bottom row indicates the projection with $N = 50, 100, 200$ and 300 singular vectors. We observe that singular vectors with large singular values largely contain information related to the boundary. We also observe that the singular vectors, even with $N = 300$ projections, do not resolve along the z -axis well for either strategy, indicating that vertical resolution in thoracic EIT is difficult. Again it appears that the $A = 23$ strategy contains slightly more information about the inclusion at a low number ($N = 50, 100$) projections, indicating that this strategy has the potential to be more useful than the traditional $A = 1$ strategy.

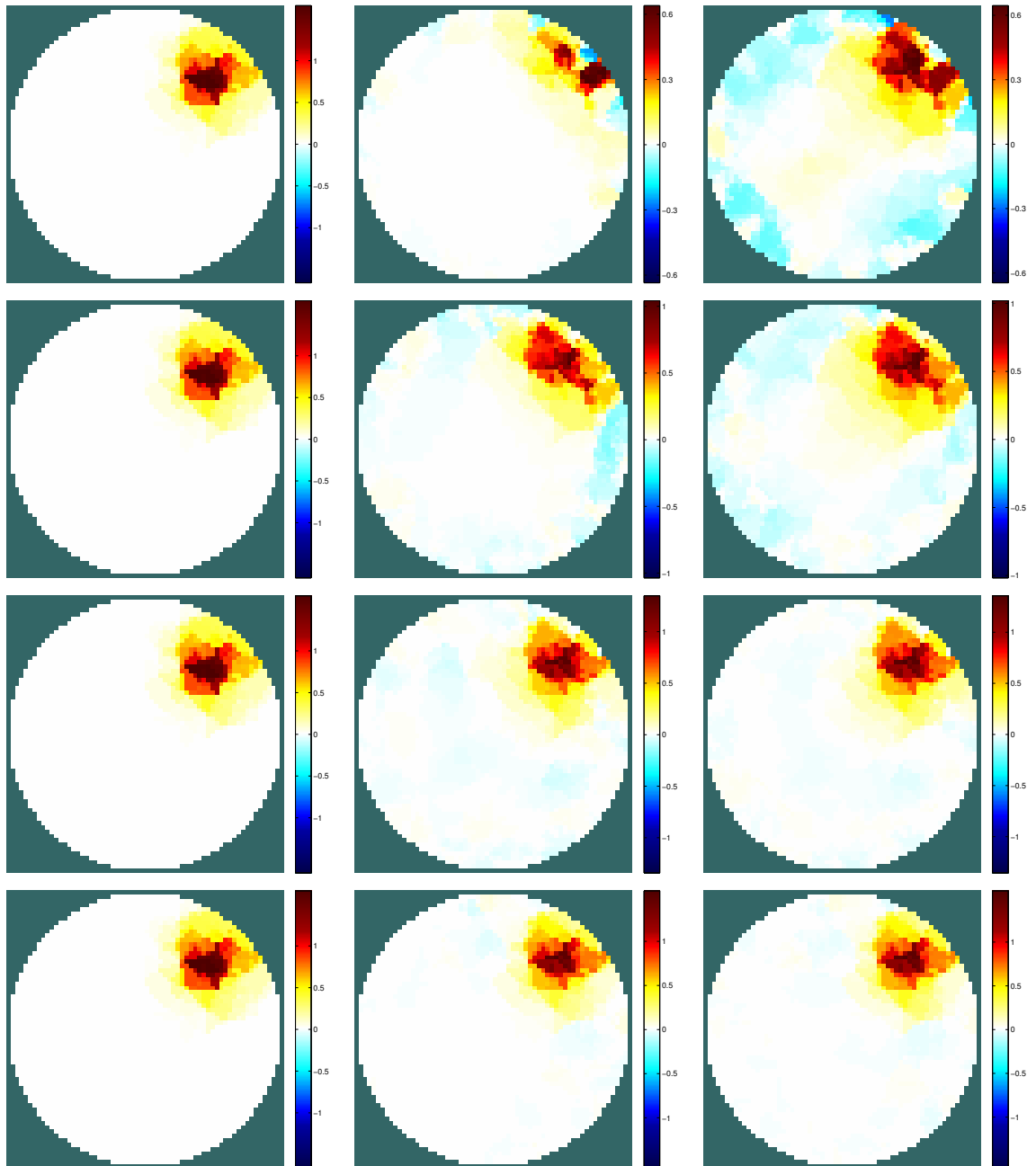


Figure 4.12: SVD projections on xy slice through the centre of spherical boundary inclusion. The left, centre and right column indicate the true inclusion, the SVD projection with $A = 1$ measurement strategy and SVD projection with $A = 23$ measurement strategy respectively. Top row to bottom row indicates the projection with $N = 50, 100, 200$ and 300 singular vectors. See table 4.2 for the singular values and errors. We observe that even with a small number of projections $N = 100$, the boundary inclusion is resolved well, highlighting that boundary inhomogeneities are easier to detect with EIT.

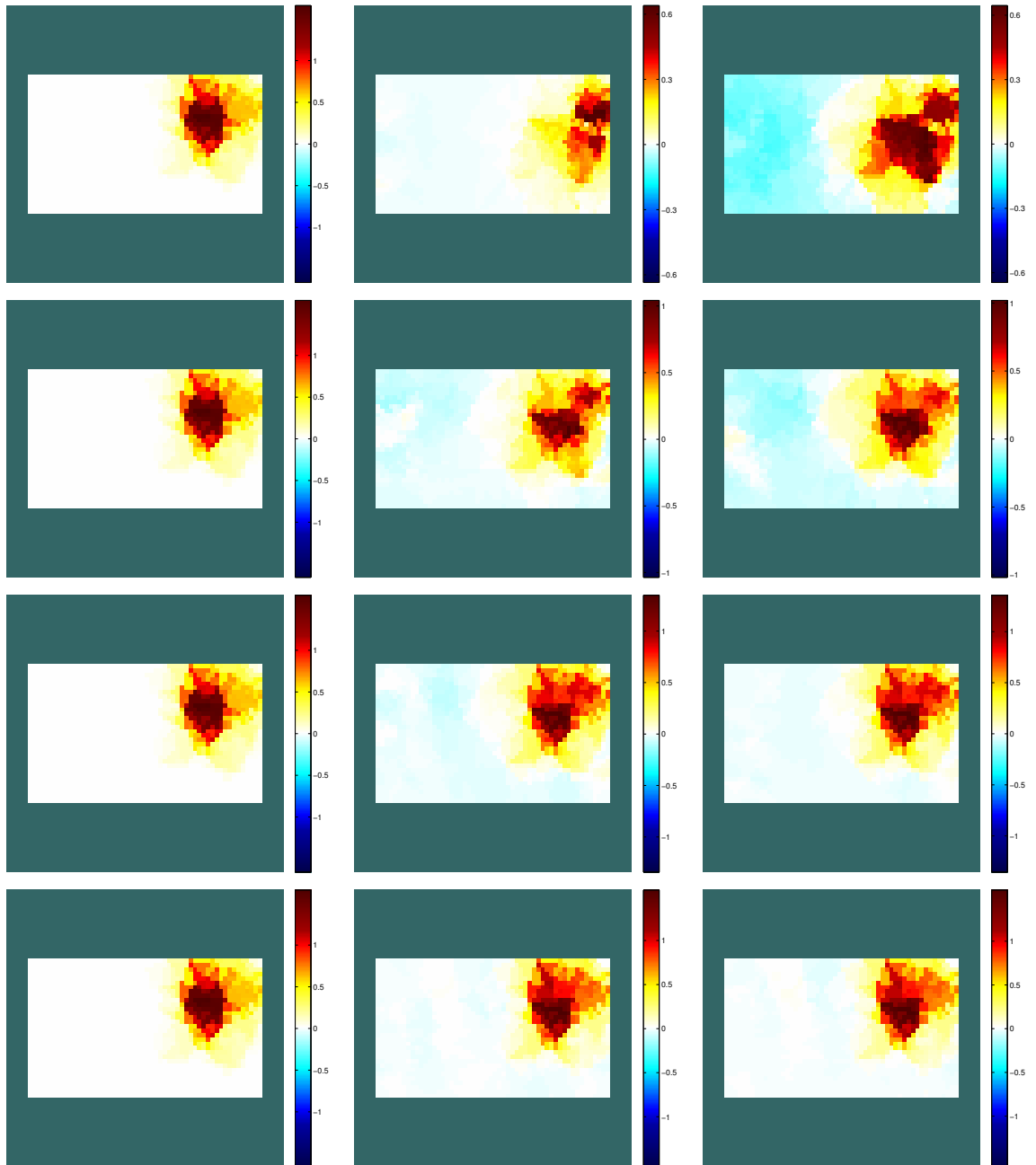


Figure 4.13: SVD projections on xz slice through the centre of spherical boundary inclusion. The left, centre and right column indicate the true inclusion, the SVD projection with $A = 1$ measurement strategy and SVD projection with $A = 23$ measurement strategy respectively. Top row to bottom row indicates the projection with $N = 50, 100, 200$ and 300 singular vectors. We observe that a large number of projections $N = 200$ is required to resolve the boundary inclusion well in the vertical direction.

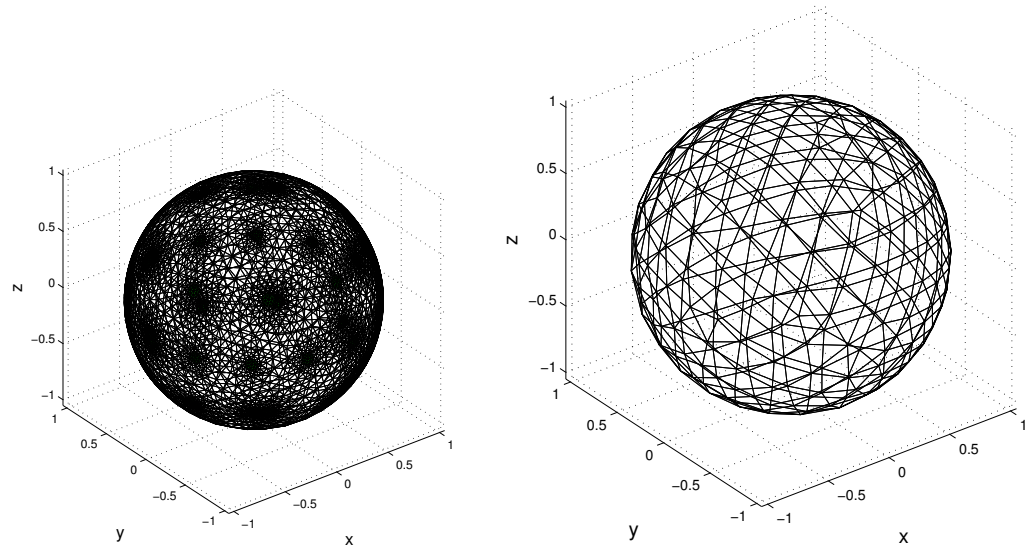


Figure 4.14: Sphere: Initial fine discretisation and coarse discretisation. The left and right hand image corresponds to the initial fine and coarse reconstruction models with approximately 32000 and 1100 elements respectively. The coarse discretisation is dilated by a factor of 1.05 from the fine discretisation.

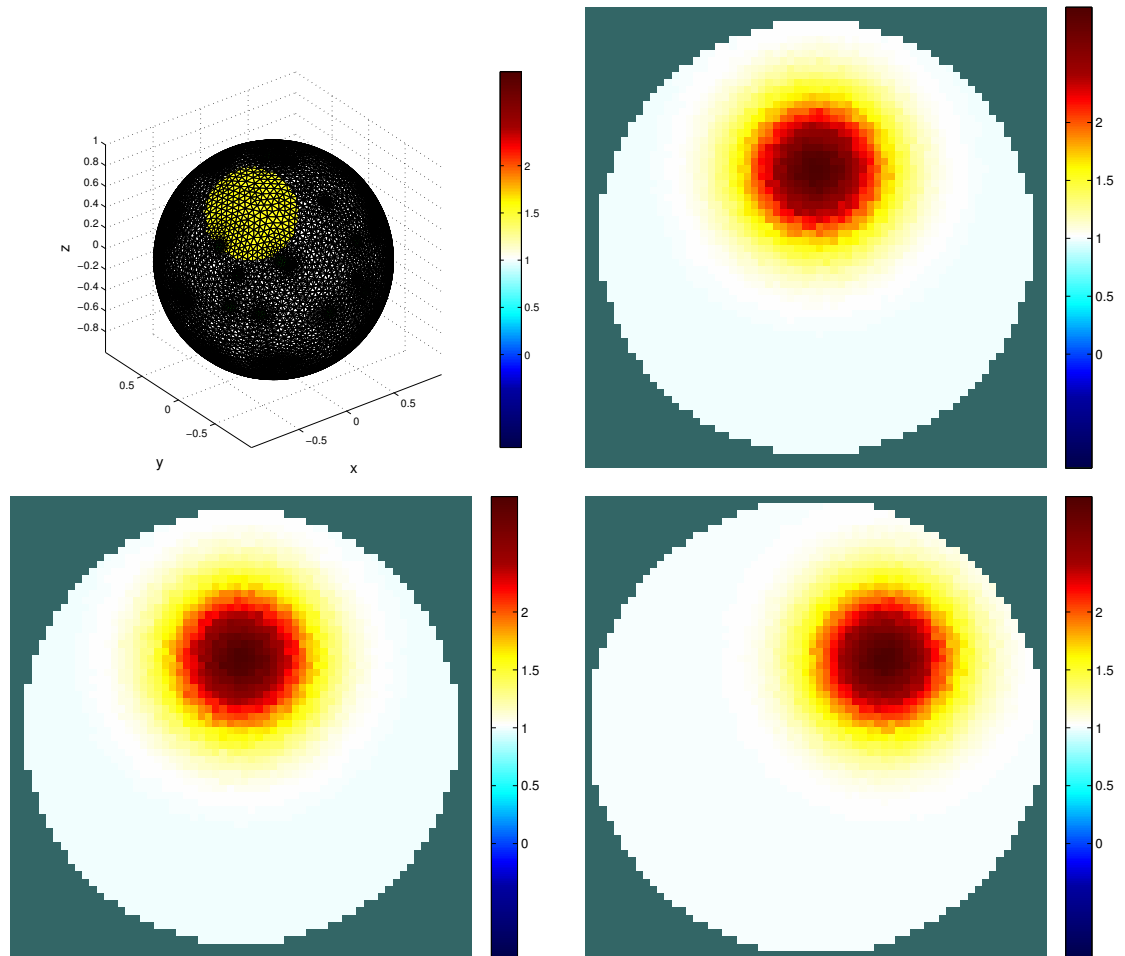


Figure 4.15: Sphere: Unknown conductivity and unknown electrode positions with $p = 0.1$. The top left hand image is a 3D visualisation, the top right, bottom left and bottom right are planes perpendicular to the z-axis, y-axis and x-axis respectively through the inclusion centre.

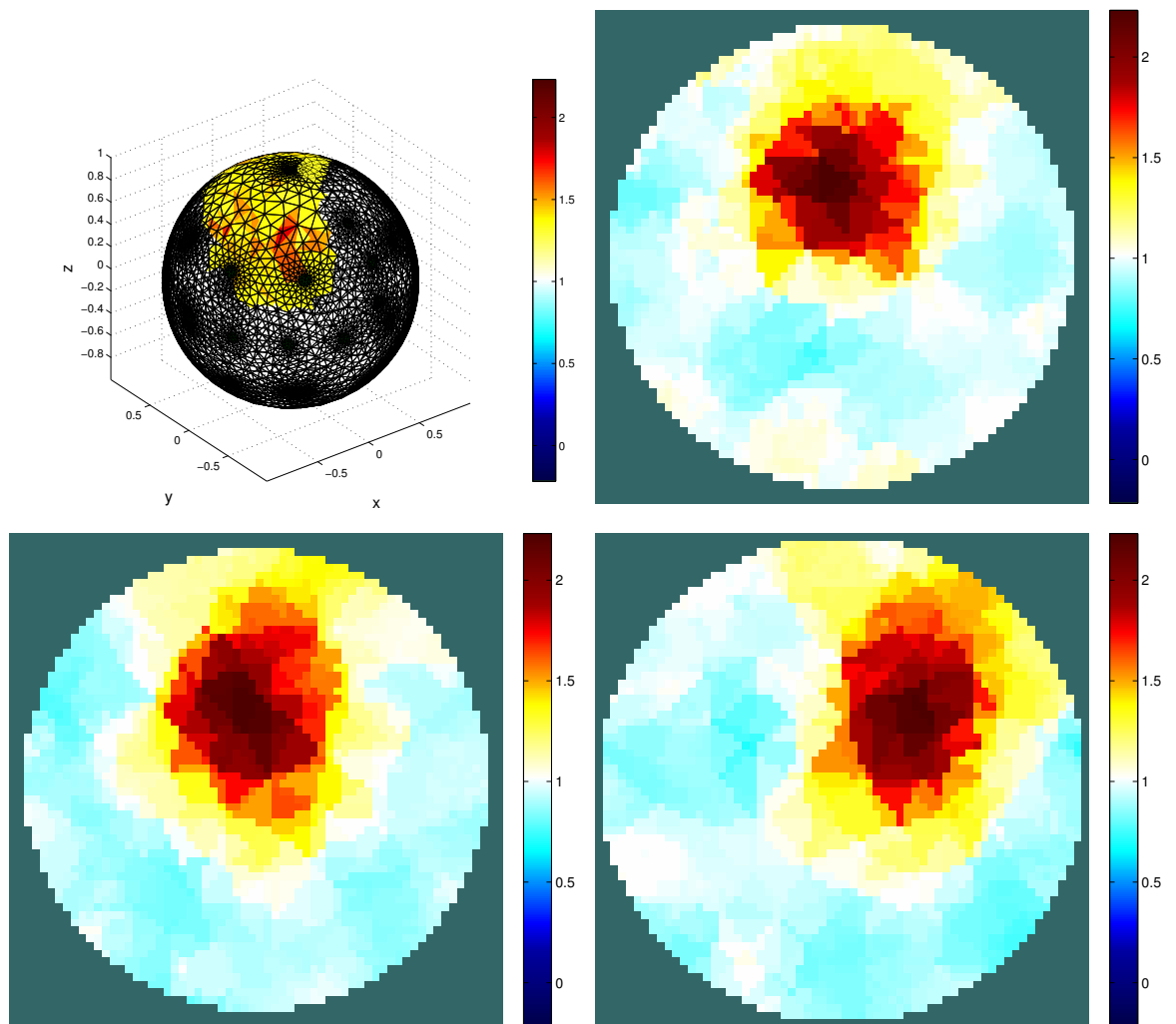


Figure 4.16: Sphere: Reconstructed conductivity with electrode positions known. The top left hand image is a 3D visualisation, the top right, bottom left and bottom right are planes perpendicular to the z-axis, y-axis and x-axis respectively through the inclusion centre. A hyperparameter of $\alpha = 10^{-5}$ was used for reconstruction.

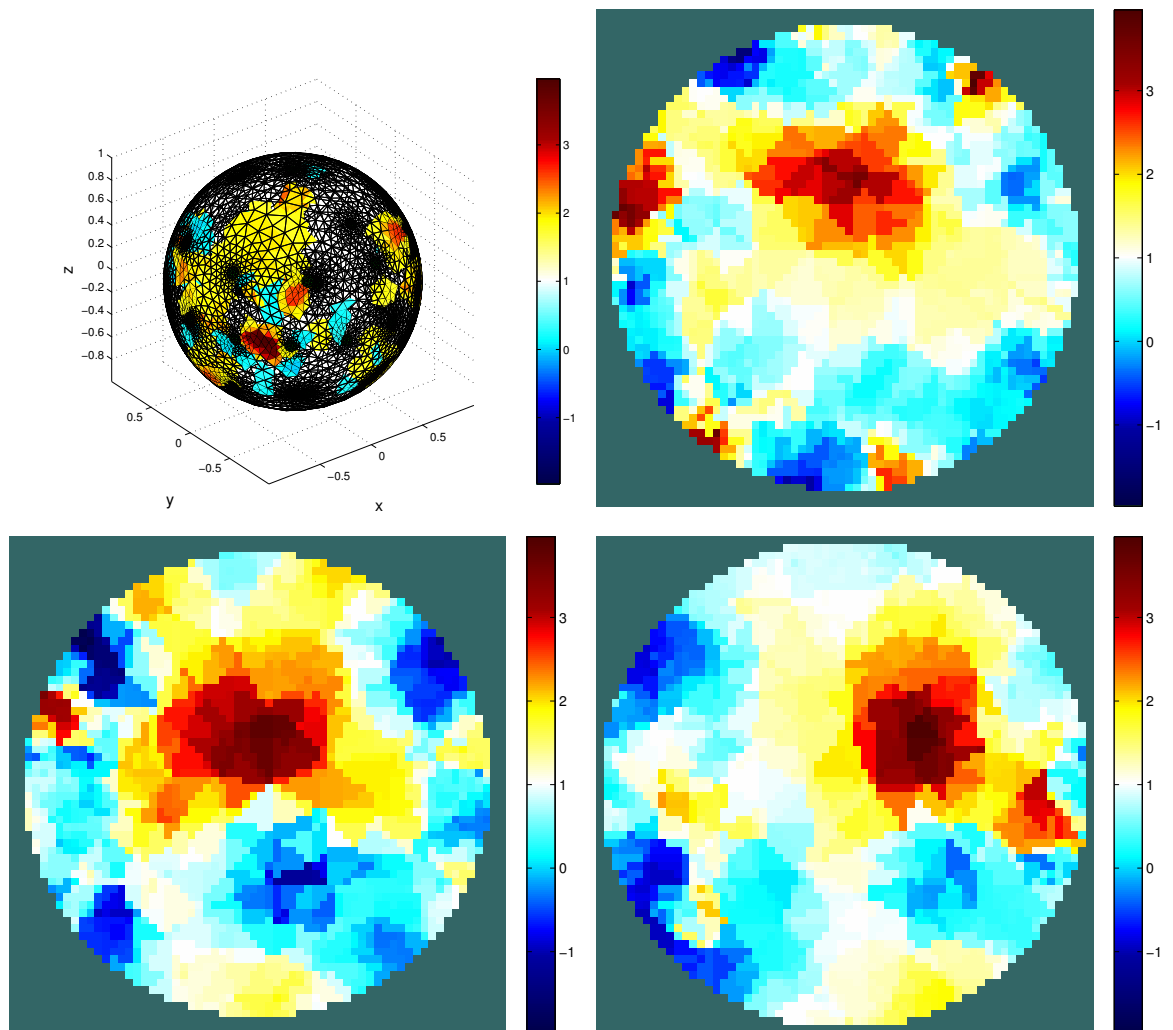


Figure 4.17: Sphere: Reconstructed conductivity without shape correction $p = 0.1$. The top left hand image is a 3D visualisation, the top right, bottom left and bottom right are planes perpendicular to the z-axis, y-axis and x-axis respectively through the inclusion centre. A hyperparameter of $\alpha = 10^{-5}$ was used for reconstruction.

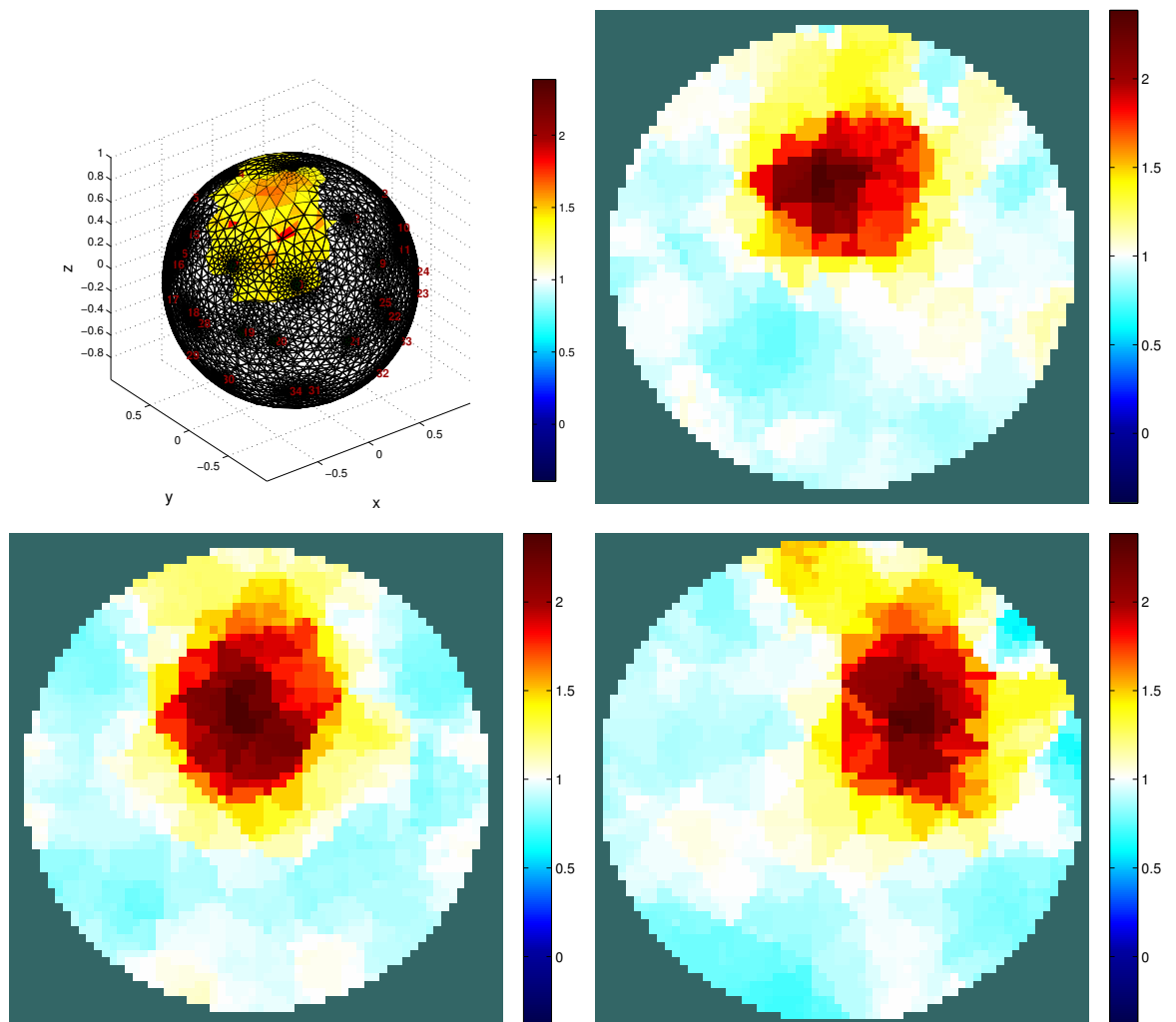


Figure 4.18: Sphere: Reconstructed conductivity using shape correction algorithm $p = 0.1$. The top left hand image is a 3D visualisation, the top right, bottom left and bottom right are planes perpendicular to the z-axis, y-axis and x-axis respectively through the inclusion centre. Hyperparameters of $\alpha = 10^{-5}$ and $\beta = 0.015$ were used for reconstruction.

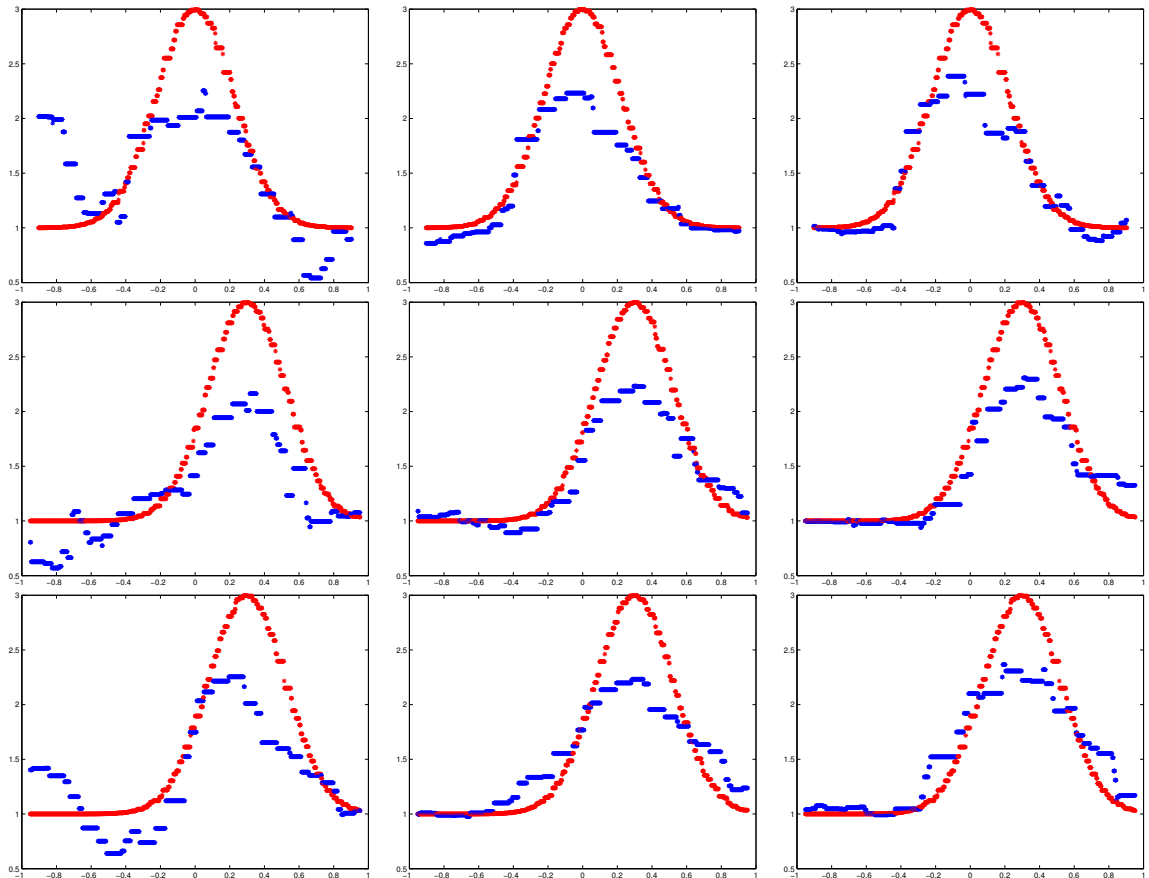


Figure 4.19: Sphere: Reconstructed conductivity lineplots with $p = 0.1$. The left and right column corresponds to a non shape correction and shape correction algorithm with electrode positions unknown respectively and the middle column to a non shape correction algorithm with electrode positions known. The top, middle and bottom row correspond to lineplots parallel to the x -, y - and z -axis respectively through the inclusion centre. The red lines indicates the actual conductivity and the blue lines the estimated conductivity. Hyperparameters of $\alpha = 10^{-5}$ and $\beta = 0.015$ were used for each reconstruction.

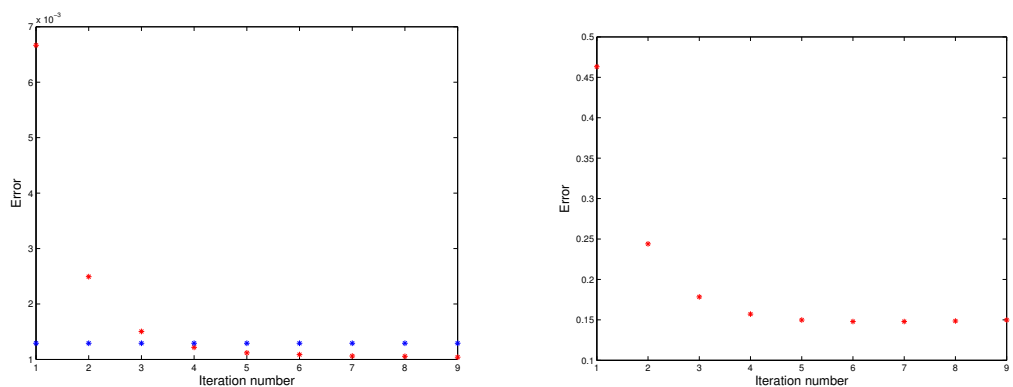


Figure 4.20: Sphere: Electrode position and voltage convergence with $p = 0.1$ and $A = 23$. A hyperparameter of $\beta = 0.015$ was used for reconstruction. The left and right image correspond to the convergence of the voltages and electrode positions respectively. The blue and red line in the left hand figure illustrates the norm of the difference in the voltages between the unknown conductivity and background conductivity with known electrode positions and the norm of the difference in voltage between the unknown conductivity and background conductivity with updated electrode positions. We observe that the voltage error is converging in such a way that the voltage misfit is largely associated with the conductivity perturbation at the end of the first stage of the algorithm.

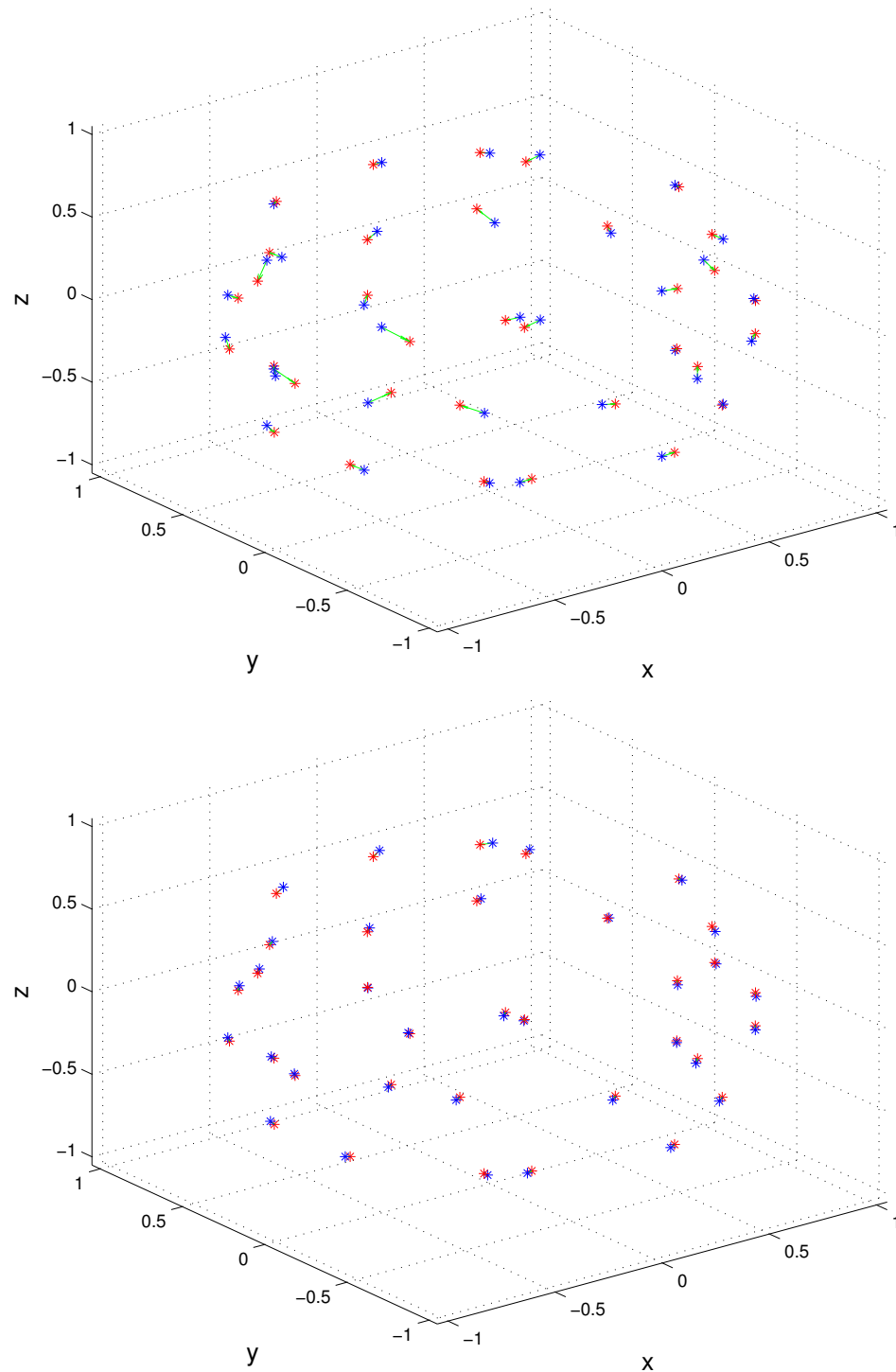


Figure 4.21: Sphere: Electrode position convergence with $p = 0.1$. The blue and red stars correspond to the model and actual electrode positions, and the top and bottom image correspond to the initial guess and final estimate of the model electrode positions. The green lines indicate the differences in electrode positions and we can observe that the electrode positions have been estimated well at the end of the algorithm. A hyperparameter $\beta = 0.015$ was used for electrode position reconstruction.

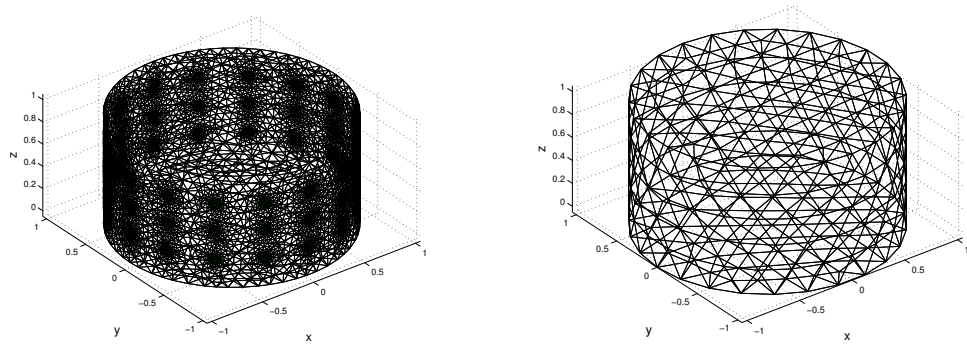


Figure 4.22: Cylinder: Initial fine and coarse discretisation. The left and right hand image corresponds to the initial fine and coarse reconstruction models with approximately 37000 and 1300 elements respectively. The coarse discretisation is dilated by a factor of 1.05 relative to the fine discretisation.

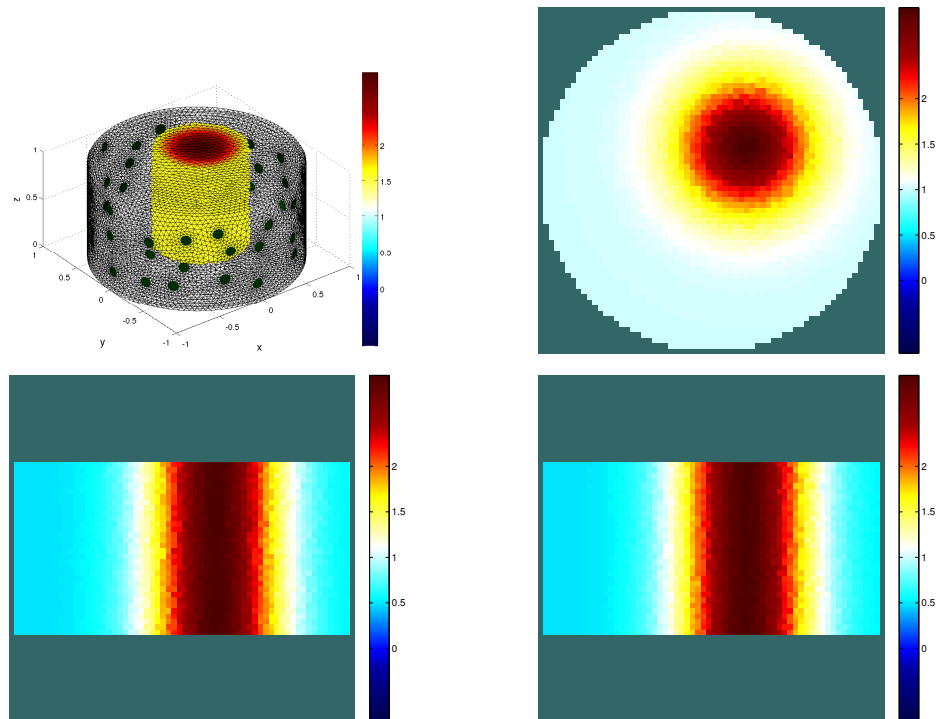


Figure 4.23: Cylinder with cylindrical inclusion: Unknown conductivity and unknown electrode positions with $p = 0.1$. The top left hand image is a 3D visualisation, the top right, bottom left and bottom right are planes perpendicular to the z , y and x axis respectively through the inclusion centre.

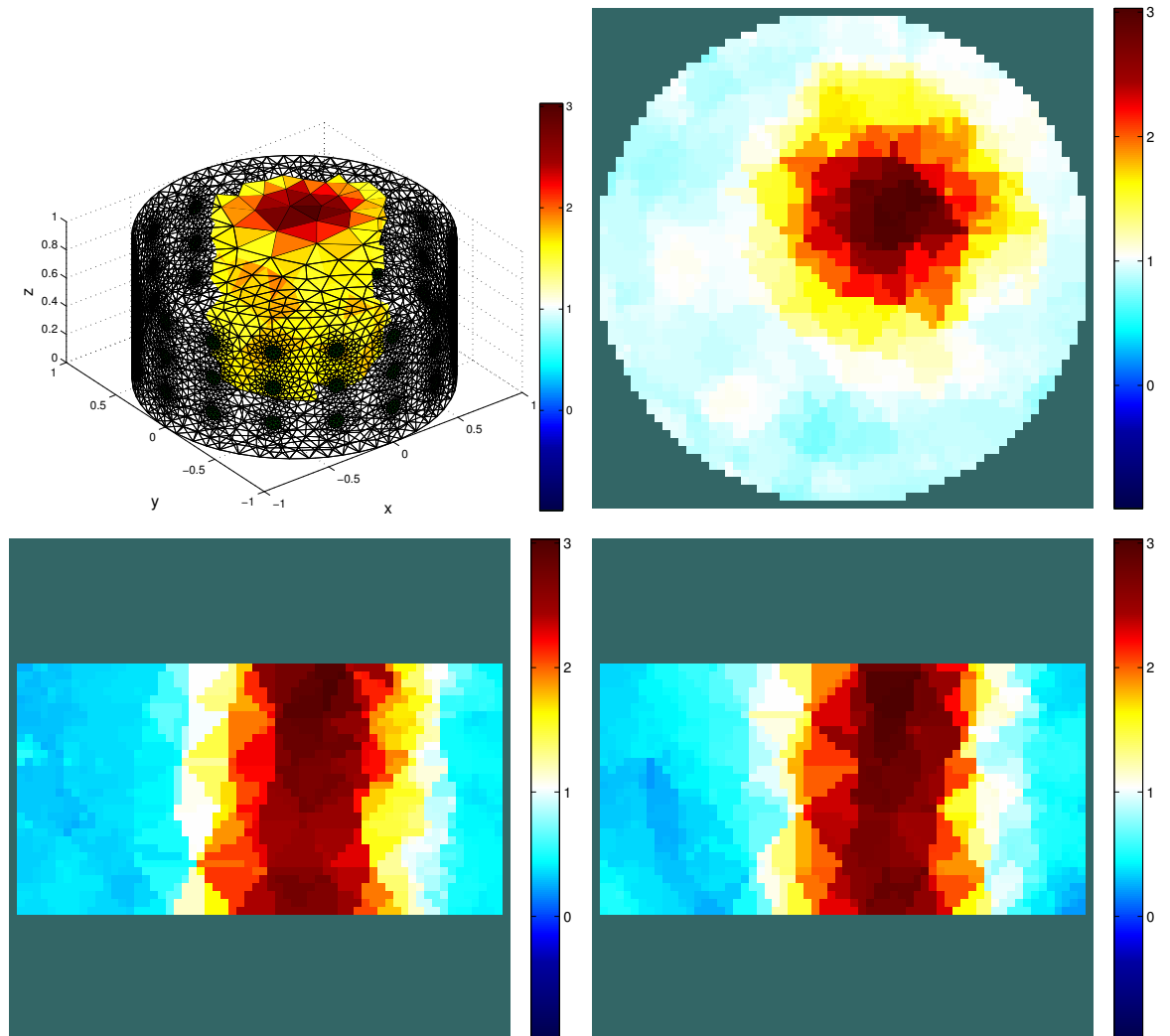


Figure 4.24: Cylinder with cylindrical inclusion. Reconstructed conductivity with electrode positions known and $A = 1$. The top left hand image is a 3D visualisation, the top right, bottom left and bottom right are planes perpendicular to the z-axis, y-axis and x-axis respectively through the inclusion centre. A hyperparameter of $\alpha = 2 \times 10^{-5}$ was used for reconstruction and an $A = 1$ measurement strategy adopted.

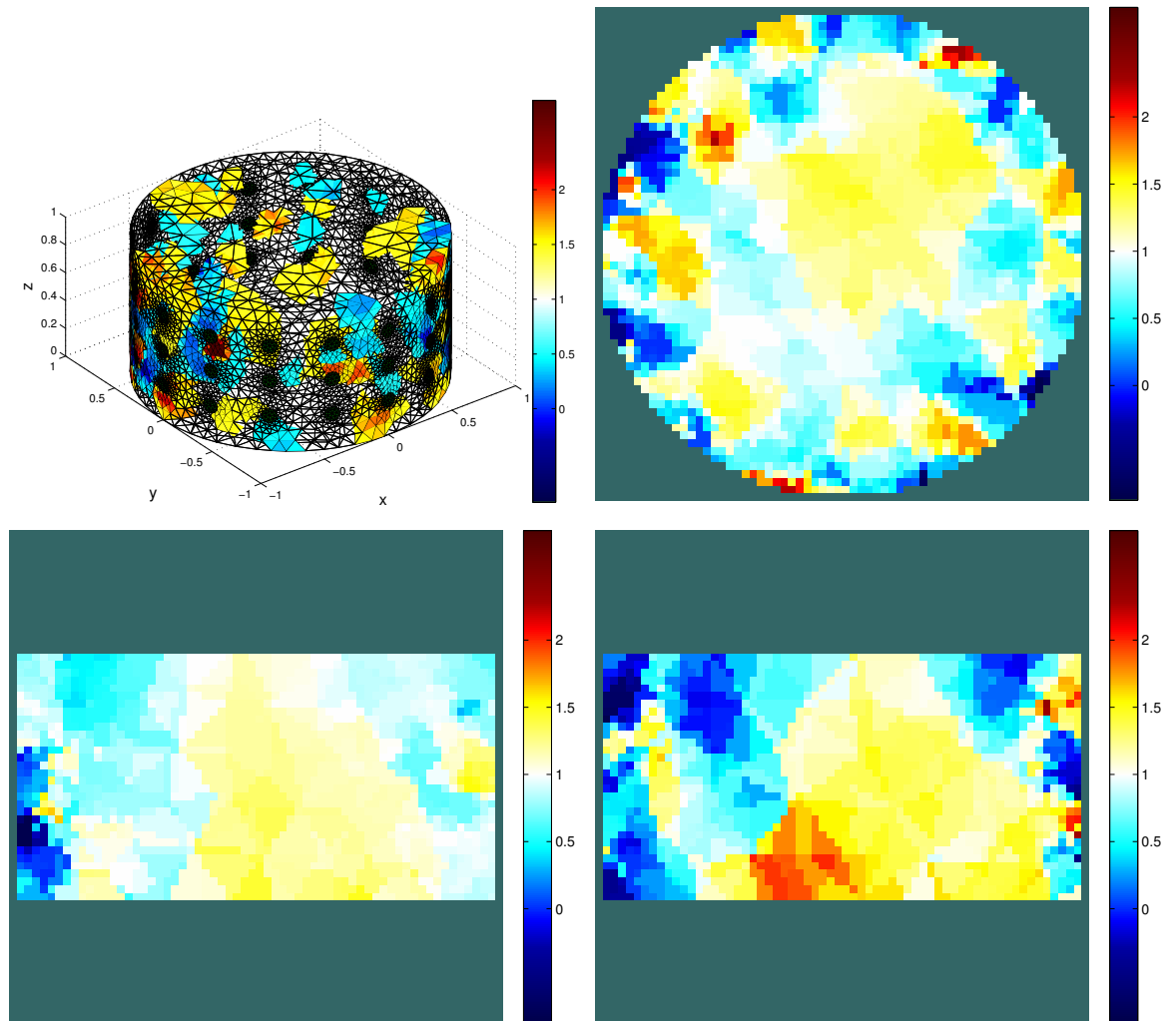


Figure 4.25: Cylinder with cylindrical inclusion: Reconstructed conductivity without shape correction $p = 0.1$ and $A = 1$. The top left hand image is a 3D visualisation, the top right, bottom left and bottom right are planes perpendicular to the z-axis, y-axis and x-axis respectively through the inclusion centre. A hyperparameter of $\alpha = 2 \times 10^{-5}$ was used for reconstruction and an $A = 1$ measurement strategy adopted.

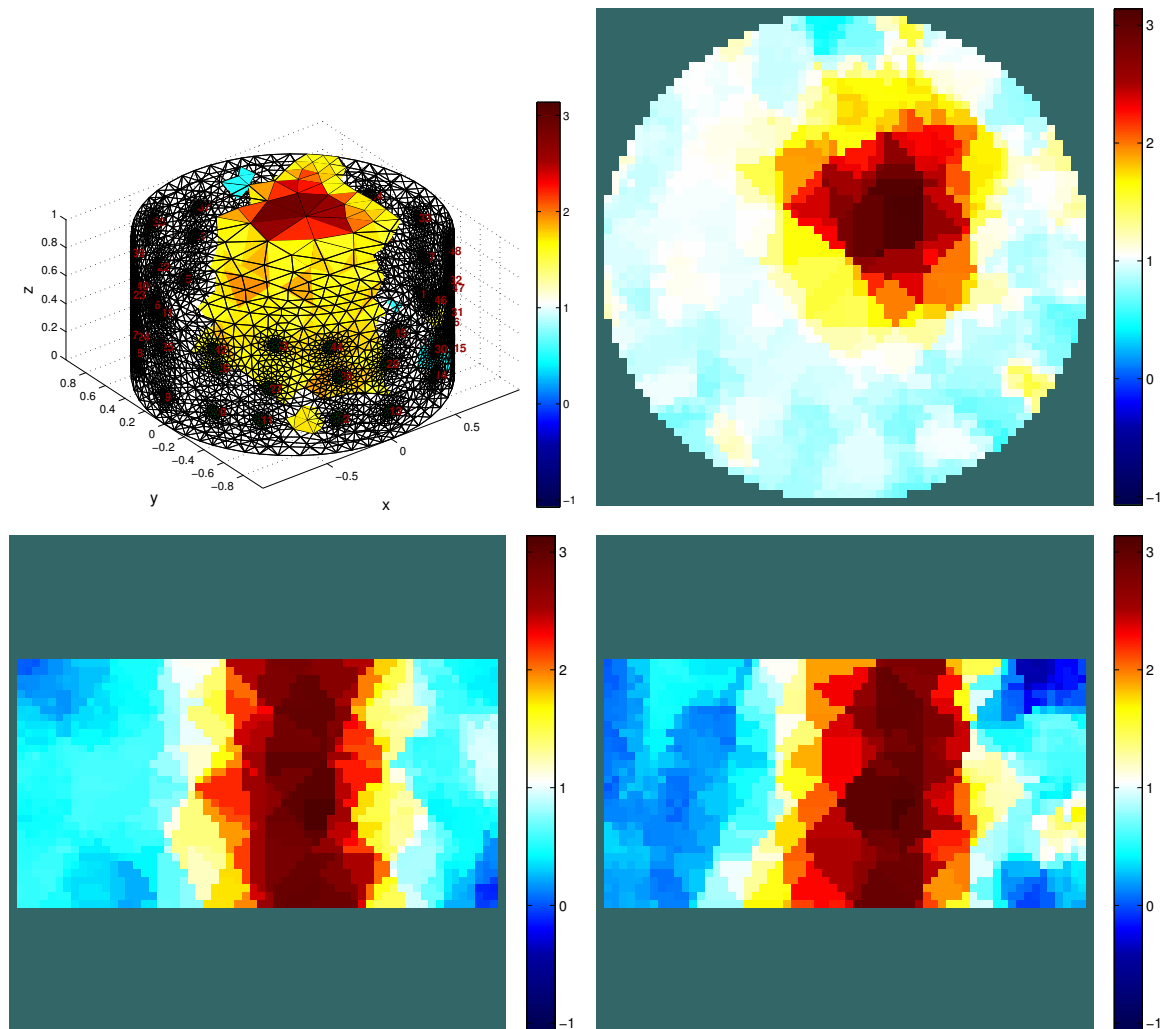


Figure 4.26: Cylinder with cylindrical inclusion: Reconstructed conductivity using shape correction algorithm $p = 0.1$ and $A = 1$. The top left hand image is a 3D visualisation, the top right, bottom left and bottom right are planes perpendicular to the z-axis, y-axis and x-axis respectively through the inclusion centre. Hyperparameters of $\alpha = 2 \times 10^{-5}$ and $\beta = 0.1$ were used for reconstruction and an $A = 1$ measurement strategy adopted.

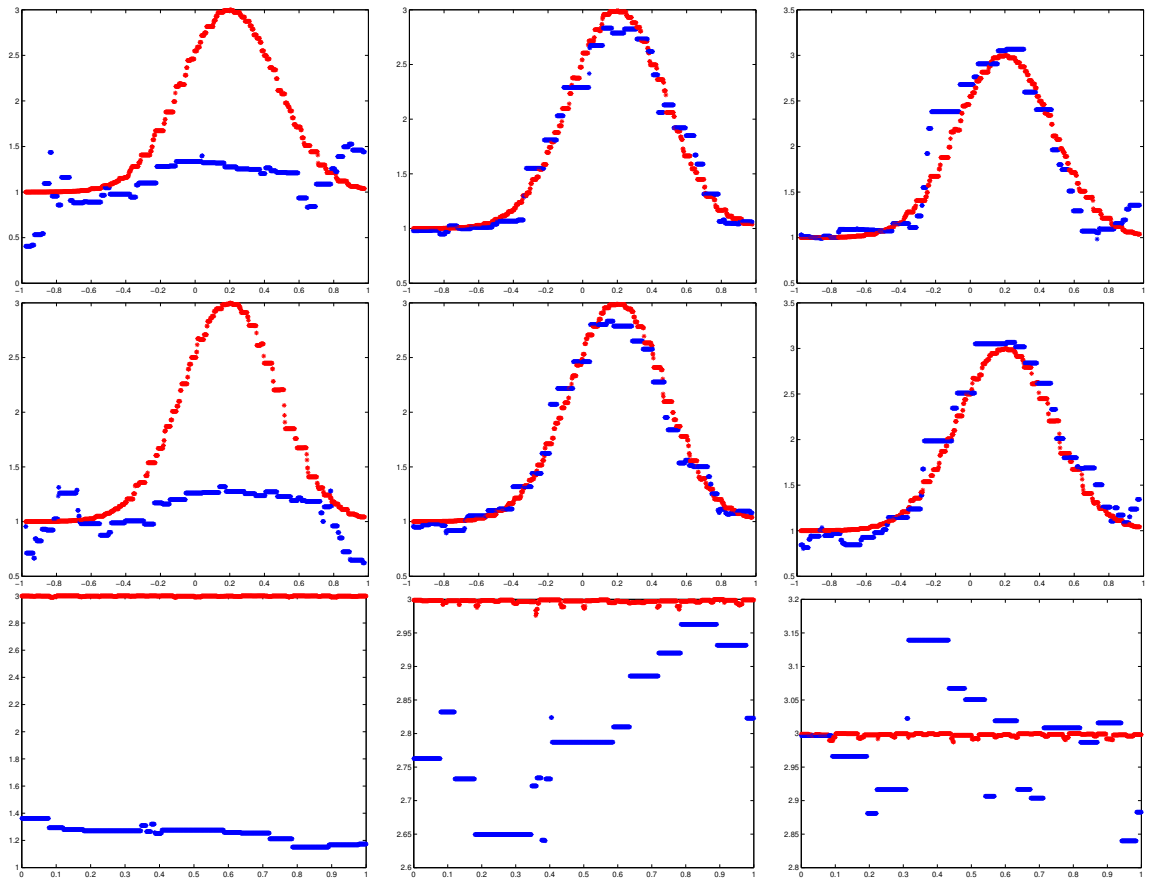


Figure 4.27: Cylinder with cylindrical inclusion: Reconstructed conductivity lineplots with $p = 0.1$ and $A = 1$ with hyperparameters $\alpha = 2 \times 10^{-5}$ and $\beta = 0.1$. The left and right column corresponds to a non shape correction and shape correction algorithm respectively and the middle column corresponds to when the electrode positions are known. The top, middle and bottom row corresponds to the following lineplots. The top row is parallel to the x-axis through $(y,z)=(0.2, 0.5)$, the middle row parallel to the y-axis through $(x,z)=(0.2, 0.5)$ and the bottom row parallel to the z-axis along the inclusion centre. The red and blue lines indicate the actual and estimated conductivity respectively.

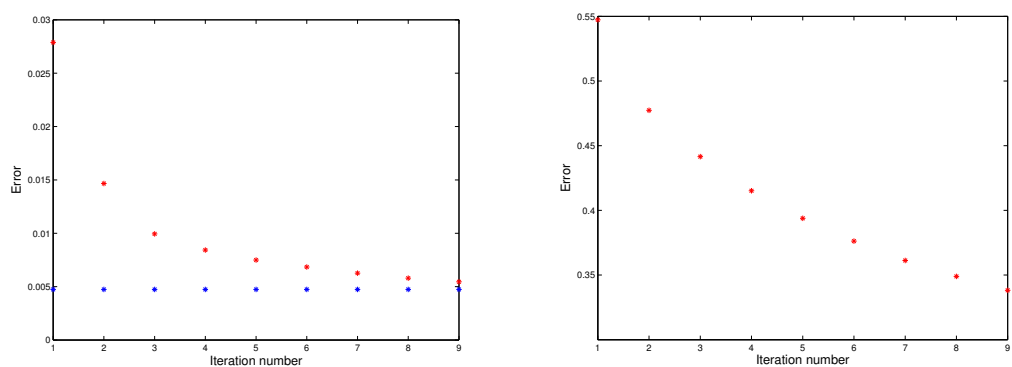


Figure 4.28: Cylinder with cylindrical inclusion: Electrode position and voltage convergence with $p = 0.1$ and $A = 1$. A hyperparameter of $\beta = 0.1$ was used for reconstruction. The left and right image correspond to the convergence of the voltages and electrode positions respectively. The blue and red line in the left hand figure illustrates the norm of the difference in the voltages between the unknown conductivity and background conductivity with known electrode positions and the norm of the difference in voltage between the unknown conductivity and background conductivity with updated electrode positions. We observe that the voltage error is converging in such a way that the voltage misfit at the end of the first stage of the algorithm is largely associated with the conductivity perturbation.

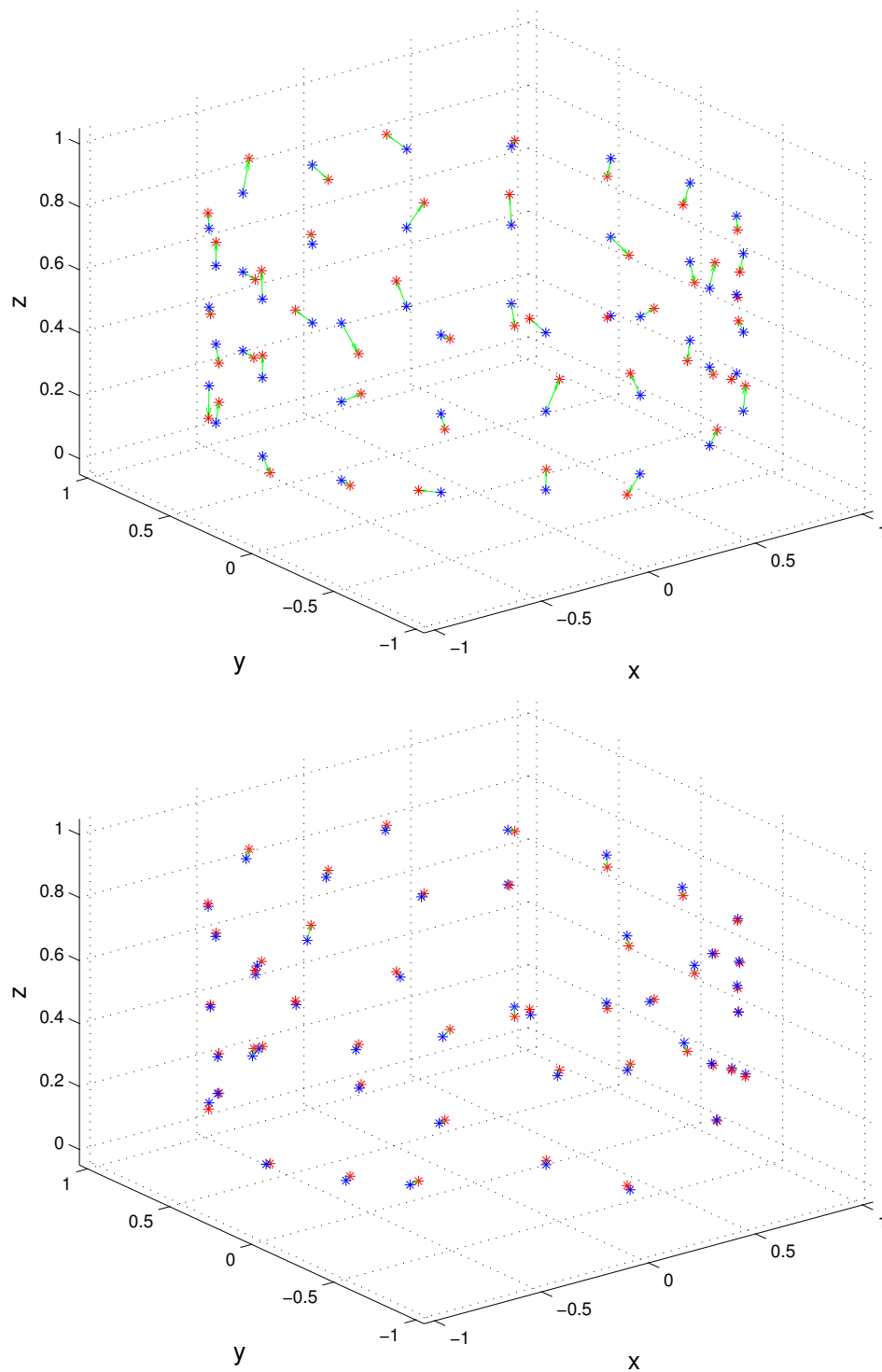


Figure 4.29: Cylinder with cylindrical inclusion: Electrode position convergence with $p = 0.1$ and $A = 1$. The blue and red stars correspond to the model and actual electrode positions, and the left and right image correspond to the initial guess and final estimate of the electrode positions. The green lines indicate the differences in electrode position and we can observe that the electrode positions have been determined well at the end of the algorithm. A hyperparameter of $\beta = 0.1$ was used for each reconstruction and an $A = 1$ measurement strategy adopted.

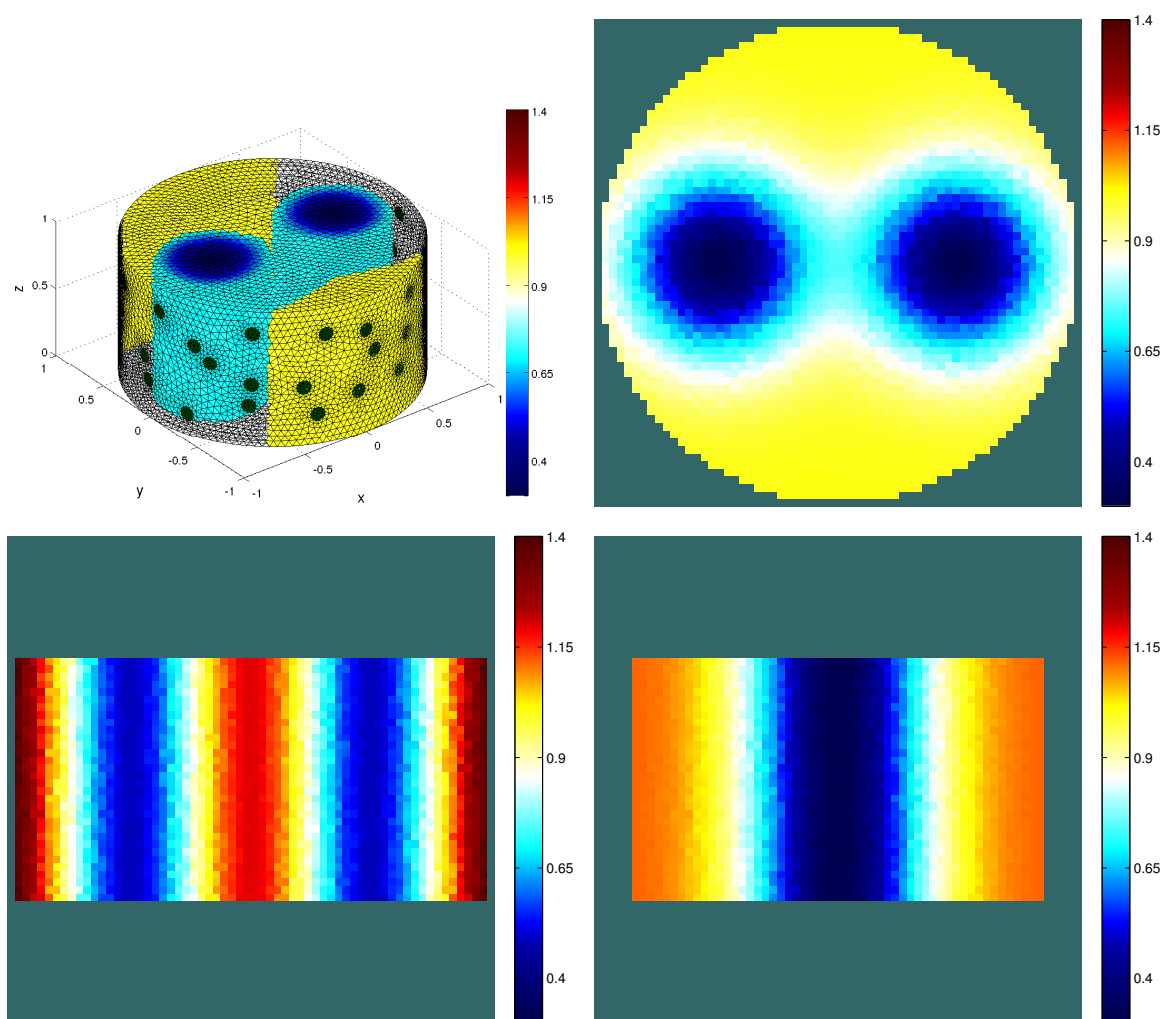


Figure 4.30: Cylinder with two cylindrical inclusions: Unknown conductivity and electrode positions with $p = 0.1$. The top left hand image is a 3D visualisation, the top right, bottom left and bottom right are planes perpendicular to the z-axis, y-axis and x-axis respectively through the centre of inclusion B_1 .

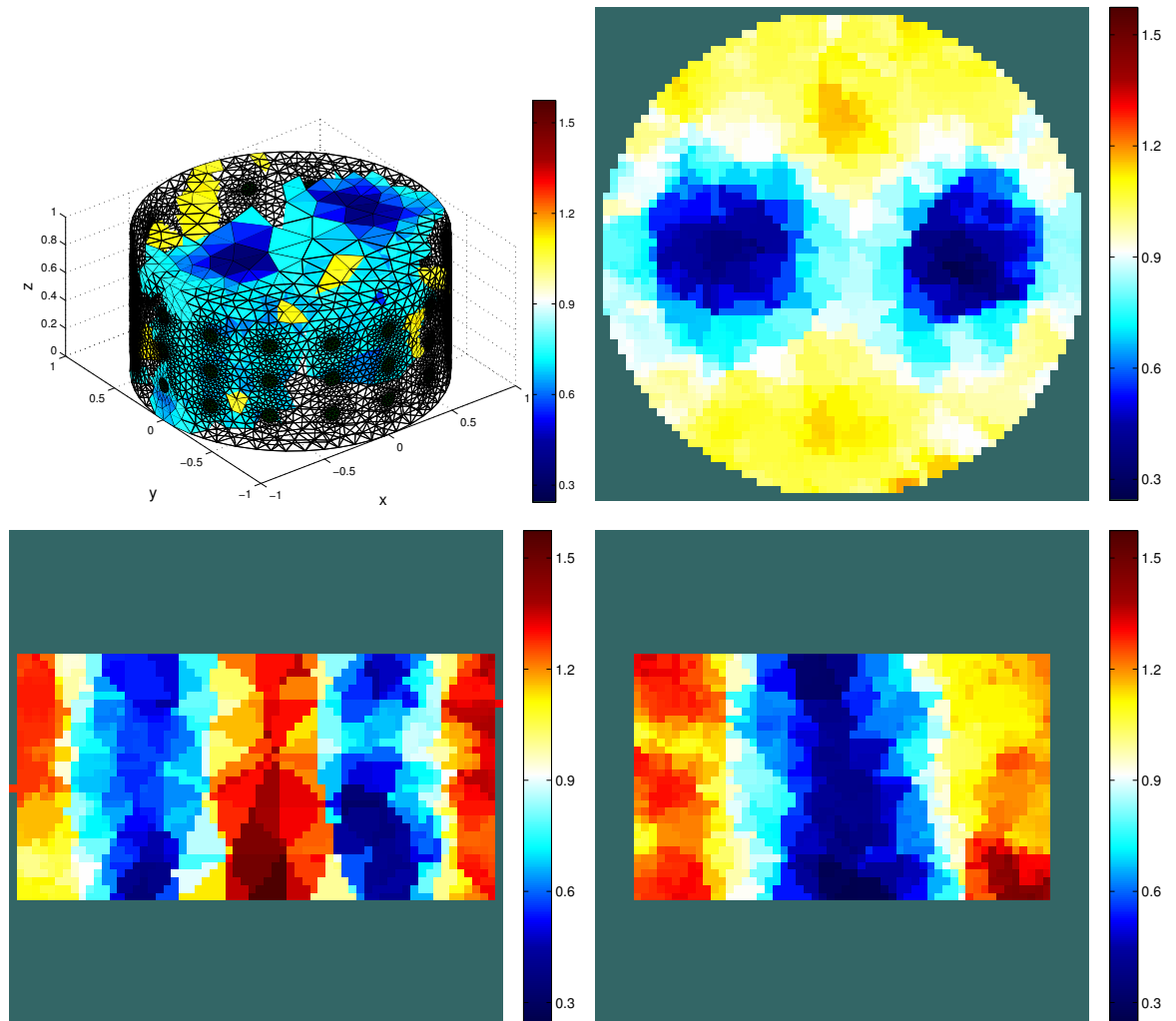


Figure 4.31: Cylinder with two cylindrical inclusions: Reconstructed conductivity with electrode positions known and $A = 1$. The top left hand image is a 3D visualisation, the top right, bottom left and bottom right are planes perpendicular to the z -axis, y -axis and x -axis respectively through the centre of inclusion B_1 . A hyperparameters of $\alpha = 2 \times 10^{-5}$ was used for reconstruction and an $A = 1$ measurement strategy adopted.

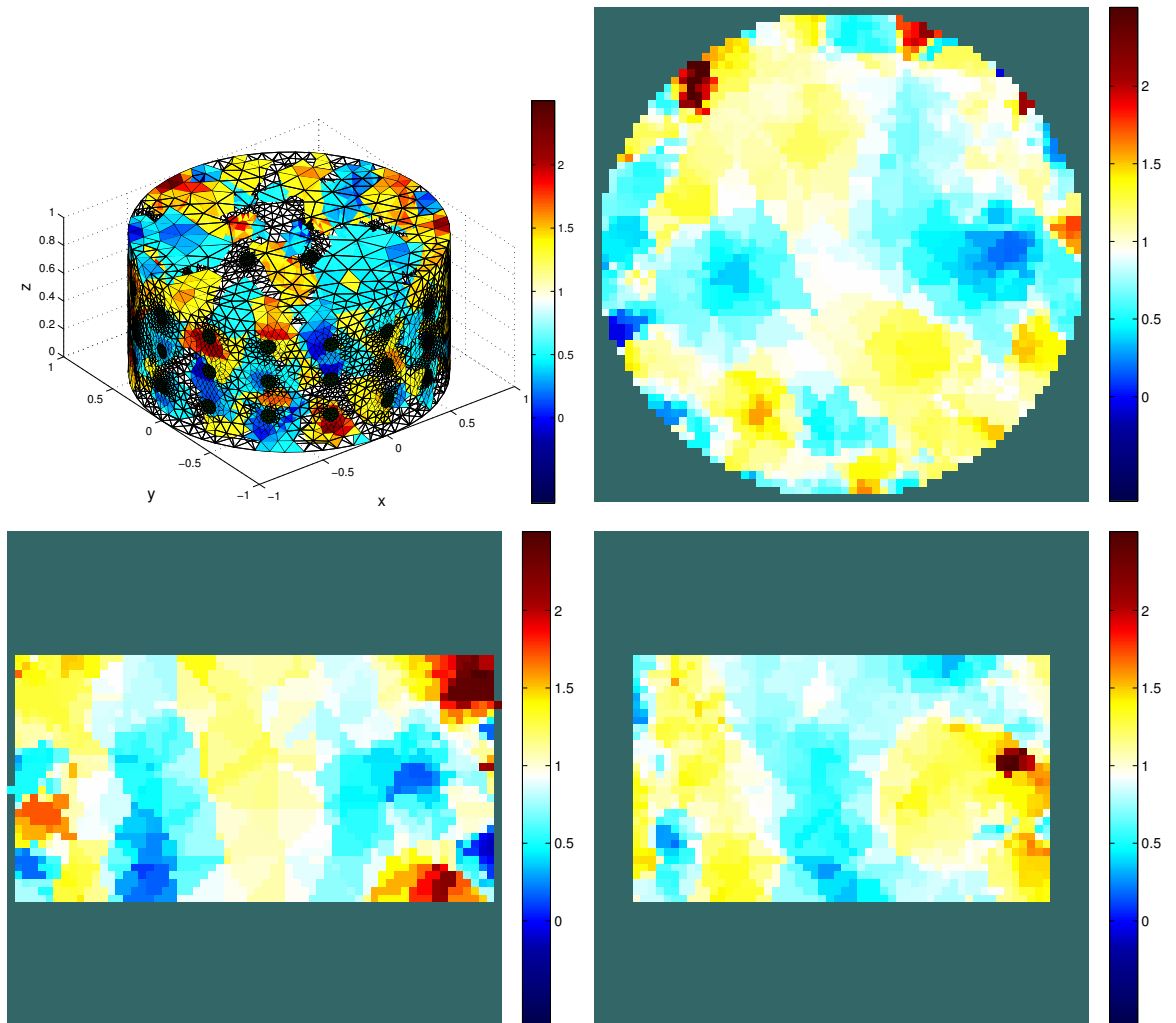


Figure 4.32: Cylinder with two cylindrical inclusions: Reconstructed conductivity without shape correction $p = 0.1$ and $A = 1$. The top left hand image is a 3D visualisation, the top right, bottom left and bottom right are planes perpendicular to the z -axis, y -axis and x -axis respectively through the centre of inclusion $B1$. A hyperparameter of $\alpha = 2 \times 10^{-5}$ was used for each reconstruction and an $A = 1$ measurement strategy adopted.

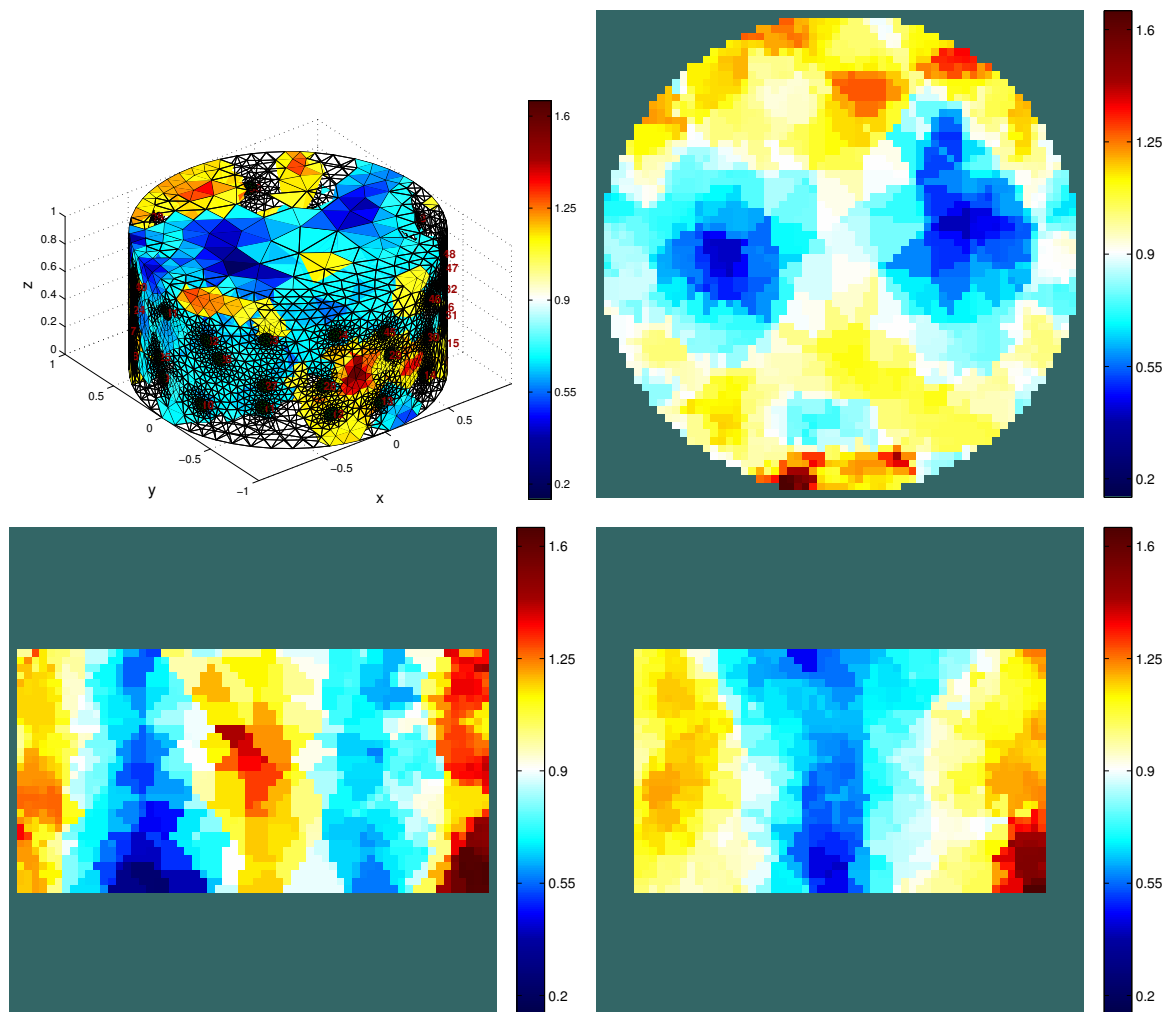


Figure 4.33: Cylinder with two cylindrical inclusions: Reconstructed conductivity using shape correction algorithm $p = 0.1$ and $A = 1$. The top left hand image is a 3D visualisation, the top right, bottom left and bottom right are planes perpendicular to the z-axis, y-axis and x-axis respectively through the centre of inclusion $B1$. Hyperparameters of $\alpha = 2 \times 10^{-5}$ and $\beta = 0.1$ were used for each reconstruction and an $A = 1$ measurement strategy adopted.

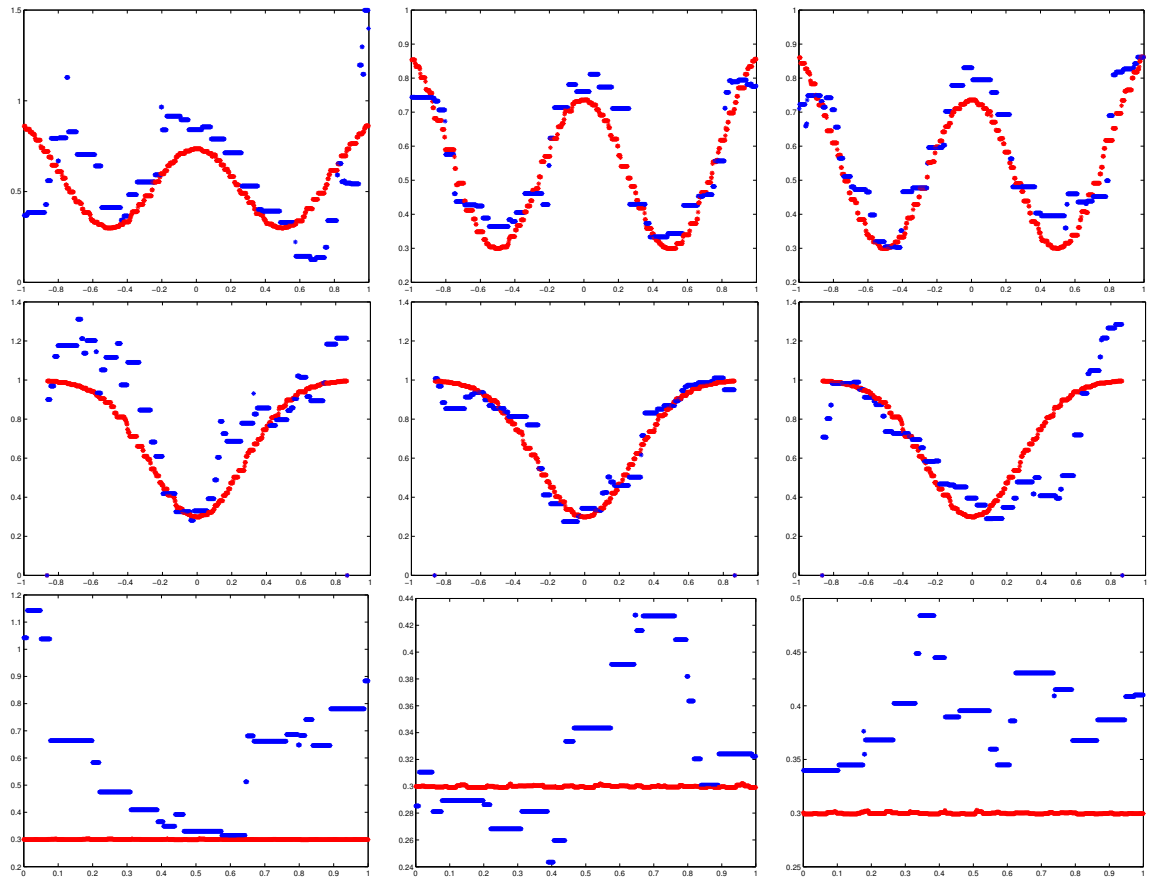


Figure 4.34: Cylinder with two cylindrical inclusions: Reconstructed conductivity lineplots with $p = 0.1$ and $A = 1$ with hyperparameters $\alpha = 2 \times 10^{-5}$ and $\beta = 0.1$. The left and right column corresponds to a non shape correction and shape correction algorithm respectively and the middle column to when the electrode positions are known. The top, middle and bottom row corresponds to the following lineplots. The top row is parallel to x-axis through $(y,z)=(0,0.5)$, the middle row parallel to y-axis through $(x,z)=(0.5,0.5)$ and the bottom row parallel to z-axis along the centre of inclusion B_1 . The red and blue lines indicate the actual and estimated conductivity respectively.

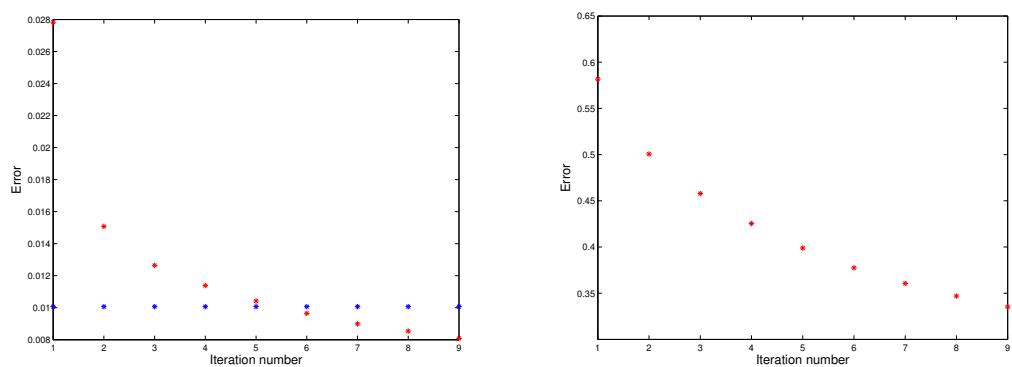


Figure 4.35: Cylinder with two cylindrical inclusions: Initial electrode position and voltage convergence with $p = 0.1$ and $A = 1$. A hyperparameter of $\beta = 0.1$ was used for reconstruction. The left and right image correspond to the convergence of the voltages and electrode positions respectively. The blue and red line in the left hand figure illustrates the norm of the difference in the voltages between the unknown conductivity and background conductivity with known electrode positions and the norm of the difference in voltage between the unknown conductivity and background conductivity with updated electrode positions. We observe that the voltage error is converging in such a way that the voltage misfit at the end of the first stage of the algorithm is largely associated with the conductivity perturbation.

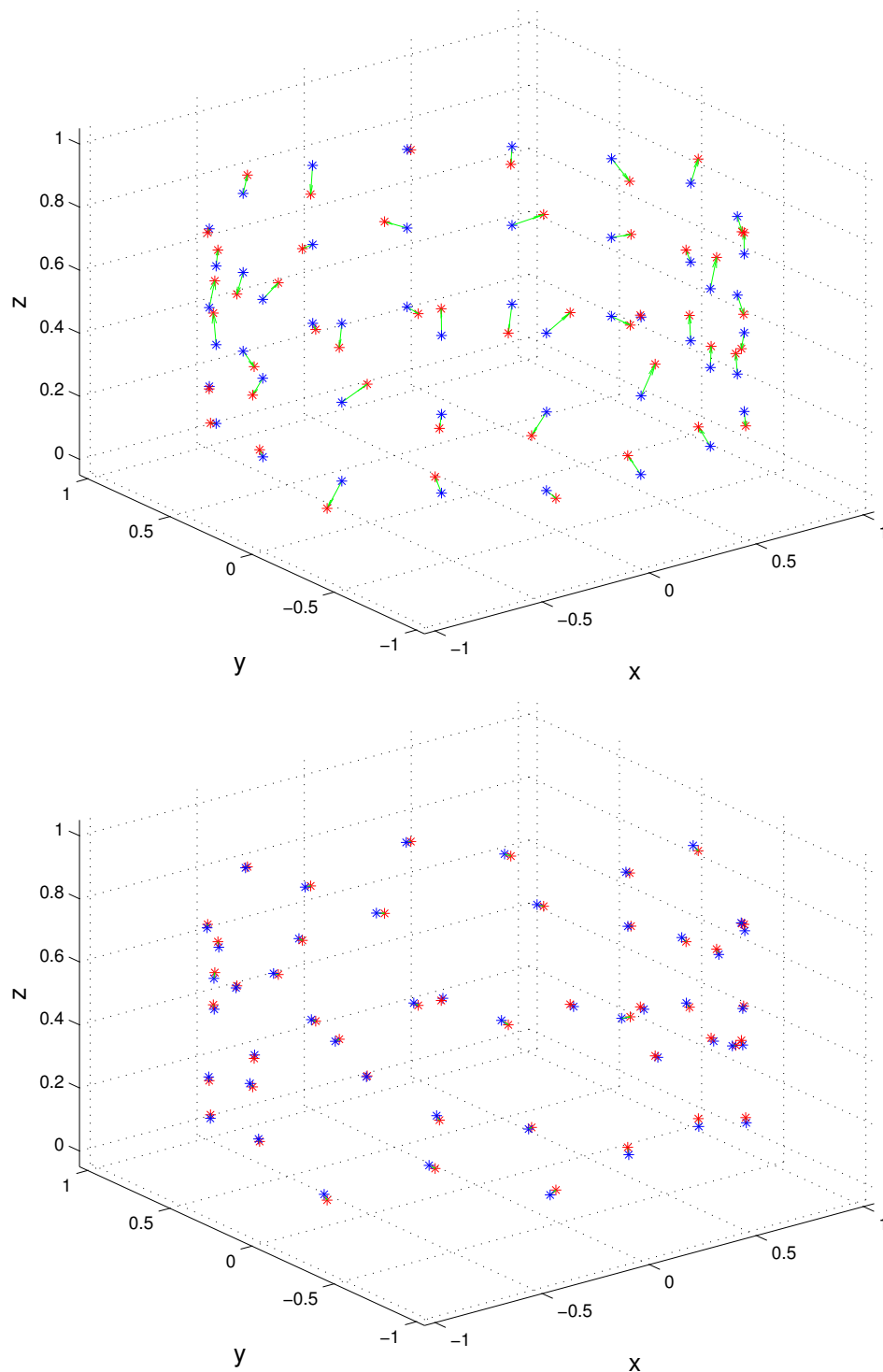


Figure 4.36: Cylinder with two cylindrical inclusions: Electrode position convergence with $p = 0.1$ and $A = 1$. The blue and red stars correspond to the model and actual electrode positions, and the left and right image correspond to the initial guess and final estimate of the electrode positions. The green lines indicate differences in the electrode positions and the electrodes have been determined well at the end of the algorithm. A hyperparameter of $\beta = 0.1$ was used for each reconstruction and an $A = 1$ measurement strategy adopted.

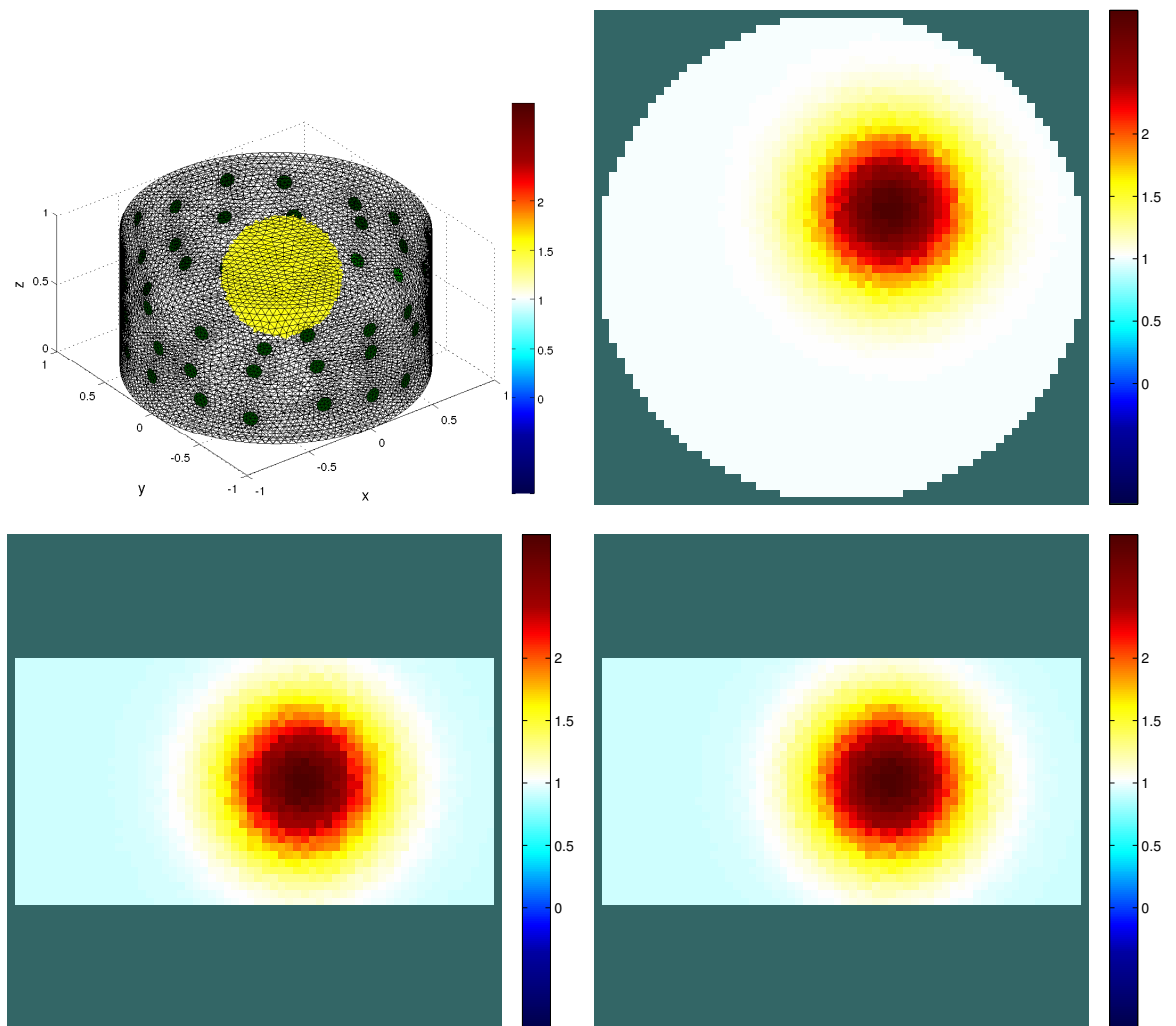


Figure 4.37: Cylinder with spherical inclusion: Unknown conductivity and unknown electrode positions with $p = 0.075$ and $A = 1$. The top left hand image is a 3D visualisation, the top right, bottom left and bottom right are planes perpendicular to the z-axis, y-axis and x-axis respectively through the inclusion centre.

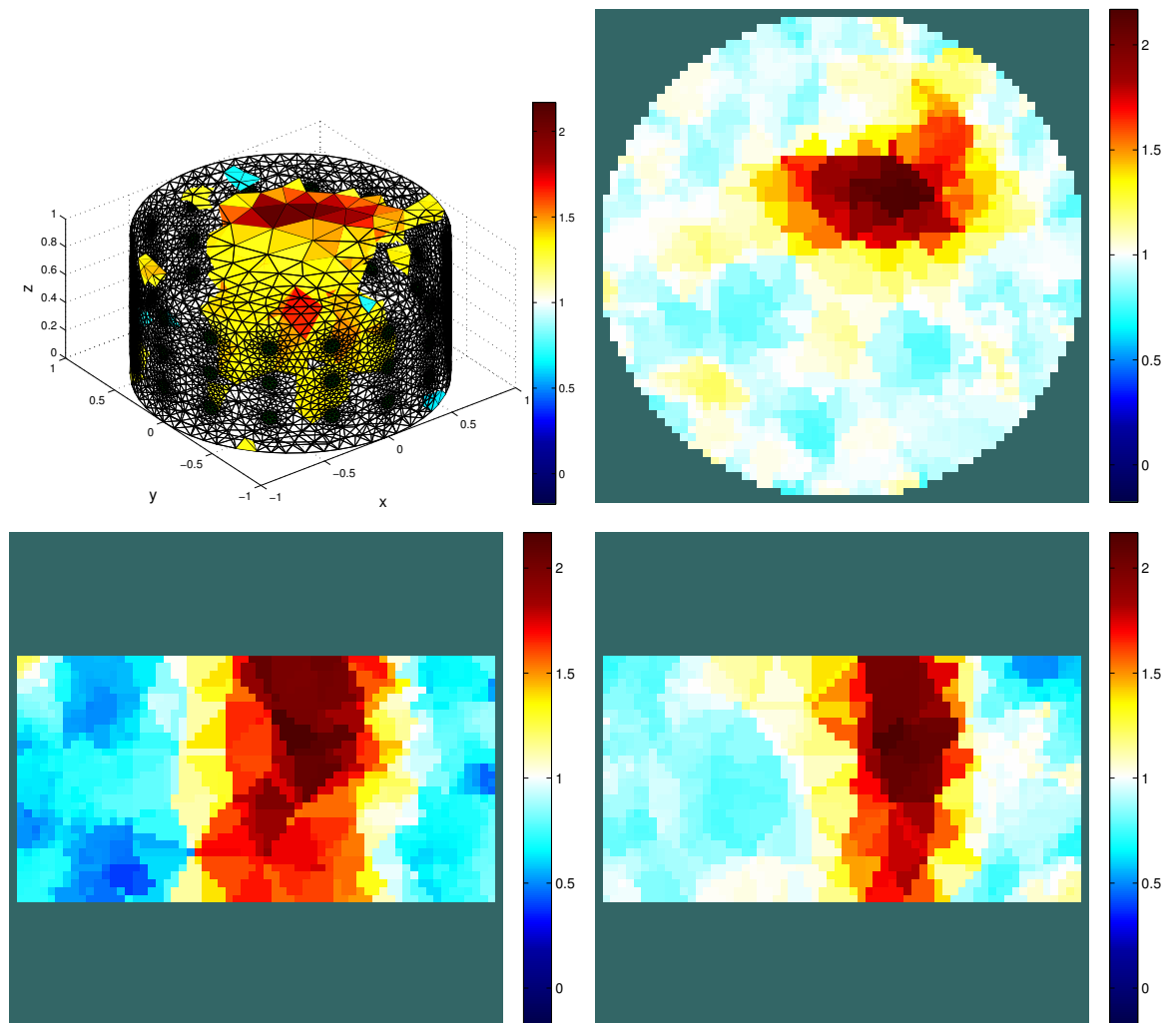


Figure 4.38: Cylinder with spherical inclusion: Reconstructed conductivity with electrode positions known and $A = 1$. The top left hand image is a 3D visualisation, the top right, bottom left and bottom right are planes perpendicular to the z-axis, y-axis and x-axis respectively through the inclusion centre. A hyperparameter of $\alpha = 10^{-5}$ was used for reconstruction and an $A = 1$ measurement strategy adopted.

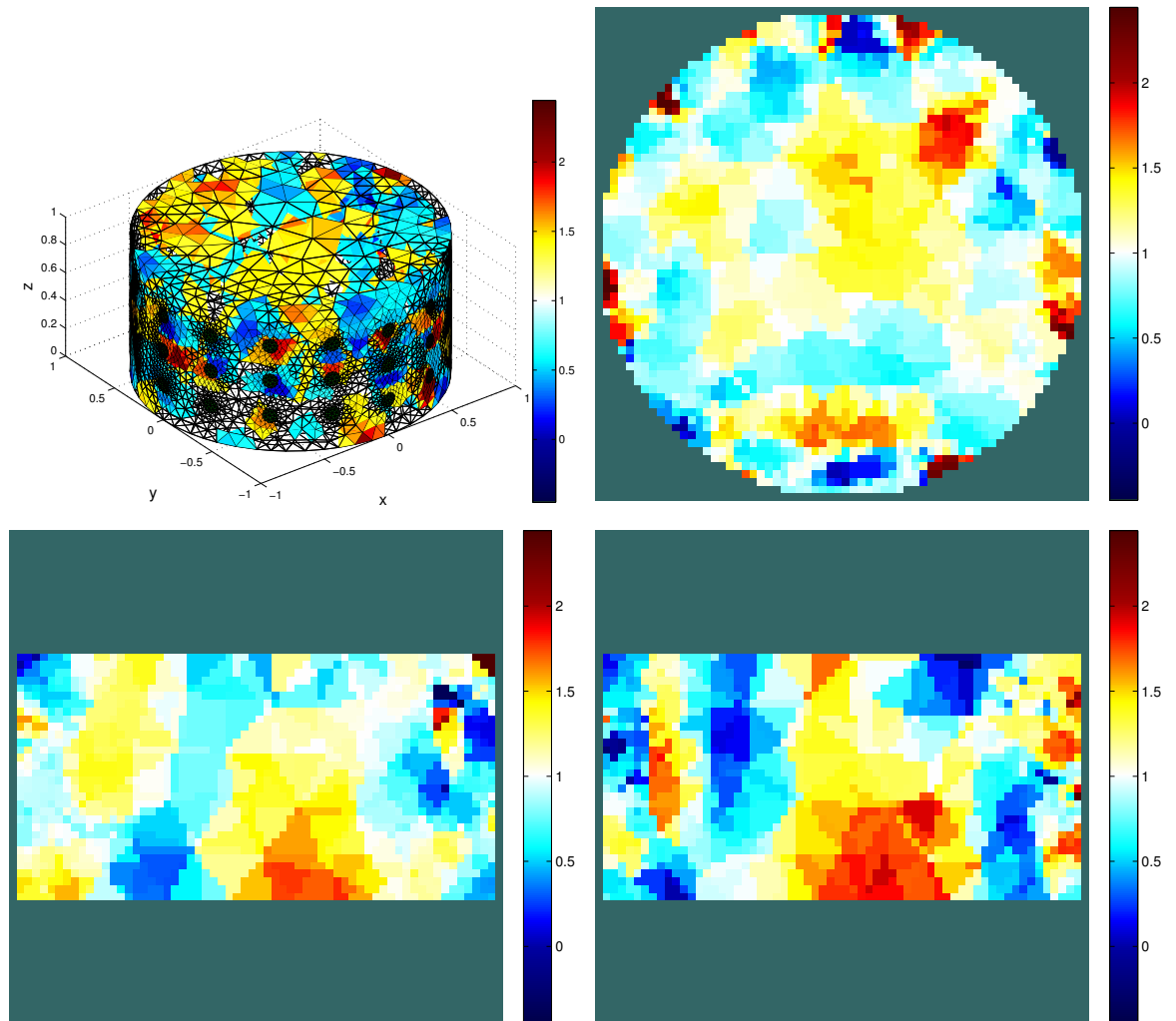


Figure 4.39: Cylinder with spherical inclusion: Reconstructed conductivity without shape correction $p = 0.075$ and $A = 1$. The top left hand image is a 3D visualisation, the top right, bottom left and bottom right are planes perpendicular to the z axis, y axis and x -axis respectively through the inclusion centre. Hyperparameters of $\alpha = 10^{-5}$ and $\beta = 0.075$ were used for reconstruction and an $A = 1$ measurement strategy adopted.

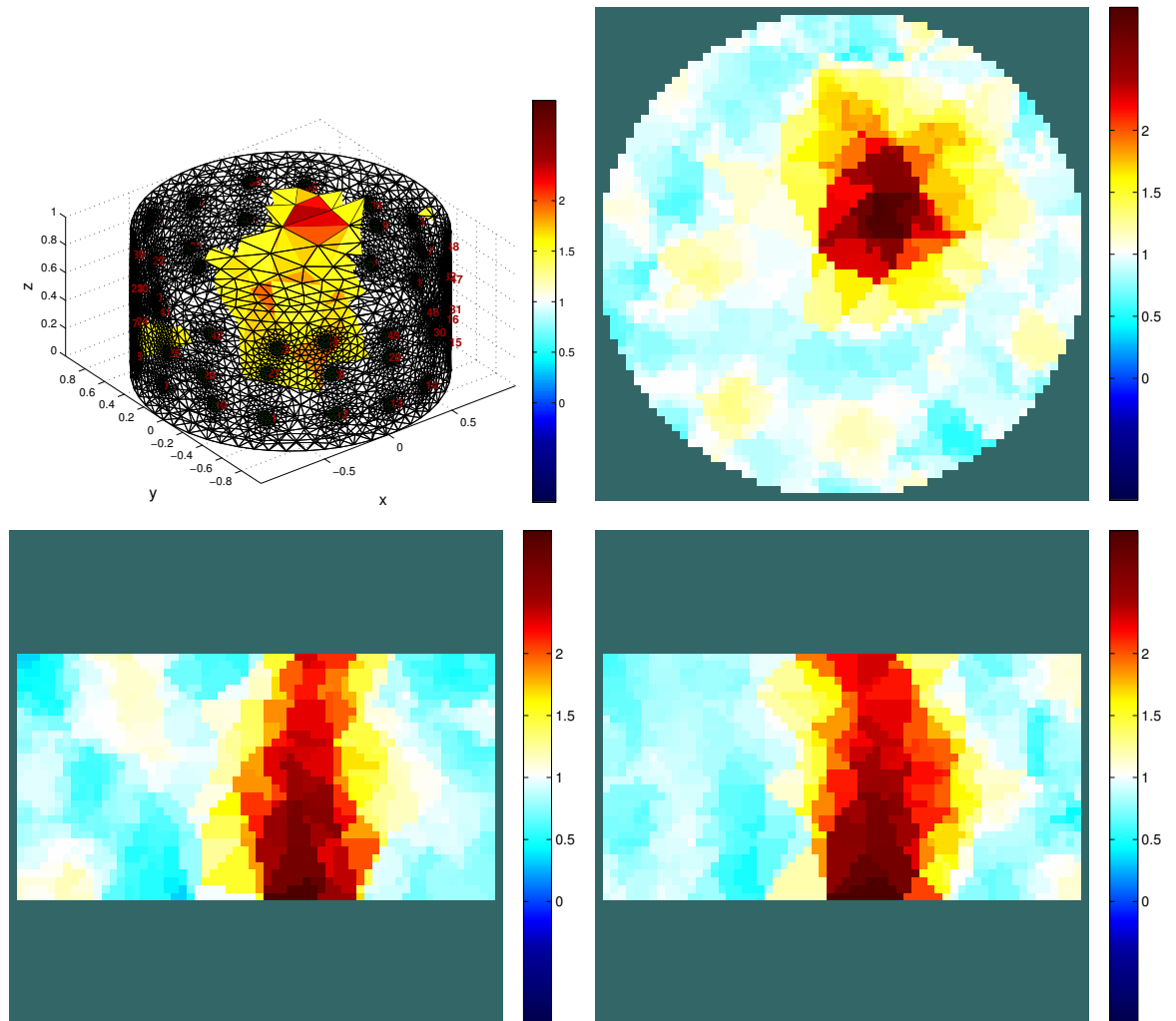


Figure 4.40: Cylinder with spherical inclusion: Reconstructed conductivity using shape correction algorithm $p = 0.075$ and $A = 1$. The top left hand image is a 3D visualisation, the top right, bottom left and bottom right are planes perpendicular to the z-axis, y-axis and x-axis respectively through the inclusion centre. Hyperparameters of $\alpha = 10^{-5}$ and $\beta = 0.075$ were used for reconstruction and an $A = 1$ measurement strategy adopted.

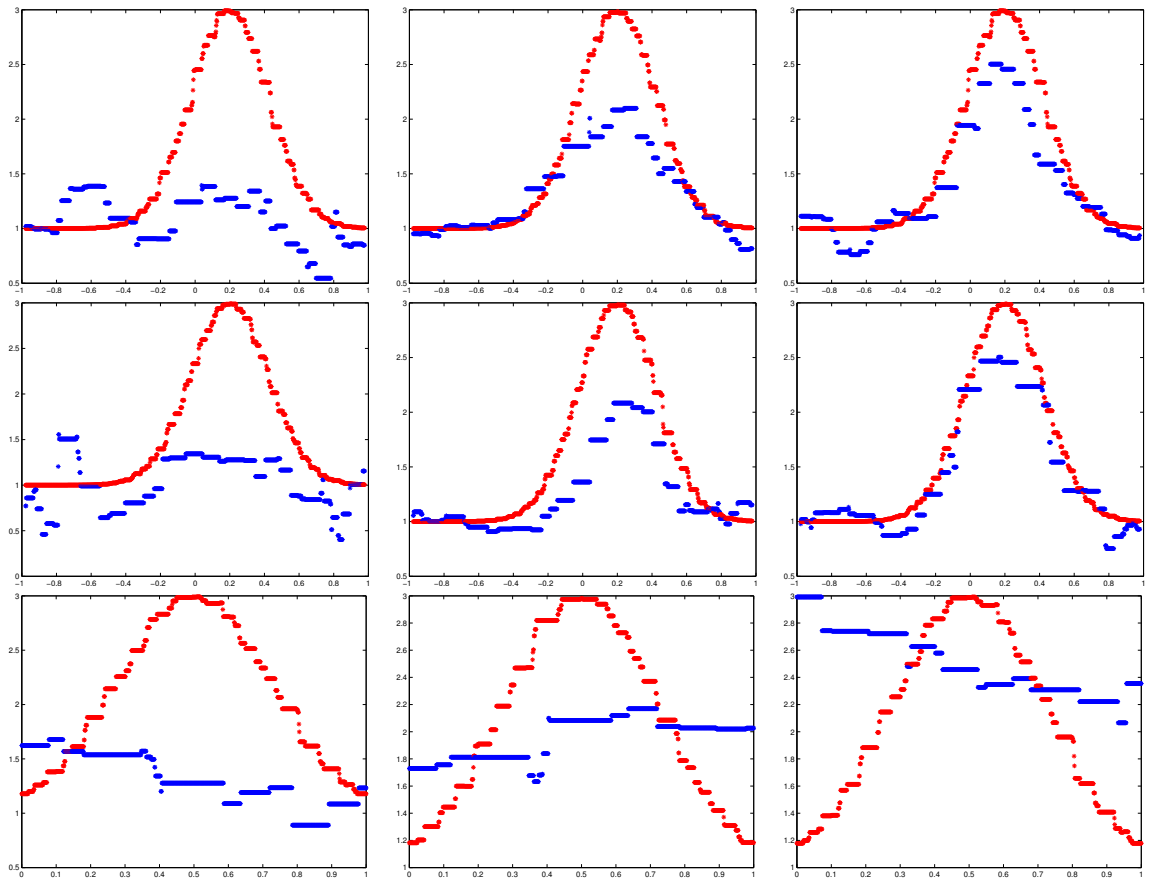


Figure 4.41: Cylinder with spherical inclusion: Reconstructed conductivity lineplots with $p = 0.075$ and $A = 1$. The left and right column corresponds to a non shape correction and shape correction algorithm respectively and the middle column to a non shape correction algorithm with electrode positions known. The top, middle and bottom row corresponds to lineplots parallel to the x -, y - and z -axis respectively through the inclusion centre. The red lines indicates the actual conductivity and the blue lines the estimated conductivity. Hyperparameters of $\alpha = 10^{-5}$ and $\beta = 0.075$ were used for each reconstruction and an $A = 1$ measurement strategy adopted.

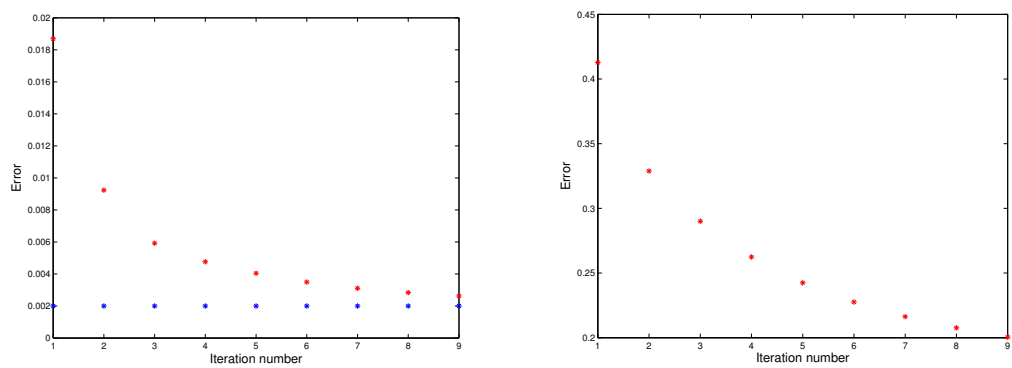


Figure 4.42: Cylinder with spherical inclusion: Initial electrode position and voltage convergence with $p = 0.075$ and $A = 1$. A hyperparameter of $\beta = 0.075$ was used for reconstruction. The left and right image correspond to the convergence of the voltages and electrode positions respectively. The blue and red line in the left hand figure illustrates the norm of the difference in the voltages between the unknown conductivity and background conductivity with known electrode positions and the norm of the difference in voltage between the unknown conductivity and background conductivity with updated electrode positions. We observe that the voltage error is converging in such a way that the voltage misfit at the end of the first stage of the algorithm is largely associated with the conductivity perturbation.

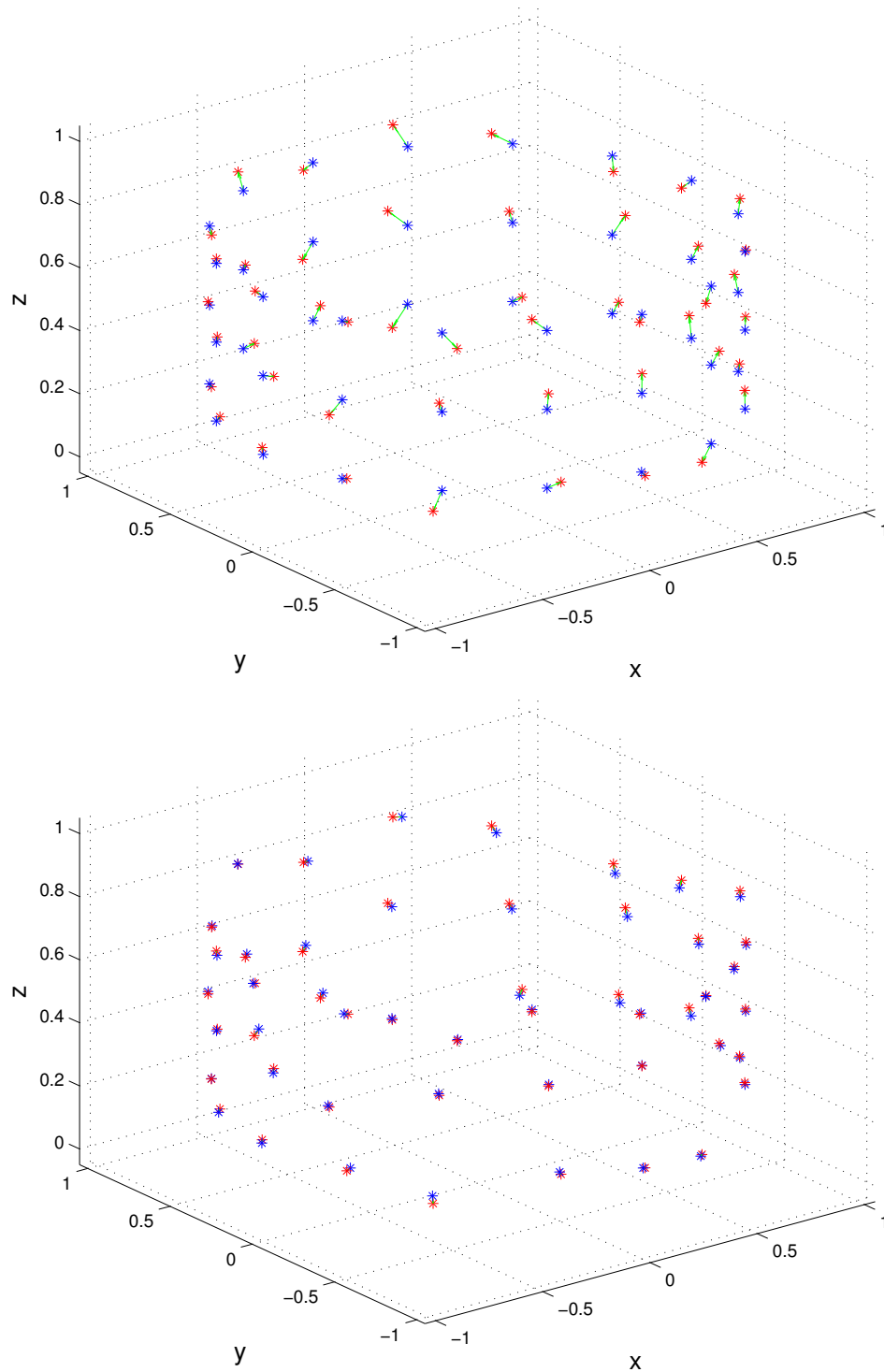


Figure 4.43: Cylinder with spherical inclusion: Electrode position convergence with $p = 0.075$ and $A = 1$. The blue and red stars correspond to the model and actual electrode positions, and the left and right image correspond to the initial guess and final estimate of the electrode positions. The green lines indicate the differences in electrode position and the electrode positions have been determined well at the end of the algorithm. A hyperparameter of $\beta = 0.075$ was used for reconstruction and an $A = 1$ measurement strategy adopted.

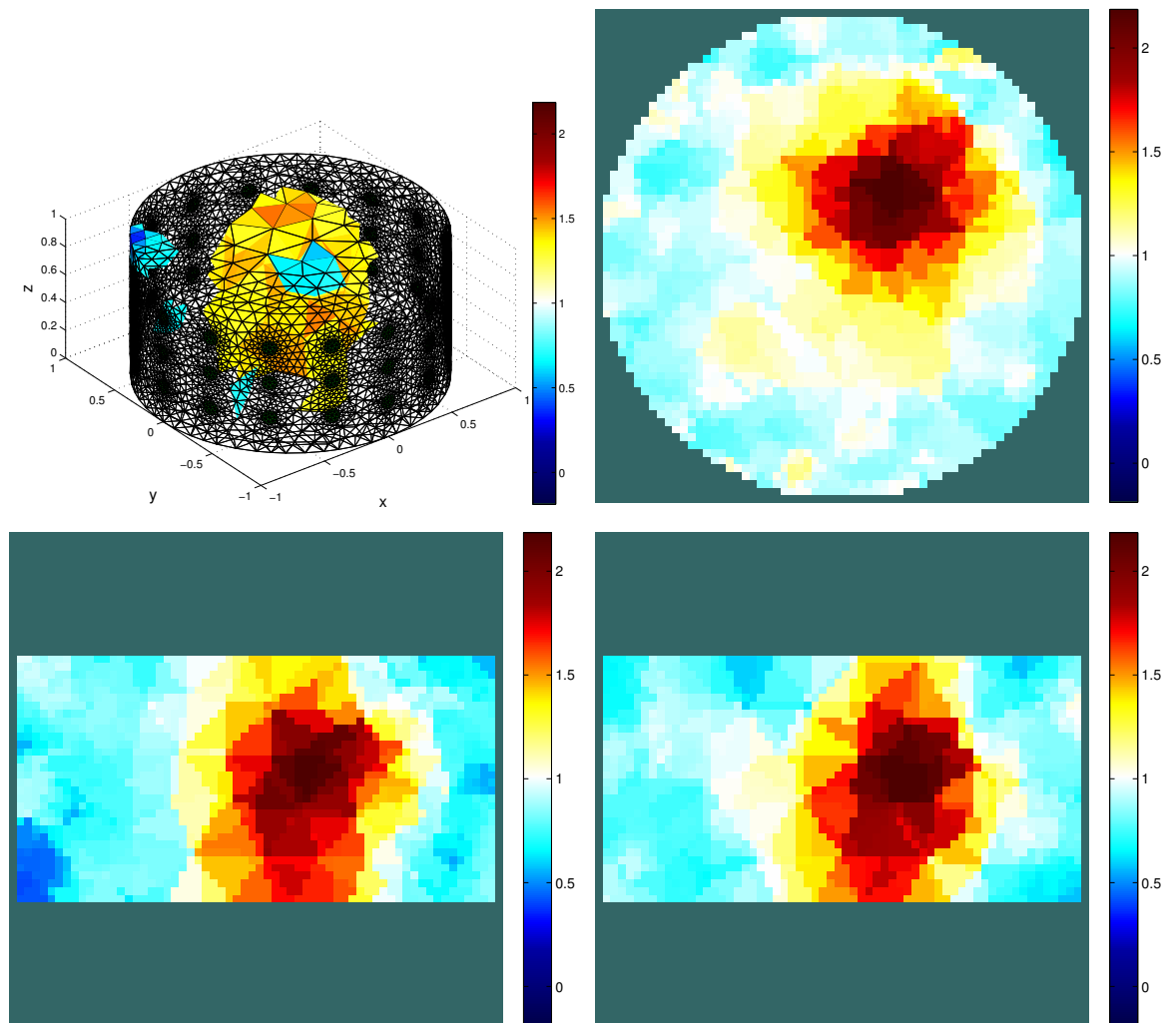


Figure 4.44: Cylinder with spherical inclusion: Reconstructed conductivity with electrode positions known and $A = 23$. The top left hand image is a 3D visualisation, the top right, bottom left and bottom right are planes perpendicular to the z-axis, y-axis and x-axis respectively through the inclusion centre. Hyperparameters of $\alpha = 5 \times 10^{-5}$ and $\beta = 0.075$ were used for reconstruction and an $A = 23$ measurement strategy adopted.

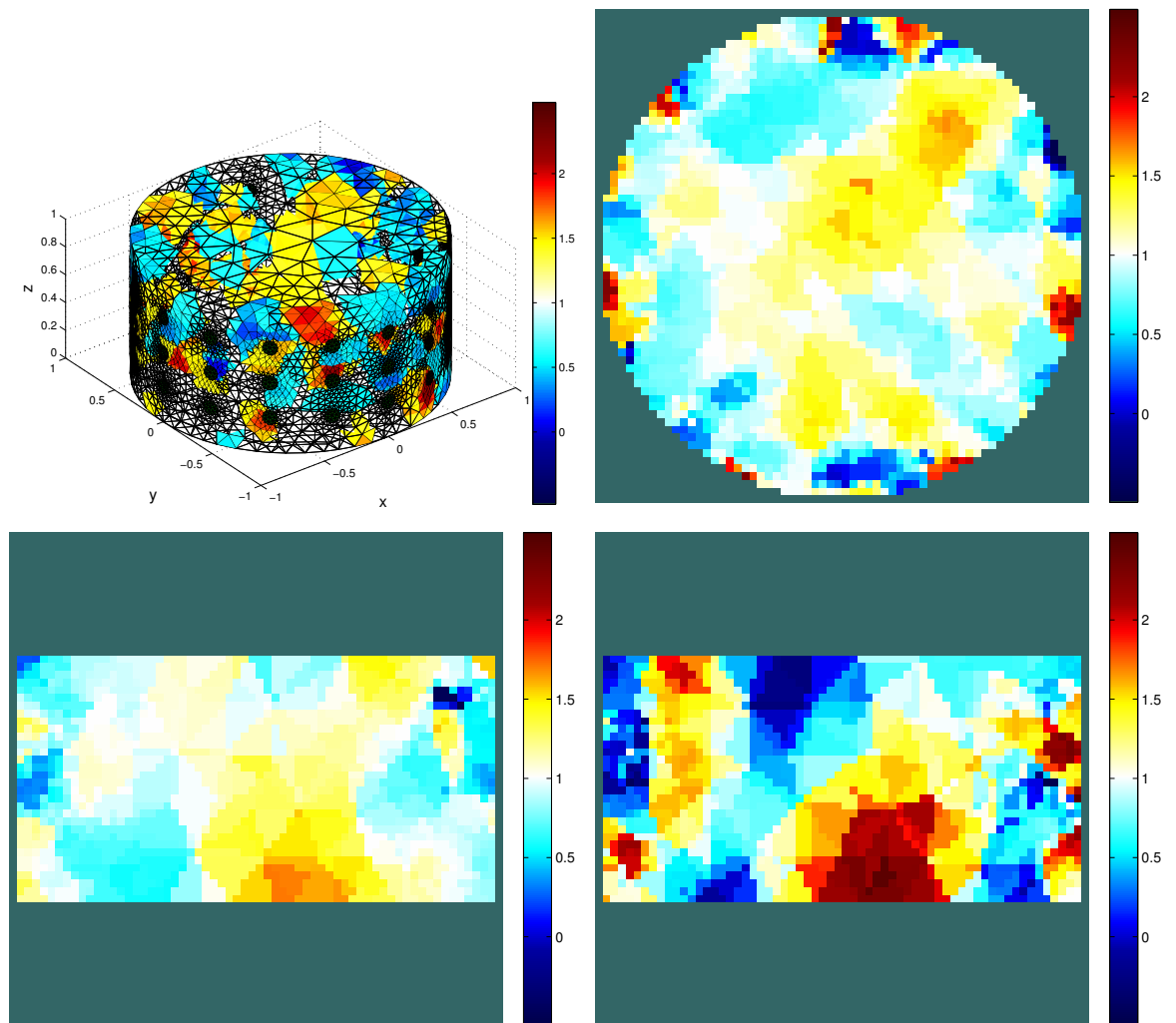


Figure 4.45: Cylinder with spherical inclusion: Reconstructed conductivity without shape correction $p = 0.075$ and $A = 23$. The top left hand image is a 3D visualisation, the top right, bottom left and bottom right are planes perpendicular to the z-axis, y-axis and x-axis respectively through the inclusion centre. A hyperparameter of $\alpha = 5 \times 10^{-5}$ was used for reconstruction and an $A = 23$ measurement strategy adopted.

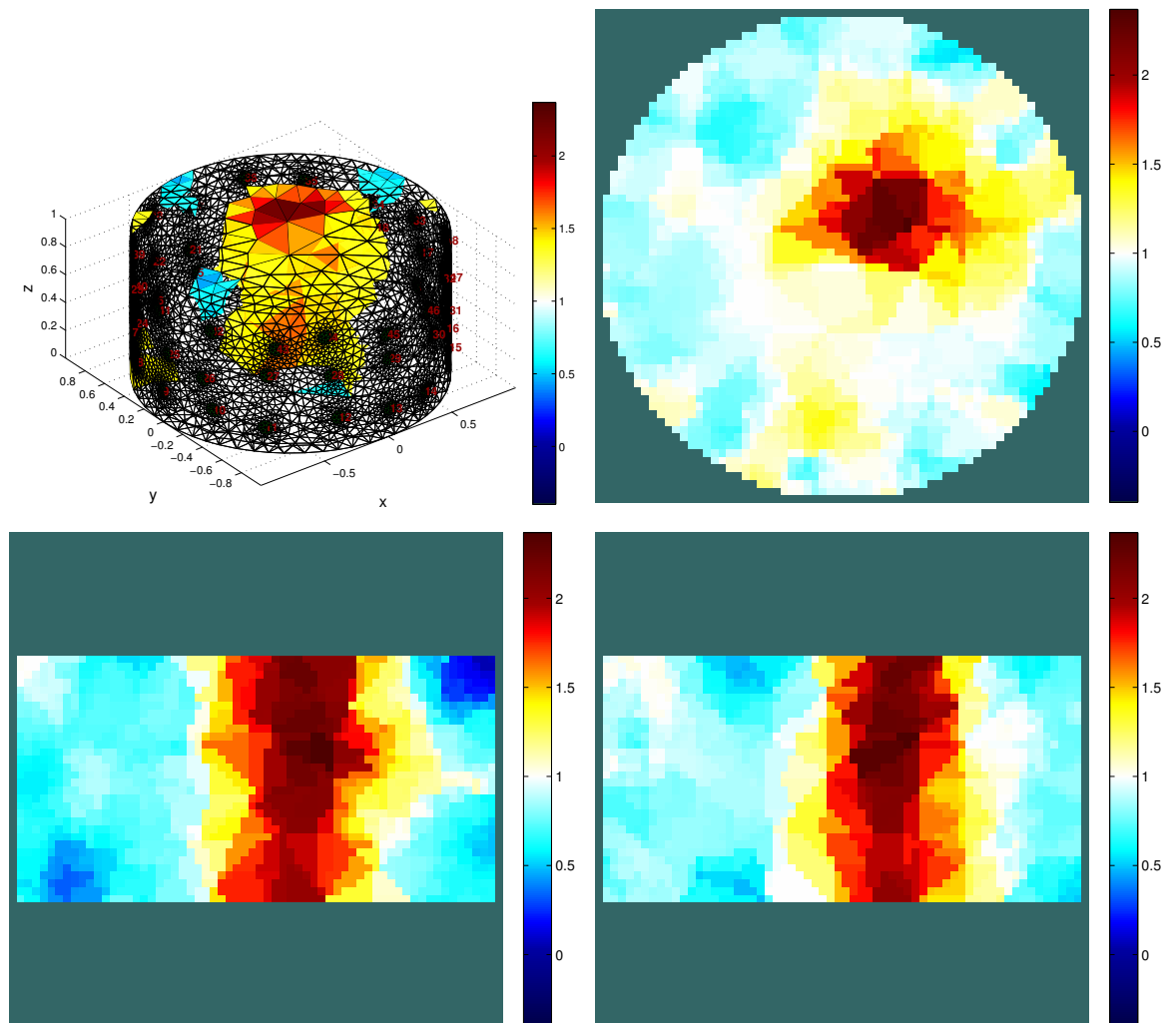


Figure 4.46: Cylinder with spherical inclusion: Reconstructed conductivity using shape correction algorithm $p = 0.075$ and $A = 23$. The top left hand image is a 3D visualisation, the top right, bottom left and bottom right are planes perpendicular to the z-axis, y-axis and x-axis respectively through the inclusion centre. Hyperparameters of $\alpha = 5 \times 10^{-5}$ and $\beta = 0.075$ were used for each reconstruction and an $A = 23$ measurement strategy adopted.

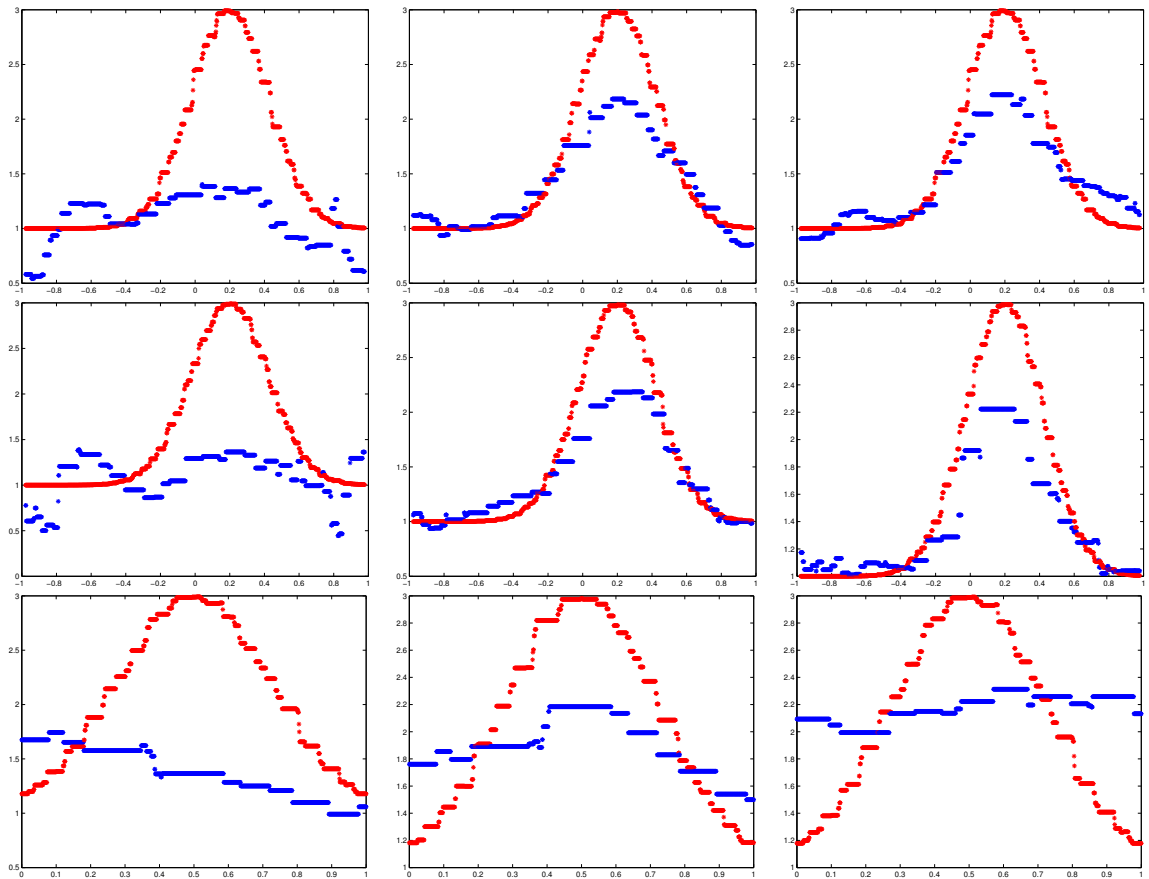


Figure 4.47: Cylinder with spherical inclusion: Reconstructed conductivity lineplots with $p = 0.075$ and $A = 23$. The left and right column corresponds to a non shape correction and shape correction algorithm respectively and the middle column corresponds to a non shape correction algorithm with the electrode positions known. The top, middle and bottom row corresponds to lineplots parallel to the x -, y - and z -axis respectively through the inclusion centre. The red lines indicates the actual conductivity and the blue lines the estimated conductivity. Hyperparameters of $\alpha = 5 \times 10^{-5}$ and $\beta = 0.075$ were used for each reconstruction and an $A = 23$ measurement strategy adopted.

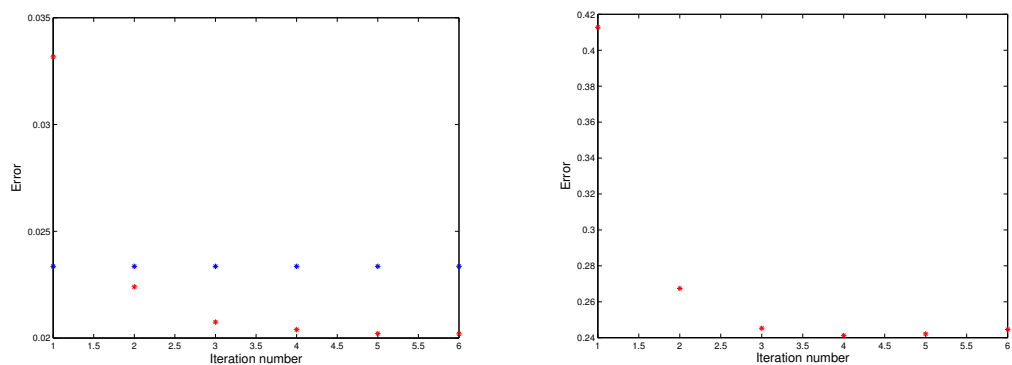


Figure 4.48: Cylinder with spherical inclusion: Initial electrode position and voltage convergence with $p = 0.075$ and $A = 23$. A hyperparameter of $\beta = 0.075$ was used for reconstruction. The left and right image correspond to the convergence of the voltages and electrode positions respectively. The blue and red line in the left and right hand figure illustrates the norm of the difference in the voltages between the unknown conductivity and background conductivity with known electrode positions and the norm of the difference in voltage between the unknown conductivity and background conductivity with updated electrode positions. We observe that the voltage error is converging in such a way that the voltage misfit at the end of the first stage of the algorithm is largely associated with the conductivity perturbation.

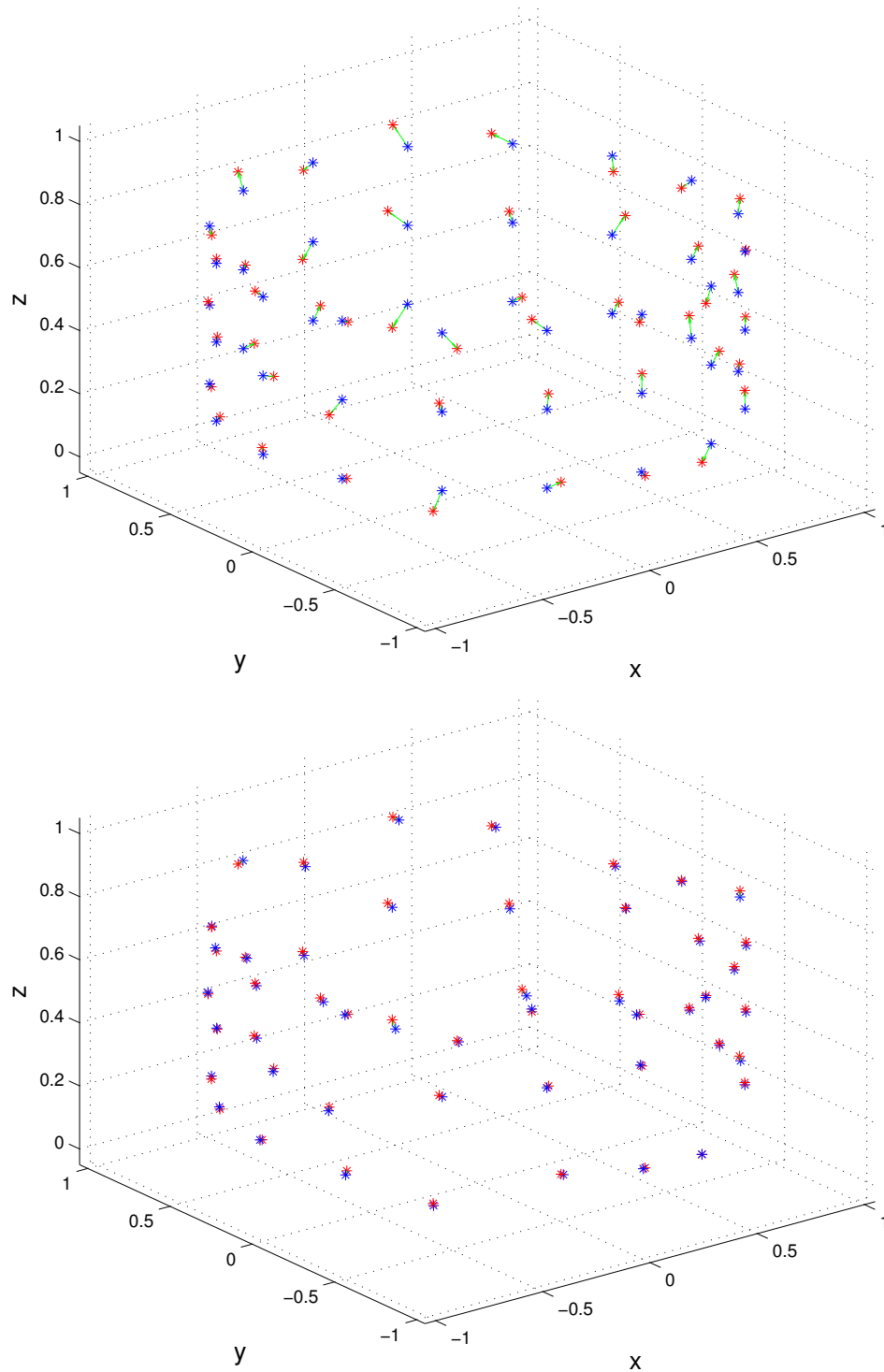


Figure 4.49: Cylinder with spherical inclusion: Electrode position convergence with $p = 0.075$ and $A = 23$. The blue and red stars correspond to the model and actual electrode positions, and the left and right image correspond to the initial guess and final estimate of the electrode positions. The green lines indicate the differences in electrode position and the electrode positions have been determined well at the end of the algorithm. A hyperparameter of $\beta = 0.075$ was used for reconstruction and an $A = 23$ measurement strategy adopted.

Chapter 5

MRI-informed dynamic lung EIT

In this chapter a methodology for MRI-informed lung EIT is presented using data obtained from a healthy subject during a pilot study at the University of Manchester in 2012. Novel aspects of this methodology include the use of MRI to inform the boundary shape, and prior information of the conductivity distribution, of the subject as well as subsequent image co-registration of the reconstructed EIT image and MR image. An original mutual information performance criterion is used to quantify the quality of the EIT reconstruction. The chapter is a combination of peer-reviewed conference papers given at ‘100 years of electrical imaging’ in Paris in 2012 [129] and at ‘XIV Conference on Electrical Impedance Tomography 2013’ in Heilbad in 2013 [132], and a journal paper published in *Physiological Measurement* in 2014 [133]. The current author was lead author, with 10 other co-authors contributing — Alex Morgan, Josephine Naish, Chris Miller, Ross Little and Geoff Parker for the MRI data sequences and collection, Ron Kikinis for help with the 3D Slicer software, John Davidson, Paul Wright and Hugh McCann for EIT data sequences using the fEITER instrument, and William Lionheart for expertise in EIT.

5.1 Data collection and model generation

5.1.1 MRI and EIT data collection

In the study 32 electrodes were arranged on a healthy subject as two transverse planes of 16 electrodes equidistantly spaced around the chest at approximately the fourth and

sixth intercostal spaces, along with an abdominal reference electrode, as illustrated in figure 5.1. EIT measurements were acquired using the EIT sub-system of the biomedical fEITER instrument [134], which offers not only a high SNR ratio approaching 80 dB on bench-top phantoms, but also has been designed to meet the IEC 60601-1 patient safety requirements. In this study, a nearest-neighbour current injection protocol was used with a total of 20 current patterns which included 8 independent horizontal injections per transverse electrode plane. Sinusoidal current injections of 0.5 mA amplitude at 10 kHz frequency were input and the EIT instrument recorded nearest-neighbour voltage pairs at 100 frames per second (fps), where a single frame corresponds to collection of all measurements for the protocol. EIT data were recorded whilst the subject carried out basic breathing procedures in 1 minute blocks. Breathing procedures involved normal and progressively deeper tidal breathing regimes interspaced with reference conditions of typically 5 second breath-holds at both inspiration and expiration. MRI fiducial markers were substituted for the EIT electrodes at all electrode locations immediately after the last EIT data collection, before carrying out an MRI scan using a T2-weighted half-Fourier acquired single-shot turbo spin-echo (HASTE) protocol on a 1.5 T Philips Achieva scanner (Philips Healthcare, Best, the Netherlands) under the same breathing procedures as used during the EIT tests. The MR scans consisted of 1 cm thick contiguous axial slices, which were cardiac gated and tuned for the conditions of normal breath-holding, at maximum inspiration and expiration. The whole procedure was approved by the local ethics committee and the subject gave written, informed consent.

5.1.2 Finite element model generation

The external boundary shape of the subject was obtained from a transverse MR image slice at the fifth intercostal spacing at a breath-hold at maximum inspiration. The contour of the external shape was defined by 50 equispaced points and the contour of each lung by approximately 25 equispaced points. A 3D finite element (FE) forward model extruded along the caudal-distal axis was then generated using EIDORS 3.6 [62]¹ calling the Netgen mesh generator [131]. The method has been applied to swine data as described by Grychtol *et al.* [117]. The FE forward model consisted of 32

¹The library function `ng_mk_extruded_model.m`

electrodes with approximately $N_E^f = 20000$ tetrahedral elements and 5000 vertices (a piecewise linear finite element approximation was used), modelled to a depth of 10 cm. The transverse MR image slice and surface mesh of a typical forward model is shown in figure 5.2. All electrodes were modelled to a diameter of 1 cm, which is consistent with those applied to the subject. A high mesh density was chosen in the vicinity of each electrode where the gradient of the potential is largest, and the lungs segmented from the MR image were also included in the finite element model. A 3D FE model was generated with the same boundary shape as the forward model, but with no electrodes and a lower mesh density, for the reconstruction problem. A reconstruction model typically consisted of $N_E^c = 10000$ tetrahedral elements and 2500 vertices. From the forward and reconstruction models a mapping matrix was generated to transform between the coarse and fine discretisations, allowing one to solve the forward problem sufficiently accurately on the fine model as well as representing the reconstructed conductivity on the coarse model [130].

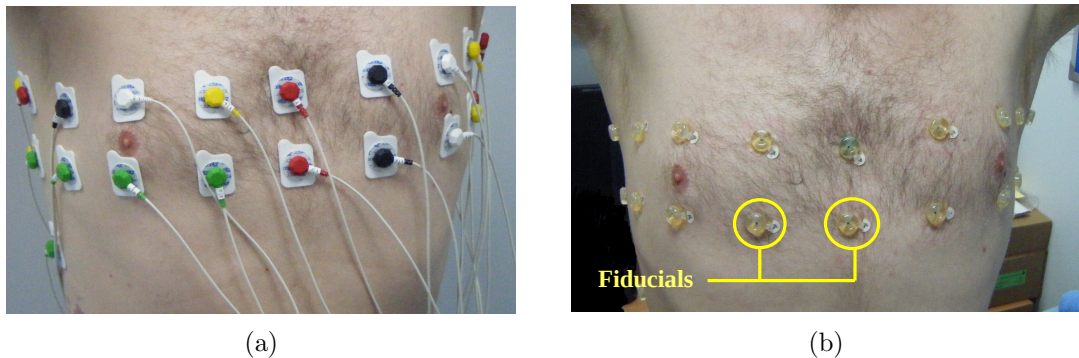


Figure 5.1: Electrode arrays; (a) electrodes attached during EIT data acquisition and (b) MRI fiducial markers to inform electrode positions.

5.2 Dynamic reconstruction algorithms

5.2.1 Electrode movement Jacobian

As the subject breathes the electrodes will move with respect to a fixed geometrical model of the thorax generating large artefacts in reconstructed images. As in section 4.3.3 a finite difference approximation of the derivative of the forward problem with respect to the boundary shape is calculated at the electrodes, leaving the rest of the boundary fixed. This method could equally be applied to other boundary locations,

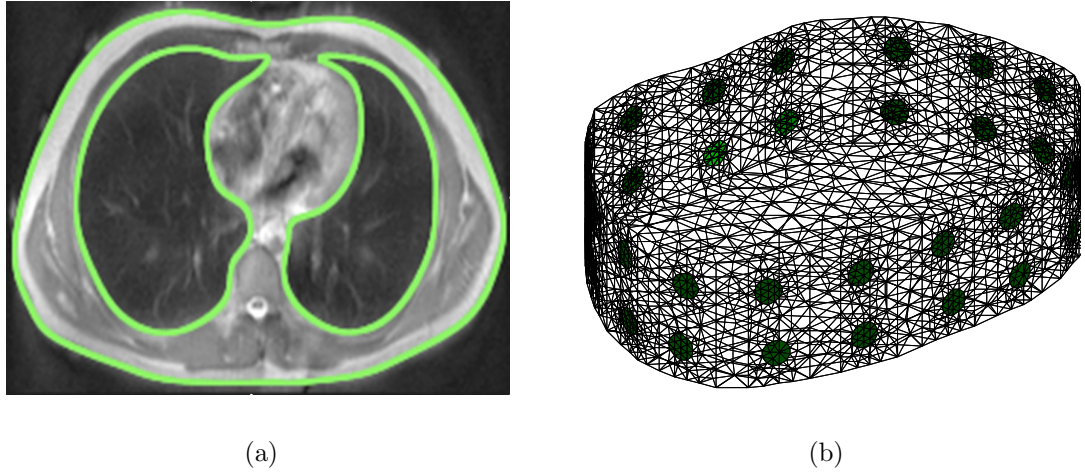


Figure 5.2: FE model generation; (a) segmented MR slice with thorax and lung shapes highlighted and (b) extruded ‘2.5D’ FE model generated in EIDORS.

but since the largest sensitivity of measured data to shape changes will be at the electrodes, we only calculate this at the electrode positions (see section 4.3.1). In effect we are assuming the shape has been sufficiently well approximated from the MR image and are only accounting for small corrections from electrode movement due to breathing. A finite difference method on the FEM formulation of the forward problem is used, and an approximate derivative with respect to electrode movement, $J_m : \mathbb{R}^{3L} \rightarrow \mathbb{R}^m$, is calculated (4.16). We note this is not projected onto the tangent space of each electrode as described in section 4.3.3, and so changes in the electrode positions normal to the fixed boundary are also being accounted for.

5.2.2 Shape correction algorithm

For small changes in the electrode positions and conductivity, the forward problem can be linearised through a first order Taylor series

$$V_{\sigma+\delta\sigma, v+\delta v} = V_{\sigma, v} + J_c(\delta\sigma) + J_m(\delta v) + O(\|(\delta\sigma, \delta v)\|^2), \quad (5.1)$$

where $\|(\delta\sigma, \delta v)\| := \|\delta\sigma\|_\infty + \|\delta v\|_\infty$. We assume an exact linear relationship between the conductivity/shape change, x , and the data change, d , between two states of interest, so that $d = Jx + n$, where $J := [J_c, J_m] \in \mathbb{R}^{m \times (3L + N_E^e)}$, $x = (\delta\sigma, \delta v)$ and $n \in \mathbb{R}^m$ represents the measurement noise. The estimation of x from d is approached from a probabilistic viewpoint. We assume Gaussian noise with covariance matrix $\Gamma_e \in \mathbb{R}^{m \times m}$ and mean zero. We further assume a Gaussian prior on the conductivity

and electrode position changes, with covariance matrix $\Gamma_x \in \mathbb{R}^{3L+N_E^c \times 3L+N_E^c}$, and prior mean $x_p := (\delta\sigma_p, \delta v_p)$, which is assumed to be zero. The measurement noise is also assumed to be independent and identically distributed (i.i.d) and the conductivity and electrode position changes are assumed to be independent from one another and separately i.i.d. These assumptions imply that $\Gamma_e^{-1} = I \in \mathbb{R}^{m \times m}$ and Γ_x^{-1} is a diagonal matrix with entries $\Gamma_x^{-1}(i, i) = \alpha^2$ if $i \leq N_E^c$ and $\Gamma_x^{-1}(i, i) = \beta^2$ if $N_E^c < i \leq N_E^c + 3L$. α and β can be physically interpreted as the ratios of expected changes of conductivity and electrode position to the measurement noise standard deviation. From (3.4) the MAP estimate is given by

$$x_{\text{MAP}} = \max_x \left\{ \|d - Jx\|_{\Gamma_e^{-1}}^2 + \|x - x_p\|_{\Gamma_x^{-1}}^2 \right\}. \quad (5.2)$$

At the maximum the gradient of the objective function must be zero. Computing this gradient, and setting to zero, gives an analytic solution for the MAP estimate as

$$x_{\text{MAP}} = (J^T \Gamma_e^{-1} J + \Gamma_x^{-1})^{-1} (J^T \Gamma_e^{-1} d + \Gamma_x^{-1} x_p). \quad (5.3)$$

This solution was computed in EIDORS via the following procedure. Firstly the extruded mesh was generated as described previously and a constant conductivity assigned to the model. Simulated boundary voltages were acquired from this model using the same measurement protocol as the experiment, and in order to get a consistent scaling between the simulated and measured voltages, V_s and V_m respectively, a best fit homogeneous reference conductivity, σ_r , was computed using a formula derived by Kaipio *et al.* [71]. The prior information of the lungs was then included by assigning the conductivity in the lung regions as $0.3\sigma_r$. Using this reference conductivity the movement Jacobian, J_m , was calculated using the finite difference method in equation (4.16). The standard conductivity Jacobian, J_c , was computed using the default Jacobian function² as described in section 3.2.2. Image reconstructions were performed using two linear difference imaging methods. Firstly using the shape correction method described in this section, and secondly a standard EIDORS method using a one-step linearised Gauss-Newton technique with standard Tikhonov regularisation. We compare with a standard method to determine what improvements in reconstruction quality can be obtained with the shape correction algorithm. In the

²The library function `jacobian.adjoint.m`

following section we discuss how optimal regularisation parameters α and β have been chosen using a mutual information technique.

5.3 Standard and shape correction algorithms

Figures 5.3 and 5.4 are typical of the 3D EIT image reconstructions acquired at 100 FPS using the fEITER system. All images displayed in this chapter are difference images relative to a maximum exhalation data frame, and blue and red indicate negative and positive conductivity changes respectively. Figure 5.3 illustrates difference images for a subject sitting upright at maximum (max) inhalation with the standard and shape correction reconstruction algorithms respectively. It can be clearly seen that the shape correction algorithm yields fewer boundary artefacts and sharper contrast between the lungs and background compared with the standard algorithm. These effects are also clearly visible in the 2D slices from the 3D image reconstructions for a second data set shown in figure 5.4. Figures 5.4a and 5.4b correspond to the standard method, $\alpha = 10^{-2}$, and the bottom figures 5.4c and 5.4d correspond to the shape correction method, $(\alpha, \beta) = (10^{-2}, 4 \times 10^{-2})$. Compensating for movement results in a large reduction in boundary artefacts which is promising as we do not expect any physiological mechanisms to produce large conductivity changes near the boundary.

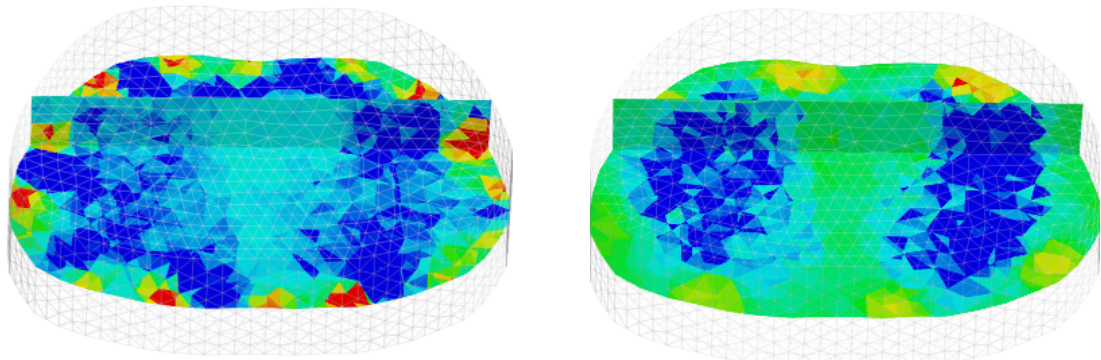


Figure 5.3: Reconstructions in 3D rendered in MayaVi software [135]; The left and right hand image are conductivity changes at max inhalation (relative to max exhalation) for a standard and shape corrected reconstruction respectively. Blue and red corresponds to negative and positive conductivity changes respectively. The front of the chest is in the background, and transverse and coronal scalar-cut planes are shown within the 3D volume.

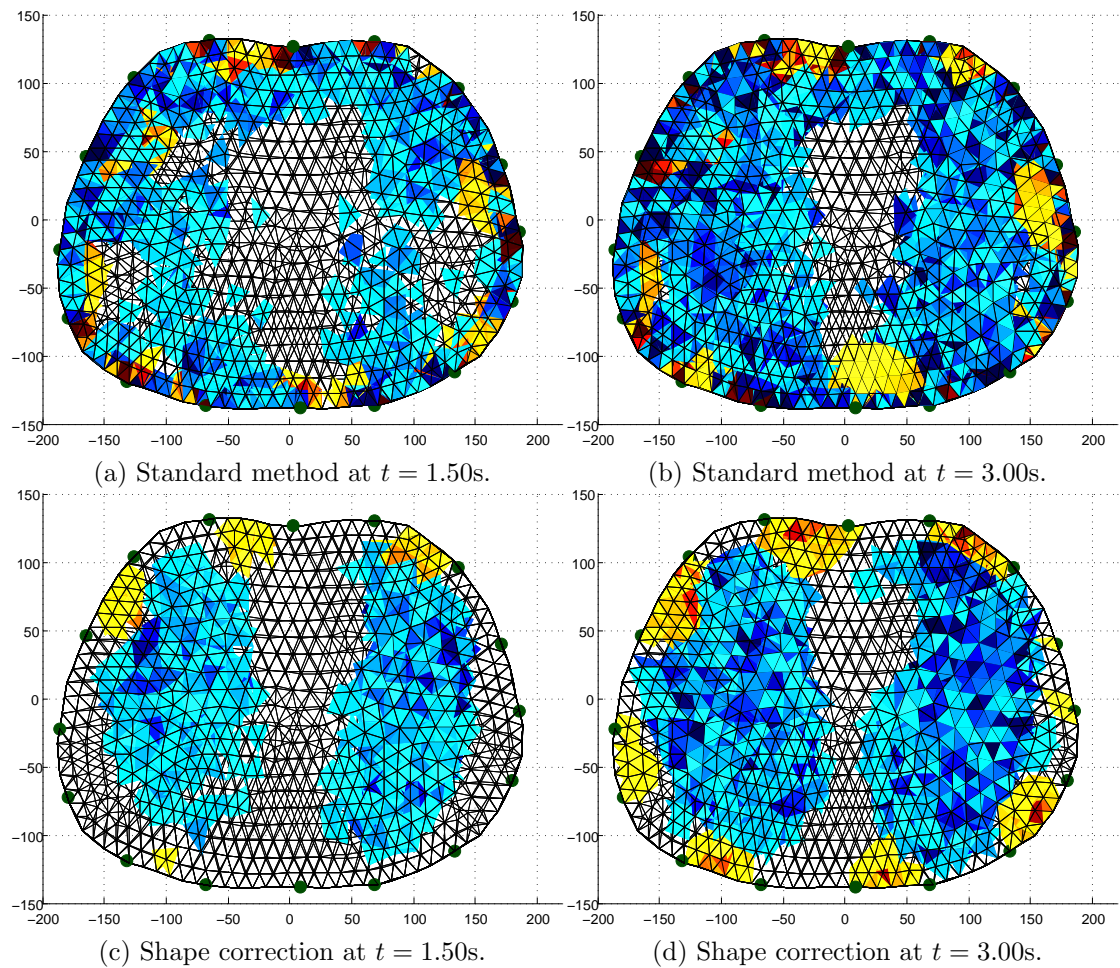


Figure 5.4: Image reconstructions viewed down the caudal-distal axis. Left and right: Mid inhalation ($t = 1.50s$) and max inhalation ($t = 3.00s$), both relative to max exhalation, Top and bottom: Standard algorithm and shape correction algorithm. Blue and red corresponds to negative and positive conductivity changes respectively.

5.3.1 Gravitational effects in the supine position

Figure 5.5 illustrates smoothed and normalised conductivity along a coronal slice shown at approximately the fifth intercostal spacing, for the subject in both the sitting and supine position. These images demonstrate the reduction in boundary artefacts and the sharper contrast of the lungs obtained using the shape correction method, and this is particularly evident when the subject is in the supine position. The MR scan was performed for the subject in this position, so it seems natural that the shape correction method should work better, as the method really is only accounting for small boundary changes due to breathing.

Figures 5.6 shows 2D transverse slices at the sixth intercostal spacing for the subject in the supine and sitting position respectively. These reconstructions are at a max inhalation frame relative to a max exhalation frame for the subject performing

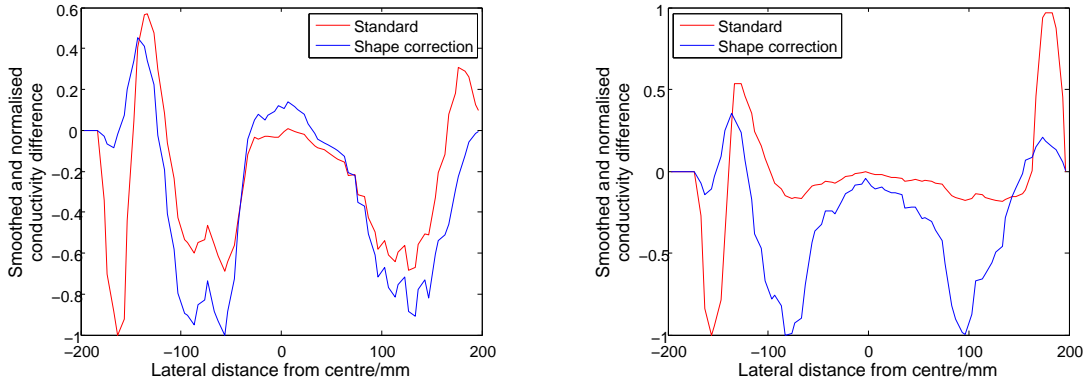


Figure 5.5: Normalized conductivity reconstructions; The left and right hand images are reconstructions at the fifth intercostal spacing for the subject in the sitting and supine position respectively. The standard and shape correction reconstructions are shown for both postures.

moderate tidal breathing. In the supine position there are large differences between the dorsal and ventral regions, which are not observed for the subject in the sitting position. The dynamic behaviour is illustrated in figure 5.6 for averaged conductivity differences within a 15 mm search radius in a ventral and dorsal region. Temporal and amplitude differences in the regional traces can be seen in a broadly consistent manner over successive breathing cycles due to gravitational effects on the subject as described by Frerichs *et al.* [16, 17]. The ability of fEITER to capture these regional differences highlights the excellent SNR characteristics of the instrument.

The MR images are useful as they allow one to generate a patient specific finite element model of the thorax and segmenting the internal organs for anatomical prior information for the finite element model. In the following section we will describe how the EIT reconstruction and MR scan can be superimposed, or co-registered, to assist clinicians with a qualitative diagnosis. The reconstruction parameters for the EIT reconstruction can be chosen by maximising the mutual information between the EIT and MRI through a mutual information calculation. This provides an alternative to methods such as the L-curve, or discrepancy principle, to optimise regularisation parameters.

5.4 EIT and MR image co-registration

In this section we describe the EIT and MR image co-registration process, and the method used to calculate the mutual information between the EIT and MR images.

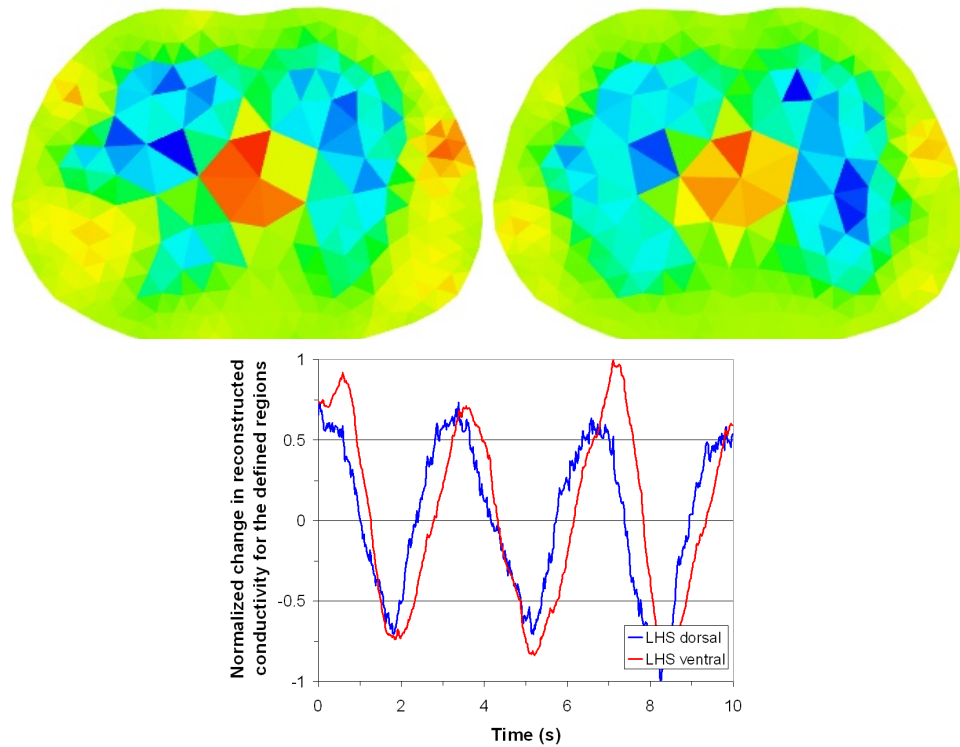


Figure 5.6: Sitting and supine image reconstruction; The two top images are transverse slices at the sixth intercostal spacing for the subject in the supine (left) and sitting (right) position respectively at max inhalation (relative to max exhalation). Blue and red corresponds to negative and positive conductivity changes respectively. The bottom image illustrates the dynamic behaviour of normalized conductivity differences, for simplices in the ventral and dorsal regions, for a subject in the supine position.

The image co-registration process and mutual information calculation provides both a qualitative and quantitative measure of EIT reconstruction performance. Although mutual information techniques have been used in previous multimodal imaging studies (see [136] for a review) such techniques have yet to be applied in the area of lung imaging using EIT.

The Manchester Confeitir [137] software was used to convert the reconstructed EIT image from the irregular tetrahedral mesh into a matrix with 2 mm-cubic isotropic voxels each representing a conductivity change and the coordinates of each voxel were then transformed so that they were in the same space as the MRI data. The software efficiently identifies the tetrahedron whose centroid is closest to the centre of any given voxel. Additionally, the application of a small threshold to the EIT data aided improved clarity of the subsequent visualisations. This typically involved discarding 5% of extreme points from the visualisation. This threshold was also applied to the EIT image in the mutual information calculation outlined in section 5.5. The EIT

images were transformed to the Nifti data format for subsequent importing into 3D Slicer [138]. The MRI data were imported into 3D Slicer separately and co-registered using methods validated with bench-top phantoms [139]. This involved marking up a set of control points around the outside of the torso on both the EIT and MRI data using the fiducial registration module of 3D Slicer, followed by least squared minimisation of the distance between the two sets of data in space.

Figure 5.7 shows an example of image co-registration of MRI and EIT using 3D Slicer, for the subject in the sitting position at maximum inhalation. The left and right column are superior and inferior transverse planes respectively. The top row is the original MR image, the middle row the EIT reconstruction and the bottom row is the resultant image co-registration. From the images, it can be seen that the EIT reconstruction typically underestimates the physiological size of the actual cross-sectional areas of the lung. Inspection of the complete 3D data along the caudal-distal axis showed this to be true for the entire scanned lung volume.

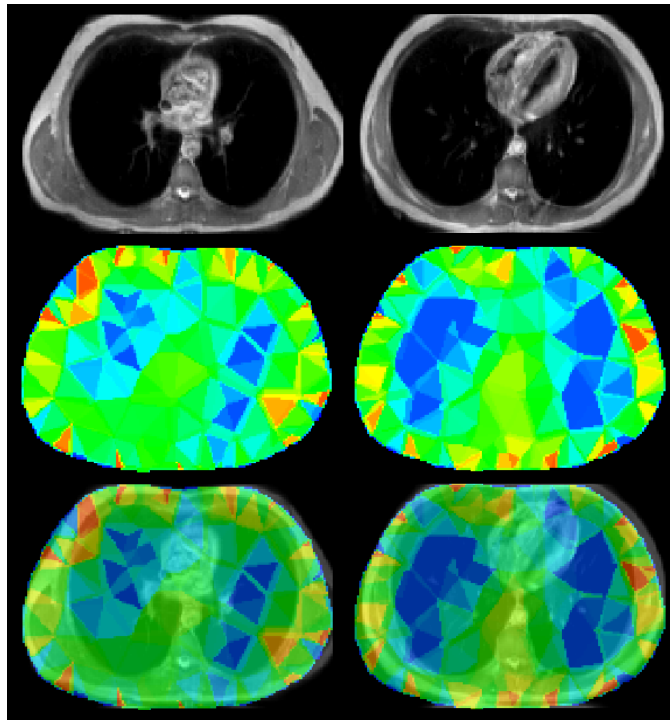


Figure 5.7: MRI and EIT image co-registration. Left to right columns: Superior and inferior transverse planes. Top to bottom rows: MRI image, EIT image and co-registered EIT and MRI images at the transverse slice. All images are at max inhalation relative to max exhalation. Blue and red correspond to negative and positive conductivity changes respectively.

Another observation to note is that the conductivity distribution exhibits a significant twisting effect in the superior transverse slice consistent with the 2D linear image

reconstructions obtained by Bikker *et al.* using the Dräger system in [140]. This is likely to be an artefact resulting from the inadequacies of the simple 2.5D extruded model used in the reconstruction. These inadequacies include the lack of inclusion of the heart in the model and possibly the model cut-off height along the caudal-distal axis being too small.

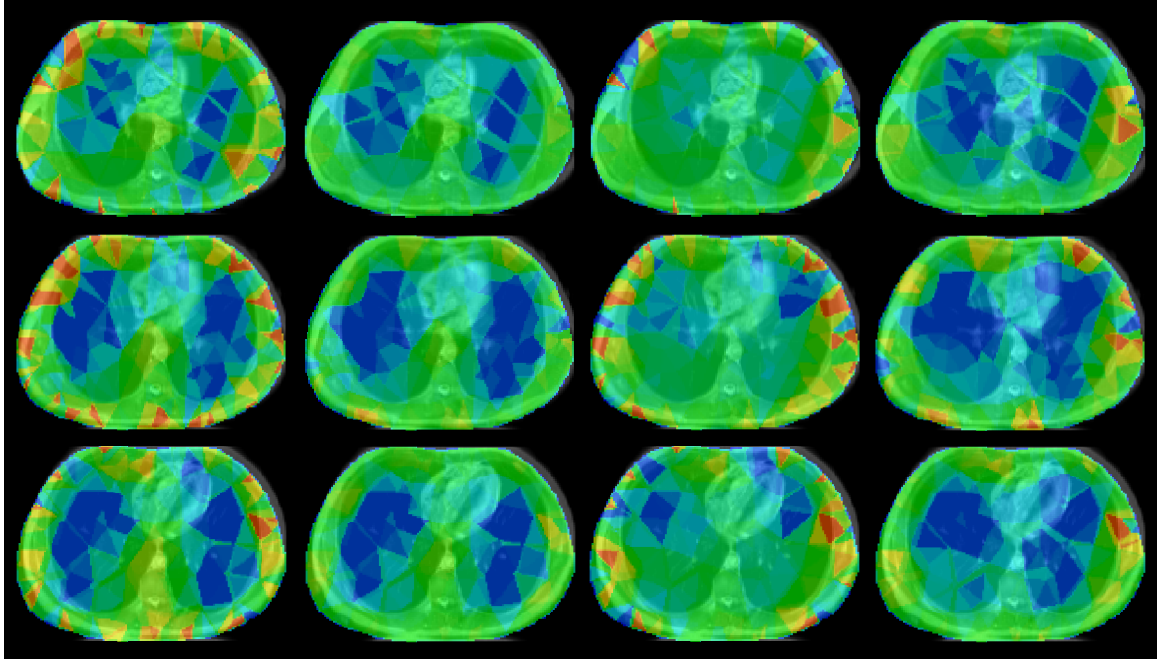


Figure 5.8: MRI and EIT image co-registration. Left to right columns: Sitting standard reconstruction, sitting shape correction reconstruction, supine standard reconstruction and supine shape correction reconstruction. Top to bottom rows: Transverse slices from superior to inferior. All images are at max inhalation relative to max exhalation. Blue and red correspond to negative and positive conductivity changes respectively.

Figure 5.8 shows EIT and MRI co-registration examples for the subject in the seated and supine positions for the two reconstruction algorithms. The images clearly show that the shape correction algorithm decreases the boundary artefacts, and the EIT reconstructions again are typically found to underestimate the total lung volume. The shape correction algorithm also has an increased tolerance to positional changes of the subject in the supine position. Additionally, moving towards the superior position, the reconstructed lung regions tend to decrease in contrast to that of inferior slices, and we believe this could be due to the natural tapering of the lungs as we move in a superior direction.

5.5 EIT and MR mutual information

We denote two images A and B , each with N cubic voxels, and each voxel having a positive grayscale value, a , with $0 \leq a \leq 1$, and consider $N_B = 256$ equispaced bins. We define two discrete probability distributions of A and B , $p_A, p_B \in \mathbb{R}^{N_B}$, and the discrete joint probability distribution of A and B , $p_{A,B} \in \mathbb{R}^{N_B \times N_B}$. $p_A(i)$ is given by the number of voxels in image A that have grayscale value in the interval $[\frac{(i-1)}{N_B}, \frac{i}{N_B}]$, normalised by N . $p_{A,B}(i, j)$ is given by the number of times out of N that a pixel in A has grayscale value in the interval $[\frac{(i-1)}{N_B}, \frac{i}{N_B}]$ and the same pixel in B has grayscale value in the interval $[\frac{(j-1)}{N_B}, \frac{j}{N_B}]$, normalised by N . The Shannon entropy, in the imaging context, is a measure of the information content of an image, measured in *bits*. The information content of a single event, that is of a particular grayscale value interval of an image, is proportional to the log of the inverse of the probability of an event. The total information content of an image, or entropy, is the information content of a single event, weighted by the probability that the event occurs, summed over all events. The total entropy of A , and the joint entropy of A and B , are expressed as

$$H_A = - \sum_{i=1}^{N_B} p_A(i) \log(p_A(i)), \quad H_{A,B} = - \sum_{i=1}^{N_B} \sum_{j=1}^{N_B} p_{A,B}(i, j) \log(p_{A,B}(i, j)), \quad (5.4)$$

respectively. The mutual information of A and B , $I_{A,B}$, is defined as the total entropy of A and B minus the joint entropy, $I_{A,B} = H_A + H_B - H_{A,B}$, which equates to

$$I_{A,B} = \sum_{i=1}^{N_B} \sum_{j=1}^{N_B} p_{A,B}(i, j) \log \frac{p_{A,B}(i, j)}{p_A(i)p_B(j)}. \quad (5.5)$$

It can be shown that $0 \leq H_A \leq \log(N)$, where $H_A = 0$ when the image conveys no information i.e. it is featureless or homogeneous, and $H_A = \log(N)$ for white noise. It is also true that $0 \leq I_{A,B} \leq H_A$, where $I_{A,B} = 0$ when A and B have no features in common and $I_{A,B} = H_A = H_B = H_{A,B}$ when A and B are the same. The larger the mutual information between two images, the more similarities the two images share.

To calculate the mutual information, a threshold is first applied to the MR image to generate a binary image representing just lungs and chest, similar to the segmentation shown in figure 5.2a. The intensity values of the cubic voxel based EIT image are then scaled linearly so they lie within the same range as the binary MR image. When computing the discrete probability distributions and a bin is empty, $0 \times \log(0)$ is

interpreted as 0 because $p \log(p) \rightarrow 0$ as $p \rightarrow 0$. The MR and EIT images are both sampled at their voxel centres to estimate H_A , H_B and $H_{A,B}$, and hence $I_{A,B}$ via (5.5). This calculation therefore measures how well a linearised EIT reconstruction is able to find the *overall shape* of the lungs. We perform the mutual information calculation over a range of regularisation parameters, (α, β) , for both a standard ($\beta = 0$) and shape corrected reconstruction algorithm. This effectively results in a numerical parameter study to maximise the mutual information between MRI and EIT as a function of the parameters α and β .

Figure 5.9 shows the mutual information with a lung-segmented MR image as a function of the parameter α , for the shape corrected and standard reconstruction in both the sitting and supine positions at maximum inspiration. For comparison, the maximum possible mutual information, that is the mutual information of the lung-segmented MR image with itself, was 1.51 bits. From figure 5.9 it can be seen for the subject in the sitting position, there is a maximum of mutual information of approximately 1.11 bits for the standard reconstruction algorithm, with $\alpha = 3 \times 10^{-2}$, and 1.21 bits for the shape corrected reconstruction, with $(\alpha, \beta) = (10^{-2}, 4 \times 10^{-2})$. In the supine position, there is a maximum of mutual information of approximately 1.09 bits for the standard reconstruction algorithm, with $\alpha = 3 \times 10^{-2}$, and 1.20 bits for the shape corrected reconstruction algorithm, with $(\alpha, \beta) = (2 \times 10^{-2}, 4 \times 10^{-2})$. This corresponds to an approximate 10% increase in the maximal mutual information with the shape correction algorithm. It can also be seen at this particular value of β that the shape corrected reconstruction generally has a greater mutual information than the standard reconstruction over a wide range of α . The increase in mutual information from a standard to shape correction reconstruction is also visually evident in the images of figures 5.3 and 5.4 (which are reconstructions at (α, β) corresponding to the maximum mutual information), when compared to figure 5.2a.

5.6 Conclusions and extensions

This chapter demonstrates results of 3D EIT dynamic lung imaging at Manchester using an array of 32 electrodes with the fEITER system. The implemented shape correction algorithm explicitly accounts for small changes in the boundary shape which

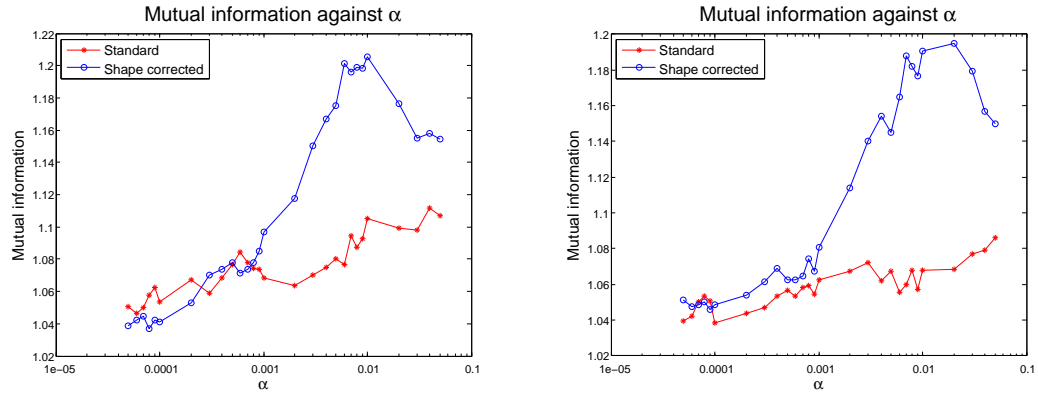


Figure 5.9: Mutual information parameter study as a function of α ; The left and right hand image are for the subject in the sitting and supine position respectively with a shape corrected ($\beta = 4 \times 10^{-2}$) and standard ($\beta = 0$) reconstruction.

occur when the subject breathes. This novel algorithm yields a reduction of boundary artefacts and improved contrast of the lungs when compared to a standard reconstruction algorithm without shape correction. The novel co-registration process, and original mutual information performance criterion, presented here provides an effective and practical method of directly comparing the spatial fidelity of EIT images with those obtained from MRI. The shape correction algorithm increased the maximum mutual information with a lung-segmented MR image by approximately 10% for both a subject in the sitting and supine positions and we believe this is the first time mutual information has been used to assess the quality of lung EIT reconstructions. Our findings suggest that shape correction would be a valuable enhancement to the reconstruction algorithms used in existing commercial EIT instruments applied to lung imaging such as the PulmoVista 500 system, developed by Dräger [24].

Previous multiple electrode plane studies, such as those by Nebuya *et al.* [141] and Bikker *et al.* [140], have typically only used successive EIT data collection at different electrode planes of the chest, resulting in 2D reconstructions of each plane, at low frame rates. One notable exception to this trend is the tomography systems of the Rensselaer group [142, 143] which have previously provided 3D lung and pulmonary images, albeit using only generic reconstruction models. Although the MRI-informed 3D reconstruction and high frame rate of our present study address these issues, the use of non-simultaneous data acquisition across the imaging modalities remains a shortcoming as it requires the subject to achieve repeatable breathing and posture for the separate data captures. For better model generation and validation of EIT using MRI,

it is thus most attractive to perform simultaneous data acquisition. If EIT were to be routinely used as a bedside monitoring tool, optical tracking techniques could plausibly be used to inform electrode positions and an approximate boundary shape such as those by Forsyth *et al.* in breast imaging [34]. However, the strength of using MRI to inform the shape is that we can also assess the spatial resolution of EIT after post processing using, for example, mutual information as presented here. Additionally, we note that many patients with serious lung injuries in intensive care units have had MR and/or CT scans during their course of treatment, and so if this information is available it is logical to use this as prior information of the external shapes for the EIT forward and reconstruction finite element models as we have described here.

The present methodology could benefit significantly from improvements in the generation of the thorax model. Firstly, it was found that the resulting image reconstructions were sensitive to the somewhat arbitrary caudal and distal cut-off heights chosen for the model. If the model cut-off height chosen is too small, a non-physical zero current flux boundary condition is set at the caudal and distal ends of the model and the simulated voltages have logarithmic decays associated with a 2D model. We believe this is a major contribution to the twisting effects seen in some image reconstructions, as noted in section 3.3. Choosing a larger cut-off height resulted in little qualitative change in the reconstruction in the electrode planes, and unrealistic conductivity changes far away from the electrode planes. A possible way to compensate for this is to use infinite elements to model the voltage decay at the caudal and distal ends of the model such as by Vauhkonen *et al.*[144]. Secondly, the image reconstructions presented here are 2.5D, in the sense that the model cross section did not vary along the caudal-distal axis. This could be addressed by generating fully 3D models incorporating the electrodes, from either commercial meshing packages such as Simpleware [145] or open source software such as iso2mesh [146]. Although demonstrated here for the MRI case, the use of imaging-informed EIT modelling and subsequent co-registration are directly transferable to other high resolution tomographic modalities, most notably CT.

Chapter 6

Coupling EIT and mechanical ventilation

Clinicians are excited about the non-invasive, portable and fast nature of EIT, but it is difficult to interpret reconstructed conductivities in a clinical setting due to both the highly ill-posed nature of the problem and inadequate modelling assumptions as discussed in this thesis. It is also apparent that a conductivity image may not necessarily be useful to a clinician. Of more practical significance in diagnosis of lung injury would be the computation of *clinically meaningful* indices, such as regional compliance, or the distribution of liquid in the lung. In this chapter we outline an original method to combine EIT with mechanical ventilation to generate clinically meaningful parameters through mechanical modelling of the respiratory system, and results of the novel algorithm, using simulated data, are presented.

6.1 Mechanical ventilation and EIT

In the mechanical ventilation of ARDS patients a PEEP is set on the ventilator to prevent lung tissue collapsing and to recruit new regions of the lungs. In a PEEP trial, the PEEP is changed over time in order to achieve better gas exchange and maximum alveolar recruitment in the lungs [13]. During a PEEP trial, we would like to simultaneously use EIT to estimate parameters such as *compliance*. Compliance is defined as the ratio of the change in air volume to the change in pressure. The more compliant a region the more air that can fill the region for a given pressure change.

A dynamic EIT image displays the reconstructed change in conductivity between two data frames at different stages along the breathing cycle. Air has a small conductivity relative to typical human tissue, and thus a conductivity change for a given voxel will largely be attributed to the movement of air within the voxel as observed experimentally in [147]. The following chapter relies on performing absolute EIT because, using a given homogenisation model, we would be able to convert the reconstructed conductivity of a voxel to air volume fraction for that voxel as we discuss next.

6.1.1 Inverse homogenization

In this chapter we implicitly assume that the air volume fraction of a particular voxel, or indeed any region of the lung, can be computed from a conductivity image. Techniques from homogenization theory could help us determine such quantities. The following subsection is based on a conference paper given in 2014 at the 15th International Conference on Biomedical Applications of Electrical Impedance Tomography 2014, titled ‘Regional lung compliance: Coupling ventilation and electrical data’, written by Henry Tregidgo, the author and Bill Lionheart [148].

We believe that the essential steps required to retrieve useful information from EIT must include (i) segmenting regions in the chest cavity from MRI or CT and assigning a model for specific micro-structures to these regions, (ii) determining the air volume fraction change from the change in conductivity, (iii) calculating regional air volume from air volume fractions and (iv) using an ordinary differential equation (ODE) mechanical model to calculate the required diagnostic parameters.

Chest Segmentation

Defining likely contents of specific anatomic regions in advance has several uses. These include refining models for retrieving air volume fractions as well as labelling functional units of the lung for which diagnostic parameters will be required. MRI and CT data can be used to segment specific regions of the chest cavity and assign properties to them based on anticipated microstructure. It would then be necessary to model how this structure changes during the breathing cycle. This modelling will require coupling of neighbouring regions through mass and volume conservation, as well as comparisons with typical deformations of the lung, chest cavity and abdomen under

forced ventilation.

Air Volume Fractions

We would like to create a homogenisation scheme, mapping the air volume fraction of an underlying microstructure to bulk conductivity. We will then need to invert this to find the air volume fraction of a region from reconstructed conductivity values. The assumed microstructure can be as simple as spherical inclusions dispersed in a homogeneous substrate [149], or can further reflect the anisotropic structures identified while segmenting the lung image [150]. However, air content is not the only quantity which will affect the bulk conductivity. In addition other features such as blood flow or lung fluid content may need to be incorporated. This could be done by combining heart rate and blood pressure measurements with dispersion relations from multi-frequency EIT to discern blood content. We note that it is desirable to perform absolute conductivity imaging, as opposed to reconstructing normalised conductivity differences, because the mapping from air volume fraction to bulk conductivity will in general be non-linear.

Regional Air Volume

As previously noted, at different times throughout the breathing cycle the domain will have deformed, changing the physical volume occupied by the lung. The volume change is non-uniform, complicating the conversion of air volume fractions to regional volumes. Models created for chest segmentation could help with this problem while the ventilator itself provides information on the amount of air passed into the lung, which can be used to constrain the total air volume within the lung.

The rest of this chapter will be devoted to the last stage of the retrieval, that is using ODE models to estimate mechanical parameters of the respiratory system.

6.2 CFD and mechanical modelling

The respiratory system is complex and mathematical modelling has proven to be an extremely difficult task. Recent advances in image-based modelling techniques and computational power have been utilised to generate computational fluid dynamics

(CFD) models of the respiratory system from high resolution CT and MRI [151, 152]. One of the aims of high resolution CFD modelling is to model different pathologies computationally to understand how these affect the respiratory output. The hope is that such models will give insight into how different pathologies generate different output signatures, and eventually be used in clinical diagnosis.

Alternatively, a mechanical model assumes the respiratory system is composed of simple mechanical units connected through a network in order to replicate the behaviour of the respiratory system. These models stretch back to the work of Mead *et al.* [44, 153]. The airways are modelled as a set of connected tubes, and the lung parenchyma as inflatable sacs with different regions assigned mechanical parameters, such as compliance and resistance, and couple through their physical locations and connectivity. The air is assumed to be an incompressible, inviscid fluid at constant temperature. These assumptions give rise to a system of coupled temporal ODEs with the dependent variables being the volumes of the individual sacs, and their temporal derivatives, and the coefficients of the ODEs being functions of the mechanical parameters [154, 155]. More complicated ODE models have also been created that include the coupling with the cardiovascular system and the brainstem [156].

An input pressure wave at the mouth will distribute air around the system according to the compliance and resistances. In this thesis we propose that the regional air volume fractions calculated from conductivity images can be treated as states of the ODEs, and we have input data as the temporal pressure wave at the mouth. Using techniques from inverse problems for ODEs, we demonstrate that for some systems we can uniquely identify the mechanical parameters in the model.

6.2.1 Electric and hydrodynamic analogies

In a hydrodynamical system there are two fundamental properties - the volume of fluid (V/L) and the pressure ($P/\text{cmH}_2\text{O}$) is the force per unit area that the fluid exerts. The flow (Q/Ls^{-1}) is the rate of change of the fluid volume. There are three fundamental relationships between P , V and Q . The compliance ($C/L(\text{cmH}_2\text{O})^{-1}$) is defined through $V = CP$ and measures the opposition to a change in volume at a fixed pressure. The resistance ($R/\text{cmH}_2\text{OsL}^{-1}$) is defined through $P = QR$ and measures the opposition to flow at a fixed pressure. The inductance ($I/\text{cmH}_2\text{Os}^2L^{-1}$) defined

| Type | Mechanical | Hydrodynamical | Electrical |
|-----------|------------------------------------|---------------------------------|---------------------------------|
| Potential | Force F | Pressure P | Voltage V |
| Quantity | Displacement x | Volume V | Charge Q |
| Flow | Velocity $v \frac{dx}{dt}$ | Flow $Q \frac{dV}{dt}$ | Current $I \frac{dQ}{dt}$ |
| | Spring $F = kx$ | Compliance $P = \frac{1}{C}V$ | Capacitance $V = \frac{1}{C}Q$ |
| | Damping $F = Bv$ | Resistance $P = RQ$ | Resistance $V = RI$ |
| | Inertial mass $F = m\frac{dv}{dt}$ | Inductance $P = I\frac{dQ}{dt}$ | Inductance $V = L\frac{dI}{dt}$ |

Table 6.1: Analogous variables in mechanical, hydrodynamic and electrical systems.

through $P = I\frac{dQ}{dt}$, measures the opposition to a change of flow at fixed pressure. We can write these relationships in the following form

$$P_C = \frac{1}{C}V, \quad P_R = R\frac{dV}{dt}, \quad P_L = L\frac{d^2V}{dt^2}.$$

If a hydrodynamical compartment has all these properties, at a fixed pressure, this results in a second order differential equation for V . The volume, flow and pressure are analogous to the charge (Q /Coulombs), current (I /Amps) and voltage (V /Volts) respectively in an electric circuit. The electrical resistance (R /Ohms), defined through $V = IR$, capacitance (C /Farad), defined through $Q = CV$, and inductance (L /Henries), defined through $V = L\frac{dI}{dt}$, are analogous to the hydrodynamical resistance, compliance and inductance respectively (see table 6.1). In the rest of this chapter it is assumed the inductance is small, $L_I \approx 0$, which is true for small enough mass of the fluid [154]. The analogies are useful as we can model the respiratory system as an electrical network, and then convert back to the hydrodynamical quantities where necessary.

6.2.2 Single and double compartment model

Perhaps the simplest mechanical model of the respiratory system is a single compartment with air volume and flow denoted V and Q respectively, as shown in figure 6.1. We denote the pressure at the input of the system as P i.e. the mouth pressure, and the pleural or ‘ground’ pressure as P_0 . We assume the total pressure drop of the system is attributed to the elastance, $P = EV = \frac{1}{C}V$, and resistance to air flow, $P = RQ$, and we can equate the pressure

$$P(t) = EV(t) + R\dot{V}(t) + P_0. \quad (6.1)$$

In practice, we can measure the pressure, volume and flow rate at the mouth using standard bedside respiratory monitoring devices. We assume these quantities have

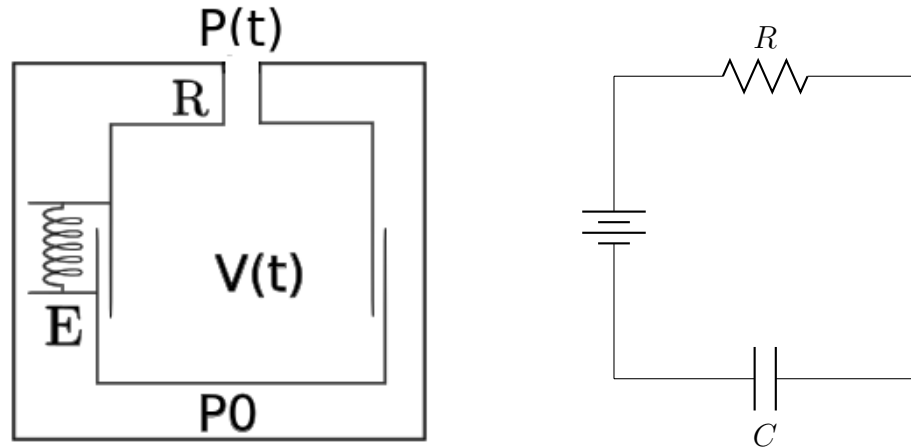


Figure 6.1: Single mechanical chamber with a spring with hydrodynamical elastance and resistance of E and R respectively and pressure differential $P(t) - P_0$. The electric circuit analogue with electrical capacitance and resistance of C and R and voltage $V(t) - V_0$ applied across the battery. The electric circuit can be represented by a single complex impedance $Z(w) = (R + \frac{1}{i\omega C})$.

been sampled at S time points, and also denote the sampled vectors of pressure, volume and flow as P, V and Q respectively. We can write the sampled ODE in the form of a matrix-vector equation

$$P = AX,$$

where $X = [E, R, P_0] \in \mathbb{R}^3$ and $A = [V|\dot{V}|\mathbf{1}] \in \mathbb{R}^{S \times 3}$, where $\mathbf{1} \in \mathbb{R}^S$ is a column vector of 1's. Assuming a time varying input pressure, the functions V, \dot{V} and $\mathbf{1}$ must be linearly independent from one another, since they solve an ODE with a non-zero forcing term. The matrix A thus has full rank and so $A^T A$ is invertible given enough independent samples of the solutions. Hence, we can use a least squares estimate

$$\hat{X} = \arg \min_X \|P - AX\|_2^2,$$

with an explicit solution given by the normal equations

$$\hat{X} = (A^T A)^{-1} A^T P.$$

A single compartment model of the respiratory system is clearly unrealistic, and an obvious extension is a model with two parallel compartments. We let $P(t)$ and $\dot{V}(t)$ denote the pressure and flow at the mouth, R_c the airway resistance and let the compartments have resistance R_i , and compliances $1/E_i$ respectively, where $i = 1, 2$, along with their respective pressure and flow as $P_i(t)$ and $\dot{V}_i(t)$. By Kirchoff's law, we

have $V = V_1 + V_2$, and three applications of Ohm's law leads to the following three equations (dropping the explicit dependence on time)

$$P_c - P_0 = R_1 \dot{V}_1 + E_1 V_1 = R_2 \dot{V}_2 + E_2 V_2, \quad P - P_c = R_c \dot{V},$$

where P_0 represents the ground voltage (pleural pressure) and $P_c(t)$ is the pressure at the branch point of the two compartments. This can be written as two coupled ordinary differential equations

$$P - P_0 = E_1 V_1 + (R_1 + R_c) \dot{V}_1 + R_c \dot{V}_2 = E_2 V_2 + (R_2 + R_c) \dot{V}_2 + R_c \dot{V}_1. \quad (6.2)$$

We would like an equation for P in terms of V , and so want to eliminate V_1 from the equations. This can be achieved by using the Laplace transform, converting the differential equations into algebraic equations in the Laplace domain, and then transforming back into the time domain. Following this procedure [154] we find that

$$(E_1 + E_2)P + (R_1 + R_2)\dot{P} = E_1 E_2 V + (E_2(R_1 + R_c) + E_1(R_2 + R_c))\dot{V} \\ + (R_c(R_1 + R_2) + R_1 R_2)\ddot{V} + P_0$$

Dividing through by $(E_1 + E_2)$, and using sampled time series of solutions, this can again be written as linear system of equations $P = AX$, where $A \in \mathbb{R}^{S \times 5}$, which has maximum rank 5. Thus the 6 parameters R_c, R_1, R_2, C_1, C_2 and P_0 , can not be uniquely determined from the pressure and volume at airway opening. A general linear model with M parallel compartments, can be written in the form [154]

$$\sum_{k=0}^{M-1} b_k P^{(k)}(t) = \sum_{k=0}^M a_k V^{(k)}(t),$$

for some coefficients a_k and b_k which are algebraic functions of the individual compliances and resistances. We are interested in the relationship between the pressure and flow (or volume) at airway opening, $\tilde{P}(\omega) = Z(\omega)i\omega\tilde{V}(\omega)$, where $Z(\omega)$ is known as the *response* function. Taking the Fourier transform of the above equation we find that

$$Z(\omega) := \frac{\tilde{P}(\omega)}{i\omega\tilde{V}(\omega)} = \frac{\sum_{k=0}^M (i\omega)^k a_k}{\sum_{k=0}^{M-1} (i\omega)^{k+1} b_k},$$

a rational function of temporal frequencies. Clearly the more parameters appearing in a mechanical model, the less that can be uniquely determined from just measuring the flow and pressure at the mouth as we observed in the two compartment model.

In particular many different models exist whose parameters can be adjusted to fit the measured data, known as the model non-uniqueness problem [154]. The response function does contain useful information, and the impedance spectra can be used to determine effective compliance, resistance and inductance of small parameter mechanical systems [157, 158].

Converting regional reconstructed conductivity changes to regional air volume provides us with information of the *interior* data of the mechanical model and not just at airway opening. In effect we have created an inverse problem on resistor networks, consisting of data of time dependent boundary measurement of pressure and volume as well as interior measurements of volume. In the following section we discuss what extra information can be gained from the extra interior measurements by considering a specific example of a multi-lobe lung model.

6.3 Multi-compartment coupled ODE model

We model the respiratory system as two lungs connected in parallel, with each lung having N compartments, or lobes, connected in parallel. Treating each lung with a number of distinct lobes connected in parallel is physiologically reasonable (see [159] for a description of lung physiology), and the illustration for electric circuit analogy for the case $N = 6$ is depicted in figure 6.2. We model the main airway with a resistance R_S branching into the lungs, and each lobe of each lung having a compliance and resistance component connected in series, as in figure 6.1.

Let $P(t)$ denote the pressure at airway opening, $P_S(t)$ the (unknown) pressure after the airway series resistance and P_0 the (unknown) pleural pressure. Further let $E_{A,B}, R_{A,B}$, where $A = L$ or R and $B = 1, \dots, N$, denote the elastance and resistance of each separate compartment. Using Ohm's law on the airway series resistance, we have

$$P(t) - P_S(t) = R_S \dot{V}(t). \quad (6.3)$$

Similarly, applying Ohm's law on each lobe results in an additional $2N$ equations

$$P_S(t) - P_0 = R_{L,i} \dot{V}_{L,i}(t) + E_{L,i} V_{L,i}(t) \quad i = 1, \dots, N, \quad (6.4)$$

$$P_S(t) - P_0 = R_{R,i} \dot{V}_{R,i}(t) + E_{R,i} V_{R,i}(t) \quad i = 1, \dots, N. \quad (6.5)$$

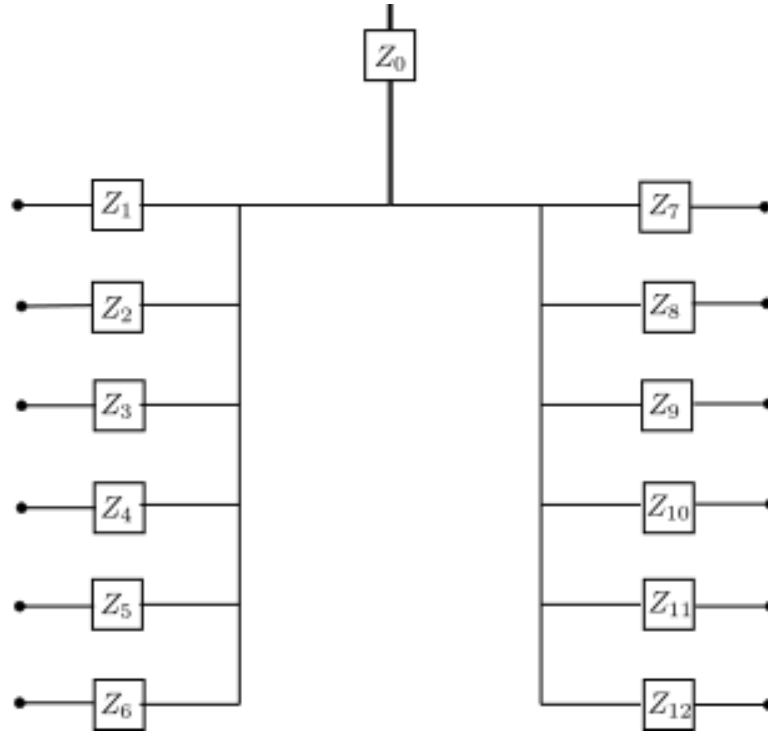


Figure 6.2: Electric circuit analogue of multi-compartment lung model with 6 compartments per lung. Each compartment has associated an impedance Z_i , consisting of a capacitor and resistor connected in series (see figure 6.1.)

Kirchoff's law also supplies us with additional constraints on the air volume and flow

$$\dot{V}(t) = \dot{V}_L(t) + \dot{V}_R(t) = \sum_{i=1}^N (\dot{V}_{L,i}(t) + \dot{V}_{R,i}(t)).$$

Let $v, f \in \mathbb{R}^{2N}$ be given by

$$v = (V_{L,1}, \dots, V_{L,N}, V_{R,1}, \dots, V_{R,N}) \quad f = (P(t) - P_0, \dots, P(t) - P_0),$$

the matrix $E \in \mathbb{R}^{2N \times 2N}$ be diagonal with entries of the elastance of each compartment respectively, and the matrix $B \in \mathbb{R}^{2N \times 2N}$ given by

$$B = \begin{pmatrix} R_S + R_{L,1} & R_S & \dots & R_S \\ R_S & R_S + R_{L,2} & \ddots & R_S \\ \vdots & \ddots & \ddots & R_S \\ R_S & \dots & R_S & R_S + R_{R,N} \end{pmatrix}.$$

Then we can write the RC network as a coupled first order system of ordinary differential equations

$$B\dot{v}(t) = -Ev(t) + f(t), \quad \dot{v}(t) = B^{-1}(-Ev(t) + f(t)) =: g(x, t).$$

To solve the forward problem, we need initial conditions on the volume of each compartment. For example at $t = 0$ we can set each compartment to have volume $V_0/(2N)$, where V_0 is the forced expiratory volume which is measurable using spirometry techniques. We also need to apply an input pressure force term, $P(t)$, which will be discussed in the subsequent section. The solution is evolved through time using a time integration method for ODE, and in particular an explicit Runge Kutta-4 (RK4) method is used

$$v_{n+1} = v_n + \frac{1}{6}(\Delta t)(k_1 + 2k_2 + 2k_3 + k_4)$$

where Δt is the (constant) time step and

$$\begin{aligned} k_1 &= g(x_n, t_n + \frac{1}{2}\Delta t) & k_2 &= g(x_n + \frac{h}{2}k_1, t_n + \frac{1}{2}\Delta t) \\ k_3 &= g(x_n + \frac{h}{2}k_2, t_n + \frac{1}{2}\Delta t) & k_4 &= g(x_n + hk_3, t_n + \Delta t) \end{aligned}$$

where v_n is the approximate solution at time $t_n = t_0 + n\Delta t$.

6.3.1 Inverse problem

We consider the following problem - given measurements of the input pressure at airway opening, and the resulting volume at all times within the mechanical network, can we infer the parameters of resistance and capacitance? To answer this question, we begin by combining equations (6.3), (6.4) and (6.5) leading to $2N$ equations of the form

$$P(t) = R_S \sum_{i=1}^N \sum_{j=1}^2 \dot{V}_{j,i}(t) + R_{L,i} \dot{V}_{L,i}(t) + E_{L,i} V_{L,i}(t) + P_0 \quad i = 1, \dots, N \quad (6.6)$$

$$P(t) = R_S \sum_{i=1}^N \sum_{j=1}^2 \dot{V}_{j,i}(t) + R_{R,i} \dot{V}_{R,i}(t) + E_{R,i} V_{R,i}(t) + P_0 \quad i = 1, \dots, N. \quad (6.7)$$

In effect each of these equations describes the pressure drop from pleural to airway opening pressure for each series circuit in the multi-compartment parallel model. Let $V_{2Li} = [V_{L,i}, \dot{V}_{L,i}] \in \mathbb{R}^{S \times 2}$ $i = 1, \dots, N$ and similar with V_{2Ri} . Then we can write the above equation as a matrix equation $d = Mx$, where $d = (P(t), \dots, P(t)) \in \mathbb{R}^{2NS}$, vector of parameters $x = (E_{L,1}, R_{L,1}, \dots, E_{R,N}, R_{R,N}, R_S, V_0) \in \mathbb{R}^{2(2N)+2}$ and $M \in$

$\mathbb{R}^{2NS \times (2(2N)+2)}$ given by

$$M = \begin{pmatrix} V_{2L1} & 0 & & & & \sum_{j=1}^2 \sum_{i=1}^N \dot{V}_{j,i} & 1 \\ 0 & \ddots & \ddots & & & \vdots & \vdots \\ & & \ddots & V_{2LN} & & & \\ & & & & V_{2R1} & \ddots & \\ & & & & \ddots & \ddots & 0 \\ & & & & & & \vdots \\ & & & & 0 & V_{2RN} & \sum_{j=1}^2 \sum_{i=1}^N \dot{V}_{j,i} & 1 \end{pmatrix}. \quad (6.8)$$

We wish to determine whether the matrix $M^T M$ is invertible to perform a least squares inversion, and so we must determine if M has full rank. We denote an arbitrary volume time series of a compartment as $V_i(t)$. We remember two functions f_1, f_2 are linearly dependent in an interval $[0, T]$ if $f_1(t) = \alpha f_2(t)$ for some $\alpha \in \mathbb{R}$ and for all $t \in [0, T]$, else the functions are linearly independent. Hence $V_i(t)$ and $\dot{V}_i(t)$ are linearly independent, unless there is a trivial zero pressure forcing term applied to the coupling ODE. The matrix consisting of the first $2NS \times 4N$ block of M and the last column of M has full rank of $4N + 1$ given enough independent samples of the volumes, and a non-trivial forcing term.

Where there is a potential rank deficiency is if the first N even columns are linearly dependent on the 2^{nd} last column of M . Using the Fourier Transform of $V(t)$, $\tilde{V}(\omega)$, this condition implies that $i\omega\tilde{V}_j(\omega) = \alpha_{jk}i\omega\tilde{V}_k(\omega)$ for all $\omega \in \mathbb{R}$, and for some non-zero constant $\alpha_{jk} \in \mathbb{R}$ for $j, k = 1, \dots, N$. Equations (6.4) and (6.5) are also equal so we must have

$$(R_j i\omega + E_j)\tilde{V}_j(\omega) = (R_k i\omega + E_k)\tilde{V}_k(\omega) \quad \text{for all } \omega,$$

and thus, if the functions are linearly dependent we must have $\alpha_{jk} = \frac{R_k i\omega + E_k}{R_j i\omega + E_j}$, for all $j, k = 1, \dots, N$. But α_{jk} must be independent from ω because it is constant and this implies either all the elastances are zero, all the resistances are zero, or

$$\frac{R_k}{E_k} = \frac{R_j}{E_j} \quad j, k = 1, \dots, N.$$

If this condition is satisfied we deduce the matrix is rank deficient by exactly one for a large enough number of samples resulting in an underdetermined system. This condition means that the impedance angle for each compartment have the same phase. In this (unlikely) case this means that we can not distinguish between the airway

resistance and the resistances of each compartment. We note that in practice, if we had raw interior volume data we could check for this condition numerically by computing the rank of the matrix M , but for our numerical simulations we will assume that at least one of the ratios is different when constructing the forward problem. In this case the matrix M does have full rank, and hence $M^T M$ is invertible, and so we can estimate the parameters using a least squares estimate

$$x = (M^T M)^{-1} M^T d. \quad (6.9)$$

The combination of electrical and mechanical data will generate measurements of the vectors $P(t) \in \mathbb{R}^S$ and $V_{A,B}(t) \in \mathbb{R}^S$ for the pressure at airway opening and the sample volumes. The EIT data will not generate measurements of the flow, $\dot{V}_{A,B}(t) \in \mathbb{R}^S$, and so we must numerically differentiate the sampled volumes of each compartment to estimate the flow. In practice the air volume time series estimated from EIT will be very noisy and so it is important to efficiently, and robustly, estimate the flow from the volume. We outline a number of different methods to estimate the flow data from the volume data.

6.3.2 Numerical differentiation

For clarity, we consider numerical differentiation for a single compartment, with a measured charge time-series $V \in \mathbb{R}^S$ sampled at regular time intervals $t_i = (i - 1)\Delta t$, $i = 1, \dots, S$, where $\Delta t = \frac{T}{S-1}$. The simplest method is to use finite differences to estimate the derivative,

$$\dot{V}(t_{i+\frac{1}{2}}) = \frac{1}{\Delta t}(V(t_{i+1}) - V(t_i)) \quad i = 1, \dots, S - 1,$$

or some higher order finite difference scheme. Differentiation, however, is unstable in the presence of noise and we seek an improved method. In this chapter two alternative methods are outlined and implemented, namely *time integration of equations* and *inverse integration*.

Time integration of equations

In this method, each equation relating the input pressure to the compartment volume and flow in (6.7) is integrated from $t = 0$ to $T = i\Delta T$ leading to

$$\int_0^T P(t) dt = \int_0^T E_{L,i} V_{L,i}(t) dt + R_{L,i} V_{L,i}(T) + R_S \sum_{i=1}^N \sum_{j=1}^2 V_{j,i}(T) + P_0 T + F_{L,i},$$

$$\int_0^T P(t) dt = \int_0^T E_{R,i} V_{R,i}(t) dt + R_{R,i} V_{R,i}(T) + R_S \sum_{i=1}^N \sum_{j=1}^2 V_{j,i}(T) + P_0 T + F_{R,i},$$

where $i = 1, \dots, N$, $F_{L,i} = -R_{L,i} V_{L,i}(0) - R_S \sum_{i=1}^N \sum_{j=1}^2 V_{j,i}(0)$ and $F_{R,i} = -R_{R,i} V_{R,i}(0) - R_S \sum_{i=1}^N \sum_{j=1}^2 V_{j,i}(0)$. This requires cumulative integration of the input pressure data and volume data and leads to an extra constant to estimate for each compartment. These can then be fed into a parameter matrix analogous to M in (6.8) with the following amendments - $V_{2Li} = [\int_0^T V_{L,i}(t) dt, V_{L,i}, 1] \in \mathbb{R}^{S \times 3}$, $V_{2Ri} = [\int_0^T V_{R,i}(t) dt, V_{R,i}, 1] \in \mathbb{R}^{S \times 3}$, the second last column is now $\sum_{j=1}^2 \sum_{i=1}^N V_{L,i}$ and the last column is a repeated vector of the sampled time points. We can then estimate the parameters $x = (E_{L,1}, R_{L,1}, F_{L,1}, \dots, E_{R,N}, R_{R,N}, F_{R,N}, R_S, V_0) \in \mathbb{R}^{2(3N)+2}$ through a least squares estimate. We denote this method as *time integration of equations*.

Inverse integration

In section 3.1 we considered differentiation and observed this to be a mildly ill-posed inverse problem and so we treat the numerical differentiation as an ill-posed inverse integration problem. This allows us to regularise the solution appropriately depending on the expected noise level and smoothness of the flow, as well as providing *a-priori* information of the flow per compartment if available. A rigorous approach to numerical differentiation and regularisation was first studied in [160]. It has been shown for smooth problems, inverse integration with generalised Tikhonov regularisation is also equivalent to fitting a cubic spline to the volume data [161]. This has also been applied to chemical reaction equations in [162] and also applied to problems with discontinuous derivatives in [163].

For the problem on ODEs, the smoothness of the input pressure wave will effectively determine the smoothness of the highest order derivative of the volume by (6.7). For example, if the pressure wave is smooth, say C^2 , then the flow data will also be

C^2 . The input pressure could be non-differentiable, or discontinuous, but since this will determine the smoothness of the flow, we can account for this explicitly as a regularisation term in the inverse integration problem. We use smooth pressure waves at airway opening which means that smooth regularisation techniques can be applied. To numerically approximate the integrals we consider a cumulative Trapezium rule matrix F mapping the time sampled flow, \dot{V} , to volume, V , vectors

$$F : \mathbb{R}^{S+1} \rightarrow \mathbb{R}^S \quad \dot{V} \mapsto V = F\dot{V}.$$

In particular the i^{th} entry of $F\dot{V}$ for $\dot{V} \in \mathbb{R}^{S+1}$ is given by

$$(F\dot{V})_i = \frac{\Delta t}{2}(\dot{V}_0 + 2\dot{V}_1 + \dots + 2\dot{V}_{i-1} + \dot{V}_i).$$

We seek the flow data \dot{V} as the minimiser of the data residual $\|F\dot{V} - V\|$. Because F is compact, and the input pressure will be smooth, we stabilise using an additional smooth penalty term, $\|V\|_{H^2} = \|LV\|_{L^2}$, where L is a finite difference approximation to the second derivative, $L : \mathbb{R}^{S+1} \rightarrow \mathbb{R}^{S-1}$, where the i^{th} entry of LV is given by

$$(LV)_i = \frac{1}{(\Delta t)^2}(-V_i + 2V_{i+1} - V_{i+2}).$$

The MAP estimate leads to the following regularised minimisation problem,

$$\dot{V}_{\text{MAP}} = \arg \min_{\dot{V}} \{ \|F\dot{V} - V\|_2^2 + \alpha \|L(V - V_p)\|_2^2 \},$$

where V_p is a prior volume vector (which we assume to be zero for this rest of this chapter). This assumes that the volume is 0 at $t = 0$ which in general is not true. We can account for this by estimating the integration constant, V_0 , by adding an additional column to F , $\tilde{F} = [F, \mathbf{1}]$, and to L , $\tilde{L} = [L, \mathbf{0}]$, where $\mathbf{1}, \mathbf{0} \in \mathbb{R}^{S+1}$. An estimate of $\tilde{V} = [\dot{V}, V_0]$ is sought through the augmented problem

$$\tilde{V}_{\text{MAP}} = \arg \min_{\tilde{V}} \{ \|\tilde{F}\tilde{V} - V\|_2^2 + \alpha \|\tilde{L}(V - V_p)\|_2^2 \}.$$

Since the operator F is linear, we have the explicit formula for the minimiser as

$$\tilde{V}_{\text{MAP}} = (\tilde{F}^T \tilde{F} + \alpha \tilde{L}^T \tilde{L})^{-1} (\tilde{F}^T V + \tilde{L}^T \tilde{L} V_p).$$

After \tilde{V}_{MAP} has been estimated a smoothed approximation to the volume, $V_{\text{MAP}} := \tilde{F} \tilde{V}_{\text{MAP}}$, is also calculated. Once the flow and volume have been estimated for each compartment, these can then be assembled into the parameter estimation matrix (6.8), and an estimate of the parameters obtained through a least squares fit (6.9). We denote this method as *inverse integration*.

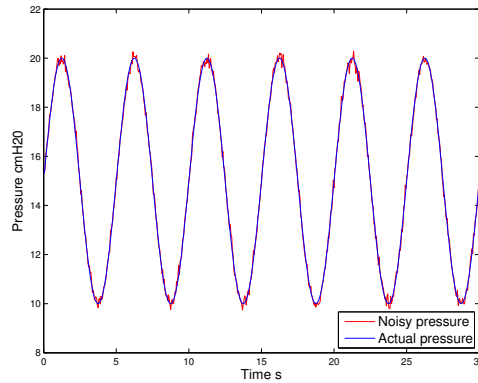


Figure 6.3: Sinusoidal pressure forcing term at mouth with $\text{SNR} = 100$ noise added.

6.4 Multi-compartment lung results

We present results with simulated data using the multi-compartment model with 3 compartments per lung. The MATLAB code used to generate the results can be seen in appendix D. A sinusoidal input pressure of amplitude 10 cmH_2O and average pressure of 15 cmH_2O is simulated, and is contaminated with white pseudo-random Gaussian noise parameterised by the SNR ratio analogously to (4.1). The sinusoidal pressure with 0.2 Hz frequency over $t = 30$ s can be seen in figure 6.3 with $\text{SNR} = 100$ noise added. In this particular model 3 compartments per lung are used, and thus we need to estimate 6 parameters for the compliance and resistance per lung. We also have a single airways resistance, R_S , and pleural pressure, P_0 . We model the lungs with each of the compartments of the lungs having the same elastance and resistance of $50 \text{ cmH}_2\text{O L}^{-1}$ and $20 \text{ cmH}_2\text{O s L}^{-1}$, apart from compartment 1 of the left lung assigned a low elastance of $5 \text{ cmH}_2\text{O L}^{-1}$ and compartment 3 of the right lung a high resistance of $50 \text{ cmH}_2\text{O s L}^{-1}$. In effect we are modelling an idealised situation where there is a highly compliant compartment in the left lung and a blockage in a compartment in the right lung. The values used are in order of magnitude agreement with experimentally determined values of mechanical resistance and elastance in [154]. We assume at $t = 0$ the volume of air in the lungs is $V(0) = 6$ L and then distribute this equally along each compartment as initial conditions for the forward problem i.e. $V_{L,1}(0) = V_{L,2}(0) = V_{L,3}(0) = V_{R,1}(0) = V_{R,2}(0) = V_{R,3}(0) = 1$ L. The volume and flow at subsequent time steps was solved using the explicit RK4 scheme. For the given parameter values the resulting ODE system matrix was relatively non-stiff with

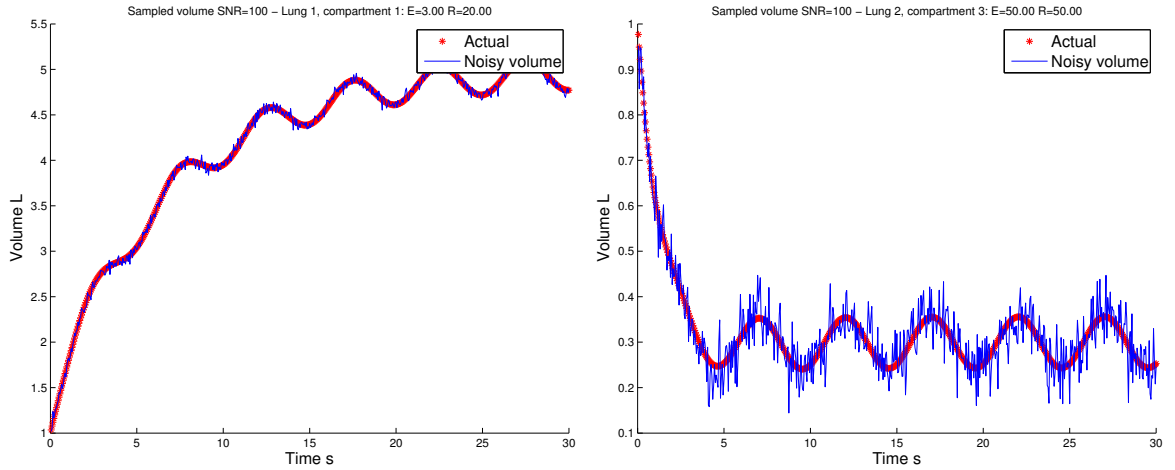


Figure 6.4: Raw volume time series of two compartments in lungs with elastance of $5 \text{ cmH}_2\text{O L}^{-1}$ (left figure) and resistance of $50 \text{ cmH}_2\text{O s L}^{-1}$ respectively with $\text{SNR} = 100$ noise added. The volume time series with high elastance is significantly affected with the addition of noise.

a small stiffness ratio of $R \approx 10.5$, which is defined through

$$R = \frac{\max |\text{Re}(\lambda_i)|}{\min |\text{Re}(\lambda_i)|},$$

where $\{\lambda_i\}_{i=1}^n$ is the set of eigenvalues of $B^{-1}E$ [164]. The set of eigenvalues are also all purely real, and negative, indicating that the homogeneous solution decays for a given set of initial conditions. The small stiffness ratio means that the numerical results were insensitive to modest timesteps in the range $\Delta t \approx 0.001 - 0.01$ s. The volume and pressure were sampled at 20 Hz which is consistent with temporal resolution of EIT data collections (see section 5.1.1) and pressure transducers [154].

Figure 6.4 indicates the volumes time series of compartment 1 in lung 1 and compartment 3 in lung 2 which have a low and high value of elastance and resistance respectively. We note there is a higher component of noise in the compartment with the larger elastance, because the time series has a smaller value of volume. The volume time series have an initial transient, from the homogeneous part of the ODE, followed by the steady state solution due to the given sinusoidal pressure forcing term. We perform an inverse integration scheme using a *single* regularisation parameter of $\alpha = 0.01$ for each compartment of each lung. The reconstructed flow and volume plots for the two compartments can be observed in figure 6.5 and figure 6.6 respectively. The reconstructed volume is close to the noise free volume, and the reconstructed flow fits reasonably well to the true flow. We also consider the reconstructed flow and volume for lung 2, compartment 3 as a function of SNR in figure 6.7 and figure 6.8

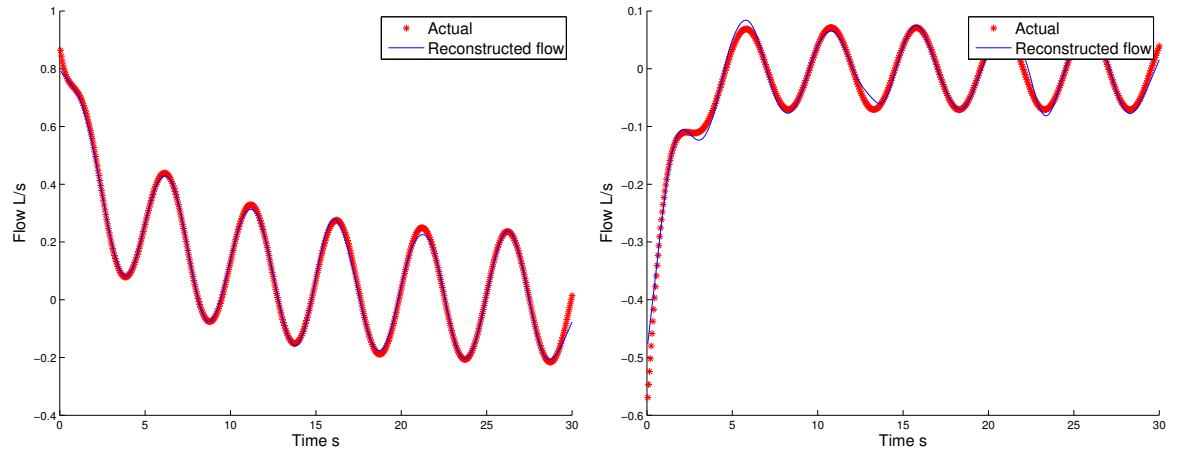


Figure 6.5: Reconstructed flow time series of two compartments in lungs with elastance of $5 \text{ cmH}_2\text{O L}^{-1}$ (left figure) and resistance of $50 \text{ cmH}_2\text{O s L}^{-1}$ (right figure) respectively with $\text{SNR} = 100$ noise added. A regularisation parameter of $\alpha = 0.005$ is used.

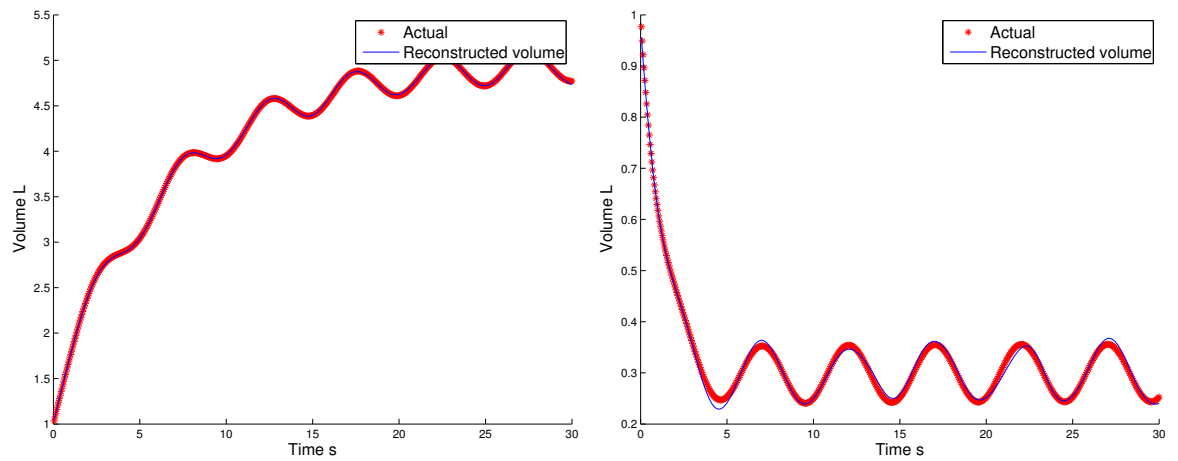


Figure 6.6: Reconstructed volume time series of two compartments in lungs with elastance of $5 \text{ cmH}_2\text{O L}^{-1}$ (left figure) and resistance of $50 \text{ cmH}_2\text{O s L}^{-1}$ respectively with $\text{SNR} = 100$ noise added, with a regularisation parameter of $\alpha = 0.005$. The noisy volume with high elastance (see figure 6.4) is reconstructed well.

using regularisation parameters of 0.1 and 0.5 respectively. An increasing SNR results in a poorer fit of the reconstructed flow to the actual flow as expected.

Parameter estimation

After volume and flow have been estimated for each compartment, we can input these into (6.8) to estimate the parameter matrix, M . Given enough samples of the pressure, we can then use a least squares estimate to determine an approximation to the parameters. It is essential that the volume and flow are estimated well before being used in the matrix M . In the absence of noise M has full rank, for the given model, because the ratios of the elastance and resistance of each compartment are not all the

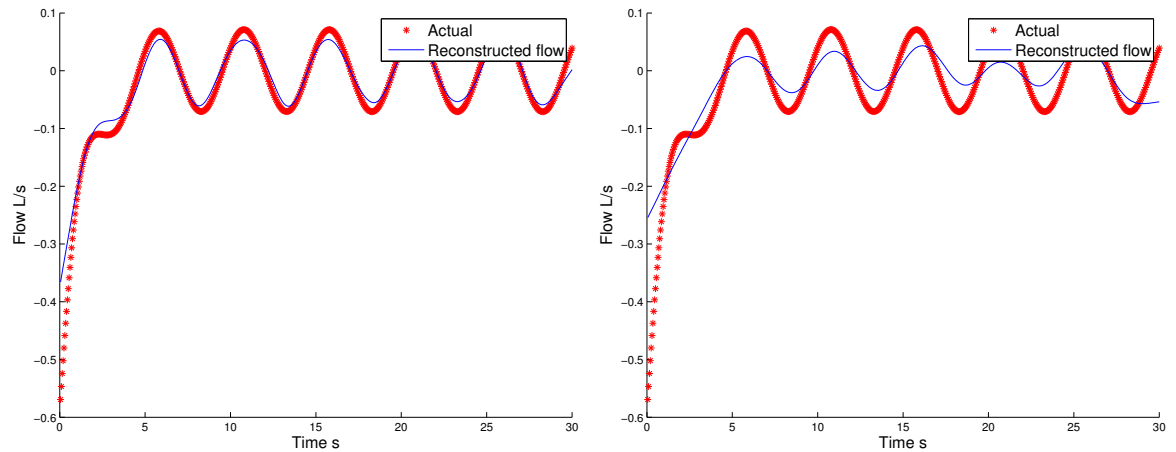


Figure 6.7: Reconstructed flow time series with SNR = 50 (left figure) and SNR = 25 (right figure) for lung 2 compartment 3 with regularisation parameters of $\alpha = 0.05$ and $\alpha = 0.5$ used respectively.

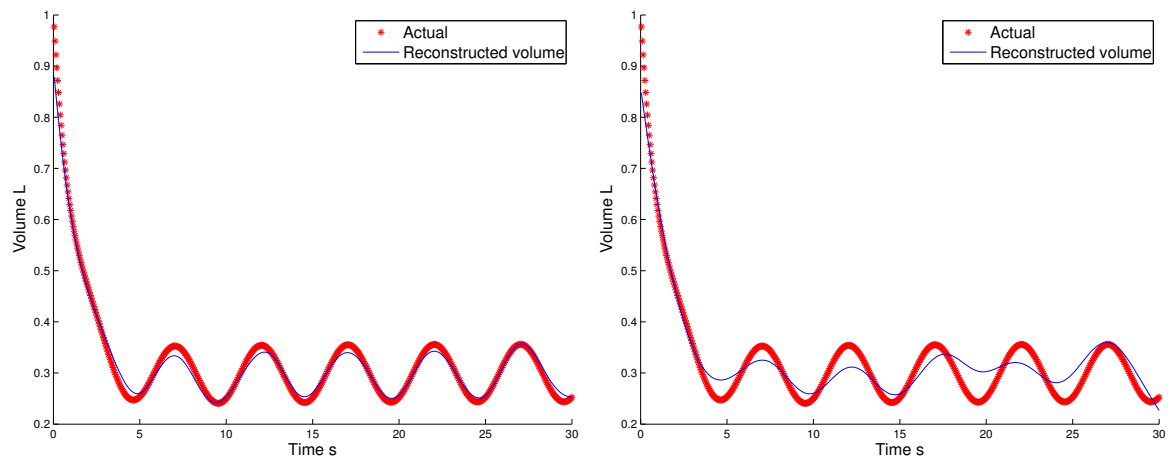


Figure 6.8: Reconstructed volume time series with SNR = 50 (left figure) and SNR = 25 (right figure) for lung 2 compartment 3 with regularisation parameters of $\alpha = 0.05$ and $\alpha = 0.5$ used respectively.

same. This property was retained numerically over all simulations run, and so suggests that we do not suffer from any ill-conditioning after discretisation.

The actual parameter matrix is plotted in figure 6.9, along with the corresponding error with no noise, and we label the matrix as M_{SNR} . From these matrices we observe that the largest source of error is in the even columns of M , corresponding to the estimated flow data. In figure 6.10, the error in the parameter matrix M is shown for an SNR of 100 and 25 respectively. We observe larger errors when increasing the amount of noise present as expected.

To estimate the parameters we first use time integration of equations, and the estimated parameters can be seen in figure 6.11. In the absence of noise the parameters are fitted almost perfectly, but in the presence of even relatively small noise (SNR of 100), the parameters are poorly estimated. In particular the resistances are very poorly

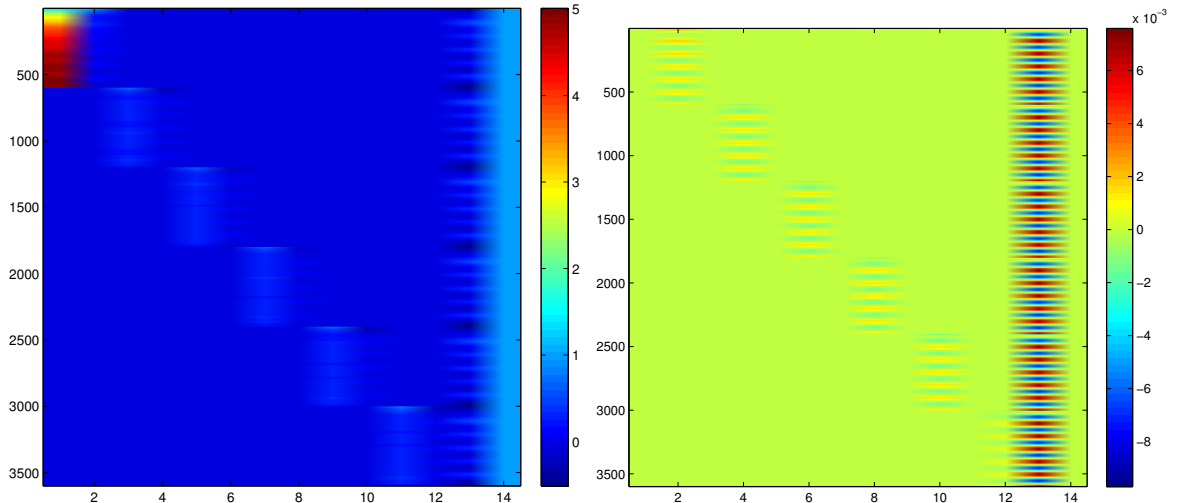


Figure 6.9: Actual parameter matrix (left figure) and error in parameter matrix with $\text{SNR} = \infty$. The errors in the parameter matrix appear in the even columns, corresponding to the reconstructed flow time series. The norm of the parameter matrix and the error is $\|M\|_2 = 108.2$ and $\|M - M_\infty\|_2 = 0.30$ respectively.

| SNR | Elastance Int | Elastance Inv | Resistance Int | Resistance Inv |
|-----|---------------|---------------|----------------|----------------|
| 100 | 19.1 | 14.2 | 24.2 | 8.5 |
| 50 | 44.6 | 21.0 | 45.3 | 16.4 |
| 25 | 46.7 | 32.0 | 45.2 | 28.2 |

Table 6.2: 2-norm errors of the estimated elastances and compliances where Int represents time integration of equations and Inv represents inverse integration. These are the 2-norm errors over all compartments. The total 2-norm of the elastance is $111.9 \text{ cmH}_2\text{OL}^{-1}$ and the total 2-norm of the resistance is $67.1 \text{ cmH}_2\text{OsL}^{-1}$.

estimated with large errors. In effect, time integration of the equations is a rather *ad-hoc* method and an improvement can be made with inverse integration. In figure 6.12 the parameter estimation is plotted using the inverse integration method (after first estimating \dot{V} and V for each compartment and hence the parameter matrix M in (6.8).) Table 6.2 illustrates the total errors in the estimated elastance and resistances. We observe that for an SNR greater than 50 that the inverse integration procedure is significantly better than time integration of the equations, with time integration of equations particularly poor at estimating the resistances.

6.5 Conclusions and extensions

EIT and homogenization models will allow us to estimate the volume of air at different regions of the lung, and thus provides us with many more measurements than just at airway opening as is standard in mechanical ventilation. This chapter is a numerical

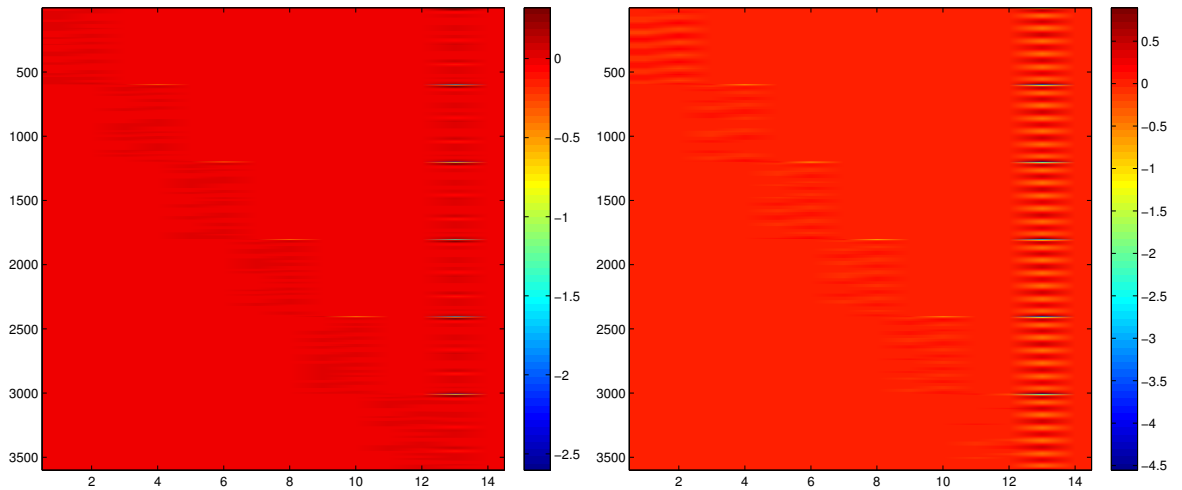


Figure 6.10: Error in parameter matrices with $\text{SNR} = 100$ (left figure) and $\text{SNR} = 25$ (right figure). The largest errors again correspond to the even columns corresponding to reconstructed flows. The error of the parameter matrices with $\text{SNR} = 100$ and 25 is $\|M - M_{100}\|_2 = 11.12$ and $\|M - M_{25}\|_2 = 28.35$ respectively.

proof of concept that we can get good estimates of mechanical properties of the lung using inverse problem techniques on systems of coupled ODEs. The main instability in the algorithm is converting the volume data to flow data to estimate the compartment resistances in the presence of noise, although inverse integration can stabilise this to some degree as illustrated in this chapter. This outperforms time integration of equations for modest noise levels and in particular for estimates of the resistances. More general regularisation schemes for non-smooth pressure inputs, such as Besov space or Total-Variation regularisation [77], could easily be extended in to this framework. CFD models of the respiratory system, such as those developed by Tawhai *et al.* [152, 151], could also be coupled with these models as they would provide *a-priori* information of the volume within different regions of the lung, under different applied pressures, to further stabilise the volume to flow mapping.

It was observed that the parameter estimation matrix M for the simple multi-compartment lobe model can be rank deficient. The simplest rank deficiency occurs if two components of the same type are placed in series inside a single compartment. For example if two resistors are placed in series in the airway they can not be distinguished because the two corresponding columns of the parameter estimation matrix M would be exactly the same and thus create an extra rank deficiency in the parameter estimation matrix (6.8). In effect we can only expect to estimate a single lumped

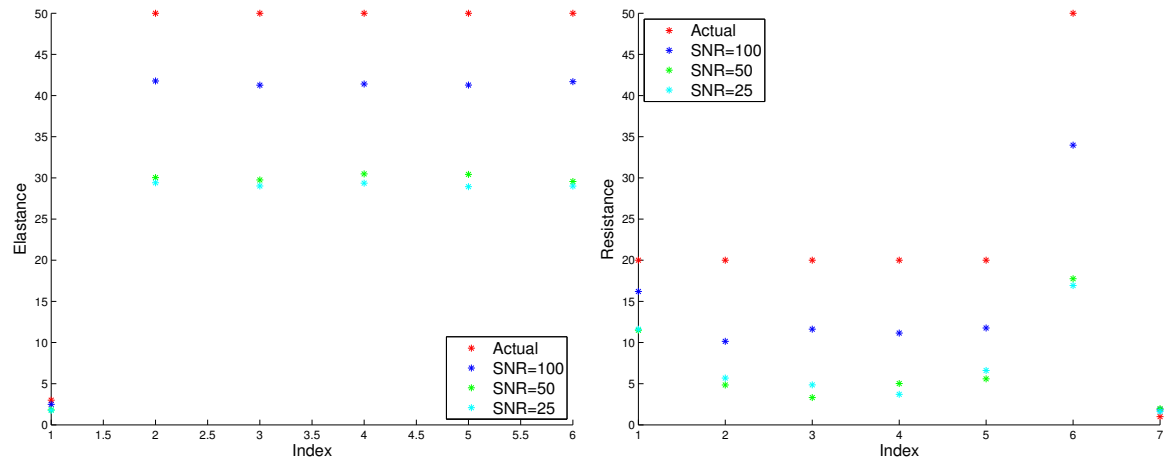


Figure 6.11: Parameters estimated as a function of noise level through time integration of equations. The left and right hand figure are the estimated elastances and resistances of lung compartments respectively. The resistances are estimated particularly poorly because these correspond to multiples of the estimated flow time series. See table 6.2 for the estimated errors.

parameter of the airway resistance which we can not localise from a single time series of the flow. We also noticed that when the ratios of the resistance to elastance of every compartment are the same this corresponds to not being able to distinguish between the airway resistance and resistance of each compartment. The difference in resistance between each compartment and airway resistance can be estimated which still provides us with clinically meaningful information. It would be an interesting extension to study how this generalises to more complicated CR networks with more parallel branches, and in particular understanding how choosing certain combinations of the capacitance and resistance can make the matrix M rank deficient. This would be useful because if we can characterise the null space for a given model by some conditions on the components of the CR network, then this should help us determine what we can identify about the system from some given data. Techniques from the inverse quadratic eigenvalue problem and inverse problems for damped vibrating systems may be helpful for future analysis of more complex models [165, 166].

The mechanical models described in this chapter are clearly quite simplistic. For example, there are no additional hydrodynamical terms because of liquid in the lung. Of even greater importance is perfusion which is the rate of blood supply to the lungs. This is fundamental physiologically because any oxygen in the air that enters the lungs can be attached to the haemoglobin in the blood. Clinicians use the term V/Q ratio to describe the relative ventilation and perfusion rates, and efficient respiration requires

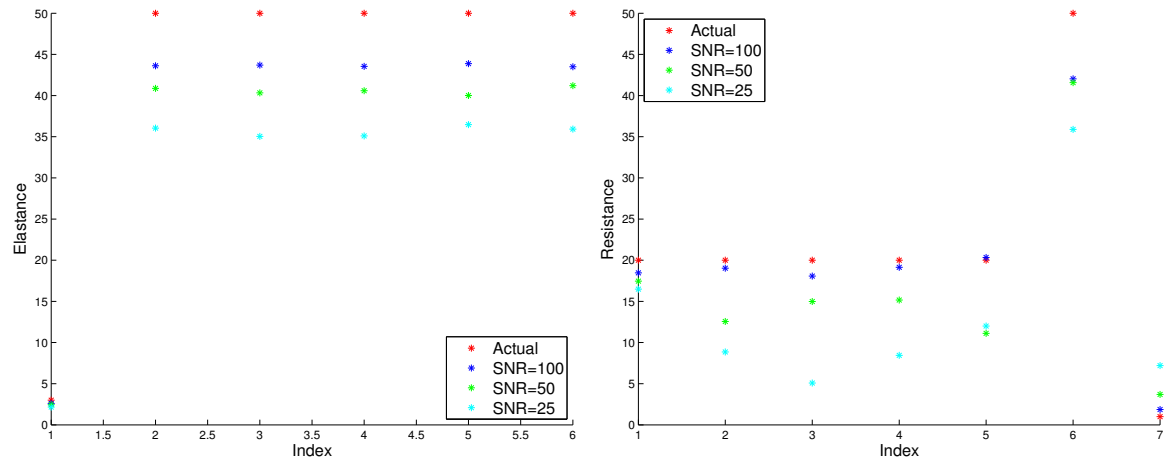


Figure 6.12: Parameters estimated as a function of noise level through inverse integration. The left and right hand figure represent the estimated elastances and resistances respectively. There is improvement of the estimated parameters compared to time integration of the equations (see figure 6.11), although with $SNR < 50$, the errors in the estimated coefficients begins to become large. See table 6.2 for the estimated errors.

this ratio to be finely tuned [159]. Equations for coupling terms of mechanical models with the cardiovascular systems have been described in [156] and multi-frequency EIT also can provide regional information on liquid gas fractions and hence would generate information of the regional interior liquid distribution for coupled ODE models. Non-linear mechanical models, such as non-linear resistor components of the form $P_{res} = R_1 \dot{V} + R_2 V \dot{V}$, can also be included in these models, through additional columns of the parameter estimation matrix M . We also note that these models are static, in the sense that the parameters do not depend on time, and do not depend on the pressure and volume. We hope to extend this work to such cases if necessary.

Chapter 7

Conclusions and future research

7.1 Thesis Summary

In this thesis we have explored a number of challenges facing the application of EIT in respiratory monitoring, with a particular focus on modelling errors in the forward problem.

In chapter 2 the computation of the forward problem with high order finite elements was outlined, and a convergence study performed for different electrode models on a square domain. High order finite element models increased the convergence rate for the forward problem in both the L^2 and H^1 norm for the continuum model. The convergence rate for the CEM, however, was independent of the global polynomial approximation order, and the point electrode model is not H^1 convergent for any approximation order. Adaptive finite element methods could be deployed to increase the accuracy of the forward problem in lung EIT, but it appears that this is currently less important than modelling errors due to an inaccurately known external shape and electrode positions.

In chapter 3 a review of uniqueness results for the isotropic inverse conductivity problem was presented along with exact reconstruction algorithms. The anisotropic problem was discussed when constraints on the permissible conductivity eigenspace are imposed. By drawing analogies with theoretical elasticity, a local uniqueness result with prescribed eigenvalues was proved, and we hope to determine conditions on a given manifold so that this can be extended to a global uniqueness result. Also a uniqueness result with prescribed eigenvectors, assuming a globally defined coordinate

system, was proved. Further definitions of fibrous and layered conductivities were made and we hope to extend these uniqueness results to these materials in the future. Anisotropic material is most definitely present in the human body, such as muscle tissue, and so developing a theoretical understanding of what can be uniquely identified from the electrical data, perhaps with additional constraints, is an important area of research. Further research would eventually lead us to understand how anisotropic tissues can be incorporated into prior conductivity models of the thorax.

In chapter 4 the importance of boundary shape and electrode positions was discussed. A theoretical review of uniqueness results with an unknown shape and conductivity were made. A novel computation of the Fréchet derivative for the continuum model under a boundary shape perturbation was outlined, along with a physical interpretation of the resulting derivative in integral form. An SVD analysis of the Fréchet derivative on a cylindrical domain was performed, highlighting how tangential components of the shape movement are easier to detect from the electrical data than normal components if measurements are not included on driven electrodes. If measurements are included at driven electrodes, however, normal changes at the electrode positions are easier to detect than tangential changes. Normal changes of the boundary away from the electrodes are fundamentally difficult to detect with any measurement strategy. Novel results with simulated data in 3D with spherical and cylindrical geometries were displayed using a non-linear two stage simultaneous shape correction and conductivity reconstruction algorithm. The first stage of the algorithm solely determines the electrode positions, followed by the second stage where the conductivity and small changes to electrode positions are determined. The reconstructions with this two stage algorithm are of similar quality as when the electrode positions are known for both spherical and cylindrical geometries.

In chapter 5 a pilot study of dynamic lung imaging with EIT was presented. EIT data was collected with the fEITER instrument using an array of 32 electrodes, and MR images were used to inform a 3D model of the subject used during the experiment. A shape correction algorithm was implemented that explicitly accounts for small changes in the boundary shape which occur when the subject breathes, yielding a reduction of boundary artefacts and improved contrast of the lungs when compared to a standard reconstruction algorithm without shape correction. A novel co-registration

process, and mutual information performance criterion, were presented providing an effective and practical method of directly comparing the spatial fidelity of EIT images with those obtained from MRI. The shape correction algorithm increased the maximum mutual information with a lung-segmented MR image by approximately 10% for both a subject in the sitting and supine positions and we believe this is the first time mutual information has been used to assess the quality of lung EIT reconstructions.

In chapter 6 the coupling of mechanical ODE models and EIT to determine clinically meaningful parameters was discussed. In these models, it is assumed that EIT can be used to determine regional air volumes, which are then states for the coupled ODE models. It was demonstrated with simulated data, that parameters of a simple multi-compartment model of the lung can be estimated, even in the presence of noise. It would be interesting to understand what can be determined when equations coupling to the cardiovascular system are included, as well as non-linear ODE models.

7.2 Future Research

7.2.1 Optimal measurement strategies

Many EIT systems typically deploy a single ring of electrodes placed approximately equidistant around the thorax and reconstructions typically performed in a plane defined by this ring. Electric current, however, can not be constrained to lie in this 2D plane making EIT inherently a 3D imaging technique. This raises the issue that not only should reconstructions be performed in 3D but also fully 3D measurement patterns should be deployed, as presented in chapters 4 and 5. The majority of systems are constrained for a source-sink current pattern operation, with excitation between two pairs of electrodes, due to the substantial increase in cost of adaptive current drives. Many systems also deploy adjacent current stimulation and adjacent voltage measurement stemming from the development of lung EIT at Sheffield in the 1980s, when imaging at a high frame rate was of paramount importance. The speed and accuracy of EIT systems, and reconstruction software, has improved dramatically since then and it is now the time to begin considering genuine optimal 3D measurement strategies in EIT. For pair driven current, recent research has argued that the traditional adjacent stimulation and measurement are the worst patterns to detect interior conductivity

changes in 2D [21]. In chapter 4 we also demonstrated that adjacent measurement strategies are not optimal for determining central conductivity perturbations in 3D.

We propose the following methodology to determine optimal electrode positions, current excitation patterns and voltage measurements. Firstly, and most importantly, the clinical objectives must be defined to understand exactly what physiological conductivity changes we are interested in and are measurable. The most obvious candidate would be to determine the gas/liquid ratio in different regions of the lung of a certain size and location, and determine what spatial resolution we are capable of measuring these to. The next step is to add constraints on the allowable electrode geometry assuming up to, say, 64 electrodes can be deployed. We would consider applying these on 2 to 4 transverse planes with interplane current excitation and voltage measurement allowed. The application of patches of electrodes grouped together would be introduced for the situation when electrodes can only be applied on a subset of a patient's thorax. After fixing the geometry, we would then consider the current excitation patterns, and in particular comparing between traditional 2D current excitation on a single transverse ring to fully 3D excitation patterns on multiple rings as an extension of work by Graham *et al.* [167] and Adler *et al.* [168]. For the pair measurement patterns we firstly need to determine which voltage measurement pairs are large enough to be above the experimental noise level. Further we must consider only voltage measurements such that the difference in the measurements between the specific conductivity change we are trying to observe is large enough to be accurately measured. An optimality criterion must be chosen to decide on optimal patterns. Traditional criteria include maximising the distinguishability suggested by Isaacson *et al.* [169], where it was shown that trigonometric current patterns are optimal for a concentric anomaly within a unit disc, or maximising the sensitivity in a region of interest by Borsic *et al.* [170]. An alternative method by Kaipio *et al.* [171], based in the framework of statistical inversion theory, optimises current patterns based on criteria that are functionals of the posterior covariance matrix. Recent advances in the optimal design of experiments for ill-posed problems are directly applicable to generate new criteria [172] which have the nice property that *a-priori* information is directly incorporated into the optimisation. The strategies would be tested using segmented MR and CT images over a range of representative categories such as male and female,

a range of body mass indices and ages as well as adults and neonates.

7.2.2 Absolute lung EIT

The problems of model dimension and shape described in chapters 4 and 5 need to be resolved adequately before repeatable absolute 3D imaging becomes a realistic possibility in thoracic EIT, as well as using genuine 3D measurement strategies as described in the previous section. With the introduction of fully 3D thorax models, we can envisage incorporating more spatial prior information of human tissue and anatomy, such as the liver, heart, ribs and spine into patient-specific thorax reconstruction models, as well as their *in vivo* conductivity values [4]. This would be a further development of the finite difference models developed by Zhang *et al.* [116]. However, these high resolution modelling approaches have not yet had a significant impact in clinical lung EIT. Fully 3D thorax models with anatomy such as the heart included would not only improve the forward problem in lung EIT, but also be important to further improve the image co-registration and mutual information techniques outlined in chapter 5. An assessment of the best prior smoothness constraints on the conductivity, and the voltage data, to offset the ill-posedness of EIT reconstruction, is another topic of paramount importance for absolute lung imaging. The use of classical Tikhonov regularization presented in chapter 5, which in the Bayesian viewpoint assumes conductivity changes for all pixels are independent and identically distributed, is somewhat unrealistic and we feel this could be significantly improved by using generalized Tikhonov regularization and non-smooth penalization norms.

Bibliography

- [1] V. Ranieri *et al.* Acute respiratory distress syndrome: the Berlin Definition. *JAMA*, 307(23):2526–2533, 2012.
- [2] J. Villar *et al.* The ALIEN study: incidence and outcome of acute respiratory distress syndrome in the era of lung protective ventilation. *Intensive Care Med.*, 37(12):1932–1941, 2011.
- [3] W. R. B. Lionheart, J. Kaipio, and C. N. McLeod. Generalized Optimal Current Patterns and Electrical Safety in EIT. *Physiol. Meas*, 22:85–90, 2001.
- [4] T. J. C. Faes, H. A. van der Meij, J. C. de Munck, and R. M. Heethaar. The electric resistivity of human tissues (100Hz-10MHz): a meta-analysis of review studies. *Physiol. Meas.*, 20(4):R1–R10, 1999.
- [5] B. H. Brown and D. C. Barber. Applied potential tomography. *J. Phys. E: Sci. Instrum.*, 17:723–733, 1984.
- [6] B. H. Brown, D. C. Barber, and A. D. Seagar. Applied potential tomography: possible clinical applications. *Clin. Phys. Physiol. Meas.*, 6(2):109–121, 1985.
- [7] T. Muders, H. Luepschen, and C. Putensen. Impedance tomography as a new monitoring technique. *Am. J. Respir. Crit. Care. Med*, 169:791–800, 2010.
- [8] M. Bodenstein, D. Matthias, and K. Markstaller. Principles of electrical impedance tomography and its clinical application. *Crit. Med.*, 37(2):713–724, 2009.
- [9] E. L. V. Costa, R. G. Lima, and M. B. P. Amato. Electrical impedance tomography. *Curr. Opin. Crit. Care.*, 15:18–24, 2009.

- [10] A. Adler, M. B. P. Amato, J. H. Arnold, R. Bayford, M. Bodenstein, S. H. Böhm, B. H. Brown, I. Frerichs, O. Stenqvist, N. Weiler, and G. K. Wolf. Whither lung EIT: where are we, where do we want to go and what do we need to get there? *Physiol. Meas.*, 33(5):679–694, 2012.
- [11] I. Frerichs. Electrical impedance tomography (EIT) in applications related to lung and ventilation: a review of experimental and clinical activities. *Physiol. Meas.*, 21:R1–R21, 2000.
- [12] S. Lundin and O. Stenqvist. Electrical impedance tomography: potentials and pitfalls. *Curr. Opin. Crit. Care*, 18:35–41, 2012.
- [13] Z. Zhao, D. Steinmann, I. Frerichs, J. Guttmann, and K. Möller. PEEP titration guided by ventilation homogeneity: a feasibility study using electrical impedance tomography. *Crit. Care*, 14(1):R8, 2010.
- [14] I. Frerichs, S. Pulletz, G. Elke, F. Reifferscheid, D. Schädler, J. Scholz, and N. Weiler. Assessment of Changes in Distribution of Lung Perfusion by Electrical Impedance Tomography. *Respiration*, 77:282–291, 2009.
- [15] P. W. A. Kunst, A. Vonk Noordegraaf, E. Raaijmakers, J. Bakker, A. B. J. Groenveld, P. E. Postmus, and P. M. J. M. de Vries. Electrical Impedance Tomography in the Assessment of Extravascular lung Water in Noncardiogenic Acute Respiratory Failure. *Chest*, 116(6):1695–1702, 1999.
- [16] I. Frerichs, G. Hahn, and G. Hellige. Gravity-dependent phenomena in lung ventilation determined by functional EIT. *Physiol. Meas*, 17:A149–A157, 1996.
- [17] I. Frerichs, M. Bodenstein, T. Dudykevych, J. Hinz, G. Hahn, and G. Hellige. Effect of lower body negative pressure and gravity on regional lung ventilation determined by EIT. *Physiol. Meas*, 26:S27–S37, 2005.
- [18] H. J. Smit, A. Vonk Nordegraaf, J. T. Marcus, S. van der Weijden, P. E. Postmus, P. M. J. M. de Vries, and A. Boonstra. Pulmonary Vascular Responses to Hypoxia and Hyperoxia in Healthy Volunteers and COPD Patients Measured by Electrical Impedance Tomography. *Chest*, 123(6):1803–1809, 2003.

- [19] J. Hinz, A. Gehoff, O. Moerer, I. Frerichs, G. Hahn, G. Hellige, and M. Quintel. Regional filling characteristics of the lungs in mechanically ventilated patients with acute lung injury. *Euro. J. of Anaesthesiology*, 24:414–424, 2007.
- [20] B. H. Brown and A. D. Seagar. The Sheffield data collection system. *Clin. Phys. Physiol. Meas.*, 8:91–97, 1987.
- [21] A. Adler, P. O. Gaggero, and Y. Maimaitijiang. Adjacent stimulation and measurement patterns considered harmful. *Physiol. Meas.*, 32:731–744, 2011.
- [22] W. R. B. Lionheart. EIT Reconstruction Algorithms: Pitfalls, Challenges and Recent Developments. *Physiol. Meas.*, 25:125–142, 2004.
- [23] A. Adler, J. H. Arnold, R. Bayford, A. Borsic, B. Brown, P. Dixon, T. J. C. Faes, I. Frerichs, H. Gagnon, Y. Gärber, B. Grychtol, G. Hahn, W. R. B. Lionheart, A. Malik, R. P. Patterson, J. Stocks, A. Tizzard, N. Weiler, and G. K. Wolf. GREIT: a unified approach to 2D linear EIT reconstruction of lung images. *Physiol. Meas.*, 30(6):S35–S55, 2009.
- [24] E. Teschner and M. Imhoff. *Electrical Impedance Tomography: The realization of regional ventilation monitoring*. Dräger, Lübeck, Germany. <http://www.draeger.com>.
- [25] M. H. Loke. Electrical imaging surveys for environmental and engineering studies: A practical guide to 2-D and 3-D surveys. <http://www.heritagegeophysics.com/images/lokenotepdf>, 2000.
- [26] P. H. Giao, S. G. Chung, D. Y. Kim, and H. Tanaka. Electric imaging and laboratory resistivity testing for geotechnical investigation of Pusan clay deposits. *Journal of Applied Geophysics*, 52(4):157–175, 2003.
- [27] D. Baines and D. G. Smith and D. G. Froese and P. Bauman and G. Nimeck. Electrical resistivity ground imaging (ERGI): a new tool for mapping the lithology and geometry of channel-belts and valley-fills. *Sedimentology*, 49(3):441–449, 2002.

- [28] J. Goble and D. Isaacson. Fast Reconstruction Algorithms For Three-Dimensional Electrical Impedance Tomography. *IEEE Engr. in Medicine and Biology*, 12(1):100–101, 1990.
- [29] M. Cheney, J. Newell, D. Gisser, and J. Goble. Thoracic Impedance Images During Ventilation. *IEEE Engr. in Medicine and Biology*, 12(1):106–107, 1990.
- [30] W. R. B. Lionheart. Boundary Shape and Electrical Impedance Tomography. *Inverse Problems*, 14:139–147, 1998.
- [31] W. R. B. Lionheart. Conformal uniqueness results in anisotropic electrical impedance imaging. *Inverse Problems*, 13:125–134, 1997.
- [32] A. Adler, R. Guardo, and Y. Berthiaume. Impedance imaging of lung ventilation: Do we need to account for chest expansion? *IEEE Trans. Biomed. Eng.*, 43(4):pp. 414–420, Apr. 1996.
- [33] A. Boyle and A. Adler. Impact of Electrode Area, Contact Impedance and Boundary Shape on EIT images. *Physiol. Meas.*, 32:745–754, 2011.
- [34] J. Forsyth, A. Borsic, R. J. Halter, A. Hartov, and K. D. Paulsen. Optical breast shape capture and finite-element mesh generation for electrical impedance tomography. *Physiol. Meas.*, 32(7):797–809, 2011.
- [35] A. Tizzard, L. Horesh, R. J. Yerworth, D. S. Holder, and R. H. Bayford. Generating accurate finite element meshes for the forward model of the human head in eit. *Physiol. Meas.*, 26:S251–S261, 2005.
- [36] A. Nissinen, V. Kolehmainen, and J. P. Kaipio. Reconstruction of domain boundary and conductivity in electrical impedance tomography using the approximation error approach. *International Journal for Uncertainty Quantification*, 1(3):203–222, 2011.
- [37] A. Nissinen, L. M. Heikkinen, and J. P. Kaipio. The Bayesian approximation error approach for electrical impedance tomography - experimental results. *Meas. Sci. Technol.*, 19:015501, 2008.

- [38] J. A. Victorino, J. B. Borges, V. N. Okamoto, G. F. Matos, M. R. Tucci, M. P. Caraméz, H. Tanaka, F. S. Sipmann, D. C. Santos, C. S. Barbas, C. R. Carvalho, and M. B. P. Amato. Imbalances in Regional Lung Ventilation: a Validation Study on Electrical Impedance Tomography. *Am. J. Respir. Crit. Care Med.*, 169(7):791–800, 2004.
- [39] E. L. V. Costa, J. B. Borges, A. Melo, F. Suarez-Sipmann, C. Toufen, S. H. Böhm, and M. B. P. Amato. Bedside estimation of recruitable alveolar collapse and hyperdistension by electrical impedance tomography. *Intensive Care. Med.*, 35:1132–1137, 2009.
- [40] P. W. A. Kunst, A. Vonk Noordegraaf, O. S. Hoekstra, P. Postmus, and P. M. J. M. de Vries. Ventilation and perfusion imaging by electrical impedance tomography: a comparison with radionuclide scanning. *Physiol. Meas.*, 19:481–490, 1998.
- [41] J. C. Richard, C. Pouzot, A. Gros, C. Tourevieille, D. Lebars, F. Lavenne, I. Frerichs, and C. Guérin. Electrical impedance tomography compared to positron emission tomography for the measurement of regional lung ventilation: an experimental study. *Crit. Care*, 13(2):R82, 2009.
- [42] J. Hinz, P. Neumann, T. Dudykevych, L. G. Andersson, H. Wrigge, H. Burchardi, and G. Hedenstierna. Regional Ventilation by Electrical Impedance Tomography: A Comparison with Ventilation Scintigraphy in Pigs. *Chest*, 124:R314–R322, 2003.
- [43] I. Frerichs, J. Hinz, P. Herrman, G. Weisser, G. Hahn, T. Dudykevych, M. Quintel, and G. Hellige. Detection of local air content by electrical impedance tomography with electron beam CT. *J. Appl. Physiol.*, 93:660–666, 2002.
- [44] A. B. Otis, C. B. McKerrow, R. A. Bartlett, J. Mead, M. B. McIlroy, N. J. Selverstone, and JR E. P. Radford. Mechanical Factors in Distribution of Pulmonary Ventilation. *J. Appl. Physiol.*, 8(4):427–443, 1956.
- [45] K. Astala and L. Päivärinta and M. Lassas. Calderón’s Inverse Problem for

- Anisotropic Conductivity in the Plane. *Comm. Partial Differential Equations*, 30:207–224, 2005.
- [46] M. Lassas and M. Taylor and G. Uhlmann. The Dirichlet-to-Neumann map for complete Riemannian manifolds with boundary. *Communications in Analysis and Geometry*, 11(2):207–221, 2003.
- [47] M. Vauhkonen. *Electrical Impedance Tomography and Prior Information*. PhD thesis, University of Kuopio, Finland, 1997.
- [48] W. Lionheart, N. Polydorides, and A. Borsic. The Reconstruction Problem. In D. S. Holder, editor, *Electrical Impedance Tomography: methods, history and applications*. Institute of Physics Pub., 2005.
- [49] K-S. Cheng, D. Isaacson, J. C. Newell, and D. G. Gisser. Electrode models for electric current computed tomography. *Trans. Biomed. Eng.*, 36(9):pp. 918–924, 1989.
- [50] K. Paulson, W. R. Breckon, and M. Pidcock. Electrode Modelling in Electrical Impedance Tomography. *SIAM J. Appl. Math.*, 52(4):1012–1022, 1992.
- [51] N. Polydorides. *Image Reconstruction Algorithms for Soft Field Tomography*. PhD thesis, UMIST, Manchester, 2002.
- [52] L. C. Evans. *Partial Differential Equations*. American Math Society, 4th edition, 2008.
- [53] H. Elman, D. Silvester, and A. Wathen. *Finite Elements and Fast Iterative Solvers with Applications in Incompressible Fluid Dynamics*. Oxford University Press, 2nd edition, 2006.
- [54] M. Hanke, B. Harrach, and N. Hyvönen. Justification of point electrode models in electrical impedance tomography. *Math. Models Methods Appl. Sci.*, 21(6):1012–1022, 2011.
- [55] E. Somersalo, M. Cheney, and D. Isaacson. Existence and uniqueness for electrode models for electric current computed tomography. *SIAM J. Appl. Math.*, 52(4):1023–1040, 1992.

- [56] J. Dardé, H. Hakula, N. Hyvönen, and S. Staboulis. Fine-tuning electrode information in electrical impedance tomography. *Inverse Problems and Imaging*, 6(3):399–421, 2012.
- [57] V. Kolehmainen, M. Lassas, and P. Ola. The inverse conductivity problem with an imperfectly known boundary in three dimensions. *SIAM Journal of Applied Maths*, 67(5):1440–1452, 2007.
- [58] G. Strang and G. J. Fix. *An Analysis of the Finite Element Method*. Prentice-Hall, New Jersey, 1973.
- [59] O. C. Zienkiewicz. *The Finite Element Method*. McGraw-Hill, Berkshire, 3rd edition, 1977.
- [60] J-L. Guermond A. Ern. *Theory and Practice of Finite Elements*. Springer-Verlag, New York, 2004.
- [61] P. G. Ciarlet. *The Finite Element Method for Elliptic Problems*. North-Holland, Amsterdam, 1st edition, 1978.
- [62] A. Adler and W. R. B. Lionheart. Uses and abuses of EIDORS: An extensible software base for EIT. *Physiol. Meas.*, 27:S25–S42, 2006.
- [63] R. H. Nochetto and A. Veerer. Primer of Adaptive Finite Element Methods. In G. Naldi and G. Russo, editors, *Multiscale and Adaptivity: Modeling, Numerics and Applications, CIME-EMS SummerSchool in Applied Mathematics*. Springer, 2010.
- [64] M. E. Taylor. *Partial Differential Equations 1 : Basic Theory*. Springer-Verlag, New York, 1996.
- [65] E. Demidenko. An analytic solution to the homogeneous EIT problem on the 2D disk and its application to estimation of electrode contact impedances. *Physiol. Meas.*, 32:1453–1471, 2011.
- [66] P. D. Ledger. *hp*-Finite Element discretisation of the electrical impedance tomography problem. *Comput. Methods Appl. Mech. Engng.*, 225-228:154–176, 2012.

- [67] H. Hakula, N. Hyvönen, and T. Tuominen. On hp -Adaptive Solution of Complete Electrode Model Forward Problems of Electrical Impedance Tomography. *Computational and Applied Mathematics*, 236:4645–4659, 2012.
- [68] J. Hadamard. Sur les problèmes aux dérivées partielles et leur signification physique. *Princeton University Bulletin*, 23:49–52, 1902.
- [69] K. Yosida. *Functional Analysis*. Springer-Verlag, 5th edition, 1980.
- [70] G. Golub and C. Van Loan. *Matrix Computations*, year =.
- [71] J. P. Kaipio, V. Kolehmainen, E. Somersalo, and M. Vauhkonen. Statistical inversion and Monte Carlo sampling methods in electrical impedance tomography. *Inverse Problems*, 16:1487–1522, 2000.
- [72] A. Tarantola. *Inverse Problem Theory*. SIAM, 2005.
- [73] C. R. Vogel. *Computational methods for inverse problems*. SIAM, Philadelphia, 2001.
- [74] V. Kolehmainen. *Novel Approaches to Image Reconstruction in Diffusion Tomography*. PhD thesis, University of Kuopio, Finland, 2001.
- [75] A. Borsic, B. M. Graham, A. Adler, and W. R. B. Lionheart. *In vivo* Impedance Imaging with Total Variation Regularization. *IEEE Trans. Med. Imaging*, 29:44–54, 2010.
- [76] W. Stefan. *Total variation regularization for linear ill-posed inverse problems: extensions and application*. PhD thesis, Arizona State University, 2008.
- [77] J. L. Mueller and S. Siltanen. *Linear and Nonlinear Inverse Problems with Practical Applications*. SIAM, 2012.
- [78] A. P. Calderón. On an inverse boundary value problem. *Comput. Appl. Maths*, 25:133–138, 2006.
- [79] W. R. Breckon. *Image reconstruction in electrical impedance tomography*. PhD thesis, Oxford Polytechnic, UK, 1990.

- [80] A. Lechleiter and A. Rieder. Newton regularizations for impedance tomography: convergence by local injectivity. *Inverse Problems*, 24(6), 2008.
- [81] T. J. Yorkey, J. G. Webster, and W. J. Tompkins. Comparing Reconstruction Algorithms for Electrical Impedance Tomography. *IEEE Trans. Biomed. Eng.*, 34(11):pp. 843–852, Nov. 1987.
- [82] P. Vauhkonen. *Image Reconstruction in Three-Dimensional Electrical Impedance Tomography*. PhD thesis, University of Kuopio, Finland, 2004.
- [83] M. Molinari. *High Fidelity Imaging in Electrical Impedance Tomography*. PhD thesis, University of Southampton, UK, 2003.
- [84] R. Kohn and M. Vogelius. Determining Conductivity by Boundary Measurements. *Commun. Pure Appl. Math.*, 37:289–298, 1984.
- [85] R. Kohn and M. Vogelius. Determining Conductivity by Boundary Measurements II. Interior Results. *Commun. Pure Appl. Math.*, 38:643–667, 1985.
- [86] J. M. Lee and G. Uhlmann. Determining Anisotropic Real-Analytic Conductivities by Boundary Measurements. *Commun. Pure Appl. Math.*, 42:1097–1112, 1989.
- [87] M. E. Taylor. *Pseudodifferential Operators*. Princeton University Press, 1981.
- [88] F. Trèves. *Introduction to Pseudodifferential and Fourier Integral Operators*, volume 1. Plenum Press, 1980.
- [89] J. Sylvester and G. Uhlmann. A Global Uniqueness Theorem for an Inverse Boundary Value Problem. *Ann. Math.*, 125:153–169, 1987.
- [90] M. Salo. Calderón problem. Lecture notes, 2008.
- [91] A. I. Nachman. Global Uniqueness for a Two-Dimensional Inverse Boundary Value Problem. *Ann. Math.*, 143:71–96, 1996.
- [92] K. Astala and L. Päivärinta. Calderón’s inverse conductivity problem in the plane. *Ann. Math.*, 163:265–299, 2006.

- [93] B. Haberman and D. Tataru. Uniqueness in Calderón’s problem with Lipschitz conductivities. *Duke Math. J.*, 162(3):497–516, 2013.
- [94] L. D. Fadeev. Increasing solutions of the Schrödinger equation. *Sov. Phys. Dokl.*, 10:1033–1035, 1966.
- [95] S. Siltanen, J. Mueller, and D. Isaacson. An implementation of the reconstruction algorithm of a nachman for the 2d inverse conductivity problem. *Inverse Problems*, 16:681–699, 2000.
- [96] D. Isaacson, J. L. Mueller, J. C. Newell, and S. Siltanen. Imaging cardiac activity by the d-bar method for electrical impedance tomography. *Physiol. Meas.*, 27:S43–S50, 2006.
- [97] S. Siltanen and J. P. Tamminen. Reconstructing conductivities with boundary corrected d-bar method, preprint.
- [98] J. Bikowski, K. Knudsen, and J. Mueller. Direct numerical reconstruction of conductivities in three dimensions. *Physiol. Meas.*, 27:015002, 2011.
- [99] F. Delbary, P. C. Hansen, and K. Knudsen. Electrical Impedance Tomography: 3D Reconstructions using Scattering Transforms. *Applicable Analysis*, 91(4):737–755, 2012.
- [100] A. Katsevitch. Analysis of an exact inversion algorithm for spiral cone-beam CT. *Phys. Med. Biol.*, 47(15):2583–2597, 2002.
- [101] A. Katsevitch. Theoretically exact filtered backprojection-type inversion algorithm for spiral CT. *SIAM J. Appl. Math.*, 62(6):2012–2026, 2002.
- [102] T. Varslot, A. Kingston, G. Myers, and A. Sheppard. High-resolution helical cone-beam micro-CT with theoretically-exact reconstruction from experimental data. *Med. Phys.*, 38:5459–5476, 2011.
- [103] J. Sylvester. An anisotropic inverse boundary value problem. *Commun. Pure Appl. Math.*, 43:201–232, 1990.
- [104] A. Adler, R. Gaburro, and W. R. B. Lionheart. *Handbook of Mathematical Methods in Imaging*. Springer, 2010.

- [105] G. Uhlmann. Electrical impedance tomography and Calderón's problem. *Inverse Problems*, 25(12):39pp, 2009.
- [106] R. D. Donaldson. *Discrete Geometric Homogenisation and Inverse Homogenisation of an Elliptic Operator*. PhD thesis, California Institute of Technology, 2008.
- [107] L. P. Eisenhart. *Riemannian Geometry*. Princeton University Press, 1950.
- [108] L. Bianchi. *Opere, Vol. 3: Sistemi Tripli Orthogonali*. Edizioni Cremonese, Roma, 1955.
- [109] D. DeTurck and D. Yang. Existence of elastic deformations with prescribed principal strains and triply orthogonal systems. *Duke Math. J.*, 51(2):243–260, 1984.
- [110] G. Alessandrini. Singular solutions of elliptic equations and the determination of conductivity by boundary measurements. *J. Differential Equations*, 84:252–272, 1990.
- [111] G. Alessandrini and R. Gaburro. Determining conductivity with special anisotropy by boundary measurements. *SIAM J. Math. Anal.*, 33(1):153–171, 2001.
- [112] C. Amrouche, P. G. Ciarlet, L. Gratie, and S. Kesavan. On Saint Venant's compatibility conditions and Poincaré's lemma. *Comptes Rendus Mathematique*, 342(11):887–891, 2006.
- [113] P. G. Ciarlet, C. Mardare, and M. Shen. Recovery of a displacement field from its linearized strain tensor field in curvilinear coordinates. *C. R. Math.*, 344(8):535–540, 2007.
- [114] E. Cartan. *Les Systèmes différentiels extérieurs et leurs applications géométriques*. Hermann, Paris, 1945.
- [115] J-F. P. J. Abascal and W. R. B. Lionheart and S. R. Arridge and M. Schweiger and D. Atkinson and D. S. Holder. Electrical impedance tomography in

- anisotropic media with known eigenvectors. *Inverse Problems*, 27(6):065004, 2011.
- [116] J. Zhang and R. P. Patterson. EIT images of ventilation: what contributes to the resistivity changes? *Physiol. Meas.*, 26:S81–S92, 2005.
- [117] B. Grychtol, W. R. B. Lionheart, M. Bodenstern, G. K. Wolf, and A. Adler. Impact of Model Shape Mismatch on Reconstruction Quality in Electrical Impedance Tomography. *IEEE Trans. Med. Imaging*, 31(9):1754–1760, 2011.
- [118] A. Boyle, A. Adler, and W. R. B. Lionheart. Shape Deformation in Two-Dimensional Electrical Impedance Tomography. *IEEE Trans. Med. Imaging*, 31(12):2185–2193, 2012.
- [119] M. Salo. The Calderón problem on Riemannian manifolds. Lecture notes, 2010.
- [120] T. Iwaniec and G. Martin. *Geometric function theory and non-linear analysis*. Oxford University Press, 2001.
- [121] V. Kolehmainen, M. Lassas, P. Ola, and S. Siltanen. Recovering boundary shape and conductivity in electrical impedance tomography. *Inverse Problems and Imaging*, 7(1):217–242, 2013.
- [122] V. Kolehmainen, M. Lassas, and P. Ola. Calderón’s Inverse Problem with an Imperfectly Known Boundary and Reconstruction Up to a Conformal Deformation. *SIAM J. Math. Anal.*, 42(3):1371–1381, 2010.
- [123] V. Kolehmainen, M. Lassas, and P. Ola. Electrical Impedance Tomography Problem With Inaccurately Known Boundary And Contact Impedances. *IEEE Trans. Med. Imaging*, 27(10):1404–1414, 2008.
- [124] V. Kolehmainen, M. Lassas, and P. Ola. Calderón’s Inverse Problem with an imperfectly known boundary in two and three dimensions. *J. Phys.: Conf. Ser.*, 73:012002, 2007.
- [125] M. Soleimani, C. Gómez-Laberge, and A. Adler. Imaging of conductivity changes and electrode movement in EIT. *Physiol. Meas.*, 27:S103–S113, 2006.

- [126] C. Gómez-Laberge and A. Adler. Direct EIT Jacobian calculations for conductivity change and electrode movement. *Physiol. Meas.*, 29:S89–S99, 2008.
- [127] J. Dardé, N. Hyvönen, A. Seppänen, and S. Staboulis. Simultaneous reconstruction of outer boundary shape and admittivity distribution in electrical impedance tomography. *SIAM J. Imaging Sciences*, 6(1):176–198, 2013.
- [128] E. Kreyszig. *Differential Geometry*. Dover Publications, 1991.
- [129] M. G. Crabb, J. L. Davidson, R. Little, P. Wright, J. H. Naish, G. J. M. Parker, H. McCann, and W. R. B. Lionheart. Accounting for electrode movement in MRI-informed functional EIT lung imaging. In *100 years of electrical imaging*, pages 83–86, Paris, France, 2012.
- [130] A. Adler, A. Borsic, N. Polydorides, and W. R. B. Lionheart. Simple FEMs aren’t as good as we thought: experiences developing EIDORS v3.3. In *Proc. 9th International Conference on Electrical Impedance Tomography*, Dartmouth College, New Hampshire, June 2008.
- [131] J. Schöberl. NETGEN - An Advancing Front 2D/3D-Mesh Generator Based On Abstract Rules. *Comput. Visual. Sci.*, 1:41–52, 1997. <http://www.hpfem.jku.at>.
- [132] M. G. Crabb, J. L. Davidson, R. Little, P. Wright, J. H. Naish, G. J. M. Parker, H. McCann, and W. R. B. Lionheart. Mutual information as a measure of reconstruction quality in 3D dynamic lung EIT. *J. Phys.: Conf. Ser.*, 434:012082, 2013.
- [133] M. G. Crabb, J. L. Davidson, R. Little, P. Wright, A. R. Morgan, C. A. Miller, J. H. Naish, G. J. M. Parker, H. McCann, R. Kikinis, and W. R. B. Lionheart. Mutual information as a measure of image quality for 3D dynamic lung imaging with EIT. *Physiol. Meas.*, 35(5):863–879, 2014.
- [134] H. McCann, T. Ahsan, J. L. Davidson, R. L. Robinson, P. Wright, and C. J. D. Pomfrett. A portable instrument for high-speed brain function imaging: FEITER. In *Proc. 33rd Annual Int. Conf. IEEE EMBS*, pages 7029–7032, Boston, MA, USA, September 2011.

- [135] P. Ramachandran and G. Varoquaux. Mayavi: A free tool kit for cfd data visualization. *4th Annual CFD Symposium, Aeronautical Society of India*, August 2001. <http://mayavi.sourceforge.net>.
- [136] J. P. W. Pluim, J. B. Antoine Maintz, and M. A. Viergever. Mutual-information-based registration of medical images: a survey. *IEEE Trans. Med. Imaging*, 22(8):986–1004, 2003.
- [137] D. McCormick, J. L. Davidson, and H. McCann. Conversion of EIT brain images for co-registration. In *Proc. 8th International Conference on Electrical Impedance Tomography*, pages 384–387, Graz, Austria, 2007.
- [138] S. Pieper, M. Halle, and R. Kikinis. 3D SLICER. *Proc. 1st IEEE International Symposium on Biomedical Imaging: From Nano to Macro*, 1:632–635, 2004. <http://www.slicer.org>.
- [139] R. A. Little, P. Wright, J. Naish, R. Kikinis, G. J. M. Parker, and H. McCann. Fusion of images obtained from EIT and MRI. *Electronics Letters*, 48(11):617–618, 2012.
- [140] I. G. Bikker, C. Preis, M. Egal, J. Bakker, and D. Gommers. Electrical impedance tomography measured at two thoracic levels can visualize the ventilation distribution changes at the bedside during a decremental positive end-expiratory lung pressure trial. *Crit. Care*, 15(4):R193, 2011.
- [141] S. Nebuya, M. Noshiro, A. Yonemoto, S. Tateno, B. H. Brown, R. H. Smallwood, and P. Milnes. Study of the optimum level of electrode placement for the evaluation of absolute lung resistivity with the Mk3.5 EIT system. *Physiol. Meas.*, 27(5):S129–S137, 2006.
- [142] R. D. Cook, G. J. Saulnier, D. G. Gisser, J. C. Goble, J. C. Newell, and D. Isaacson. ACT3: a high-speed, high-precision electrical impedance tomograph. *IEEE Trans. Biomed. Eng.*, 41(8):713–722, 1994.
- [143] G. J. Saulnier, N. Liu, C. Tamma, H. Xia, T. J. Kao, J. C. Newell, and D. Isaacson. An electrical impedance spectroscopy system for breast cancer detection. In

- Conf Proc. IEEE Eng. Med. Biol. Soc.*, pages 4154–4157, Lyon, France, August 2007.
- [144] P. J. Vauhkonen, M. Vauhkonen, and J. P. Kaipio. Errors due to the truncation of the computational domain in static three-dimensional electrical impedance tomography. *Physiol. Meas.*, 21(1):125–135, 2000.
- [145] Simpleware Ltd., Exeter, UK: Innovation Centre. *ScanIP, +ScanFE and +ScanCAD software v. 2.0 reference guide*. <http://www.simpleware.com>.
- [146] Q. Fang and D. Boas. Tetrahedral mesh generation from volumetric binary and grayscale images. In *IEEE International Symposium on Biomedical Imaging 2009*, pages 1142–1145, 2009.
- [147] A. Adler, R. Amyot, R. Guardo, J. H. T. Bates, and Y. Berthiaume. Monitoring changes in lung air and liquid volume changes with electrical impedance tomography. *J. Appl. Phys.*, 83:1762–1767, 1997.
- [148] H. Tregidgo, M. Crabb, and W. Lionheart. Regional lung compliance: Coupling ventilation and electrical data. In *Proc. 15th International Conference on Electrical Impedance Tomography*, page 79, Gananoque, Canada, 2014.
- [149] L. K. H. Van Beek. The Maxwell-Wagner-Sillars effect describing apparent dielectric loss in inhomogeneous media. *Physica*, 26:66–68, 1960.
- [150] S. K. Kanaun and S. B. Kochecksaraii. Effective conductive and dielectric properties of matrix composites with inclusions of arbitrary shapes. *Int. J. Eng. Sci.*, 46:147–163, 2008.
- [151] C.-L. Lin, M. H. Tawhai, and E. A. Hoffman. Multiscale image-based modeling and simulation of gas flow and particle transport in the human lungs. *WIREs Syst. Biol. Med.*, 5:643–655, 2013.
- [152] M. H. Tawhai, A. R. Clark, G. M. Donovan, and K. S. Burrowes. Computational Modeling of Airway and Pulmonary Vascular Structure and Function: Development of a ‘Lung Physiome’. *Crit. Rev. Biomed. Eng.*, 39(4):319–336, 2011.

- [153] J. Mead, T. Takishima, and D. Leith. Stress distribution in lungs: a model of pulmonary elasticity. *J. Appl. Physiol.*, 28(5):596–608, 1970.
- [154] J. H. T. Bates. *Lung Mechanics: An Inverse Modeling Approach*. Cambridge University Press, 2009.
- [155] A. Ben-Tal. Simplified models for gas exchange in the human lungs. *J. Theor. Biol.*, 238:474–495, 2006.
- [156] A. Ben-Tal and J. C. Smith. A model for control of breathing in mammals: coupling neural dynamics to peripheral gas exchange and transport. *J. Theor. Biol.*, 251(3):480–497, 2008.
- [157] J. G. Eyles and R. L. Pimmel. Estimating Respiratory Mechanical Parameters in Parallel Compartment Models. *IEEE Trans. Biomed. Eng.*, BME-28(4):313–317, 1981.
- [158] J. G. Eyles, R. L. Pimmel, J. M. Fullton, and P. A. Bromberg. Parameter Estimates in a Five-Element Respiratory Mechanical Model. *IEEE Trans. Biomed. Eng.*, BME-29(6):460–463, 1982.
- [159] M. M. Cloutier and R. S. Thrall. The Respiratory System. In R. M. Berne, B. M. Koeppen, M. N. Levy, and B. A. Stanton, editors, *Physiology*. Mosby Elsevier, 6th edition, 2010.
- [160] J. Cullum. Numerical Differentiation and Regularization. *SIAM J. Numer. Anal.*, 8(2):254–265, 1971.
- [161] M. Hanke and O. Scherzer. Inverse Problems Light: Numerical Differentiation. *Amer. Math. Monthly*, 108(6):512–521, 2001.
- [162] A. S. Lubansky, Y. L. Yeow, Y.-K. Leong, S. R. Wickramasinghe, and B. Han. A method for computing the derivative of experimental data. *J. AIChE*, 52:323–332, 2006.
- [163] R. Chartrand. Numerical Differentiation of Noisy, Nonsmooth Data. *ISRN Appl. Math.*, pages 1–11, 2011.

- [164] J. D. Lambert. *Numerical Methods for Ordinary Differential Systems*. Wiley, 1992.
- [165] Y. Cai and S. Xu. Inverse Problems. *On a quadratic inverse eigenvalue problem*, 25(8):085004, 2009.
- [166] P. Lancaster and U. Prells. Inverse problems for damped vibrating systems. *Journal of Sound and Vibration*, 283(3-5):891–914, 2005.
- [167] A. Adler and B. Graham. Electrode placement configurations for 3D EIT. *Physiol. Meas.*, 28:S29–S44, 2007.
- [168] A. Adler, D. Gürsoy, and Y. Marmatjan. Electrode positions and current patterns for 3D EIT. In *Proceedings of 12th International Conference in Electrical Impedance Tomography, University of Bath, 2011*.
- [169] D. Isaacson. Distinguishability of conductivities by electrical current computed tomography. *IEEE Trans. Med. Imaging*, 5:91–95, 1986.
- [170] A. Borsic, R. Halter, Y. Wan, A. Hartov, and K. D. Paulsen. Sensitivity study and optimization of a 3d electric impedance tomography prostate probe. *Physiol. Meas.*, 30(6):S1–S18, 2009.
- [171] J. P. Kaipio, A. Seppänen, E. Somersalo, and H. Haario. Posterior covariance related optimal current patterns in electrical impedance tomography. *Inverse Problems*, 20:919–936, 2004.
- [172] L. Horesh, E. Haber, and L. Tenorio. Optimal Experimental Design for the Large-Scale Non-linear Ill-posed Problem of Impedance Imaging. In L. Biegler, G. Biros, O. Ghattas, M. Heinkenschloss, D. Keyes, B. Mallick, L. Tenorio, B. van Bloemen Waanders, and K. Willcox, editors, *Large-Scale Inverse Problems and Quantification of Uncertainty*. John Wiley & Sons, Ltd, 2010.
- [173] E. Kreyszig. *Introductory Functional Analysis with Applications*. Wiley, New Jersey, 1989.
- [174] M. Renardy and R. C. Rogers. *An Introduction to Partial Differential Equations*. Springer-Verlag, New York, 2nd edition, 2004.

- [175] M. E. Taylor. *Partial Differential Equations 3 : Nonlinear Equations*. Springer-Verlag, New York, 2010.
- [176] R. S. Hamilton. The inverse function theorem of Nash and Moser. *Bull. Amer. Math. Soc.*, 7:65–222, 1982.
- [177] T. Frankel. *The Geometry of Physics: An Introduction*. Cambridge University Press, 3rd edition, 2012.
- [178] R. Abraham, J. E. Marsden, and T. Ratiu. *Manifolds, Tensor Analysis, and Applications*. Springer-Verlag, New York, 2nd edition, 1988.
- [179] W. M. Boothby. *An Introduction to Differentiable Manifolds and Riemannian Geometry*. Academic Press, 2nd edition, 1986.
- [180] M. P. Do Carmo. *Riemannian Geometry*. Birkhäuser, 2nd edition, 1988.

Appendix A

Mathematical notation

A.1 PDE theory

We outline some essential notation used to analyse PDEs used throughout this thesis. Some good texts on basic functional analysis and PDE include [64, 69, 173, 174].

An n -dimensional multi-index α is an n -tuple, $\alpha = (\alpha_1, \alpha_2, \dots, \alpha_n)$, of non-negative integers. Given $x = (x_1, x_2, \dots, x_n) \in \mathbb{R}^n$, the length, the partial derivative and the power of the multi-index are defined as

$$|\alpha| := \sum_{i=1}^n \alpha_i, \quad \partial^\alpha := \partial_1^{\alpha_1} \partial_2^{\alpha_2} \dots \partial_n^{\alpha_n}, \quad x^\alpha = x_1^{\alpha_1} x_2^{\alpha_2} \dots x_n^{\alpha_n},$$

respectively, where $\partial_i^{\alpha_i} := \frac{\partial^{\alpha_i}}{\partial x_i^{\alpha_i}}$. A normed vector space V is a vector space equipped with a norm, denoted $\|\cdot\| : V \rightarrow \mathbb{R}$. A vector space is complete if every Cauchy sequence v_n has a limit point $v \in V$, and a normed vector space $(V, \|\cdot\|)$ is a *Banach* space if V is complete. An inner-product space V is a vector space with an inner product, denoted $\langle \cdot, \cdot \rangle : V \times V \rightarrow \mathbb{R}$. A *Hilbert* space is a complete inner product space $(H, \|\cdot\|, \langle \cdot, \cdot \rangle)$ and a natural norm on a Hilbert space H is given by, $\|u\|_H = \langle u, u \rangle_H^{\frac{1}{2}}$

Fundamental Hilbert space properties

A fundamental property is the Cauchy-Schwarz inequality: $|\langle x, y \rangle_V| \leq \|x\|_V \cdot \|y\|_V$, with equality iff $x = cy$ for some $c \in \mathbb{R}$. If we are working on a Hilbert space with an orthonormal basis, $\{e_j\}_{j=1}^\infty$, the following hold:

1. $f \in H$ can be written uniquely $f = \sum_{j=1}^\infty \langle f, e_j \rangle e_j$.

2. $f \in H$ has norm $\|f\|^2 = \sum_{j=1}^{\infty} |\langle f, e_j \rangle|^2$ known as *Plancherel's identity*.
3. $f \in H$ and $\langle f, e_j \rangle = 0$ for all j then $f = 0$.

Dual Spaces

Let X, Y be Banach spaces. Denote $L(X, Y)$ as the set of all bounded linear mappings from X to Y , then $L(X, Y)$ is a Banach space with norm

$$\|T\| := \sup_{0 \neq x \in X} \frac{\|Tx\|_Y}{\|x\|_X}.$$

A *linear functional* is a bounded linear map from X to \mathbb{R} , and the vector space of all linear functionals on X is the *dual space* denoted X^* and is Banach. We now state the Lax Milgram lemma (see [174]):

Theorem A.1.1 (Lax Milgram Lemma). *Let V be a complex valued Hilbert space and denote V' as the dual space. Let $a(u, v)$ be a sesquilinear, bounded and coercive form defined on the product space $V \times V$. Then given any linear functional $f \in v'$, $f : V \rightarrow \mathbb{C}$, there exists a unique solution of the problem : Find $u \in V$ such that*

$$a(u, v) = f(v) \quad \forall v \in V,$$

We denote the solution as $u = Tf$, where $T : V' \rightarrow V$.

Fréchet derivative

Let X and Y be Banach spaces and $W \subset X$. An operator $T : X \rightarrow Y$ is Fréchet differentiable at $x \in X$, in the direction $h \in U \subset X$, if there exists a bounded linear operator $DT_x : U \rightarrow Y$ such that

$$\lim_{h \rightarrow 0} \frac{\|T(x+h) - T(x) - DT_x(h)\|_Y}{\|h\|_X} = 0. \tag{A.1}$$

Standard spaces

Let $\Omega \subset \mathbb{R}^n$. The Lebesgue space $L^p(\Omega)$, $1 < p < \infty$, is the space of distributions, $u : \Omega \subset \mathbb{R}^n \rightarrow \mathbb{R}$, whose value raised to the p^{th} power are integrable over Ω

$$L^p(\Omega) := \left\{ u : \int_{\Omega} |u(x)|^p < \infty \right\} \quad \|u\|_p = \left(\int_{\Omega} |u(x)|^p \right)^{\frac{1}{p}}.$$

For $p = \infty$, the definition is

$$L^\infty(\Omega) := \{u : \sup_{x \in \Omega} |u(x)| < \infty\} \quad \|u\|_\infty = \sup_{x \in \Omega} |u(x)|$$

$L^p(\Omega)$ is a Banach space. For $p = 2$ it is a Hilbert space with inner product

$$\langle f, g \rangle_{L^2(\Omega)} = \int_{\Omega} fg. \quad (\text{A.2})$$

$C^k(\Omega, \mathbb{R}^n)$ is the space of k -times continuously differentiable functions. It is a Banach space with norm

$$\|f\|_{k,\infty} := \sum_{n=0}^k \|f^{(n)}\|_\infty \quad \text{where} \quad \|f\|_\infty := \sup_{x \in \Omega} |f(x)|.$$

A.1.1 Sobolev spaces

To define non-integer Sobolev spaces, we need basic definitions of Fourier series and transform.

Fourier series

Let f be a periodic, integrable function on the torus $\mathbb{T}^n = \mathbb{R}^n / \mathbb{Z}^n$. The set $\{e^{-ik \cdot \theta}\}_{k=-\infty}^{\infty}$ forms an orthogonal basis for $L^2(\mathbb{T}^n)$. Any $f \in L^2(\mathbb{T}^n)$ can be written as

$$f(\theta) = \sum_{k=-\infty}^{\infty} \tilde{f}(k) e^{ik \cdot \theta} \quad \text{where} \quad \tilde{f}(k) = \frac{1}{(2\pi)^n} \int_{\mathbb{T}^n} f(\theta) e^{-ik \cdot \theta}.$$

\tilde{f} denotes the Fourier Transform. Plancherel's theorem states that $\langle \tilde{f}, \tilde{g} \rangle = \langle f, g \rangle$, so

$$\|f\|_{L^2} = \sum_{k=-\infty}^{k=+\infty} |\tilde{f}(k)|^2.$$

Fourier transform

If we consider a function defined on \mathbb{R}^n , we instead use the Fourier Transform. The Fourier transform, valid for a function $f \in L^2(\mathbb{R}^n)$, and the inverse Fourier transform, valid for $\tilde{f} \in L^2(\mathbb{R}^n)$ are respectively

$$\tilde{f}(k) = \frac{1}{(2\pi)^n} \int_{\mathbb{R}^n} f(x) e^{-ik \cdot x}, \quad f(x) = \int_{\mathbb{R}^n} \tilde{f}(k) e^{ik \cdot x}. \quad (\text{A.3})$$

We also have Plancherel's theorem, which states that

$$\int_{\mathbb{R}^n} f(x)g(x) = \int_{\mathbb{R}^n} \tilde{f}(k)\tilde{g}(k). \quad (\text{A.4})$$

These results are also true for a compact manifold M (see [87].)

We also need to define the generalized derivative of a function $f \in L^1_{\text{loc}}(\Omega)$. Denote $C_c^\infty(\Omega)$ as the set of smooth functions, ψ , compactly supported in Ω . v is the generalized derivative of $f \in L^1_{\text{loc}}(\Omega)$ if

$$\int_{\Omega} v \psi = (-1)^{|\alpha|} \int_{\Omega} f \partial^\alpha \psi \quad \forall \psi \in C_c^\infty(\Omega)$$

where α is a multi-index. If this exists we denote this as $\partial^\alpha f = v$.

Integer order Sobolev spaces

Let k be a non-negative integer, then the Sobolev space $W^{k,p}(\Omega)$ is defined as the set of all distributions, $f \in L^p(\Omega)$, such that $D^\alpha f \in L^p(\Omega)$ for $|\alpha| \leq k$,

$$W^{k,p}(\Omega) = \{u \in L^1_{\text{loc}}(\Omega) : \partial^\alpha u \in L^p(\Omega) \quad \forall |\alpha| \leq k\}. \quad (\text{A.5})$$

When $p = 2$ we define $H^k(\Omega) := W^{k,2}(\Omega)$, and is a Hilbert space with inner product

$$\langle f, g \rangle_{H^k(\Omega)} = \sum_{|\alpha| \leq k} \langle D^\alpha f, D^\alpha g \rangle_{L^2(\Omega)}.$$

Fractional Sobolev spaces

It is also useful to define non-integer order Sobolev spaces. These naturally arise when restricting a distribution defined in a Sobolev space on a compact manifold with boundary Ω to the boundary $\partial\Omega$. From the definition of the generalized derivative, the Fourier Transform and derivative of a function are related through $(\partial^{\hat{\alpha}} f)(\omega) = (-2\pi i \omega)^\alpha \hat{f}(\omega)$. This identity effectively enables us to extend Sobolev spaces to non-integer derivatives. Let k be any real number, then we have

$$f \in H^k(\Omega) \quad \text{if and only if} \quad (2\pi i \omega)^\alpha \hat{f}(\omega) \in L^2(\Omega), \quad (\text{A.6})$$

for any α with $|\alpha| \leq k$. For an unbounded domain $\Omega = \mathbb{R}^n$, then the norm can be defined with the Fourier transform as

$$\|f\|_{H^s}^2 = \int_{\mathbb{R}^n} (1 + |k|^2)^{s/2} |\tilde{f}(k)|^2.$$

where $\langle k \rangle^2 = \sum_{i=1}^n k_i^2$. In a similar spirit, for a periodic domain $\mathbb{T}^n = \mathbb{R}^n \setminus \mathbb{Z}^n$, we have the norm defined with the Fourier series as

$$\|f\|_{H^s}^2 = \sum_{k=-\infty}^{k=+\infty} (1 + |k|^2)^{s/2} |\tilde{f}(k)|^2. \quad (\text{A.7})$$

These results can be extended to a compact manifold M (see [64] for more details.)

Trace theorem

A function $u \in C^0(\bar{\Omega})$ where $\Omega \subset \mathbb{R}^n$ has a natural restriction to $\partial\Omega$ preserving continuity. If the function lies in, say, $L^2(\Omega)$ or $H^k(\Omega)$, this is not true because $\partial\Omega$ is a subset of Ω of measure zero. If a function defined on $\partial\Omega$ lies in a Sobolev space $H^k(\partial\Omega)$, then how smooth does this have to be so that a function in $H^p(\Omega)$ assumes this data? This problem is addressed by the following trace theorem [64]:

Theorem A.1.2 (Trace). *Let $k > 1/2$ and assume Ω is a bounded domain in \mathbb{R}^n with smooth boundary. Then there is a bounded trace operator $\tau : H^k(\Omega) \rightarrow H^{k-\frac{1}{2}}(\partial\Omega)$. Moreover τ has a bounded inverse.*

Dual spaces

Let $H^{-k}(\Omega)$ denote set of all bounded linear functionals on $H_0^k(\Omega)$. If Ω is \mathbb{R}^m , or a compact manifold of class C^k with $k > s$, $H^{-s}(\Omega)$ denotes the dual space of $H_0^s(\Omega)$.

Sobolev's first embedding theorem

The 'first' Sobolev embedding theorem states that functions with large enough Sobolev indices are continuous in the conventional sense. In particular from [64] given a compact manifold Ω of dimension n , there exists the inclusion

$$H^s(\Omega) \subset C^k(\Omega) \quad \text{for all} \quad s > n/2 + k. \quad (\text{A.8})$$

A.1.2 Symmetric hyperbolic PDEs

In this section we outline essential theory on first order systems of symmetric hyperbolic PDE following DeTurck and Yang [109] (see [87, 175] for more details on such systems). This class of PDE will appear when discussing theoretical elasticity and the anisotropic problem with constrained eigendata in sections 3.4.3 and 3.4.4.

Let M be a compact $(n-1)$ -manifold, and $X = M \times [0, 1]$ with coordinates $x' = (x^1, \dots, x^{n-1})$ on M and $x = (x', t) = (x^1, \dots, x^{n-1}, t)$ on X . The differential operator $P : C^\infty(X, \mathbb{R}^m) \rightarrow C^\infty(X, \mathbb{R}^m)$ is *symmetric hyperbolic* if

$$P = \frac{\partial}{\partial t} + \sum_{i=1}^n A^i \frac{\partial}{\partial x^i} + B, \quad (\text{A.9})$$

with $A^i, B \in C^\infty(X, \text{End}(\mathbb{R}^m))$ and each matrix A^i symmetric. Consider a non-linear system of PDE

$$\frac{\partial u}{\partial t} = F(x, u, \frac{\partial u}{\partial x^1}, \dots, \frac{\partial u}{\partial x^{n-1}}), \tag{A.10}$$

with $F \in C^\infty(V, \mathbb{R}^m)$, and V is an open subset of $X \times \mathbb{R}^m \times \mathbb{R}^{(n-1)m}$. This is defined to be symmetric hyperbolic if the associated linearised operator L

$$L := \frac{\partial}{\partial t} - \sum_{\alpha} \frac{\partial F}{\partial u_{\alpha}} \frac{\partial}{\partial x^{\alpha}}, \quad \text{where} \quad \frac{\partial F}{\partial u_{\alpha}} = \left[\frac{\partial F^i}{\partial u_{\alpha}^j} \right] \quad 1 \leq i, j \leq m \quad 1 \leq \alpha \leq n-1,$$

is symmetric hyperbolic for all $(x, u, u_{\alpha} dx^{\alpha}) \in V$. The following two theorems by DeTurck and Yang [109], based on the Nash-Moser inverse function theorem [176], asserts uniqueness of solution for the non-linear system.

Theorem A.1.3. *Let F define a non-linear symmetric hyperbolic system. If $u_0 : M \rightarrow \mathbb{R}^m$ is such that $(x', 0, u_0(x'), \frac{\partial u_0}{\partial x^{\alpha}} dx^{\alpha}) \in V$ for all $x' \in M$, then there exists an $\epsilon > 0$ and a unique smooth function $u : M \times [0, \epsilon] \rightarrow \mathbb{R}^m$ such that (A.10) is satisfied for all $x \in M \times [0, \epsilon]$ and $u(x', 0) = u_0(x')$.*

Theorem A.1.4. *Let F define a non-linear symmetric hyperbolic system, and let $u \in C^\infty(X, \mathbb{R}^m)$ solve*

$$\frac{\partial u}{\partial t} = F(x, u, \frac{\partial u}{\partial x^{\alpha}} dx^{\alpha}) \tag{A.11}$$

on all of X . Then for G sufficiently close to F in the $C^\infty(V, \mathbb{R}^m)$ -topology, there is a unique solution v of

$$\frac{\partial v}{\partial t} = G(x, v, \frac{\partial v}{\partial x^{\alpha}} dx^{\alpha}) \tag{A.12}$$

such that $v(x', 0) = u(x', 0)$ for all $x' \in M$.

Let D_1, \dots, D_m be real vector fields on X such that for $x = (x', t) \in X$, $D_{\alpha}(x)$ is not tangent to $M \times \{t\}$ for any $1 \leq \alpha \leq m$. The matrix differential operator $P = \text{diag}(D_1, \dots, D_m) + B$ is said to be *diagonal symmetric*. As before a non-linear system $\frac{\partial u}{\partial t} = F(x, u, \frac{\partial u}{\partial x^{\alpha}} dx^{\alpha})$ is said to be diagonal if it's linearisation is diagonal. The symbol of the linear operator P , or the linearisation of a non-linear operator, is the linear mapping $\sigma_P(\xi) = \sum_{i=1}^n A^i(x) \xi_i$ which, for each $\xi \in T_x^* X$, maps \mathbb{R}^m to \mathbb{R}^m . The set for which $\sigma_P(\xi)$ is not invertible is the *characteristic variety*. Consider the PDE

$$P = \sum_{i=1}^n A^i \frac{\partial}{\partial x^i} + B. \tag{A.13}$$

DeTurck and Yang show that (A.13) is diagonal symmetric hyperbolic under the following conditions [109]:

Theorem A.1.5. *Sufficient condition conditions that (A.13) is equivalent to a diagonal hyperbolic operator is that: (i) for each x , the set of cotangent vectors ξ for which $\sigma_P(\xi)$ is not invertible comprise n hyperplanes, with linearly independent normal vectors, and (ii) that for any $\xi \in T_x^*X$ the dimension of the kernel of $\sigma_P(\xi)$ is the number of characteristic hyperplanes passing through ξ .*

A.2 Manifolds and Riemannian geometry

In this section we outline some essential definitions from differentiable manifolds and Riemannian geometry in order to pose a geometric formulation of the inverse conductivity problem. See [107, 177, 178, 179] for deeper texts on this subject.

A.2.1 Differentiable manifolds

Definition A.2.1. *A differentiable manifold of dimension n is a set M^n such that for each $p \in M^n$, there is an open set U of p and a function $\psi : U \rightarrow \mathbb{R}^n$ that is homeomorphic with an open subset of \mathbb{R}^n .*

We denote M^n as simply M , and the pair (U, ψ) is called a coordinate chart. We write $\psi(q) = (x^1(q), x^2(q), \dots, x^n(q))$, where $x^i(q)$ are *local coordinates* of M at q . Given two coordinate charts (U, ψ) and (V, Ψ) on M , with $U \cup V \neq \emptyset$, $\psi \circ \Psi^{-1}$ a transition map. This is a homeomorphism from an open set in \mathbb{R}^n to another open set in \mathbb{R}^n . M is smooth (or C^∞) if all transition maps are smooth (or C^∞), and M is orientable if all the transition maps are orientation-preserving.

Definition A.2.2. *Let $f : M \rightarrow N$ where M, N are smooth manifolds. f is smooth if for every pair of charts (U, ψ) of M and (V, Ψ) of N , the function is smooth*

$$\psi \circ \Psi^{-1} : \psi(U \cup f^{-1}(V)) \rightarrow \Psi(f(U) \cup V)$$

We denote $C^\infty(M)$ as the set of smooth $f : M \rightarrow \mathbb{R}$. If $f : M \rightarrow N$ is smooth, with smooth inverse, then f is a *diffeomorphism* and M and N are *diffeomorphic*.

Tangent and cotangent space

Consider a smooth function (or curve) $\gamma : (-\epsilon, \epsilon) \rightarrow M$ on a manifold with $\gamma(0) = p$. Let f be a smooth function defined in a neighbourhood of $p \in M$. The directional derivative of f w.r.t. the vector $\gamma'(0)$ at p is $\frac{d}{dt}f(\gamma(t))|_{t=0} = (\alpha'_i(0)\frac{\partial}{\partial x^i})f$. The tangent vector of the curve α at $t = 0$ is a function $\alpha'(0) : C^\infty(M) \rightarrow \mathbb{R}$ through $\alpha'(0)f = \frac{d}{dt}f(\gamma(t))|_{t=0}$. This can be generalised with derivations.

Definition A.2.3. A tangent vector to a smooth manifold M at $p \in M$ is a derivation, that is an \mathbb{R} linear function $X : C^\infty(M) \rightarrow \mathbb{R}$ satisfying the product rule

$$X(fg) = X(f)g(p) + f(p)X(g).$$

The set of all tangent vectors to an n -manifold M^n at p forms an n -dimensional vector space, $T_p(M^n)$. If (x^i) is a local coordinate system about $p \in M$, the set of all derivations $\{\partial/\partial x^i, i = 1 : n\}$ forms a basis for T_pM , and we write $\partial_i := \partial/\partial x^i$. The set of all tangent vectors of all points of M form a $(2n)$ -manifold, namely the tangent bundle, $TM = \sqcup_{x \in M} T_xM$. A vector field on M is a smoothly varying choice of tangent vector at each $p \in M$ (smoothly varying means $X(f) \in C^\infty(M)$ for any $f \in C^\infty(M)$.)

The cotangent space at $p \in M$, $T_p^*(M)$, consists of all linear functionals acting on $T_p(M)$ (the 1-forms at p). The set of all cotangent spaces at all points $p \in M$ forms a $(2n)$ -dimensional manifold, the cotangent bundle, $T^*M = \sqcup_{x \in M} T_x^*M$. Given local coordinates $\{x^i\}_{i=1}^n$ at p on an n -manifold M , the set of covectors $dx^i : i = 1 : n$ (where $dx^i(X) := X(x^i)$) forms a basis for $T_p^*(M)$.

Tensor fields

A (k, l) -tensor field is a multilinear map sending l copies of the tangent bundle and k copies of the cotangent bundle to \mathbb{R} , and is a member of

$$T_l^k(M) := \left\{ t : \underbrace{T^*(M) \times \dots \times T^*(M)}_{k \text{ times}} \times \underbrace{TM \times \dots \times TM}_{l \text{ times}} \rightarrow \mathbb{R} \right\}.$$

Given a local coordinate system $\{x^i\}$ at $p \in M$, and dx^j, ∂_m are basis for T_p^*M and T_pM we can express tensor field $F \in T_l^k(M)$ in a local coordinate system at p as

$$F = F_{i_1 \dots i_k}^{j_1 \dots j_l} \partial_{j_1} \otimes \dots \otimes \partial_{j_l} \otimes dx^{i_1} \otimes \dots \otimes dx^{i_k},$$

where repeated indices are summed over (Einstein summation convention). \otimes is the tensor product (for $(k, 0)$ -tensors)

$$T^k(M) \times T^l(M) \rightarrow T^{k+l}(M), \quad (u, u') \mapsto u \otimes u',$$

where $(u \otimes u')(v, v') := u(v)u'(v')$ for $v \in T_p(M)$ and $v' \in T_p(M)$.

Pullback and pushforward

Definition A.2.4. Given a smooth map $\Psi : M \rightarrow N$, we define the derivative map between the tangent spaces $\Psi_* : T_p(M) \rightarrow T_{\Psi(p)}(N)$ by

$$(\psi_* V)(f) = V(f \circ \Psi)$$

for all $V \in T_p M$ and $f \in C^\infty(N)$. This is known as the pushforward of V at p . We can define the derivative map between cotangent spaces $\Psi^* : T_{\Psi(p)}^*(N) \rightarrow T_p^*(M)$ by

$$(\Psi^* \omega)(V) = \omega(\Psi_* V)$$

for all $V \in T_p M$ and $\omega \in T_{\Psi(p)}^*(N)$. This is known as the pullback of ω by f .

This pullback can be extended to tensor fields A and B through $\Psi_*(A \otimes B) := \Psi_*(A) \otimes \Psi_*(B)$, and for differential forms $\Psi^*(\alpha \wedge \beta) := F^* \alpha \wedge F^* \beta$.

Differential forms

A k -form on M is a section of $\wedge^k T^*(M)$ (the set of $(k, 0)$ -tensor fields that are anti-symmetric in all its indices.) A k -form can be written $\alpha = \alpha_I dx^I$ where $I = (i_1, \dots, i_k)$ and $dx^I = dx^{i_1} \wedge \dots \wedge dx^{i_k}$. A k -vector field on M is a section of $\wedge^k TM$. The wedge product maps a k -form, α , and l -form, β , to a $(k + l)$ -form

$$\alpha \wedge \beta = \sum_{\substack{i_n, j_n \\ i, j=1}} a_i b_j dx_{i_1} \wedge \dots \wedge dx_{i_n} \wedge dx_{j_1} \wedge \dots \wedge dx_{j_n}.$$

This relation means that

$$\alpha \wedge \beta = \frac{1}{2}(\alpha \otimes \beta - \beta \otimes \alpha).$$

For such forms we have that $\alpha \wedge \beta = (-1)^{kl} \beta \wedge \alpha$. The exterior derivative d is a differential operator mapping k -forms to $(k + 1)$ -forms, $d : \wedge^k T^* M \rightarrow \wedge^{k+1} T^* M$. The

exterior derivative of a function f is given by

$$df = \sum_{i=1}^n \frac{\partial f}{\partial x^i} dx^i, \quad (\text{A.14})$$

and for a k -form $\alpha = \alpha_I dx^I$,

$$d\alpha := \sum_I d\alpha_I \wedge dx^I. \quad (\text{A.15})$$

Stokes' Theorem

Let M be an oriented n -manifold with an atlas of charts (U_α, ψ_α) . Let β be a smooth n -form compactly supported in U_α , and $((\psi_\alpha)^{-1})^* \beta|_{\psi_\alpha(U_\alpha)} = A(x) dx^1 \wedge \dots \wedge dx^n$, then

$$\int_M \beta := \int_{\psi_\alpha(U_\alpha)} b(x) dx^1 \wedge \dots \wedge dx^n.$$

Suppose β is an arbitrary smooth n -form on M . Let $\{f_\alpha\}$ be a partition of unity subordinate to $\{U_\alpha\}$, then

$$\int_M \beta := \sum_\alpha \int_M f_\alpha \beta$$

Theorem A.2.5 (Stokes'). *Let M be an oriented n -manifold. Then*

$$\int_{\partial M} \iota^* \beta = \int_M d\beta,$$

where β is a smooth $(n-1)$ -form and $\iota : \partial M \hookrightarrow M$ is the inclusion.

A.2.2 Riemannian geometry

A Riemannian metric, g , on a smooth manifold M is a smoothly varying inner product on the tangent space at each point of M . $g_{ij}(p)$ is the representation in coordinates at $p \in M$ and is a positive definite matrix. There is an induced norm on each $T_p(M)$ which written $|X|_g := \sqrt{\langle X, X \rangle}$, where $\langle X, Y \rangle = g(X, Y)$. A manifold with a Riemannian metric, (M, g) , is called a Riemannian manifold. Given a Riemannian manifold (M, g) and a manifold N embedded in M (a submanifold of M), there is an induced Riemannian metric \bar{g} on N defined by restricting g to $T_p(N)$ at each point $p \in N$.

Given the metric g_{ij} we define g^{ij} to be the inverse of the metric at each point i.e. $g^{ij} g_{jk} = \delta_k^i$. Any inner product on a vector space gives a natural isomorphism $V \cong V^*$ via $X \rightarrow X^b$, where $X^b(Y) = \langle X, Y \rangle$. In coordinates, $(X^b)_i = g_{ij} X^j$. Similarly, we

have $X \rightarrow X^\sharp$, where $X^\sharp(Y) = \langle X, Y \rangle$, in coordinates $(X^\sharp)^i = g^{ij}X_j$. These operations are known as lowering and raising indices by the metric. In general we can lower an index i on a tensor F_{pq}^{ijk} , for example, we have $F_{ipq}^{jk} := g_{im}F_{pq}^{mjk}$, which is a map from $T_l^k(M)$ to $T_{l-1}^{k+1}(M)$. Similarly we can raise an index using g^{ij} .

Covariant derivative

The rate of change of a function f in direction of tangent vector X , is given by $X(f) = X^i \frac{\partial f}{\partial x_i}$. To differentiate a vector field, Y , in the direction of a tangent vector, X , we need the notion of a covariant derivative, because $T_p(M)$ varies between points on a manifold. Let $C^\infty(E)$ denote the set of all C^∞ vector fields on M . An *affine* connection ∇ in E is a map

$$\nabla : C^\infty(E) \times C^\infty(E) \rightarrow C^\infty(E), (X, Y) \mapsto \nabla_X Y,$$

such that (i) $\nabla_X Y$ is linear over $C^\infty(M)$ in X , (ii) $\nabla_X Y$ is linear over \mathbb{R} in Y and (iii) ∇ satisfies the Leibniz rule: $\nabla_X(fY) = X(f)Y + f\nabla_X Y$. We call $\nabla_X Y$ the covariant derivative of Y in the direction X . A connection on TM is specified by its Christoffel symbols, Γ_{ij}^k , in a local coordinate system x^i , which are defined through

$$\nabla_{\partial_i} \partial_j = \Gamma_{ij}^k \partial_k.$$

We consider connections on the bundles $T_l^k(M)$ as an important special case. Given a connection ∇ on the tangent bundle TM , we can define all connections on all of the tensor bundles $T_l^k(M)$ satisfying (i) ∇ is the given connection on TM , (ii) for a scalar function, $\nabla_X f = X(f)$ and (iii) $\nabla_X(F \otimes G) = (\nabla_X F) \otimes G + F \otimes (\nabla_X G)$. There are many possible connections on the tangent bundle TM . If M is equipped with a Riemannian metric, there is one in particular, the Levi-Civita connection, with the following properties (see [180] for a proof).

Lemma A.2.6. *Given a Riemannian manifold M , there is a unique affine connection ∇ on M , the Levi-Civita connection, satisfying (i) $X(g(Y, Z)) = g(\nabla_X Y, Z) + g(Y, \nabla_X Z)$ and (ii) the torsion, $\tau(X, Y) := \nabla_X Y - \nabla_Y X - [X, Y]$, is identically 0.*

The Christoffel symbols of the Levi-Civita connection in local coordinates are

$$\Gamma_{ij}^k = \frac{1}{2} g^{kl} (\partial_i g_{jl} + \partial_j g_{il} - \partial_l g_{ij}). \quad (\text{A.16})$$

Cartan's structural equations

Let A be a 1-contravariant, p -covariant, tensor field, skew-symmetric in covariant indices,

$$A = \partial_i \otimes \sum_J A_{j_1, \dots, j_p}^i dx^{j_1} \wedge \dots \wedge dx^{j_p}.$$

A is of the form $\partial_i \otimes \alpha^i$, where α^i is the p -form coefficient of ∂_i , and we associate to A a vector-valued p -form α

$$\alpha(X^1, \dots, X^p) := \partial_i \alpha^i(X^1, \dots, X^p).$$

Let v be a vector field in M with Levi-Civita connection. Then $\nabla_j v^i := \frac{\partial v^i}{\partial x^j} + \Gamma_{jk}^i v^k$ forms a mixed tensor field, called the covariant derivative, $\nabla v = \partial_i \otimes \nabla_j v^i dx^j$, which can be considered as a vector-valued 1-form

$$\nabla v(X) = \partial_i (X^j \nabla_j v^i).$$

However $\partial_k \otimes \Gamma_{rj}^k dx^r$ is a vector valued 1-form when applied to ∂_i of the same value, and hence $\nabla e_j = e_k \otimes \Gamma_{rj}^k dx^r$. We define the local matrix ω of connection 1-forms by

$$\omega_j^k := \Gamma_{rj}^k dx^r. \tag{A.17}$$

Finally we have Cartan's structural equations, which state that the exterior derivative of a differential form is given by (see [177, pg.249])

$$d\omega^i = -\omega_k^i \wedge \omega^k. \tag{A.18}$$

Lie derivative

Given a vector field X on M , we define a time-dependent family of diffeomorphisms of M to itself, $\psi_t : M \rightarrow M$, for $t \in (-\epsilon, \epsilon)$, such that $\psi_0 = id$ and $\frac{d}{dt} \psi_t = X$. The existence of ψ_t given X comes from the Picard-Lindelöf theorem of solutions to ODEs, and ψ_t is a *flow* of the manifold in the direction of the vector field X . Denote

$$\begin{aligned} (\psi_t)^* F_p(X_1, \dots, X_k, \omega^1, \dots, \omega^l) &:= F_{\psi_t(p)}((\psi_t^{-1})^* X_{1(p)}, \dots, (\psi_t^{-1})^* (X_{k(p)}), \\ &(\psi_t^{-1})^* \omega_{(p)}^1, \dots, (\psi_t^{-1})^* \omega_{(p)}^l). \end{aligned}$$

The Lie derivative of a (k, l) -tensor field F in the direction of X , is the infinitesimal change in F after flowing along X

$$\mathcal{L}_X F = \left(\frac{d}{dt} ((\psi_t)^* F) \right) |_{t=0}.$$

We reference [178] for Lie derivatives of some important objects. The Lie derivative of a scalar field f is given by $X(f)$, and that of a vector field Y is $[X, Y]$, and the covariant metric tensor

$$(\mathcal{L}_X g)_{ij} = (X^k \frac{\partial g_{ij}}{\partial x^k} + g_{kj} \frac{\partial X^k}{\partial x^i} + g_{ik} \frac{\partial X^k}{\partial x^j}). \quad (\text{A.19})$$

If M is oriented, a volume form on M in local coordinates $\{x^i\}_{i=1}^n$ is given by $\mu_g := \sqrt{|g|} dx^1 \wedge \dots \wedge dx^n$, where $|g|$ is the determinant of the covariant metric tensor. The divergence div of a vector field X on a manifold can be defined as

$$\text{div}(X)\mu_g := L_X(\mu_g). \quad (\text{A.20})$$

In coordinates, the divergence of a vector field $X = X^j \partial_j$ is given by

$$\text{div}(X) = \frac{1}{\sqrt{|g|}} \frac{\partial}{\partial x_i} (\sqrt{|g|} X^i).$$

The gradient of a function f , $\text{grad}_g(f)$ is a vector field, $Y = Y^j \partial_j$ with coordinate expression $Y^j = g^{ij} \frac{\partial f}{\partial x_i}$.

Riemann curvature tensor

The curvature of a manifold is the deviation of the space from being Euclidean. Non-zero curvature at $p \in M$ is what stops us choosing local coordinates such that the metric is Euclidean

$$g_{ij}(x) = \delta_{ij} + \frac{1}{3} R_{ipqj} x^p x^q + O(x^3).$$

The (3, 1)-Riemann curvature tensor can be defined using the Levi-Civita connection ∇ , and can be defined for vector fields X, Y, Z by

$$\begin{aligned} R &: C^\infty(E) \times C^\infty(E) \times C^\infty(E) \rightarrow C^\infty(E) \\ R &: (X, Y, Z) \mapsto R(X, Y)Z = \nabla_X(\nabla_Y Z) - \nabla_Y(\nabla_X Z) - \nabla_{[X, Y]}Z. \end{aligned}$$

The (3, 1)-Riemann curvature tensor has the explicit coordinate form

$$R^l_{ijk} = \partial_i \Gamma^l_{jk} - \partial_j \Gamma^l_{ik} + \Gamma^p_{jk} \Gamma^l_{ip} - \Gamma^p_{ik} \Gamma^l_{jp}. \quad (\text{A.21})$$

The Riemann tensor has the following symmetries:

Lemma A.2.7 (Riemann - symmetries). *The Riemann curvature tensor has the following symmetries (i) $R_{ijkl} = R_{klij} = -R_{jikl} = -R_{ijlk}$, (ii) $R_{ijkl} + R_{jkil} + R_{kijl} = 0$, and (iii) $\nabla_p R_{ijkl} + \nabla_i R_{jpkl} + \nabla_j R_{pikl} = 0$.*

The *Ricci tensor*, R_{ij} , is a $(2, 0)$ -tensor that is a contraction of the Riemann tensor,

$$R_{ij} := R^p_{pij}. \quad (\text{A.22})$$

R_{ij} is symmetric, and the *Ricci scalar* is the trace of the Ricci tensor, $R := g^{ij}R_{ij}$.

Cotton-York tensor

Two Riemannian manifolds (M, g) and (\bar{M}, \bar{g}) are conformally related if

$$\bar{g}_{ij} = e^{2\sigma} g_{ij}$$

where σ is any function of x . From this relationship we have immediately $\bar{g}^{ij} = e^{-2\sigma} g^{ij}$. The Christoffel symbols $\{l, ij\} := \Gamma^l_{ij} = g^{lk}\Gamma_{kij}$ are given by (A.16) along with the lowered version $[ij, k] := \Gamma_{kij} = g_{kl}\Gamma^l_{ij}$. By direct substitution we see that the Christoffel symbols in the two frames are related through the following expressions

$$\begin{aligned} [ij, k] &= e^{2\sigma}([ij, k] + g_{ik}\sigma_{,j} + g_{jk}\sigma_{,i} - g_{ij}\sigma_{,k}) \\ \{l, ij\} &= \{l, ij\} + \delta^l_i\sigma_{,j} + \delta^l_j\sigma_{,i} - g_{ij}g^{lm}\sigma_{,m} \end{aligned}$$

where $\sigma_{,i} = \frac{\partial\sigma}{\partial x_i}$. Denote $\sigma_{,ij}$ the second derivative of σ , and define $\sigma_{ij} = \sigma_{,ij} - \sigma_{,i}\sigma_{,j}$.

Substituting the Christoffel symbols into the expression for the Riemann tensor (A.21) we have the following relationship between the curvature tensors

$$e^{-2\sigma} R_{hijk}^- = R_{hijk} + g_{hk}\sigma_{ij} + g_{ij}\sigma_{hk} - g_{hj}\sigma_{ik} - g_{ik}\sigma_{hj} + (g_{hk}g_{ij} - g_{hj}g_{ik})\Delta_1\sigma, \quad (\text{A.23})$$

where $\Delta_1 f = g^{ij} \frac{\partial f}{\partial x_i} \frac{\partial f}{\partial x_j}$. Similarly the Ricci tensor is given by

$$\bar{R}_{ij} = g^{\bar{h}k} R_{hijk}^- = R_{ij} + (n-2)\sigma_{ij} + g_{ij}(\Delta_2\sigma + (n-2)\Delta_1\sigma), \quad (\text{A.24})$$

where $\Delta_2 f = g^{ij}(\frac{\partial^2 f}{\partial x^i \partial x^j} - \frac{\partial f}{\partial x^k} \{k, ij\})$. Also the the Ricci scalar is given by

$$\bar{R} = g^{\bar{ij}} \bar{R}_{ij} = e^{-2\sigma}(R + 2(n-1)\Delta_2\sigma + (n-1)(n-2)\Delta_1\sigma), \quad (\text{A.25})$$

which can be written

$$\bar{g}_{ij} \bar{R} = g_{ij}(R + 2(n-1)\Delta_2\sigma + (n-1)(n-2)\Delta_1\sigma). \quad (\text{A.26})$$

Now $\Delta_2\sigma$ can be eliminated from equations (A.26) and (A.24) to obtain

$$\sigma_{ij} = \frac{1}{n-2}(\bar{R}_{ij} - R_{ij}) - \frac{1}{2(n-1)(n-2)}(\bar{g}_{ij} \bar{R} - g_{ij} R) - \frac{1}{2}g_{ij}\Delta_1\sigma \quad (\text{A.27})$$

We can write the transformed Riemann tensor (A.23)

$$R_{ijk}^{\bar{h}} = R_{ijk}^h + \delta_k^h \sigma_{ij} - \delta_j^h \sigma_{ik} + g^{hl} (g_{ij} \sigma_{lk} - g_{ik} \sigma_{lj}) + (\delta_k^h g_{ij} - \delta_j^h g_{ik}) \Delta_1 \sigma.$$

We can now substitute the equations (A.27) in the above identity, and we find that

$$W_{ijk}^{\bar{h}} = W_{ijk}^h$$

where

$$W_{ijk}^h = R_{ijk}^h + \frac{1}{n-2} (\delta_j^h R_{ik} - \delta_k^h R_{ij} + g_{ik} R_j^h - g_{ij} R_k^h) + \frac{R}{(n-1)(n-2)} (\delta_k^h g_{ij} - \delta_j^h g_{ik}). \quad (\text{A.28})$$

Since this is invariant this forms the components of a tensor known as the *conformal curvature* or *Weyl* tensor. From the properties of the Riemann tensor (A.2.7) we have

$$W_{ijk,l}^h + W_{ikl,j}^h + W_{ilj,k}^h = \frac{1}{n-2} (\delta_j^h C_{ikl} + \delta_k^h C_{ilj} + \delta_l^h C_{ijk} + g_{ik} C_{jl}^h + g_{il} C_{kj}^h + g_{ij} C_{lk}^h) \quad (\text{A.29})$$

where the *Cotton-York* tensor C_{ijk} is defined as

$$C_{ijk} := R_{ij,k} - R_{ik,j} + \frac{1}{2(n-1)} (g_{ik} R_{,j} - g_{ij} R_{,k}), \quad R_{jk}^h = g^{hi} R_{ijk}. \quad (\text{A.30})$$

In three dimensions, if \bar{M} is a flat space then $\bar{R}_{ijkl} = 0$, which implies $C_{ijkl} = 0$. Hence if a tensor is conformally flat the Cotton-York tensor must be a zero tensor. This condition is in fact necessary and sufficient (see [107] for a proof).

Theorem A.2.8 (Conformal flatness - Cotton-York tensor). *A necessary and sufficient condition that a V_n for $n > 2$ can be mapped conformally on an S_n is that the tensor C_{ijk} be a zero tensor when $n = 3$ and when $n > 3$ that W_{hijk} be a zero tensor.*

A.2.3 Frobenius' theorem

We make a brief summary of the essential definitions to state Frobenius' theorem from [179]. Integrability conditions are useful as they will help us define a layered anisotropic conductivity. Let M be a manifold with $\dim(M) = n + k$ and suppose each $p \in M$ is assigned a subspace of dimension n , Δ_p , of $T_p(M)$. Suppose moreover in each neighbourhood U of each $p \in M$, there are n linearly independent C^∞ vector fields X_1, X_2, \dots, X_n forming a basis of Δ_q for each $q \in U$. Then $\Delta \subset TM$ is a C^∞ *distribution* of $\dim n$ on M and X_1, \dots, X_n is a local basis of Δ . A distribution is in

involution if there exists a basis X_1, \dots, X_n in each neighbourhood of each point $p \in M$ such that for $i, j = 1, \dots, N$, $[X_i, X_j] = \sum_{k=1}^n c_{ijk} X_k$, where c_{ijk} are C^∞ functions. So the Lie bracket of two distribution vector fields lies within the distribution. A *foliation* of space of dimension k is a collection of disjoint, connected immersed k -dim submanifolds of M , such that the leaves of the foliation is all of M . For example \mathbb{R}^n is foliated by copies of \mathbb{R}^k , and $x^2 + y^2 + z^2 = r^2$, where r varies, is a 1-parameter family of spherical surfaces that foliate \mathbb{R}^3 . Finally, if Δ is a C^∞ distribution on M , N is connected C^∞ manifold and $F : N \rightarrow M$ is a bijective immersion such that for each $q \in N$ where we have $F_*(T_q(N)) \subset \Delta_{F(q)}$. The immersed submanifold is an *integral manifold* of Δ .

The following theorem on equivalence is Frobenius' theorem (see [178, pg. 441]):

Theorem A.2.9 (Frobenius). *Let M be a manifold of dimension $n+k$ and $\Delta \subset TM$ a distribution. Then the following are equivalent: (i) Δ is integrable, (ii) Δ is involutive and (iii) For every point of M there exists an open set U and $\omega_1, \dots, \omega_k \in \Omega^1(U)$ generating $I(E)$ such that both*

$$d\omega_i = \sum_{j=1}^k \omega_{ij} \wedge \omega_j \quad \text{for some } \omega_{ij} \in \Omega^1(U) \quad i = 1, \dots, k. \quad \text{and} \quad (\text{A.31})$$

$$d\omega_i \wedge \omega_1 \wedge \dots \wedge \omega_k = 0 \quad i = 1, \dots, k \quad (\text{A.32})$$

We will require the codimension 1 case, that is if we have a single vector field n , then when is this normal to a family of surfaces? An application of Frobenius' theorem shows that the leaves of a foliation form an integrable family of surfaces if and only if

$$w \wedge dw = 0 \quad (\text{A.33})$$

where w is the 1-form associated with n , $w = n_i dx^i$.

Appendix B

High order FEM code in EIDORS

B.1 Forward problem

The author has implemented open source high order FEM code to compute the forward problem, and Fréchet derivative (see section B.2), in 2D and 3D into the EIDORS software suite written in MATLAB [62]. The source files to compute the forward solver are available in the directory `/eidors3d/eidors/solvers/forward/` of EIDORS. The high order FEM solution can be computed on any feasible geometry, conductivity or stimulation/measurement protocol in EIDORS through the function `fwd_solve_higher_order.m`.

The function `system_mat_higher_order.m` computes the complete electrode model matrices (or point electrode model matrices) as described in this section. The standard forward problem solver in EIDORS uses piecewise linear approximation to the potential and it is necessary to add additional nodes to the elements and boundaries to compute the higher order solution. The function `fem_1st_to_higher_order.m` performs this task and is automatically called in `system_mat_higher_order.m`, using the relevant shape functions (and their derivatives) and quadrature points (see appendices B.3 and B.4 for more details on this).

The following fields are attached to an EIDORS forward model structure through the assignment `fmdl.system_mat=@system_mat_higher_order` and `fmdl.solve=@fwd_solve_higher_order`. The specific approximation is attached to the forward model structure by adding a field `fmdl.approx_type=type`, where `type` can be `'tri3'`, `'tri6'` and `'tri10'`, for linear, quadratic and cubic finite elements

in two dimensions, or 'tet4' and 'tet10' for linear and quadratic approximation in three dimensions. A simple test code that computes the solution is given below.

```

1 %Geometry
2 imdl = mk_common_model('c2C0',16);
3 fmdl = imdl.fwd_model;
4
5 %Stimulation/Measurement
6 stim=mk_stim_patterns(16,1,[0 1],[0 1]);
7 fmdl.stimulation=stim;
8
9 %High-order EIDORS solver
10 fmdl.solve = @fwd_solve_higher_order;
11 fmdl.system_mat = @system_mat_higher_order;
12 fmdl.approx_type = 'tri10'; %cubic
13
14 %Unit conductivity image and forward solve
15 img = mk_image(fmdl,1);
16 v = fwd_solve(img);

```

B.2 Inverse problem

The author has implemented open source high order FEM code to compute the Fréchet derivative (3.9), in 2D and 3D into the EIDORS for any feasible geometry, conductivity or stimulation/measurement protocol. The source files to compute the derivative is available in the directory `/eidors3d/eidors/solvers/forward/` of EIDORS.

The function `jacobian_adjoint_higher_order.m` computes the Jacobian on a given image structure in EIDORS. The field must be attached to the forward model of the given image through `fmdl.jacobian=@jacobian_adjoint_higher_order.m`, along with the `fmdl.system_mat`, `fmdl.solve` and `fmdl.approx_type` as described in appendix B.1. A simple test code that computes a Jacobian is given below.

```

1 %Geometry
2 imdl = mk_common_model('c2C0',16);
3 fmdl = imdl.fwd_model;
4
5 %Stimulation/Measurement

```

```

6 stim=mk_stim_patterns(16,1,[0 1],[0 1]);
7 fmdl.stimulation=stim;
8
9 %High-order EIDORS solver
10 fmdl.solve = @fwd_solve_higher_order;
11 fmdl.system_mat = @system_mat_higher_order;
12 fmdl.approx_type = 'tri10'; %cubic
13 fmdl.jacobian=@jacobian_adjoint_higher_order;
14
15 %Unit conductivity image and forward solve
16 img = mk_image(fmdl,1);
17 J=calc_jacobian(img);

```

The code is fully compatible with any EIDORS inverse solvers. For example the following test code computes a Tikhonov regularised linearised inverse problem solution for a ball of conductivity 2 inside a medium of conductivity 1 using piecewise cubic approximation to the potential.

```

1 %Stim patterns
2 stim=mk_stim_patterns(16,1,[0 1],[0 1]);
3
4 %True model
5 imdl_i = mk_common_model('d2C0',16);
6 fmdl_i = imdl.fwd_model;
7 ctr = interp_mesh(fmdl_i); ctr=(ctr(:,1)-0.2).^2 + (ctr(:,2)-0.2).^2;
8 fmdl_i.approx_type='tri10';
9 fmdl_i.stimulation=stim;
10 fmdl_i.solve = @fwd_solve_higher_order;
11 fmdl_i.system_mat = @system_mat_higher_order;
12 img_i= mk_image(fmdl_i, 1 + 1*(ctr<0.2^2));
13 figure; show_fem(img_i);
14 v_i=fwd_solve(img_i);
15
16 %Reconstruction model
17 imdl_h = mk_common_model('c2C0',16);
18 fmdl_h = imdl.fwd_model;
19 fmdl_h.approx_type='tri10';
20 fmdl_h.solve = @fwd_solve_higher_order;
21 fmdl_h.system_mat = @system_mat_higher_order;

```

```

22 fmdl_h.jacobian=@jacobian_adjoint_higher_order;
23 fmdl_h.stimulation=stim;
24
25 %Create image and solve
26 img_h=mk_image(fmdl_h,1);
27 figure; show_fem(img_h);
28 v_h=fwd_solve(img_h);
29
30 %Inverse Model
31 inv2d= eidors_obj('inv_model', 'EIT inverse');
32 inv2d.reconst_type= 'difference';
33 inv2d.jacobian_bkgnd.value= 1;
34 inv2d.fwd_model=img_h.fwd_model;
35 inv2d.solve=      @inv_solve_diff_GN_one_step;
36 inv2d.hyperparameter.value = 1e-4;
37 inv2d.RtR_prior=  @prior_tikhonov;
38
39 %Inverse solve
40 imgr= inv_solve( inv2d, v_h, v_i);
41 figure; show_fem(imgr)

```

B.3 Shape functions

The element shape functions, and the derivative of shape functions, are available in EIDORS in the directory `/eidors3d/eidors/solvers/forward/` in the functions `element_shape_function.m` and `d_element_shape_function.m` respectively. The shape functions are automatically called when computing the system matrix as described in section B.1. For clarity we list the element and boundary shape functions for a 3D quadratic finite element only.

3D Element shape functions

The element shape functions for quadratic approximation in 3D are listed below and the location of each node (ϵ, η, γ) in the reference element can be seen in figure B.1.

$$\begin{aligned} \psi_1(\epsilon, \eta, \gamma) &= 0.5(1 - \epsilon - \eta - \gamma)(1 - 2\epsilon - 2\eta - 2\gamma) & \psi_2(\epsilon, \eta, \gamma) &= \epsilon(2\epsilon - 1) \\ \psi_3(\epsilon, \eta, \gamma) &= \eta(2\eta - 1) & \psi_4(\epsilon, \eta, \gamma) &= \gamma(2\gamma - 1) \\ \psi_5(\epsilon, \eta, \gamma) &= 4\epsilon(1 - \epsilon - \eta - \gamma) & \psi_6(\epsilon, \eta, \gamma) &= 4\eta(1 - \epsilon - \eta - \gamma) \\ \psi_7(\epsilon, \eta, \gamma) &= 4\gamma(1 - \epsilon - \eta - \gamma) & \psi_8(\epsilon, \eta, \gamma) &= 4\epsilon\eta \\ \psi_9(\epsilon, \eta, \gamma) &= 4\eta\gamma & \psi_{10}(\epsilon, \eta, \gamma) &= 4\epsilon\gamma \end{aligned}$$

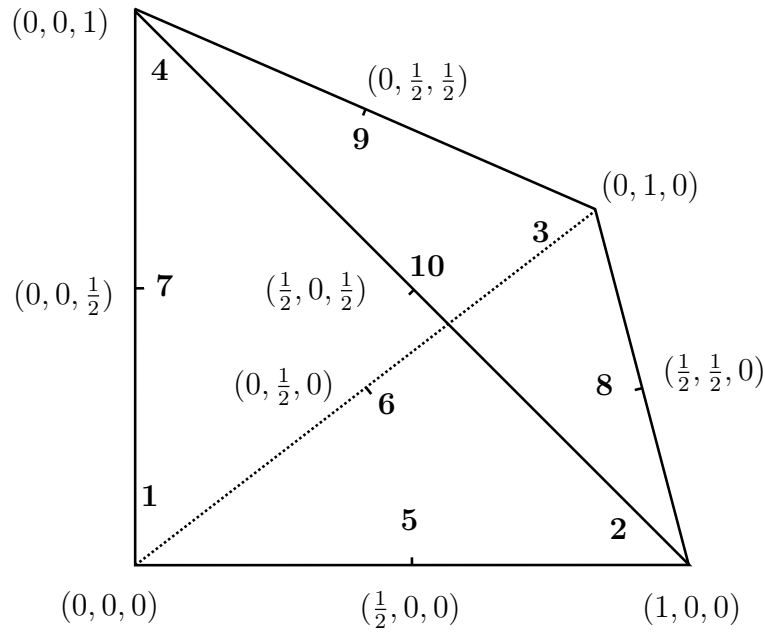


Figure B.1: The position of nodes locally within 3D reference element for a quadratic approximation.

3D Boundary shape functions

The boundary shape functions for quadratic approximation in 3D, $\psi_i^Q(\epsilon, \eta)$ are listed below. The location of each node (ϵ, η) in the reference can be seen in figure B.2.

$$\begin{aligned} \psi_1(\epsilon, \eta) &= (1 - \epsilon - \eta)(1 - 2\epsilon - 2\eta) & \psi_2(\epsilon, \eta) &= \epsilon(2\epsilon - 1) \\ \psi_3(\epsilon, \eta) &= \eta(2\eta - 1) & \psi_4(\epsilon, \eta) &= 4\epsilon(1 - \epsilon - \eta) \\ \psi_5(\epsilon, \eta) &= 4\epsilon\eta & \psi_6(\epsilon, \eta) &= 4\eta(1 - \epsilon - \eta) \end{aligned}$$

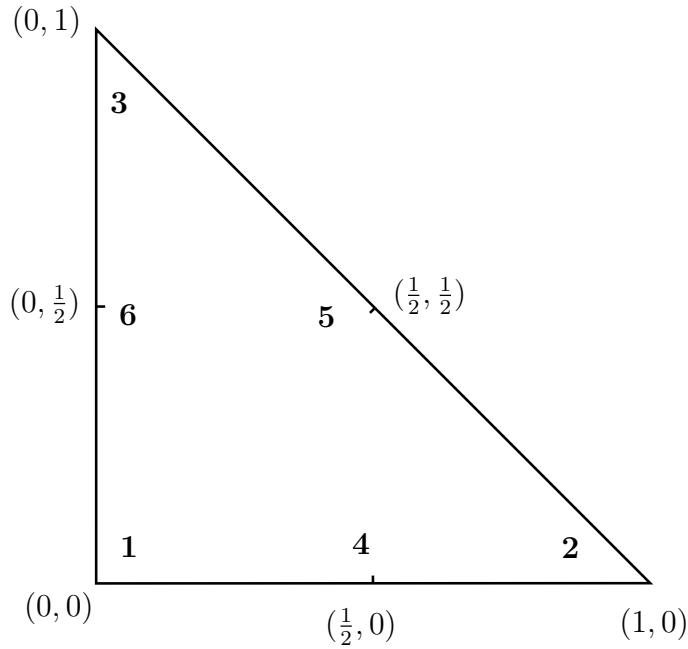


Figure B.2: Position of nodes on 3D reference boundary for quadratic approximation.

B.4 Quadrature rules

Standard numerical quadrature rules are listed below to evaluate the various integrals appearing in the system matrices when solving the forward problem using a FEM from [60]. The quadrature points are available in `/eidors3d/eidors/solvers/forward/` in the function `gauss_points.m`. The quadrature points are automatically called when computing the system matrices as described in section B.1.

1D rules

We require quadrature rules for a function $g : \mathbb{R} \rightarrow \mathbb{R}$ over the interval $[-1, 1]$,

$$\int_{-1}^1 g(x) \, dx = \sum_{l=1}^{l_q} \omega_l g(\epsilon_l) \quad (\text{B.1})$$

We list quadrature rules for boundary terms for linear, quadratic and cubic approximation. Integrals of degree 2, 4 and 6 polynomials are sufficient.

2D rules

We require quadrature rules for a function $g : \mathbb{R}^2 \rightarrow \mathbb{R}$ defined over the unit triangle,

$$\int_0^1 \int_0^{1-y} g(x, y) \, dx \, dy = \sum_{l=1}^{l_q} \omega_l g(\epsilon_l, \eta_l) \quad (\text{B.2})$$

| k_q | l_q | ϵ_l | ω_l |
|-------|-------|--|--|
| 3 | 2 | $\pm \frac{\sqrt{3}}{3}$ | 1 |
| 5 | 3 | $\pm \frac{\sqrt{3}}{3}$ 0 | $\frac{5}{9}$ $\frac{8}{9}$ |
| 7 | 4 | $\pm \sqrt{\frac{1}{35}(15 - 2\sqrt{30})}$ $\pm \sqrt{\frac{1}{35}(15 + 2\sqrt{30})}$ | $\frac{1}{36}(18 + \sqrt{30})$ $\frac{1}{36}(18 - \sqrt{30})$ |

Table B.1: Nodes and weights for quadrature over the interval $[-1, 1]$ in 1D

We list quadrature rules for element terms for linear, quadratic and cubic approximation. Integrals of degree 2, 4 and 6 polynomials are sufficient to perform this task. The rules below are also sufficient to evaluate the surface integrals over the boundary in 3D for linear and quadratic approximation, because these require rules that evaluate integrals of degree 2 and 4 polynomials exactly. The table below differs to the 1D rules for two reasons. Firstly, the Gauss points are now in barycentric or *area* coordinates $\mathbf{b} = (b_1, b_2, b_3)$. The vertices of the unit triangle are at the coordinates $\mathbf{v}_1 = (0, 0)$, $\mathbf{v}_2 = (1, 0)$ and $\mathbf{v}_3 = (0, 1)$, and for a given Gauss point, \mathbf{b}^G , in barycentric coordinates, the Gauss point in Cartesian coordinates, $\mathbf{x}^G = (\epsilon, \eta)$, can be recovered through the formula

$$\mathbf{x}^G = \sum_{i=1}^3 b_i^G \mathbf{v}_i.$$

Secondly, there is a column ‘p’ which is the number of permutations that must be performed on the barycentric coordinates to obtain all the quadrature points.

| k_q | l_q | (b_1, b_2, b_3) | p | ω_l |
|-------|-------|--|---|--|
| 1 | 1 | $(\frac{1}{3}, \frac{1}{3}, \frac{1}{3})$ | 1 | $\frac{1}{2}$ |
| 2 | 3 | $(\frac{1}{6}, \frac{1}{6}, \frac{2}{3})$ | 3 | $\frac{1}{6}$ |
| 4 | 6 | $(a_i, a_i, 1 - 2a_i)$ for $i = 1 : 2$ $a_1 = 0.4459484909160$ $a_2 = 0.0915762135098$ | 3 | ω_i for $i = 1 : 2$ $0.5 \times 0.2233815896780$ $0.5 \times 0.1099517436553$ |

Table B.2: Nodes and weights for quadrature over the unit triangle in 2D

3D rules

We require quadrature rules for a function $g : \mathbb{R}^3 \rightarrow \mathbb{R}$ defined over the unit tetrahedron, that is

$$\int_0^1 \int_0^{1-z} \int_0^{1-y-z} g \, dx \, dy \, dz = \sum_{l=1}^{l_q} \omega_l g(\epsilon_l, \eta_l, \gamma_l) \tag{B.3}$$

We list the quadrature rules required for element terms for linear and quadratic approximation. Integrals of degree 0 and 2 polynomials are sufficient to perform this task. As with the 2D rules, the Gauss points are in barycentric or *volume* coordinates $\mathbf{b} = (b_1, b_2, b_3, b_4)$. The vertices of the unit triangle are at the coordinates $\mathbf{v}_1 = (0, 0, 0)$, $\mathbf{v}_2 = (1, 0, 0)$, $\mathbf{v}_3 = (0, 1, 0)$ and $\mathbf{v}_4 = (0, 0, 1)$, and for a given Gauss point, \mathbf{b}^G , in barycentric coordinates, the Gauss point in Cartesian coordinates, $\mathbf{x}^G = (\epsilon, \eta, \gamma)$, can be recovered through the formula

$$\mathbf{x}^G = \sum_{i=1}^4 b_i^G \mathbf{v}_i.$$

Again, the column ‘p’ is the number of permutations that must be performed on the barycentric coordinates to obtain all the quadrature points.

| k_q | l_q | (b_1, b_2, b_3, b_4) | p | ω_l |
|-------|-------|--|---|----------------|
| 1 | 1 | $(\frac{1}{4}, \frac{1}{4}, \frac{1}{4}, \frac{1}{4})$ | 1 | $\frac{1}{6}$ |
| 2 | 4 | $(a, a, a, 1 - 3a)$ $a = \frac{5 - \sqrt{5}}{20}$ | 4 | $\frac{1}{24}$ |

Table B.3: Nodes and weights for quadrature over the unit tetrahedron in 3D

Appendix C

Shape derivative code

C.1 Driver code

The following code performs simultaneous retrieval of electrode positions and conductivity for the spherical model as presented in chapter 4.4. This driver code requires the additional codes in sections C.2, C.3 and C.4 of this appendix in the same working directory. This also will require svn version 4430M of EIDORS, available to download at <http://eidors3d.sourceforge.net/>.

```
1 %Choose shape, noise and movement and hyperparams
2 noise=50; shape='sphere'; move_fac=0.1;
3 hpmt_params_diff=0.01; hp_params=[10^-5]; hpmt_params=[1250];
4 shape_iteration=8; max_its=5;
5
6 %Parameter for conductivity, electrode shapes
7 cond_inc=3; elec_ref=0.05; dom_ref=0.5; dom_h=1;
8 n_elec_m=14; n_elec_mt=9; h_mt=0.5; elec_t=[0.05,0,elec_ref];
9 n_elec_t=n_elec_m+2*n_elec_mt+2; n_elec=n_elec_t;
10
11 %Stimulation patterns
12 stim=mk_stim_patterns(n_elec_t,1,[0 1],[0 1]);
13
14 %% CREATE COARSE, FINE AND ACTUAL MODEL
15 elec_pos=zeros(n_elec_m+2*n_elec_mt+2,6); elec_pos_cart=elec_pos;
16 for i=1
17     elec_pos(i,1)=0.0;
18     elec_pos(i,2)=0.0;
```

```

19     elec_pos(i,3)=1.0;
20     elec_pos(i,4:6)=elec_pos(i,1:3);
21 end
22 for i=1+1:n_elec_mt+1
23     psi=acos(h_mt);
24     elec_pos(i,1)=cos((i-2)*2*pi/n_elec_mt)*sin(psi);
25     elec_pos(i,2)=sin((i-2)*2*pi/n_elec_mt)*sin(psi);
26     elec_pos(i,3)=h_mt;
27     elec_pos(i,4:6)=elec_pos(i,1:3);
28 end
29 for i=1+n_elec_mt+1:1+n_elec_mt+n_elec_m
30     elec_pos(i,1)=cos((i-2-n_elec_mt)*2*pi/n_elec_m);
31     elec_pos(i,2)=sin((i-2-n_elec_mt)*2*pi/n_elec_m);
32     elec_pos(i,3)=0;
33     elec_pos(i,4:6)=elec_pos(i,1:3);
34 end
35 for i=1+n_elec_mt+n_elec_m+1:1+n_elec_mt+n_elec_m+n_elec_mt
36     psi=acos(-h_mt);
37     elec_pos(i,1)=cos((i-2-n_elec_mt-n_elec_m)*2*pi/n_elec_mt)...
38                     *sin(psi);
39     elec_pos(i,2)=sin((i-2-n_elec_mt-n_elec_m)*2*pi/n_elec_mt)...
40                     *sin(psi);
41     elec_pos(i,3)=-h_mt;
42     elec_pos(i,4:6)=elec_pos(i,1:3);
43 end
44 for i=2+n_elec_m+2*n_elec_mt
45     elec_pos(i,1)=0;
46     elec_pos(i,2)=0;
47     elec_pos(i,3)=-1.0;
48     elec_pos(i,4:6)=elec_pos(i,1:3);
49 end
50
51 %Homogeneous sphere - 1 top/bottom, 8 above/below, 16 middle
52 shape_str = ...
53 ['solid top      = ellipsoid(0,0,0; 0,0,1; 1,0,0; 0,1,0); \n' ...
54  'solid mainobj = top -maxh=0.8;\n'];
55 elec_shape=elec_t;
56 elec_obj = 'top';
57 mdl_h = ng_mk_gen_models(shape_str, elec_pos, elec_shape, elec_obj);

```

```

58 figure; show_fem(mdl_h);
59 nodes=mdl_h.nodes;
60
61 %Homogeneous sphere with no electrodes
62 shape_str_c = ...
63 ['solid top      = ellipsoid(0,0,0; 0,0,1.05; 1.05,0,0; 0,1.05,0); \n'
   ...
64      'solid mainobj = top -maxh=0.25;\n'];
65 mdl_c = ng_mk_gen_models(shape_str_c, [], [] , {} );
66 figure; show_fem(mdl_c);
67 nodes_c=mdl_c.nodes;
68
69 %Move the electrode positions and renormalize
70 elec_pos_i=elec_pos;
71 for i=1:length(elec_pos_i(:,1))
72     for j=1:3
73         elec_pos_i(i,j)= elec_pos(i,j) + move_fac*(-1+2*rand(1,1));
74     end
75     elec_pos_i(i,1:3)=elec_pos_i(i,1:3)/norm(elec_pos_i(i,1:3));
76     elec_pos_i(i,4:6)=elec_pos_i(i,1:3);
77 end
78 %Inhomogeneous sphere - 1 top/bottom, 8 above/below, 16 middle
79 shape_str_i = ...
80 ['solid top      = ellipsoid(0,0,0; 0,0,1; 1,0,0; 0,1,0); \n' ...
81      'solid ball   = sphere(0.0,0.3,0.3;0.3); tlo ball; \n' ...
82      'solid mainobj = top and not ball -maxh=0.8; \n'];
83 elec_shape_i=elec_t;
84 elec_obj_i = 'top';
85 mdl_i = ng_mk_gen_models(shape_str_i, elec_pos_i, ...
86                             elec_shape_i, elec_obj_i);
87                             nodes=mdl_i.nodes;
88
89 %Make inhomogeneous image
90 img_h=mk_image(mdl_h,1);
91 img_i=mk_image(mdl_i,1); img_i.elem_data(mdl_i.mat_idx{1})=cond_inc;
92 figure; show_fem(img_i);
93 mdl_h.stimulation= stim; img_h.fwd_model.stimulation=stim;
94 mdl_i.stimulation= stim; img_i.fwd_model.stimulation=stim;
95

```

```

95 %Inhomogeneous voltages
96 v_i=fwd_solve(img_i.fwd_model,img_i);
97 v_h=fwd_solve(img_h.fwd_model,img_h); v_hd = v_h.meas;
98 v_in=add_noise(noise,v_i); v_i=v_in; %Add noise
99
100 %% STEP 1 : ELECTRODES ONLY
101 for kk=1:shape_iteration
102 %Create the inverse model
103 inv_tik_2d=eidors_obj('inv_model','EIT inverse');
104 mdl_h.jacobian=@jacobian_adjoint;
105 img_h.fwd_model.jacobian=@jacobian_adjoint;
106 inv_tik_2d.fwd_model= mdl_h;
107 inv_tik_2d.reconst_type='absolute';
108 inv_tik_2d.jacobian_bkgnd.value=img_h.elem_data;
109 inv_tik_2d.RtR_prior=@prior_movement_tangential_only;
110 inv_tik_2d.solve=@inv_solve_diff_tangential;
111 inv_tik_2d.hyperparameter.value(1)=hpmt_params_diff;
112 inv_tik_2d.parameters.max_iterations=1;
113
114 %Add the fields for inversion
115 inv_tik_2d.shape=shape;
116 inv_tik_2d.img_fine=img_h;
117 inv_tik_2d.mdl_coarse=mdl_c;
118
119 %Differene solve on the inverse model (this has mdl_fine and c2f)
120 img_recon=inv_solve(inv_tik_2d,v_i);
121 %Calculate the new electrode positions from tangent data
122 elec_comp_h=calc_electrode_components(img_h.fwd_model);
123 elec_posH=[]; elec_pos_NEW=[];
124 for i=1:length(elec_comp_h)
125     elec_posH(i,:)=elec_comp_h{i}.com;
126
127     %We can then decompose this to update the direction
128     a_i_elec_ii = img_recon.movement_data(i)* ...
129         elec_comp_h{i}.tangent(:,1) + ...
130         img_recon.movement_data(i+n_elec)* ...
131         elec_comp_h{i}.tangent(:,2);
132
133     %Get the old coords of node and update the end point

```

```

134     elec_pos_NEW(i,1:3) = elec_posH(i,1:3) + a_i_elec_ii';
135     elec_pos_NEW(i,1:3) = ...
136         elec_pos_NEW(i,1:3)/norm(elec_pos_NEW(i,1:3));
137 end
138 %Put the normals back in for sphere or cylinder
139 elec_pos_NEW(:,4:6)=elec_pos_NEW(:,1:3);
140 mdl_h = ng_mk_gen_models(shape_str, elec_pos_NEW, ...
141                         elec_shape, elec_obj);
142
143 %Create new forward model
144 img_h=mk_image(mdl_h,1);
145 inv_tik_2d.fwd_model=mdl_h;
146 mdl_h.stimulation= stim; img_h.fwd_model.stimulation=stim;
147 end
148
149 %Make new c2f map and create new images
150 cfmap = mk_coarse_fine_mapping( mdl_h, mdl_c);
151 cfmap2 = cfmap./(sum(cfmap,2) * ones(1,size(cfmap,2)));
152 img_h=mk_image(mdl_h,1);img_c=mk_image(mdl_c,1);
153
154 %% STEP 2 : SIMULTANEOUS SOLVER
155
156 %Get the prior for the conductivity and positions
157 prior_c=img_c.elem_data; prior_e=zeros(2*n_elec,1);
158 prior_ce=[prior_c;prior_e];
159
160 %Elements on coarse model
161 n_elemsc=length(mdl_c elems(:,1));
162 n_elems=length(mdl_h elems(:,1));
163 n_elec=length(mdl_h.electrode);
164 inv_tik_2d=eidors_obj('inv_model','EIT inverse');
165 mdl_h.jacobian=@jacobian_adjoint;
166 img_h.fwd_model.jacobian=@jacobian_adjoint;
167 mdl_h.n_elemsc=n_elemsc; %Assign coarse elements
168 inv_tik_2d.fwd_model= mdl_h;
169 inv_tik_2d.fwd_model.coarse2fine = cfmap;
170 inv_tik_2d.reconst_type='absolute';
171 inv_tik_2d.jacobian_bkgnd.value=img_h.elem_data;
172 inv_tik_2d.RtR_prior=@prior_movement_tangential;

```

```

173 inv_tik_2d.prior_movement.RegC.func=@prior_laplace;
174 inv_tik_2d.prior_movement.RegM.func=@tikhonov_movement_image_prior;
175 inv_tik_2d.solve=@inv_solve_abs_GN_diff_tangential;
176 inv_tik_2d.prior_movement.parameters=hpmt_params;
177 inv_tik_2d.hyperparameter.value=hp_params;
178 inv_tik_2d.parameters.max_iterations=max_its;
179
180 %Add some new fields to the inversion
181 inv_tik_2d.prior_c = prior_c;
182 inv_tik_2d.prior_e = prior_e;
183 inv_tik_2d.c2f2 = cfmap2; %Another coarse2 fine for the
184 img_h.fwd_model.n_elemsc=n_elemsc;
185 inv_tik_2d.img_fine=img_h;
186 inv_tik_2d.mdl_coarse=mdl_c;
187
188 %Differene solve on the inverse model (this has mdl_fine and c2f)
189 img_recon=inv_solve(inv_tik_2d,v_i);
190 img_reconc=img_c;
191 img_reconc.elem_data=img_recon.elem_data(1:n_elemsc);
192 figure; show_fem(img_reconc)

```

C.2 Geometry and Jacobian calculation

Electrode geometry

The following function `calc_electrode_components.m` computes the COM, normal and tangents of electrodes for a given EIDORS forward model structure.

```

1 function elec_comp = calc_electrode_components(fwd_model)
2 %Calculates the following storing in elec_comp{i}.NAME
3 %1. COM - Centre of mass of electrode
4 %2. NORMAL - The (average by area) normal vector to the electrode
5 %3. TANGENT - The (average by area) tangent space of the electrode
6           %2D - Single vector - Defined so these are clockwise basis
7           %3D - Two vectors - Defined for some basis.
8
9 %Get the boundaries so that they are in a consistent numbering
10 fwd_model=linear_bound_reorder(fwd_model,-1);

```

```

11
12 %Get all the nodes, elems, elems and boundary info
13 elecstruc = fwd_model.electrode; n_elec = length(elecstruc);
14 boundstruc = fwd_model.boundary;
15 nodestruc = fwd_model.nodes; nodedim = length(nodestruc(1,:));
16
17 %For each electrode
18 for i=1:n_elec
19     %Calculate the centre of mass of the electrode and store
20     elec_nodes = elecstruc(i).nodes;
21     pos = mean(nodestruc(elec_nodes,:),1);
22     elec_comp{i}.com = pos;
23
24     %Find which boundary electrode has
25     [bdy_idx, bdy_area]=find_electrode_bdy...
26         (boundstruc(:,1:nodedim), nodestruc, elecstruc(i).nodes);
27     boundidx_i=bdy_idx;
28     n_bound_i = length(boundidx_i);
29
30     %Calculate the (area averaged) normal to boundary and tangent
31     norm_i=zeros(nodedim,1);
32
33     %Loop on elec bdys - area weighted normal/tangent
34     for j=1:n_bound_i
35         %The coordinates of this boundarys nodes
36         thisb=nodestruc(boundstruc(boundidx_i(j),:),:);
37
38         %Find its outer unit normal and its area
39         if(nodedim==2)
40             %Calculate area and normalised clockwise tangent
41             area_j = norm( thisb(1,:)-thisb(2,:) );
42             tang_j = (thisb(2,:)-thisb(1,:))'/area_j;
43             norm_j = [0,-1;1,0]*tang_j; %90 acw rotation
44         elseif(nodedim==3)
45             %Calculate the normalised outer normal to surface
46             norm_j = cross(thisb(3,:)-thisb(1,:), ...
47                 thisb(2,:)-thisb(3,:))';
48             area_j = norm(norm_j);
49         end

```

```

50     %Add on to normal weighted by its area
51     norm_i = norm_i + norm_j*area_j;
52 end
53 %Normalise the normal
54 norm_i = norm_i/norm(norm_i);
55
56 %Calculate the tangents to normal
57 if(nodedim==2)
58     %Average tangent vector is 90 rotation clockwise of normal
59     tang_i = [0,1;-1,0]*norm_i;
60 elseif(nodedim==3)
61     %Case by case ortohognal basis on electrode
62     if(abs(norm_i(1))>0.2)
63         tang_i1 = [-norm_i(2)/norm_i(1),1,0];
64         tang_i1=tang_i1/norm(tang_i1);
65         tang_i2=cross(tang_i1,norm_i);
66         tang_i2=tang_i2/norm(tang_i2);
67     elseif(abs(norm_i(2))>0.2)
68         tang_i1 = [-norm_i(2)/norm_i(1),1,0];
69         tang_i1=tang_i1/norm(tang_i1);
70         tang_i2=cross(tang_i1,norm_i);
71         tang_i2=tang_i2/norm(tang_i2);
72     elseif(abs(norm_i(3))>0.2)
73         tang_i1 = [-norm_i(2)/norm_i(1),1,0];
74         tang_i1=tang_i1/norm(tang_i1);
75         tang_i2=cross(tang_i1,norm_i);
76         tang_i2=tang_i2/norm(tang_i2);
77     else
78         error('Can not compute normals correctly')
79     end
80     %Now put this tangents as two columns of a matrix
81     tang_i=[tang_i1;tang_i2]';
82 end
83
84 %Store the tangent(s) and normal in the structure
85 elec_comp{i}.tangent = tang_i; %Tangent vectors by column
86 elec_comp{i}.normal = norm_i; %Normal vector by column
87 end
88 end

```

```

89
90 function [mdl]=linear_bound_reorder(mdl,ccw)
91     %Find boundary, elems, nodes, elecs
92     boundstruc=mdl.boundary; elemstruc=mdl.elems;
93     nodestruc=mdl.nodes; elecstruc=mdl.electrode;
94     %Find no. elecs and node dimension
95     nelecs=size(elecstruc,2); nodedim=size(nodestruc,2);
96
97     %Reorder boundaries belonging to electrodes
98     for ke=1:nelecs
99         %Boundary numbers/areas, output rows
100        bdy_idx=find_electrode_bdy(boundstruc(:,1:nodedim), ...
101            nodestruc,elecstruc(ke).nodes);
102
103        for ii=1:length(bdy_idx);
104            bb=bdy_idx(ii);
105
106            %Vector of vertes numbers of this boundary
107            bbnodes=boundstruc(bb,:);
108            if(nodedim==2) %2D problem
109                %Row(s) of elems which each bdy vertex belongs
110                [rownode1,~]=find(elemstruc==bbnodes(1));
111                [rownode2,~]=find(elemstruc==bbnodes(2));
112
113                %Intersectionr rownode1/rownode2
114                boundiielem=intersect(rownode1,rownode2);
115            elseif(nodedim==3) %3D problem
116                %Row(s) of elems which each bdy vertex belongs
117                [rownode1,~]=find(elemstruc==bbnodes(1));
118                [rownode2,~]=find(elemstruc==bbnodes(2));
119                [rownode3,~]=find(elemstruc==bbnodes(3));
120
121                %Intersection rownode1/rownode2
122                rownode1node2=intersect(rownode1,rownode2);
123                %Intersection rownode3 is unique element
124                boundiielem=intersect(rownode3,rownode1node2);
125            end
126            %Store this unique number in a vector
127            beleind=boundiielem(1);

```

```

128
129     %Coordinate of nodes of boundaries element
130     belenodes=elemstruc(beleind,:);
131
132     %Unique internal nodes
133     intnode=setdiff(belenodes,bbnodes);
134     elemboundnode=[intnode,bbnodes];
135
136     %List by row coordinates of the element
137     nodepos=nodestruc(elemboundnode,:);
138     nvertices=size(belenodes,2);
139
140     %Calculate area(2D)/volume(3D) from vertices
141     area=det([ones(nvertices,1),nodepos]);
142     areassign=sign(area);
143
144     %If positive area, swap the last two nodes
145     if(areassign == -ccw) %Swap last two entries of enodes
146         temp=elemboundnode(end-1);
147         elemboundnode(end-1)=elemboundnode(end);
148         elemboundnode(end) = temp;
149     end
150
151     %Put the node numbers back into mdl.bound(bb)
152     boundstruc(bb,:)=elemboundnode(2:end);
153     end
154 end
155 %Reassign the boundary
156 mdl.boundary=boundstruc;
157 end

```

Electrode position Jacobian

The following code computes the (tangential) movement Jacobian, by computing the movement Jacobian in EIDORS `jacobian_movement.m`, and then projecting onto normal and tangential components through the function `calc_electrode_components.m`.

```

1 function [J_new] = jac_move_eidors_elec_tang_only(fwd_model,img)

```

```

2 %Movement Jacobian projected onto normal and tangential components
3
4 %Calculate movement Jacobian through eiders
5 J=jacobian_movement(img);
6 %Get all the nodes, elems, elems and boundary info
7 elecstruc = img.fwd_model.electrode; n_elec = length(elecstruc);
8 elemstruc = img.fwd_model.elems;
9 nodestruc = img.fwd_model.nodes; nodedim = length(nodestruc(1,:));
10
11 %Calculate the normal and tangential space of each electrode
12 elec_comp = calc_electrode_components(img.fwd_model);
13
14 %Ok we have split into tangential and normal components
15 J_move = J(:,end-3*n_elec+1:end); %c2f
16
17 for i=1:n_elec
18     if(nodedim==2)
19         %Two columns for this electrode i.e. in x and y
20         xd = J_move(:,i);
21         yd = J_move(:,i+n_elec);
22         xyd=[xd,yd];
23         td = xyd*elec_comp{i}.tangent; %Tangent
24         J_move_comp(:,i)=td;
25     elseif(nodedim==3)
26         %Two columns for this electrode i.e. in x and y
27         xd = J_move(:,i); yd = J_move(:,i+n_elec);
28         zd = J_move(:,i+2*n_elec);
29         xyzd=[xd,yd,zd];
30         t1d = xyzd*elec_comp{i}.tangent(:,1); %T1
31         t2d = xyzd*elec_comp{i}.tangent(:,2); %T2
32         J_move_comp(:,i)=t1d;
33         J_move_comp(:,i+n_elec)=t2d;
34     end
35 end
36 J_new=J_move_comp; %Only keep movement
37 end

```

C.3 Electrode position inverse solver

Electrode inverse solver

The following function `inv_solve_diff_tangential.m` computes a single Gauss-Newton iteration, with a linearised movement linesearch, to estimate the electrode positions from measured voltages.

```

1 function img= inv_solve_diff_tangential( inv_model, data0);
2 %INV_SOLVE_DIFF_TANGENTIAL Absolute solver using Gauss Newton
3 % img= inv_solve_abs_GN( inv_model, data0)
4 % img      => output image (or vector of images)
5 % inv_model => inverse model struct
6 % data0    => EIT data
7
8 %Get the options
9 opt = parse_options(inv_model);
10 img = initial_estimate( inv_model, data0 ); %bckgrnd c2f
11
12 %Number electrodes, hyperparameter and Tikhonov reg
13 n_elec=length(inv_model.img_fine.fwd_model.electrode);
14 hp = calc_hyperparameter( inv_model );
15 RtR = eye(n_elec*2); hp2RtR= hp^2*RtR;
16
17 %Prior conductivity and tangential change
18 prior_e(1:2*n_elec,1)=0; cur_e=prior_e; cur_move=cur_e;
19
20 %Get fine image and calc electrode components
21 img_h=inv_model.img_fine;
22 elec_comp_h=calc_electrode_components(img_h.fwd_model);
23 for jj=1:length(elec_comp_h)
24     elec_posHS(jj,:)=elec_comp_h{jj}.com;
25 end
26 elec_posH = elec_posHS;
27
28 %Compute the dat and regularisaiton residuals
29 vsim=fwd_solve(img_h);
30 data_res=zeros(opt.max_iter+1,1);
31 data_res(1) = 0.5*(vsim.meas-data0)'*(vsim.meas-data0);

```

```

32 regu_res=zeros(opt.max_iter+1,1); regu_res(1) = 0;
33
34 %Calculate the movement Jacobian outside loop
35 J=jac_move_eidors_elec_tang_only(inv_model.fwd_model,img_h);
36
37 %Loop over iterations
38 for i = 1:opt.max_iter
39     %Simulate measured data on FINE image and calc diff data
40     vsim = fwd_solve( img_h );
41     vsim.meas=vsim.meas+J*cur_move;
42     dv = calc_difference_data( vsim , data0, img.fwd_model);
43
44     %Compute the search direction -inv(H)*J'
45     RDx = hp2RtR*(prior_e - cur_e);
46     dx = (J'*J + hp2RtR)\(J'*dv + RDx);
47
48     %Perform a linesearch on this using polynomial search
49     opt.line_optimize.hp2RtR = hp2RtR;
50     cur_move = feval(opt.line_optimize_func, dx, data0, img_h, ...
51         img, J,prior_e,cur_move,opt.line_optimize);
52
53     %Calculate the electrode components
54     for jj=1:length(elec_comp_h)
55         %We can then decompose this to update the direction
56         a_i_elec_ii = cur_move(jj)*elec_comp_h{jj}.tangent(:,1) + ...
57             cur_move(jj+n_elec)*elec_comp_h{jj}.tangent(:,2);
58         %Calculate the new coordinates
59         elec_pos_NEW(jj,1:3) = elec_posHS(jj,1:3) + a_i_elec_ii';
60     end
61     %Get the normals
62     elec_pos_NEW(:,4:6)=elec_pos_NEW(:,1:3);
63
64     %Compute the data residual
65     vsim=fwd_solve(img_h);
66     vsim.meas=vsim.meas+J*cur_move;
67
68     %The new residuals and message screen
69     data_res(i+1) = 0.5*(vsim.meas-data0)'*(vsim.meas-data0);
70     regu_res(i+1) = 0.5*(cur_e-prior_e)'*hp2RtR*(cur_e-prior_e);

```

```

71     eiders_msg('#%02d residual=%.3g', i, data_res(i+1)+regu_res(i+1),
72             1);
73
74     %Attach the movement
75     img.movement_data = cur_move; %this is on tangents
76
77     function val = GN_objective_function(data0, data, ...
78         cur_move, prior_e, img_h, img, opt)
79         dv = calc_difference_data(data, data0, img.fwd_model);
80         de = cur_move - prior_e;
81         val = 0.5*( dv'*dv + de' * opt.hp2RtR * de);
82
83     function img = initial_estimate( imdl, data )
84         img = calc_jacobian_bkgnd( imdl );
85         vs = fwd_solve(img);
86         pf = polyfit(data, vs.meas, 1);
87         img = physics_data_mapper(img);
88         if isfield(img.fwd_model, 'coarse2fine');
89             nc = size(img.fwd_model.coarse2fine, 2);
90             img.elem_data = mean(img.elem_data)*ones(nc, 1)*pf(1);
91         else
92             img.elem_data = img.elem_data*pf(1);
93         end
94         % remove elem_data
95         img = physics_data_mapper(img, 1);
96
97     function opt = parse_options(imdl)
98         try
99             opt = imdl.parameters;
100         end
101         opt.max_iter = 1;
102         try
103             opt.max_iter = imdl.parameters.max_iterations;
104         end
105         if ~isfield(opt, 'line_optimize_func')
106             opt.line_optimize_func = @line_optimize_diff_tangential;
107         end
108         if ~isfield(opt, 'line_optimize')

```

```

109     opt.line_optimize = [];
110 end
111 if ~isfield(opt, 'line_optimize') || ...
112     ~isfield(opt.line_optimize, 'objective_func')
113     % not sure this should be allowed to change
114     opt.line_optimize.objective_func = @GN_objective_function;
115 end
116 if ~isfield(opt, 'do_starting_estimate')
117     opt.do_starting_estimate = 1;
118 end

```

Electrode linesearch

The following function `line_optimize_diff_tangential.m` computes a linesearch, for a sufficiently small change in electrode positions.

```

1 function [cur_move] = line_optimize_diff_tangential(dx,...
2     data0, img_h,img, Jm,prior_e,cur_move, opt)
3 %% Bracket the local minimum - Get 3 points such that
4 %    0 < s1 < s2 < s3 with f(s2) \leq min{ f(s1),f(s3) }
5
6 %Step 1: Get step_length s.t. f(step_length) < f(0)
7 step_length=1;
8 vsim = fwd_solve(img_h);
9 vsim.meas=vsim.meas + Jm*cur_move; %Linearise movement
10
11 %calculate the misfit at 0
12 mlist(1) = feval(opt.objective_func,data0,vsim, ...
13     cur_move,prior_e,img_h,img,opt);
14
15 %Iterate through and find minimal point
16 for i=1:10 %while loop here
17     %Perturb image (s,v) |-> (s,v) +p*dx(1:n_elemsc)
18     vsim = fwd_solve(img_h);
19     vsim.meas=vsim.meas + Jm*cur_move*step_length; %Linear
20
21     %calculate the misfit
22     mlist(i+1) = feval(opt.objective_func,data0,vsim, ...
23         cur_move*step_length,prior_e,img_h,img,opt);

```

```

24     if(mlist(i+1) < mlist(1))
25         break; %Bracket now [i-1,i,i+1]
26     else
27         %Decrease step length and try again
28         step_length=step_length/2;
29     end
30 end
31
32 %% Get the third point
33 lambda(1)=0; lambda(2)=step_length;
34
35 %Data at current iterate
36 cur_movek=cur_move; vsim = fwd_solve(img_h);
37 vsim.meas=vsim.meas + Jm*cur_move; %Linear
38
39 %calculate the misfit at 0
40 mlist(1) = feval(opt.objective_func,data0,vsim,...
41     cur_movek,prior_e,img_h,img,opt);
42
43 %Data at perturb image (s,v) |-> (s,v) +p*dx(1:n_elemsc)
44 cur_movei = cur_movek + step_length*dx;
45 vsim = fwd_solve(img_h);
46 vsim.meas=vsim.meas + Jm*cur_movei; %Linear
47
48 %calculate the misfit
49 mlist(2) = feval(opt.objective_func,data0,vsim,...
50     cur_movei,prior_e,img_h,img,opt);
51
52 %0 < s1 < s2 < s3 with f(s2) \leq min{ f(s1),f(s3) }
53 for i=1:10 %How many
54     %Increase step length
55     lambda(i+2) = lambda(i+1) + step_length;
56
57     %Data at perturb image (s,v) |-> (s,v) +p*dx(1:n_elemsc)
58     cur_movei = cur_movek + lambda(i+2)*dx;
59     vsim = fwd_solve(img_h);
60     vsim.meas=vsim.meas + Jm*cur_movei;
61
62     %calculate the misfit

```

```

63     mlist(i+2) = feval(opt.objective_func,data0,vsim,...
64         cur_movei,prior_e,img_h,img,opt);
65     if(mlist(i+2) > mlist(i+1))
66         break; %We have a bracket now [i-1,i,i+1]
67     else
68         %Continue iterations
69     end
70 end
71
72 %We have bracket - now quad line fit in log space
73 opt.perturb = [lambda(i),lambda(i+1),lambda(i+2)]
74 mlist = [mlist(i),mlist(i+1),mlist(i+2)]
75 pf = polyfit(opt.perturb, mlist, 2);
76 fmin = -pf(2)/pf(1)/2 % poly minimum for a 2nd order poly
77
78 %Return the current iterate
79 cur_move = cur_movek + fmin*dx;

```

C.4 Electrode and conductivity inverse solver

Electrode and conductivity inverse solver

The following function `inv_solve_abs_GN_diff_tangential.m` computes a simultaneous absolute conductivity and linearised electrode position estimate from the measured voltages.

```

1  function img= inv_solve_abs_GN_diff_tangential( inv_model, data0);
2  %INV_SOLVE_ABS_GN_TANGENTIAL Absolute solver using GN
3  % img= inv_solve_abs_GN( inv_model, data0)
4  % img      => output image (or vector of images)
5  % inv_model => inverse model struct
6  % data0    => EIT data
7
8  %Get the options
9  opt = parse_options(inv_model);
10 img = initial_estimate( inv_model, data0 ); %bckgnd c2f
11
12 %Calculate hyperparameter and RtR (movement prior!!!)

```

```

13 hp = calc_hyperparameter( inv_model );
14 RtR = calc_RtR_prior( inv_model ); hp2RtR= hp^2*RtR;
15
16 % Physics and initial estimates
17 img0 = physics_data_mapper(img);
18 img0.elem_data=inv_model.prior_c;
19 img.elem_data=inv_model.prior_c;
20
21 %get the number of electrodes and coarse elements
22 n_elec=length(inv_model.img_fine.fwd_model.electrode);
23 n_elemsc=inv_model.fwd_model.n_elemsc;
24
25 %We want to get the prior conductivity and tangential change
26 prior_ce=img0.elem_data;
27 prior_ce(n_elemsc+1:n_elemsc+2*n_elec)=inv_model.prior_e;
28 cur_ce=prior_ce;
29 cur_move=prior_ce(n_elemsc+1:n_elemsc+2*n_elec);
30
31 %Get the fine image and coarse model
32 img_h=inv_model.img_fine;
33 mdl_c=inv_model.mdl_coarse;
34
35 %Calculate the electrode components on fine model
36 elec_comp_h=calc_electrode_components(img_h.fwd_model);
37 for jj=1:length(elec_comp_h)
38     elec_posHS(jj,:)=elec_comp_h{jj}.com;
39 end
40 elec_posH = elec_posHS;
41
42 %Compute the dat and regularisaiton residuals
43 vsim=fwd_solve(img_h);
44 data_res=zeros(opt.max_iter+1,1);
45 data_res(1) = 0.5*(vsim.meas-data0)'+(vsim.meas-data0);
46 regu_res=zeros(opt.max_iter+1,1);
47 regu_res(1) = 0;
48
49 %Movement and conductivity Jacobian
50 Jm=jac_move_eidors_elec_tang_only(inv_model.fwd_model,img_h);
51 J = calc_jacobian( img ); J=[J,Jm]; resolve_jacobian=0;

```

```

52
53 %Loop over iterations
54 for i = 1:opt.max_iter
55     %Simulate measured data on FINE image and calc diff data
56     vsim = fwd_solve( img_h );
57     vsim.meas=vsim.meas+Jm*cur_move;
58     dv = calc_difference_data( vsim , data0, img.fwd_model);
59
60     %Jacobian here
61     if(resolve_jacobian==1)
62         %Jacobian adjoint and coarse2fine field to get movement
63         J = calc_jacobian( img ); J=[J,Jm];
64     end
65
66     %Compute the search direction -inv(H)*J'
67     RDx = hp2RtR*(prior_ce - cur_ce);
68     dx = (J'*J + hp2RtR)\(J'*dv + RDx);
69
70     %Perform a linesearch on this using polynomial search
71     opt.line_optimize.hp2RtR = hp2RtR;
72     img.elem_data=cur_ce; %Elem_data with conductivity AND move
73     img0.elem_data=prior_ce;
74     img = feval(opt.line_optimize_func,img, dx, data0, ...
75         img_h, inv_model.c2f2,n_elemsc,Jm,img0,opt.line_optimize);
76
77     %Reassign tangential and conductivity (fine already sorted out)
78     cur_ce = img.elem_data;
79     cur_move=cur_ce(n_elemsc+1:n_elemsc+2*n_elec);
80     img.elem_data = cur_ce(1:n_elemsc);
81
82     %Add coarse data convert to fine differential as a test
83     fine_from_c = inv_model.c2f2*img.elem_data;
84     img_h=mk_image(inv_model.fwd_model,fine_from_c);
85
86     %Calculate the electrode components
87     for jj=1:length(elec_comp_h)
88         %We can then decompose this to update the direction
89         a_i_elec_ii = cur_move(jj)*elec_comp_h{jj}.tangent(:,1) + ...
90             cur_move(jj+n_elec)*elec_comp_h{jj}.tangent(:,2);

```

```

91     %Calculate the new coordinates
92     elec_pos_NEW(jj,1:3) = elec_posHS(jj,1:3) + a_i_elec_ii';
93 end
94 %Get the normals
95 elec_pos_NEW(:,4:6)=elec_pos_NEW(:,1:3);
96
97 %Compute the data residual
98 vsim=fwd_solve(img_h); %This is conductivity change
99 vsim.meas=vsim.meas+Jm*cur_move;
100
101 %The new residuals and message
102 data_res(i+1) = 0.5*(vsim.meas-data0)'*(vsim.meas-data0);
103 regu_res(i+1) = 0.5*(cur_ce-prior_ce)'*hp2RtR*(cur_ce-prior_ce);
104 eidors_msg('%#02d squared summed residual=%.3g', i, ...
105     data_res(i+1)+regu_res(i+1), 1);
106 end
107 img.movement_data = cur_move; %attach tangential movement
108
109 function val = GN_objective_function(data0, data, img_k,img0,opt)
110     dv = calc_difference_data(data, data0, img0.fwd_model);
111     de = img_k.elem_data - img0.elem_data;
112     val = 0.5*( dv'*dv + de' * opt.hp2RtR * de);
113
114 function img = initial_estimate( imdl, data )
115     img = calc_jacobian_bkgnd( imdl );
116     vs = fwd_solve(img);
117     pf = polyfit(data,vs.meas,1);
118     img = physics_data_mapper(img);
119     if isfield(img.fwd_model,'coarse2fine');
120         nc = size(img.fwd_model.coarse2fine,2);
121         img.elem_data = mean(img.elem_data)*ones(nc,1)*pf(1);
122     else
123         img.elem_data = img.elem_data*pf(1);
124     end
125     % remove elem_data
126     img = physics_data_mapper(img,1);
127
128 function opt = parse_options(imdl)
129     try

```

```

130     % for any general options
131     opt = imdl.parameters;
132 end
133 opt.max_iter = 1;
134 try
135     opt.max_iter = imdl.parameters.max_iterations;
136 end
137
138 if isfield(imdl, 'inv_solve_abs_GN');
139     fnames = fieldnames(imdl.inv_solve_abs_GN);
140     for i = 1:length(fnames)
141         opt.(fnames{i}) = imdl.inv_solve_abs_GN.(fnames{i});
142     end
143 end
144
145 if ~isfield(opt, 'line_optimize_func')
146     opt.line_optimize_func = @line_optimize_tangential;
147 end
148
149 if ~isfield(opt, 'line_optimize')
150     opt.line_optimize = [];
151 end
152
153 if ~isfield(opt, 'line_optimize') || ...
154     ~isfield(opt.line_optimize, 'objective_func')
155     % not sure this should be allowed to change
156     opt.line_optimize.objective_func = @GN_objective_function;
157 end
158
159 if ~isfield(opt, 'do_starting_estimate')
160     opt.do_starting_estimate = 1;
161 end

```

Electrode and conductivity prior

The following function `prior_movement_tangential.m` computes an inverse prior covariance matrix for simultaneous conductivity and tangential electrode position reconstruction.

```

1 function Reg= prior_movement_tangential( inv_model );
2 % PRIOR_MOVEMENT calculate image prior
3 % Reg= prior_movement( inv_model )
4 % Reg      => output regularization term
5 % inv_model => inverse model struct
6 % Parameters:
7 %   inv_model.image_prior.parameters(1) movement/image frac
8 %   inv_model.prior_movement.RegC.func = Cond Reg fcn
9
10 % relative strengths of conductivity and movement priors
11 hp_move= inv_model.prior_movement.parameters(1);
12 pp= fwd_model_parameters( inv_model.fwd_model );
13
14 % calc conductivity portion
15 inv_model.RtR_prior = inv_model.prior_movement.RegC.func;
16 pp= fwd_model_parameters( inv_model.fwd_model );
17 RegC= calc_RtR_prior( inv_model);
18 szC = size(RegC,1);
19 RegM = eye((pp.n_dims-1)*pp.n_elec);
20
21 %Create full regularisation
22 RegCM= sparse( szC, (pp.n_dims-1)*pp.n_elec );
23 Reg= [RegC,          RegCM;
24       RegCM', hp_move^2*RegM ];

```

Electrode and conductivity linesearch

The following function `line_optimize_tangential.m` computes a linesearch, for a sufficiently small change in electrode positions, but fully non-linear in the conductivity.

```

1 function [img] = line_optimize_tangential(imgk, dx, data0, ...
2     img_h, c2f2, n_elemsc, Jm, img0, opt)
3 %% Bracket the local minimum - Get 3 points such that
4 %   0 < s1 < s2 < s3 with f(s2) \leq min{ f(s1),f(s3) }
5
6 %Step 1: Get step_length s.t. f(step_length) < f(0)
7 step_length=1;
8 %Copy the image across

```

```

9  img = imgk; img_h.elem_data = c2f2*img.elem_data(1:n_elemsc);
10 vsim = fwd_solve(img_h);
11 vsim.meas=vsim.meas + Jm*img.elem_data(n_elemsc+1:end); %Linear
12
13 %Misfit at 0
14 mlist(1) = feval(opt.objective_func,data0,vsim,img,img0,opt);
15
16 %Iterate through and find minimal point
17 for i=1:10 %while loop here
18     %Data at perturb image (s,v) |-> (s,v) +p*dx(1:n_elemsc)
19     img.elem_data = imgk.elem_data + step_length*dx;
20     img_h.elem_data = c2f2*img.elem_data(1:n_elemsc);
21     vsim = fwd_solve(img_h);
22     vsim.meas=vsim.meas + Jm*img.elem_data(n_elemsc+1:end); %Linear
23
24     %calculate the misfit
25     mlist(i+1) = feval(opt.objective_func,data0,vsim,img,img0,opt);
26     if(mlist(i+1) < mlist(1))
27         break; %Bracket now [i-1,i,i+1]
28     else
29         step_length=step_length/2; %Else try again
30     end
31 end
32
33 %% Get the third point
34 lambda(1)=0; lambda(2)=step_length;
35
36 %Image at current iterate
37 img.elem_data = imgk.elem_data;
38 img_h.elem_data = c2f2*img.elem_data(1:n_elemsc);
39 vsim = fwd_solve(img_h);
40 vsim.meas=vsim.meas + Jm*img.elem_data(n_elemsc+1:end); %Linear
41
42 %calculate the misfit at 0
43 mlist(1) = feval(opt.objective_func,data0,vsim,img,img0,opt);
44
45 %Data at steplength
46 %Perturb image (s,v) |-> (s,v) +p*dx(1:n_elemsc)
47 img.elem_data = imgk.elem_data + step_length*dx;

```

```

48 img_h.elem_data = c2f2*img.elem_data(1:n_elemsc);
49 vsim = fwd_solve(img_h);
50 vsim.meas=vsim.meas + Jm*img.elem_data(n_elemsc+1:end); %Linear
51
52 %calculate the misfit
53 mlist(2) = feval(opt.objective_func,data0,vsim,img,img0,opt);
54
55 %0 < s1 < s2 < s3 with f(s2) \leq min{ f(s1),f(s3) }
56 for i=1:10 %How many
57     %Increase step length
58     lambda(i+2) = lambda(i+1) + step_length;
59
60     %Data at perturb image (s,v) |-> (s,v) +p*dx(1:n_elemsc)
61     img.elem_data = imgk.elem_data + lambda(i+2)*dx;
62     img_h.elem_data = c2f2*img.elem_data(1:n_elemsc);
63     vsim = fwd_solve(img_h);
64     vsim.meas=vsim.meas + Jm*img.elem_data(n_elemsc+1:end); %Linear
65
66     %calculate the misfit
67     mlist(i+2) = feval(opt.objective_func,data0,vsim,img,img0,opt);
68     if(mlist(i+2) > mlist(i+1))
69         break; %Found bracket exit
70     else %continue
71     end
72 end
73
74 %We have bracket - now quad line fit in log space
75 opt.perturb = [lambda(i),lambda(i+1),lambda(i+2)];
76 mlist = [mlist(i),mlist(i+1),mlist(i+2)];
77 pf = polyfit(opt.perturb, mlist, 2);
78 fmin = -pf(2)/pf(1)/2; % poly minimum for a 2nd order poly
79
80 %Return the image
81 img.elem_data = imgk.elem_data + fmin*dx;

```

Appendix D

Mechanical ODE modelling code

The following code computes the ODE modelling results in chapter 6. All plots have been removed for clarity.

```
1 %% DOUBLE LUNG WITH AIRWAY SERIES RESISTANCE AND MULTI-COMPARTMENTS
2 %
3 % MODEL:
4 % Branching two lungs. Single airway resistance.
5 % Model branches into N parallel (lung lobes) with series CR circuits
6 %
7 % VARIABLES:
8 % (i) Inputs: Voltage V(t) at mouth
9 % (ii) States:
10 % (a) Controls: Voltage/current at mouth V(t), \sum I(t)
11 % (b) Voltages V_S(t) after airway resistance (NOT measure)
12 % (c) Compartment charge and derivative (CAN measure)
13 % (iii) Parameters: E R per compartment + lung V0 pleural pressure
14 % (iv) Measure: I(t), V(t) at mouth and Q(t) I(t) at every point
15 %
16 % EQUATIONS:
17 % V(t) - V_S(t) = R_S dot_Q_L(t) %Top branch
18 % dot_Q(t) = dot_Q_L(t) + dot_Q_R(t)
19 % For each lung (A={L,R}) and each compartment (B={1:N}) we have
20 % V_S(t) - V0 = E_A_B (Q_A_B(t)-Q_A_B_0) + R_A_B dot_Q_A_B(t)
21 % dot_Q_A(t) = \sum_{B} dot_Q_A_B(t)
22
23 %Sinusoidal PEEP setting
24 PEEP_freq=0.2; PEEP_min=10; PEEP_max=20;
```

```
25 for run_type=[1,2,3,4,5,6,7]
26 %run_type=1:4 (tikhonov) 5:7 (integrate equations)
27 if(run_type==1)
28     SNR=inf; type=3; alpha_reg_d=0.0000000001;
29 elseif(run_type==2)
30     SNR=100; type=3; alpha_reg_d=0.005;
31 elseif(run_type==3)
32     SNR=50; type=3; alpha_reg_d=0.05;
33 elseif(run_type==4)
34     SNR=25; type=3; alpha_reg_d=0.5;
35 elseif(run_type==5)
36     SNR=100; type=1;
37 elseif(run_type==6)
38     SNR=50; type=1;
39 elseif(run_type==7)
40     SNR=50; type=1;
41 end
42
43 %Total monitoring time, time step increment, sample (Hz)
44 total_time=30; delta_t=0.01;ode_steps=total_time/delta_t;
45 time_stepper=1; %RK4 = 1. Explicit Euler = 2.
46 sample_freq=20; n_sample=sample_freq*total_time; %Alias?
47
48 %% PARAMETERS
49 %Pleural pressure (non measurable) and exhaled volume
50 P_p=0; V_0=6;
51
52 %Number compartments and E, R per compartment
53 n_compartments=3;
54 for j=1:2
55     for i=1:n_compartments
56         E_parallel(i,j)=50;
57         R_parallel(i,j)=20;
58     end
59 end
60 R_series=1.0; %Series resistance
61
62 %High compliance and low elastance for two compartments
63 E_parallel(1,1)=3.0; R_parallel(3,2)=50.0;
```

```

64
65 %Pick out the reconstructed parameters from this matrix
66 for j=1:2
67     for i=1:n_compartments
68         Xm_act(2*n_compartments*(j-1)+1+2*(i-1))=E_parallel(i,j);
69         Xm_act(2*n_compartments*(j-1)+2+2*(i-1))=R_parallel(i,j);
70     end
71 end
72 Xm_act(2*n_compartments*2+1)=R_series;
73 Xm_act(2*n_compartments*2+1+1)=P_p;
74
75 %% INPUT PRESSURE WAVE
76 %Sinusoidal pressure vector simulating PEEP manoeuvre
77 Ptp_s=zeros(ode_steps,1);
78 for i=1:ode_steps
79     t_r = total_time*(i/ode_steps);
80     Ptp_s(i) = PEEP_min + 0.5*(PEEP_max-PEEP_min)* ...
81         ( 1 + sin( 2*pi*PEEP_freq*t_r ) );
82 end
83
84 %% ODE MODEL
85 %Pdot_x = A x + b: x is vol/flow, A is coefficient, b is RHS
86 %Initialise the A,P x, x_dot and b (these will vary over timesteps)
87 x=zeros(2*n_compartments,ode_steps);
88 x_dot=zeros(2*n_compartments,ode_steps);
89 b=zeros(2*n_compartments,ode_steps);
90 A=zeros(2*n_compartments,2*n_compartments);
91 P=zeros(2*n_compartments,2*n_compartments);
92 for i=1:2*n_compartments
93     for j=1:2*n_compartments
94         P(i,j)=R_series;
95     end
96 end
97 for i=1:n_compartments
98     P(i,i)=P(i,i)+R_parallel(i,1);
99     P(i+n_compartments,i+n_compartments)= ...
100         P(i+n_compartments,i+n_compartments)+R_parallel(i,2);
101 end
102

```

```

103 %Set up ODE coefficient matrix A
104 for i=1:n_compartments
105     A(i,i) = -E_parallel(i,1);
106     A(i+n_compartments,i+n_compartments) = -E_parallel(i,2);
107 end
108
109 %Initial values x - exhaled initial condition
110 for i=1:2*n_compartments
111     x(i,1)=V_0/(2*n_compartments); %Distribute evenly
112     x_dot(i,1)=0.0;
113 end
114
115 %Setup RHS vector
116 for i=1:n_compartments
117     for j=1:ode_steps
118         b(i,j) = (Ptp_s(j)-P_p);
119         b(i+n_compartments,j) = (Ptp_s(j)-P_p);
120     end
121 end
122
123 %% FORWARD PROBLEM SOLVE ODE
124 %Find P_inv and P_inv*A
125 P_inv=inv(P); P_invA=P\A;
126 if(time_stepper==1) %RK4 explicit
127 %x_dot(t) = P_invA*x(t) + P_inv*b(t) = f(t,x)
128 %x_{n+1} = x_{n} + 1/6*h*(k_{1}+2k_{2}+2k_{3}+k_{4})
129 %k1 = f(tn,xn)
130 %k2 = f(tn + h/2 , xn + h/2 k1)
131 %k3 = f(tn + h/2 , xn + h/2 k2)
132 %k4 = f(tn + h , xn + h k3)
133 for i=1:ode_steps-1
134     k1 = P_invA*( x(:,i) ) + ...
135         P_inv*( b(:,i) );
136     k2 = P_invA*( x(:,i) + delta_t/2*k1 ) + ...
137         P_inv*( b(:,i) + (b(:,i+1)-b(:,i))*delta_t/2 );
138     k3 = P_invA*( x(:,i) + delta_t/2*k2 ) + ...
139         P_inv*( b(:,i) + (b(:,i+1)-b(:,i))*delta_t/2 );
140     k4 = P_invA*( x(:,i) + delta_t*k3 ) + ...
141         P_inv*( b(:,i) + (b(:,i+1)-b(:,i))*delta_t );

```

```

142     x_dot(:,i) = k1;
143     x(:,i+1) = x(:,i) + (delta_t/6)*(k1+2*k2+2*k3+k4);
144 end
145 x_dot(:,ode_steps) = P_invA*x(:,ode_steps) + P_inv*b(:,ode_steps);
146
147 elseif(time_stepper==2) %Euler explicit
148 %Compute max eigs of P_invA - determines stable timesteps
149 fprintf(1,'Stable Euler step = %2.5f \n',2/abs(max(eig(P_invA))));
150 for i=1:ode_steps-1
151     x_dot(:,i) = P_invA*x(:,i) + P_inv*b(:,i);
152     x(:,i+1) = x(:,i) + delta_t*x_dot(:,i);
153 end
154 x_dot(:,ode_steps) = P_invA*x(:,ode_steps) + P_inv*b(:,ode_steps);
155
156 end
157 %Stiffness ratio
158 fprintf(1,'Stiffness ratio = %1.2f\n', ...
159     max(abs(eig(P_invA)))/min(abs(eig(P_invA))));
160
161 %% SAMPLE THE DATA AT INTERVALS
162 %Sample ODE solution at regular intervals to simulate measured data
163 t_s=zeros(n_sample,1); Ptp=zeros(n_sample,1);
164 V=zeros(2*n_compartments,n_sample);
165 Vdot=zeros(2*n_compartments,n_sample);
166 for i=1:n_sample
167     t_s(i)=total_time*i/n_sample; %Real time
168     Ptp(i)=Ptp_s(ceil(ode_steps*i/n_sample)); %Sample pressure
169     V(1:2*n_compartments,i) = ...
170         x(1:2*n_compartments,ceil(ode_steps*i/n_sample)); %Volume
171     Vdot(1:2*n_compartments,i) = ...
172         x_dot(1:2*n_compartments,ceil(ode_steps*i/n_sample));%Flow
173 end
174
175 %Copy clean signals
176 V_nn=V; Vdot_nn=Vdot; Ptp_nn=Ptp;
177 %Add Gaussian noise
178 V = add_noise(SNR,V); V=V.meas;
179 Vdot = add_noise(SNR,Vdot); Vdot=Vdot.meas;
180 Ptp = add_noise(SNR,Ptp); Ptp=Ptp.meas;

```

```

181 %Copy volume and charge data
182 Vcopy=V; Vdotcopy=Vdot; Ptpcopy=Ptp;
183
184 %Generate flow from volume using inverse integration
185 %TRAPEZIUM RULE
186 Areg=zeros(n_sample,n_sample+1);
187 Ireg=eye(n_sample+1);
188 Areg(:,1)=0.5;
189 Areg(n_sample,n_sample+1)=0.5;
190 for i=1:n_sample-1
191     Areg(i,i+1)=0.5;
192     Areg(i+1:n_sample,i+1)=1.0;
193 end
194 Areg=Areg*(t_r/(n_sample-1));%dx
195
196 %Create the smoothing operator
197 L_2=zeros(n_sample-1,n_sample+1);
198 for kkk=1:n_sample-1
199     L_2(kkk,kkk)=-1;L_2(kkk,kkk+1)= 2; L_2(kkk,kkk+2)=-1;
200 end
201 L_2=L_2/(t_r/(n_sample-1))^2;
202
203 %Numerical integrate
204 if(type==1)
205     %Pressure
206     Ptp_int=zeros(n_sample,1); Ptp_int(1)=0;
207     Ptp_nn_int=zeros(n_sample,1); Ptp_nn_int(1)=0;
208     %Volume
209     V_int=zeros(1:2*n_compartments,n_sample);
210     V_int(1:2*n_compartments,1)=0;
211     V_nn_int=zeros(1:2*n_compartments,n_sample);
212     V_nn_int(1:2*n_compartments,1)=0;
213
214     %Time step for numerical integraiton
215     dt=total_time/n_sample;
216     %First step
217     Ptp_nn_int(2) = 0.5*dt*( Ptp(1)+Ptp(2) );
218     Ptp_int(2) = 0.5*dt*( Ptp(1)+Ptp(2) );
219     V_int(1:2*n_compartments,2) = ...

```

```

220         0.5*dt*( V(1:2*n_compartments,1)+V(1:2*n_compartments,2) );
221     V_nn_int(1:2*n_compartments,2) = ...
222         0.5*dt*( V_nn(1:2*n_compartments,1)+ ...
223         V_nn(1:2*n_compartments,2) );
224
225     %Integrate the derivatives
226     for i=1:n_sample-2
227         %Pressure integral
228         Ptp_int(i+2) = Ptp_int(i+1) + ...
229             0.5*dt*( Ptp(i+1) + Ptp(i+2) );
230         Ptp_nn_int(i+2) = Ptp_int(i+1) + ...
231             0.5*dt*( Ptp_nn(i+1) + Ptp_nn(i+2) );
232         %Volume integral
233         V_int(1:2*n_compartments,i+2) = ...
234             V_int(1:2*n_compartments,i+1) ...
235             + 0.5*dt*( V(1:2*n_compartments,i+1) ...
236             + V(1:2*n_compartments,i+2) );
237         V_nn_int(1:2*n_compartments,i+2) = ...
238             V_nn_int(1:2*n_compartments,i+1) ...
239             + 0.5*dt*( V_nn(1:2*n_compartments,i+1) ...
240             + V_nn(1:2*n_compartments,i+2) );
241     end
242 elseif(type==3) %Generalised Tikhonov
243     %Include the constant term
244     Areg=[Areg,ones(n_sample,1)];
245     L_2=[L_2,zeros(n_sample-1,1)];
246
247     %Regularised inverse of Vdot -> V
248     Reginv_d = (Areg'*Areg+alpha_reg_d*(L_2'*L_2))\Areg';
249     for jj=1:2*n_compartments
250         ccc=Reginv_d*Vcopy(jj,:)';
251         Vdotcopy(jj,:)=ccc(2:end-1)'; %Ignore first/last flow
252         Vcopyrec(jj,:)=Areg*ccc;
253     end
254 end
255
256 if(type==1)
257     %Do nothing
258 else

```

```

259 %Add the charges and currents to show the mouth volume and flow
260 Volu_mouth_nn      = sum(V_nn,1);
261 Volu_mouth         = sum(Vcopy,1);
262 Volu_mouth_rec     = sum(Vcopyrec,1);
263 Flow_mouth_nn      = sum(Vdot_nn,1);
264 Flow_mouth         = sum(Vdot,1);
265 Flow_mouth_rec     = sum(Vdotcopy,1);
266
267 %Sample the volume and flow for each compartment
268 for i=1:n_sample
269     for j=1:n_compartments
270         vol(1,j,i)=V_nn(j,i);
271         vol_n(1,j,i)=V(j,i);
272         vol_n_rec(1,j,i)=Vcopyrec(j,i);
273         vol(2,j,i)=V_nn(j+n_compartments,i);
274         vol_n(2,j,i)=V(j+n_compartments,i);
275         vol_n_rec(2,j,i)=Vcopyrec(j+n_compartments,i);
276         flow(1,j,i)= Vdot_nn(j,i);
277         flow_n(1,j,i)=Vdot(j,i);
278         flow_n_rec(1,j,i)=Vdotcopy(j,i);
279         flow(2,j,i)= Vdot_nn(j+n_compartments,i);
280         flow_n(2,j,i)=Vdot(j+n_compartments,i);
281         flow_n_rec(2,j,i)=Vdotcopy(j+n_compartments,i);
282     end
283 end
284 %Copy across
285 V=Vcopyrec; Vdot=Vdotcopy;
286 end
287
288 %INTEGRATION EQUATIONS
289 if(type==1)
290 % Least squares estimate of the parameters
291 % A - SPARSE:  n_sample*n_compartment x (2*n_compartment)*(2+1) + 1 +
292 % (Q1i,Q1, 1, 0 , 0 , 0 , 0 ,0,0 ... sum(QL/Rdi) t )
293 % (0 , 0 , , 0 , Q2i, Q2 , 1 ,0,0 ... sum(QL/Rdi) t )
294 %
295 % X - parameters to estimate (2*n_compartment)*(2+1) + 1 + 1 vector
296 % order CL1 RL1 AL1 CL2 ..... CR1 RR2 RL2 .... RS P0
297 % where A B are integration constants, P0 is pleural pressure

```

```

298 % D - data n_sample*n_compartment vector P P P P ... P
299 % Write ODE in matrix form P = AX. Least squares estimate of A
300 %       Xhat = arg min ||D - X*A||_{2}^{2}
301
302 %Remove first few integration samples
303 n_sample_int=1:n_sample;
304 n_sample=length(n_sample_int);
305
306 % Explicit formula: Xhat = ( (A'*A)\A' ) * D
307 Am = zeros(n_sample*n_compartment,(2*n_compartment)*(2+1)+1+1);
308 Am_nn=Am;
309 Dm = zeros(n_sample*n_compartment,1); Dm_nn=Dm;
310 Xm = zeros((2*n_compartment)*(2+1)+1+1,1);
311
312 %Independent data as matrix of column vectors
313 for i=1:2*n_compartment
314     Am((i-1)*n_sample+1:i*n_sample,(i-1)*(2+1)+1) = ...
315         V_int(i,n_sample_int)';
316     Am((i-1)*n_sample+1:i*n_sample,(i-1)*(2+1)+2) = ...
317         V(i,n_sample_int)';
318     Am((i-1)*n_sample+1:i*n_sample,(i-1)*(2+1)+3) = ...
319         ones(size(n_sample_int));
320     Dm((i-1)*n_sample+1:i*n_sample,1)=Ptp_int(n_sample_int);
321
322     Am_nn((i-1)*n_sample+1:i*n_sample,(i-1)*(2+1)+1) = ...
323         V_nn_int(i,n_sample_int)';
324     Am_nn((i-1)*n_sample+1:i*n_sample,(i-1)*(2+1)+2) = ...
325         V_nn(i,n_sample_int)';
326     Am_nn((i-1)*n_sample+1:i*n_sample,(i-1)*(2+1)+3) = ...
327         ones(size(n_sample_int));
328     Dm_nn((i-1)*n_sample+1:i*n_sample,1) = ...
329         Ptp_nn_int(n_sample_int);
330 end
331
332 %Add the extra condition for the series resistors
333 V_intS=zeros(size(V(1,n_sample_int)'));
334 V_nn_intS=zeros(size(V(1,n_sample_int)'));
335 for i=1:2*n_compartment
336     V_intS = V_intS + V(i,n_sample_int)';

```

```

337
338     V_nn_intS = V_nn_intS + V_nn(i,n_sample_int)';
339 end
340
341 %Add the extra for the series resistances
342 for i=1:2*n_compartments
343     Am((i-1)*n_sample+1:i*n_sample,2*n_compartments*(2+1)+1) = ...
344         V_intS;
345
346     Am_nn((i-1)*n_sample+1:i*n_sample,2*n_compartments*(2+1)+1) = ...
347         V_nn_intS;
348 end
349 for i=1:2*n_compartments
350     %Add the ones for the pleural pressure
351     Am((i-1)*n_sample+1:i*n_sample,2*n_compartments*(2+1)+1+1) = ...
352         t_s(n_sample_int);%
353     Am_nn((i-1)*n_sample+1:i*n_sample,2*n_compartments*(2+1)+1+1)=...
354         t_s(n_sample_int);%
355 end
356
357 %Least squares inverse
358 Xm_int = (Am'*Am)\Am'*Dm;
359 Int_Recon_Xm{run_type}.Xm=Xm_int;
360 Xm_nn_int = (Am_nn'*Am_nn)\Am_nn'*Dm_nn;
361
362 %Print out the absolute difference in sensitivity
363 fprintf(1,' Actual No Noise Noise %3.0f SNR\n',SNR);
364 cnt=0;
365 for j=1:2*n_compartments*(2+1)+1+1
366     cnt=cnt+1;
367     if(mod(j,3)==0)
368         cnt=cnt-1;
369         fprintf(1,' %2.2f %2.2f %2.2f\n', ...
370             0, Xm_nn_int(j), Xm_int(j));
371     else
372         fprintf(1,' %2.2f %2.2f %2.2f\n', ...
373             Xm_act(cnt), Xm_nn_int(j), Xm_int(j));
374     end
375 end

```

```

376
377 else
378
379 %INVERSE INTERGATION
380 % Least squares estimate of the parameters
381 % A - SPARSE n_sample*n_compartment x (2*n_compartment)*3 + 1 + 1
382 % (Q1,Q1d,Q1dd,0 , 0 ,0 , 0 ... sum(QL/Rdi) 1)
383 % (0 , 0 , 0 ,Q2,Q2d,Q2dd, 0 ... sum(QL/Rdi) 1)
384 % X - parameters to estimate (2*n_compartment)*3 + 1 +1 vector
385 % order EL1 RL1 LL1 EL2 ..... LLN ER1 RR2 RL2 ..... RS PO
386 % D - data n_sample*n_compartment vector P P P P ... P
387 % Write the ODE in matrix form P = AX. Least squares estimate of A
388 % Xhat = arg min ||D - X*A||_{2}^{2}
389 % Explicit formula: Xhat = ( A'*A)\A' )*D
390
391 %Sampling lengths
392 n_sample_int=1:n_sample;
393 n_sample=length(n_sample_int);
394 Am = zeros(n_sample*n_compartment,(2*n_compartment)*2+1+1);
395 Am_nn=Am;
396 Dm = zeros(n_sample*n_compartment,1); Dm_nn=Dm;
397
398 %Independent data as matrix of column vectors
399 for i=1:2*n_compartment
400     Am((i-1)*n_sample+1:i*n_sample,(i-1)*2+1) = ...
401         V(i,n_sample_int)';
402     Am((i-1)*n_sample+1:i*n_sample,(i-1)*2+2) = ...
403         Vdot(i,n_sample_int)';
404     Dm((i-1)*n_sample+1:i*n_sample,1) = ...
405         Ptp(n_sample_int);
406
407     Am_nn((i-1)*n_sample+1:i*n_sample,(i-1)*2+1) = ...
408         V_nn(i,n_sample_int)';
409     Am_nn((i-1)*n_sample+1:i*n_sample,(i-1)*2+2) = ...
410         Vdot_nn(i,n_sample_int)';
411     Dm_nn((i-1)*n_sample+1:i*n_sample,1) = ...
412         Ptp_nn(n_sample_int);
413 end
414

```

```

415 %Add extra condition for series resistors
416 VdotS=zeros(size(Vdot(1,n_sample_int)'));
417 VdotS_nn=VdotS;
418 for i=1:2*n_compartments
419     VdotS = VdotS + Vdot(i,n_sample_int)';
420     VdotS_nn = VdotS_nn + Vdot_nn(i,n_sample_int)';
421 end
422
423 %Add the extra for the series resistances
424 for i=1:2*n_compartments
425     Am((i-1)*n_sample+1:i*n_sample,2*n_compartments*2+1) = ...
426         VdotS;
427     Am_nn((i-1)*n_sample+1:i*n_sample,2*n_compartments*2+1) = ...
428         VdotS_nn;
429 end
430
431 %Add the ones for the pleural pressure
432 Am(1:end,2*n_compartments*2+1+1)=1;
433 Am_nn(1:end,2*n_compartments*2+1+1)=1;
434
435 %Least square inverse
436 Tik_Recon_Xm{run_type}.Xm = (Am'*Am)\Am'*Dm;
437 Xm_nn = (Am_nn'*Am_nn)\Am_nn'*Dm_nn;
438
439 end
440 end
441
442 %Print out the absolute difference in sensitivity
443 fprintf(1,' Actual No Noise and Noisy decreasing SNR');
444 for j=1:2*n_compartments*2+1+1
445     fprintf(1,' %2.2f %2.2f %2.2f %2.2f %2.2f %2.2f\n',
446         ...
447         Xm_act(j), Xm_nn(j), Tik_Recon_Xm{1}.Xm(j), ...
448         Tik_Recon_Xm{2}.Xm(j), Tik_Recon_Xm{3}.Xm(j), ...
449         Tik_Recon_Xm{4}.Xm(j));
449 end

```